Traitement tout-optique du signal à base de nouvelles fibres optiques non-linéaires

Sy Dat Le

N° d'ordre : 2012REN1E013 **ANNÉE 2012**

UNIVERSITÉ DE RENNES 1

ueb

THÈSE / UNIVERSITÉ DE RENNES 1
sous le sceau de l'Université Européenne de Bretagne

pour le grade de

DOCTEUR DE L'UNIVERSITÉ DE RENNES 1

Mention : Physique

Ecole doctorale : Sciences de la Matière

présentée par

Sy Dat LE

Préparée à l'unité de recherche FOTON CNRS UMR 6082
Equipe SYSTEMES PHOTONIQUES
U.F.R. S.D.L.M.

TRAITEMENT TOUT-OPTIQUE DU SIGNAL A BASE DE NOUVELLES FIBRES OPTIQUES NON-LINEAIRES

Thèse soutenue à Lannion
le 11/12/2012

devant le jury composé de :

Philippe DELAYE
Directeur de Recherche CNRS, Institut d'optique
Rapporteur

Christophe FINOT
Professeur, Université de Bourgogne
Rapporteur

Periklis PETROPOULOS
Professeur, University of Southampton, UK
Examinateur

Thibault SYLVESTRE
Chargé de recherche, Université de Franche-Comté
Examinateur

Johann TROLES
Professeur, Université de Rennes 1
Examinateur

Thierry CHARTIER
Maître de conférences, Université de Rennes 1
Directeur de thèse

All-Optical Signal Processing Based on New Nonlinear Optical Fibers

by

Sy Dat LE

Submitted in Partial Fulfillment

of the

Requirements for the Degree

Doctor of Philosophy

in

Physics

Supervised by

Thierry CHARTIER

FOTON CNRS UMR 6082
U.F.R. S.D.L.M.

University of Rennes 1
France

2012

To my wife, Huyen Thu,
and our children, Minh Dang and Lam Giang

Acknowledgements

Firstly, I would like to express my sincere gratitude to my supervisor, Dr. Thierry Chartier for the guidance, advice, and encouragement he has provided throughout my thesis. He has always shown me great kindness, both in work and in life, that has helped me much over the last three years in Lannion.

I would like to thank the examiner board: Dr. Philipe Delaye, Prof. Christophe Finot, Prof. Periklis Petropoulos, Dr. Thibaut Sylvestre and Prof. Johann Troles for agreeing to be the reviewers and examiners of my thesis.

I would like to thank the directors of the Foton laboratory, Prof. Jean-Claude Simon and Prof. Pascal Besnard, for having me as a PhD student in the Foton laboratory.

The work in the thesis has been contributed to by many individuals from the Foton Laboratory. In particular, I would like to thank Laurent Bramerie, Mathilde Gay, Marcia Costa e Silva, Sébastien Lobo, Monique Thual and PhD students Duc Minh Nguyen, Kevin Lenglé, and Kenny Hey Tow, from all of whom I have received good advice and have had the pleasure of working with. I also wish to express my sincere thanks to all the Foton members and Enssat staff who helped me, not only my work but also with administrative business.

I warmly thank Art O'Hare for his patience in correcting my English grammar during the manuscript preparation. Our discussions also helped me to much improve the quality of the thesis.

The thesis has been carried out in collaboration with our partners Perfos and EVC. I would like to thank to Perfos and EVC personnel, particularly Laurent Brilland, Johann Troles, and Perrine Toupin for fiber fabrication.

My sincere thanks are due to the Conseil Régional de Bretagne, the Conseil Général des Côtes d'Armor, the European Union Feder program, and the French government for financial support which enabled me to come and pursue a PhD in France.

To the Vietnamese people in Lannion, we are a community of solidarity. I warmly thank all of them for their friendship and for their generous help.

Lastly, I would like to thank my parents and my siblings for all their love and encouragement.

Most of all, thanks to my loving, supportive, encouraging wife, Huyen Thu, whose love and faith have supported me in my PhD studies.

Finally, I dedicate this PhD thesis to my lovely children, Minh Dang and Lam Giang.

Lannion, France
December 2012

Contents

Introduction

The growth of network capacity is nowadays at an almost incredible rate. This is driven by both an increase in the number of connections as well as the demand for higher bandwidth applications, mainly for high-resolution video contents. Optical transmission systems are the unique choice due to their capacity, distance capability, and propagation quality. Nowadays, not only are backbone transmission networks optical but also access networks are being widely developed with passive optical network (PON) based fiber-to-the-x (FTTx). A lot of studies on increasing the bandwidth of optical transmission systems have been carried out. For signals modulated at bit rates higher than 50 Gb/s, conventional signal processing, which is limited to about 50 GHz due to a limitation in electric domain of the optical-electrical-optical (O-E-O) conversions, can not be used. As a result, high-bit-rate optical signals need to be directly processed in the light domain. This is *all-optical signal processing*. All-optical signal processing is a technological terminology which includes all the optical engineering that deals with operations on, or analysis of, optical signals while eliminating the need for O-E-O conversions.

Exploiting nonlinear effects is a solution for all-optical signal processing and optical fibers are an excellent choice as a nonlinear medium. The study of nonlinear propagation in optical fiber dates back to the early 1970s [1]. Soon after this, researchers at Bell labs used silica fibers for demonstrating a variety of nonlinear effects, including stimulated Brillouin scattering (SBS) [2], stimulated Raman scattering (SRS) [3], self-phase modulation (SPM) [4], and four-wave mixing (FWM) [5]. It led to the advent of a new branch of nonlinear optics that became an active area of research during the 1980s. Since then, the field of nonlinear fiber optics has grown considerably. Recently, with the advent of highly nonlinear fibers (HNLFs) and microstructured optical fibers (MOFs), nonlinear fiber optics has particularly become more interesting.

Highly nonlinear fibers (HNLFs) are silica optical fibers but with a smaller core and a higher core dopant concentration than standard single-mode fibers (SMFs) used for signal transmission. This allows HNLFs having a higher nonlinear coefficient γ than SMFs. Typically, the nonlinear coefficient γ of HNLFs can reach 20 $W^{-1}km^{-1}$ [6] while it is only 1.3 $W^{-1}km^{-1}$ for SMFs [7]. The first HNLF with relatively low attenuation was developed by Nippon Telegraph and Telephone Corporation (NTT) in 1986 [8]. In 1997, the Sumitomo

company demonstrated a dispersion-shifted HNLF with a zero-dispersion wavelength λ_{ZD} at 1550 nm [9]. The use of HNLFs in all-optical signal processing has been widely demonstrated [10]. HNLFs, however, have the drawbacks of λ_{ZD} fluctuations along the fiber [11] and low SBS threshold which limit their use for some applications.

Dispersion is an important parameter of optical fibers, not only for HNLFs but also for transmission fibers. Usually, a dispersion-managed transmission link uses two types of SMFs with opposite sign of dispersion in a map length equal to (or more than) the amplifier span. However, the performance of conventional dispersion-managed systems fails as the bit-rate of the signal grows [12]. Dense dispersion-managed (DDM) fibers are fibers with a periodic dispersion map shorter than the amplification map. DDM fibers have been proposed for bit-rate transmission higher than 40 Gb/s [13]. The use of DDM fibers for nonlinear optical signal processing is an interesting objective that should be considered.

Microstructured optical fibers (MOFs) began to be studied in the early 1990s [14]. Research on MOFs was initially motivated to create fibers with the desire of light guidance by means of a photonic band-gap effect. This mechanism allows a guidance in a hollow core. Such air-guiding hollow-core fibers may have low nonlinearity and high damage threshold. However, the first successful MOF was fabricated with a solid core surrounded by an array of air holes allowing for light guiding relying on core-cladding refractive index difference. With solid-core MOFs, the core-diameter of fibers can be reduced much more compared with step-index fibers leading to an increase of the nonlinear coefficient γ. They are now an active branch of nonlinear fiber optics, and are most often used when aiming at all-optical signal processing applications, supercontinuum generation, or fiber-based lasers. For silica-based MOFs, to the best of our knowledge, the highest nonlinear coefficient γ is 70 $\mathrm{W^{-1}km^{-1}}$ [15]. This value is obtained with a very strong confinement of light in the fiber core, close to the physical limit of guiding. Due to the relatively low nonlinear refractive index n_2 of silica (2.6×10^{-20} $\mathrm{m^2/W}$) this value is the maximum that can be achieved in silica fibers. For higher nonlinearity, one need to think about other nonlinear materials such as bismuth, tellurite, chalcogenide, etc.

Chalcogenide glasses, whose nonlinear refractive index may be up to 500 times [16] greater than that of fused silica, have attracted much interest for nonlinear fiber optics. Chalcogenide glasses contain one element or more of the chalcogen elements from Group 6a of the periodic table of elements. Chalcogenide glasses also have a fast response time in the femtosecond range, which is much faster than semiconductor optical amplifiers (SOA) or saturable absorbers (SA), leading to much interest for high-bit-rate telecommunications applications. Although the first chalcogenide fiber was reported in 1960s [17], the use of chalcogenide fibers became widespread only in the 2000s when the fiber losses and nonlinearity were improved. The first chalcogenide MOF was demonstrated in 2000 [18]. Many chalcogenide MOFs were then fabricated with the aim of nonlinearity enhancement. With the purpose of being applied in the field of all-optical signal processing, supercontinuum

generation, fiber lasers, and optical sensors, many studies on the fabrication of chalcogenide MOFs have been performed. Particularly, chalcogenide MOFs, which have the advantage of a high magnitude of the nonlinearity-length product (γL) are one of the most interesting choice for highly nonlinear components.

In that context, my PhD thesis topic *"all-optical signal processing based on new nonlinear optical fibers"* has been proposed in 2009 in order to exploit highly nonlinear optical fibers for high bit rate all-optical signal processing. This work is financially supported by the *Conseil Régional de Bretagne* and the *Conseil Général des Côtes d'Armor* and has been carried out in the framework of a collaboration between the Foton laboratory (UMR CNRS 6028), the EVC (Equipe Verres et Céramiques, UMR 6226 Sciences Chimiques de Rennes), and PERFOS, the R&D platform of Photonics Bretagne.

The collaboration between these three partners began in 2005 with the PhD thesis of T. N. Nguyen (defended in 2008 at Foton laboratory) [19]. One objective of the thesis was the demonstration of efficient optical regenerators based on chalcogenide MOFs. As the thesis began, the first chalogenide fibers were fabricated and a nonlinear coefficient of 200 $W^{-1}km^{-1}$ was achieved. In 2007, the project received the support of the *Agence Nationale de la Recherche* in the framework of the FUTUR project (2007-2010) and the *Laboratoire Interdisciplinaire Carnot de Bourgogne* (UMR CNRS 6303) came to reinforce the consortium. This work also received additional financial support from the *Ministère de l'Enseignement Supérieur et de la Recherche* (2008-2011) and the *Université Européenne de Bretagne* (2009-2010). This collaborative work has also benefited from some achievements obtained during the PhD thesis of D. M. Nguyen, defended in November 2011, at Foton laboratory [20].

During these years of collaboration, much progress has been made on the fabrication of chalcogenide MOFs. In 2009, at the time of my thesis began, the consortium has been able to demonstrate highly-efficient nonlinear effects in a chalcogenide MOF with a nonlinear coefficient of 15000 $W^{-1}km^{-1}$ [21]. Even if it constitutes a major result in the field of nonlinear fibers, the value of loss in this fiber (15 dB/m) did not allow demonstration high-performance all-optical signal processing achievements.

In 2009, the objectives of my thesis could be summarized in the following points:

- Contribution to the study of highly-nonlinear chalcogenide fiber designs with the aim of increasing the nonlinearity and reducing the fiber losses and the coupling losses.
- Characterisation of the newly fabricated fibers (loss, propagation modes, dispersion, nonlinear effects, etc.).
- Study of fiber-based all-optical functions such as regeneration, wavelength conversion, optical demultiplexing at bit rates from 40 Gb/s to 160 Gb/s. The material may be silica, chalcogenide glasses or others.

- Testing experimentally the system performance of the all-optical functions based on the new nonlinear fibers.

The thesis is organized in four chapters. The contents of each chapter are outlined as following:

Chapter 1: The thesis starts with a broad introduction to optical transmission systems including optical transmitters, optical receivers, and optical fibers. A large part of this chapter deals with nonlinear fiber optics. Dispersion-tailored fibers and nonlinear fibers, which will be used for all-optical signal processing applications in the following chapters, are reviewed. The criteria used to assess the performance of an optical communication system are described. In this chapter also, an overview of all-optical signal processing is provided to make clear the following discussions. The following chapters describe the main topics of this project.

Chapter 2: The influence of not only the second-order dispersion but also the third-order dispersion on a Mamyshev 2R regenerator at high bit-rate is numerically investigated. Dense dispersion-managed (DDM) fibers are proposed with the aim of avoiding dispersive effects in the 2R regeneration. A 160 Gb/s 2R regeneration using a single DDM fiber is demonstrated theoretically.

Chapter 3: This chapter considers nonlinear chalcogenide fibers. Characterization methods, which are used to characterize chalcogenide fibers, are presented. A large part of this chapter is dedicated to presenting chronologically the evolution of the nonlinear chalcogenide fibers we have studied. We report, in this chapter, records of nonlinearity for MOFs. The advantages as well as the disadvantages of the MOFs are highlighted. Then, solutions to overcome the drawbacks will be discussed.

Chapter 4: This chapter is devoted to the demonstration of nonlinear chalcogenide fibers for all-optical signal processing applications. Two elementary functions, wavelength conversion and time-division demultiplexing, are presented. We experimentally demonstrate, for the first time in chalcogenide MOFs, all-optical wavelength conversion for 42.7 Gb/s on-off keying (OOK) signal, 56 Gb/s differential quadrature phase shift keying (DQPSK) signal, and 170.8 Gb/s OOK signal. For all-optical demultiplexing, we experimentally demonstrate demultiplexing of a 85.4 Gb/s signal down to 2 channels at 42.7 Gb/s and demultiplexing of a 170.8 Gb/s signal down to 4 channels at 42.7 Gb/s. Total powers used in these experiments are compatible with telecommunications and better, in some cases, than the state of the art.

Chapter 1

Optical communication systems and nonlinear optics

Development of fibers and devices for optical communications began in the early 1960s [22]. Modern optical communications indeed has been developed dramatically from the 1980s after the advent of low losses optical fibers and optical amplifiers. Nowadays, optical communication systems are the most important for data transport due to the long distances and huge capacities. An generic optical communication system is shown in Figure 1.1. It consists of an optical transmitter, an optical fiber for propagation of light and an optical receiver. The transmitter converts the input electrical signal into light and couples light into the optical fiber. Transmitted along the optical fiber, light reaches the optical receiver. The receiver then re-converts the light back to an electrical signal.

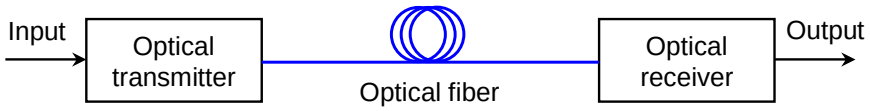

Figure 1.1: Diagram of a generic optical communication system.

This chapter considers all the fundamental elements of an optical communication system as well as nonlinear optics. We introduce, in the first section, the comprehension of optical transmitters and receivers. In this section, the optical signal criteria used to assess quantitatively the signal are also discussed. Basic concepts on optical fibers are provided in Section 1.2. This section considers not only geometric description of optical fibers but also the physical understanding of wave propagation. Section 1.3 deals with optical dispersion-tailored fibers which can be used to limit the influence of dispersion on optical transmission and in all-optical regeneration at high bit-rate (being demonstrated in Chapter 2). Particular attention is paid to nonlinear effects in optical fibers in Section 1.4. Nonlinear fibers are described in Section 1.5 with the emphasis on non-silica nonlinear fibers which will be considered further in Chapter 3. Section 1.6 introduces nonlinear all-optical signal processing for telecommunications, which will be considered in Chapter 4.

1.1 Optical transmitter and receiver

The role of an optical transmitter is to convert an electrical signal into an optical signal which carries the same data as in the electrical signal. Generally, the two main components of a transmitter are the laser source and the modulator as seen in Figure 1.2.

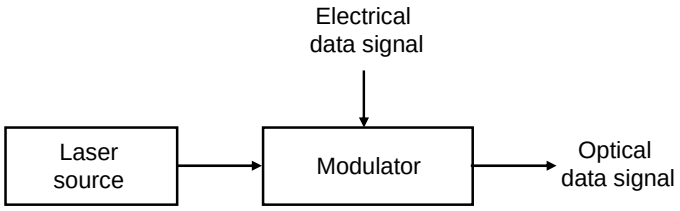

Figure 1.2: Generic scheme of an optical transmitter.

1.1.1 Transmitter

1.1.1.1 Laser

The laser sources of optical transmitters are semiconductor lasers which exhibit many advantages for optical fiber communication: compact size, high efficiency of electron/photon conversion, emission in a telecommunication wavelength range of 1550 nm, and possibility of direct modulation through the injection current. Semiconductor lasers also have relatively narrow spectra and low power consumption.

A laser is a device that emits light through the phenomenon of stimulated emission. In a semiconductor, an electron can pass from one state to another in three different ways (Figure 1.3):

- Absorption: the principle of absorption is illustrated in Figure 1.3(a). If the photon energy $h\nu$ of the incident light of frequency ν is about the energy difference $E_g = E_2 - E_1$, the photon is absorbed, then an electron moves from the ground state E_1 (electron and hole combined) to exited state E_2 (electron in the conduction band and hole in the valence band).

- Spontaneous emission: the principle of spontaneous emission is illustrated in Figure 1.3(b). In a proper condition, the excited electron can fall from the high energy level to the lower energy level to emit photons in random directions with no phase relationship among them.

- Stimulated emission: the principle of stimulated emission is illustrated in Figure 1.3(c). This is initiated by an existing photon. The electron can fall into the lowest energy state (ground state) by emitting photons which have the same frequency, the same phase, the same polarization state and the same directivity as the incident photon. The stimulated emission introduces the concept of gain or amplification of the incident radiation since, from one photon, two are obtained.

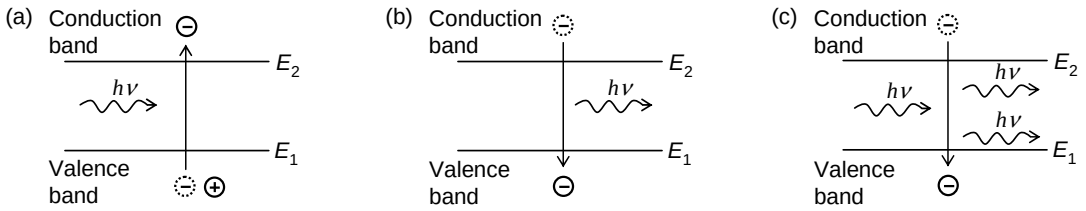

Figure 1.3: Three fundamental processes occurring between the two energy states of an electron: (a) absorption, (b) spontaneous emission, (c) stimulated emission.

In an optical laser, the major component is optical cavity, which is a specially sized chamber with two face-to-face mirrors as seen in Figure 1.4. The two reflective surfaces of mirrors cause photons trapped inside to reflect back and forth through the gain medium, increasing in number with each pass. When this effect reaches equilibrium, the gain is said to be saturated and the output beam becomes true laser light. Different gain mediums can emit light with different wavelengths.

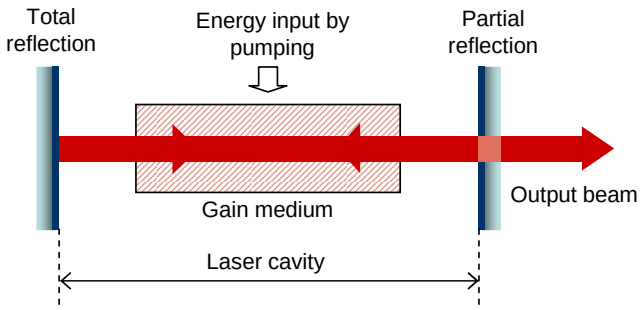

Figure 1.4: Laser cavity with a semiconductor gain medium.

The laser cavity has several important functions. It helps the light increase in intensity by multiple passes through the gain medium so that it rapidly builds up into an intense beam. The cavity ensures that the divergence of the beam is small. Only light that travels in a direction closely parallel to the axis of the cavity can undergo multiple reflections at the mirrors and make multiple passes through the gain medium. The other photons go out of the cavity. The laser cavity also improves the spectral purity of the laser beam because the gain medium will normally amplify light within a narrow range of wavelengths.

To have an effective laser generated by stimulated emission, two conditions must be fulfilled. First, the number of electrons in the state of higher energy must be more than in the lower energy state. When this occurs, the population inversion is achieved. In a semiconductor, this inversion is attained by the "pumping" operation whose role is to provide electrical energy to electrons so that they pass into the conduction band. Secondly, number of photons passing through the gain medium must be sufficient to compensate for the losses due to transmission. For this, it requires light energy to accumulate in a limited volume such as in a resonant Fabry-Perot cavity, for example.

All lasers, including semiconductor lasers, emit light through the process of stimulated emission and are said to emit coherent light. In contrast, a light-emitting diode (LED) emits light through the incoherent process of spontaneous emission. Figure 1.5 illustrates the transfer function of the electrical/optical conversion of a laser.

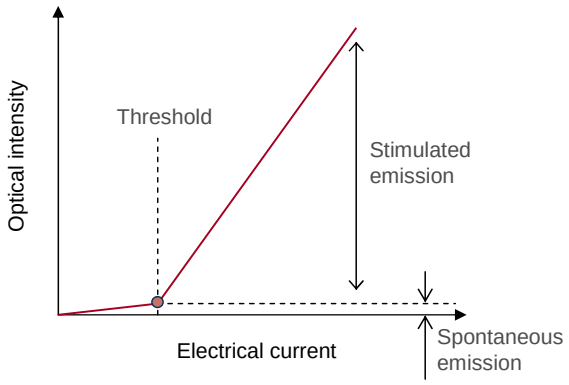

Figure 1.5: Transfer function of electrical/optical conversion of a laser.

Lasers can operate continuously or by emitting optical pulses. The spectral width of a continuous wave (CW) laser is usually in the range 10 kHz - 100 MHz while a picosecond pulse laser has a spectral width of the order of 100 GHz ($\sim$ 1 nm). Figure 1.6 shows examples of the spectrum of a CW laser (Figure 1.6(a)), and a mode-locked fiber laser (Figure 1.6(b)). For the CW laser the linewidth is not resolved by the optical spectrum analyser (resolution of 0.07 nm). For comparison, the spectrum of a broadband source, based on amplified spontaneous noise, is also represented (Figure 1.6(c)).

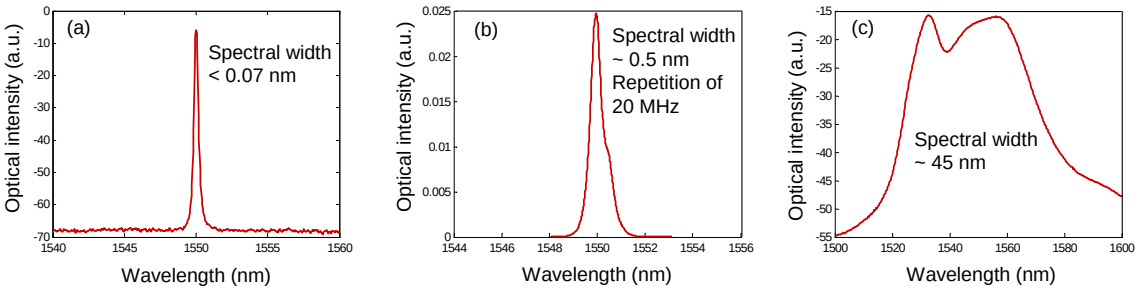

Figure 1.6: Spectra of (a) a continuous laser, (b) a pulsed laser, and (c) a broadband source.

1.1.1.2 Signal modulation

An optical data signal is obtained by modulating the light from a laser using a modulator. In some cases, the output light of semiconductor lasers is directly modulated through the injection electrical current. This direct modulation allows the reduction of the transmitter cost. It, however, has a limitation of bit rate about 10 Gb/s and the modulated signal is chirped (frequency fluctuation). External modulation is therefore widely used. Here, the

modulator is separate from the laser as shown in Figure 1.2. It modulates the continuous optical signal from a laser to carry data obtained from a electrical signal.

In current optical systems, two common types of modulator are used: ElectroAbsorption (EA) modulators and $LiNbO_3$ modulators in a Mach-Zehnder interferometer configuration. EA modulators have the advantage of a potential modulation as high as 100 GHz. But the most attractive feature of the EA modulators is that they can easily be integrated on to the same chip as a semiconductor laser to achieve compact, low cost, and tunable transmitters. The high performance of a 40 Gb/s transmitter using a EA modulator with wavelength tunability covering the whole C-band was demonstrated [23]. However, the residual chirp on the optical signal generated by EA modulators still limits their application range. On the other hand, the $LiNbO_3$ modulators in a Mach-Zehnder interferometer can provide chirpless optical signal. This property, among others, explains their use in optical transmission systems. Another great advantage of $LiNbO_3$ modulators is their extinction ratios which may exceed 20 dB. They can also be modulated at high speeds, up to 75 GHz.

Modulation formats

In optical communication systems, optical signals are digitally encoded. This means that the optical signal comprises a number of pulses or symbols, which carries "one" and "zero" bits of the data. Each symbol corresponds to one or more bit ("1" or "0") depending on the modulation types. The *data rate* or *bit rate* is the number of bits transmitted in a time interval of one second and expressed in bit/s. Each bit corresponds to an elementary interval of time called bit duration (T_{bit}) which is equal to the inverse of the bit rate (Figure 1.7). For example, bit duration T_{bit} of an optical signal at 40 Gb/s is 25 ps. Each pulse corresponds to a period of time which is called pulse duration. The number of symbols transmitted per second is known as *baud rate* or *modulation rate*, expressed in Bd/s. For example, a differential quadrature phase shift keying (DQPSK) optical signal with a bit rate of 56 Gb/s means its baud rate is 28 GBd/s since in DQPSK modulation a pulse carries two bits.

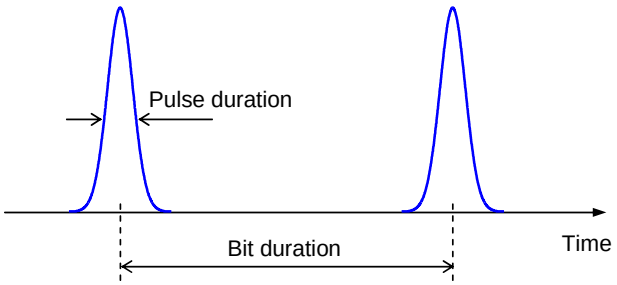

Figure 1.7: Illustration of bit duration and pulse duration of a modulated signal.

Modulation formats define the association between the "0" bit and "1" bit, and physical parameters of the optical carrier. In general, modulation schemes can be amplitude modulated (ASK for amplitude shift keying), frequency modulated (FSK for frequency shift keying) or phase modulated (PSK for phase shift keying). The most largely used formats in

current telecommunication systems are the ASK and PSK formats. In ASK modulation, the intensity of the light is modulated such that the presence of light corrresponds to the symbol "1" and the absence of light to the symbol "0". In PSK modulation, the light is present for both symbols but there is a phase difference between two symbols "1" and "0". In fact, in PSK modulation, the signal amplitude is also modulated. There are several different types of PSK modulation such as binary phase-shift keying (BPSK), differential phase-shift keying (DPSK), DQPSK, etc. that helps to utilize optical bandwidth efficiently. For example, the 56 Gb/s DQPSK signal above requires a bandwidth of only 28 GHz. Note also that on-off keying (OOK) is the simplest form of ASK modulation. In this work, we consider signals of both ASK and PSK modulations (in Chapter 4).

For both ASK and PSK modulation, two common formats are the return-to-zero (RZ) and the non-return-to-zero (NRZ) formats. For an NRZ format signal, the signal amplitude is maintained constant during the whole bit duration T_{bit} and remains unchanged between two consecutive bits exhibiting identical symbols. Therefore, there is no return to the zero level between two consecutive "1" symbols. In other words, a succession of several "1" symbols corresponds to a constant intensity of the optical signal during the total duration of all these bits. An example of a NRZ signal in time domain is displayed in Figure 1.8(a).

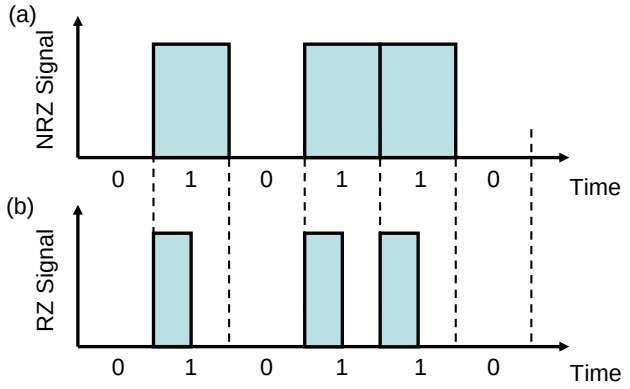

Figure 1.8: Examples of (a) NRZ and (b) RZ format signals.

For a RZ format signal, the signal amplitude is not constant during the whole bit duration but drops to zero between each pulse. A "0" symbol corresponds to the absence of light, and a "1" symbol corresponds to the presence of light exhibiting time dependent amplitude. In this case, it is said that "1" symbols are expressed by optical pulses. Depending on the ratio between the pulse duration and the bit duration (duty cycle), several types of RZ formats can be considered as RZ-66% duty cycle, RZ-33% duty cycle, etc. An example of an RZ-50% signal in the time domain is displayed in Figure 1.8(b).

Modulated-signal spectrum

The optical spectrum of a light source in general or a modulated signal in particular contains information on how the optical power is distributed over different wavelengths. Usually, the spectrum represents the power spectral density plotted as a function of the

wavelength or the optical frequency. Depending on the type of modulation format used, the spectra of different modulated format signals are different. Figure. 1.9 shows examples of spectra of three types of modulated signal. The spectrum of a 40 GHz clock signal is shown in Figure 1.9(a). The spectra of an intensity-modulated signal at 40 Gb/s RZ-33% and a phase-modulated signal at 56 Gb/s RZ-50% are illustrated in Figure 1.9(b) and Figure 1.9(c), respectively. Note that, since a clock signal (Figure 1.9(a)) carries no information, its spectrum only consists in modulation lines, separated by a multiple of the modulation frequency.

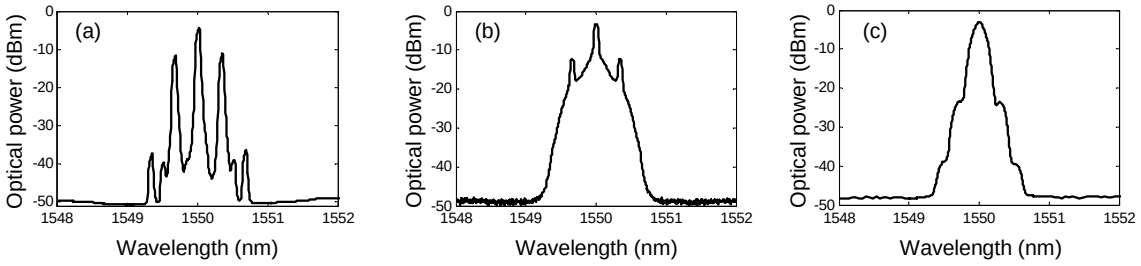

Figure 1.9: Examples of spectra of (a) 40 GHz clock signal (b) a 40 Gb/s OOK RZ-33% data signal, and (c) a 56 Gb/s DQPSK RZ-50% signal.

1.1.2 Receiver

The transmitter and the receiver are located at the ends of transmission links. They have opposite functions. If the role of the transmitter is to convert an electrical signal into an optical signal, then the role of an optical receiver is to convert the optical signal back into an electrical form and recover the data transmitted through the transmission system. The receiver's main component is a photodetector or photodiode that converts light into electrical current through the photoelectric effect. The generic scheme of a receiver which is used for intensity modulation with direct detection is illustrated in Figure 1.10.

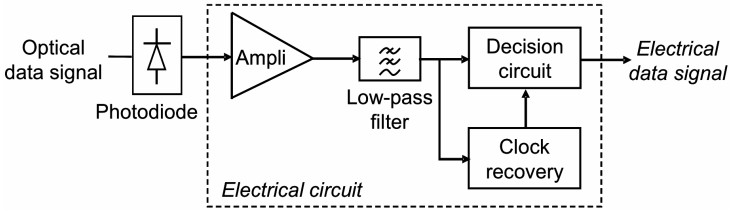

Figure 1.10: Generic scheme of an optical receiver.

The optical data signal arriving at the receiver is detected by a photodiode. The photodiode converts the optical data stream into a time-dependent electrical current signal. The signal is amplified by a high-gain amplifier and filtered by a low-pass filter for noise reduction. After being filtered, the signal is processed by a decision circuit for data recovery. Simultaneously, a fraction of the signal is sent to a clock recovery circuit which provides

a time reference for sampling. The decision circuit compares input electric intensities to a threshold and takes a decision on whether a "1" or "0" bit is present at that moment.

Detection schemes can be *direct detection* or *coherent detection*. Figure 1.11 illustrates the two detection schemes. In a direct detection receiver, the incoming optical signal at the receiver input is directly converted to an electrical current using a photodiode. In coherent detection, the incoming optical signal is mixed with light from a local oscillator. With coherent detection, the phase information of the optical signal is preserved after the opto-electric detection. For an ASK (OOK) signal, in which information is encoded on the amplitude (power) of the optical signal, direct detection is normally used. For a PSK signal, coherent detection is used. However, for differential phase-shift keying signals such as DPSK or DQPSK direct detection may be used instead of coherent detection. A receiver can demodulate DPSK or DQPSK signals without the need for a local oscillator. The incoming signal can be multiplied by a delayed version of itself to obtain a signal that is a function of the phase difference for detection [24].

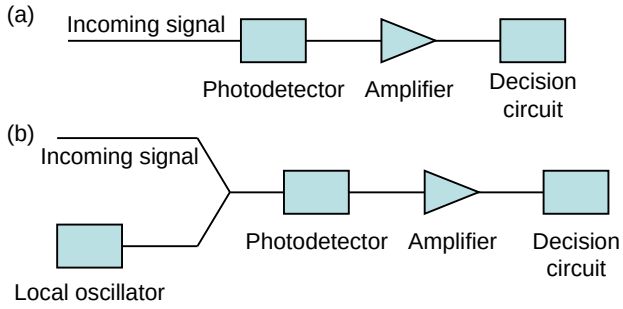

Figure 1.11: (a) Direct detection and (b) coherent detection schemes.

1.1.2.1 Photodetector

Photodetectors are normally made of semiconductors. Figure 1.12(a) shows an example of the structure of a P-N photodiode under reverse bias. The reverse bias operation induces a *depletion region* that is essentially devoid of free charge carriers.

When the light strikes a photodiode and has enough energy, the electrons become stimulated and are pulled up into the conduction band, leaving holes in their place in the valence band as seen in Figure 1.12(b). Electron-hole pairs are generated in proportion to the amount of incident light. In the depletion region the electric field accelerates these electrons toward the N-layer and the holes toward the P-layer. If an external circuit is connected to photodiode, these electrons and holes generate an electric current I_p. The converted intensity I_p is proportional to the optical power P_{in} [7]:

$$I_p = RP_{in}, \tag{1-1}$$

where R is the responsivity of the photodiode (in units of A/W).

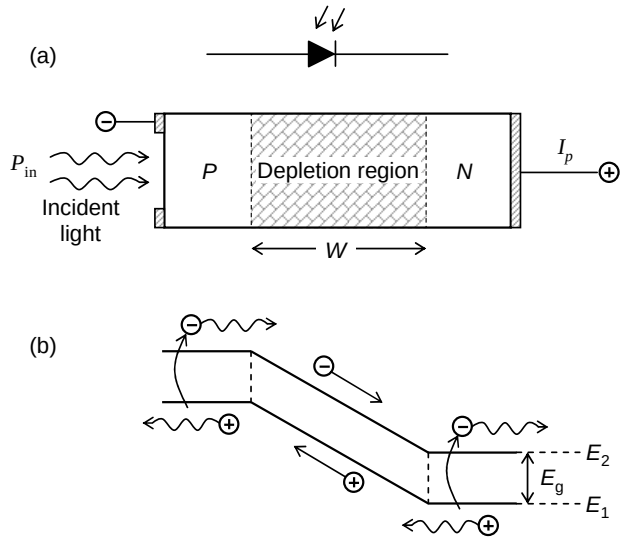

Figure 1.12: (a) a P-N photodiode under reverse bias (b) Energy-band diagram showing movement through drift and diffusion.

1.1.2.2 Noise

An optical receiver converts incident optical power P_{in} into electric current through a photodiode by Eq. (1-1). This equation assumes noise-free operation in the conversion. In fact, noise always exists at the receiver whether the incident optical signal exhibits noise or not. Two fundamental noise mechanisms are shot noise and thermal noise. These produce noise current $i_{sh}(t)$ and $i_{th}(t)$, respectively. The total noise current at photodiode is $i_n(t) = i_{sh}(t) + i_{th}(t)$. This noise leads to fluctuations in the converted current. The converted current I_p thus has added noise $i_n(t)$ so that:

$$I(t) = I_p + i_n(t) \tag{1-2}$$

In optical transmission, optical amplifiers (i.e. EDFA or Raman amplifiers) are normally used to compensate for attenuation losses. Amplification of an optical signal relies on the stimulated emission mechanism. Unfortunately, it is always accompanied by spontaneous emission. The spontaneous emission is also amplified during the propagation inside the amplifiers and is considered as a noise source. The amplifiers enhance the signal intensity in terms of power but they also degrade the signal quality by adding amplified spontaneous emission (ASE) noise.

Noise accumulated along the propagation distance (ASE noise) and noise due to the photodetector (shot noise and thermal noise) both degrade the signal. The quality of the signal is thus affected. For a good quality of received signal, after propagation through a number of amplifiers, a regenerator may be placed to regenerate signal before further transmission. In fact, ASE noise caused by amplifiers is the dominant noise at the photodetector.

1.1.2.3 Decision

At the receiver, a decision scheme is used to decide on whether a bit is "0" or "1". For this, the detected signal is carried through to a decision block. This is composed of a threshold detector and a clock recovery circuit, also called a synchronization circuit. Figure 1.13 illustrates the principle of the decision threshold through an eye diagram.

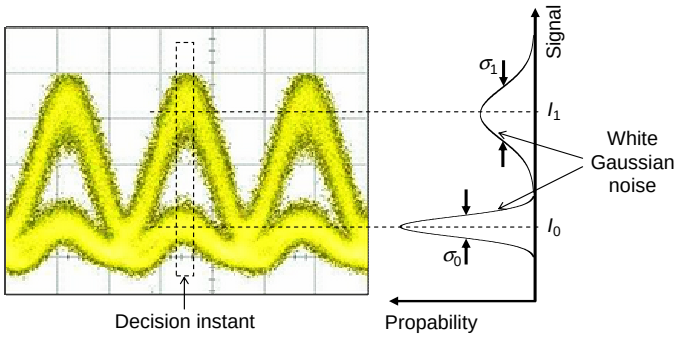

Figure 1.13: Principle of decision with a threshold for a OOK-RZ format signal.

At a given moment, called the decision instant, the signal level is measured. Generally, the levels measured are distributed around two mean values I_1 and I_0. Fluctuations around the high level I_1 is called noise on "1" and the square root of the variance of the probability density is called σ_1. Fluctuation around the low level is called the noise on "0" and the square root of the variance of the probability density is σ_0. Both these noises are considered to be white noise with Gaussian distributions. The decision circuit determines whether a bit is "0" or "1" depending on how close the received level of signal is to level I_0 or I_1. The signal, after propagating along a distance, is normally distorted and noisy. Some pulses of "1" are attenuated to be below the threshold level. These pulses may be detected as "zeros". On the other hand, some spaces of "zero" level, have acquired enough noise to be higher than the threshold, and so are detected as pulses.

A decision threshold, I_{th}, is set to make a separation of the two states of the signal. At each decision instant (determined by the clock recovery circuit), the decision circuit compares the detected voltage I to a threshold I_{th}. If $I > I_{th}$, the transmitted bit is considered as being "1" and if $I < I_{th}$, the transmitted bit is considered as being "0". Due to noise, an error occurs if $I < I_{th}$ while the transmitted bit is "1", and $I > I_{th}$ while the transmitted bit is "0". At the receiver, the number of bits with detected errors is counted in a total number of transmitted bits. This is called bit-error rate (BER) measurement. BER is an important criterion used to assess the transmission performance. It will be considered in Section 1.1.3.5.

The decision instant is also important. The clock that is used as a reference for decision must be synchronized with the received signal. The decision instant can be extracted by a recovery clock signal from the received signal.

1.1.3 Optical signal quality criteria

1.1.3.1 Eye diagram

An eye diagram is a superposition of all the waveforms corresponding to all the possible bit sequences in a signal. In general, eye diagrams of signals are obtained in the electrical domain after being detected by a photodiode, and are observed by using an electrical sampling oscilloscope (ESO). The electrical eye diagrams are representative for the optical signal only if the photodiode speed is high enough. According to the Nyquist criterion, its bandwidth must be at least equal to half of the bit rate [25]. In practice, a photodiode bandwidth exceeding this value is necessary for more accuracy. At high bit rate, the quality of the electrical eye diagrams is limited by the photodiode bandwidth, which depends on the photodiode but the maximum is around 50 GHz.

Optical sampling oscilloscopes (OSOs) with time resolution of 1 ps are therefore preferable to use for monitoring high bit-rate optical signals. OSOs may be based on linear or nonlinear optics. In Foton laboratory, we use a FWM-based OSO with a time resolution of 1 ps. Figure 1.14 displays an example of the electrical (a) and optical (b) eye diagrams of a 42.7 Gb/s OOK RZ-33% signal. We can see in this figure that the visualisation quality of OSO is clearly better than ESO. The OSO will be used for optical signal monitoring in our experiments in the following chapters.

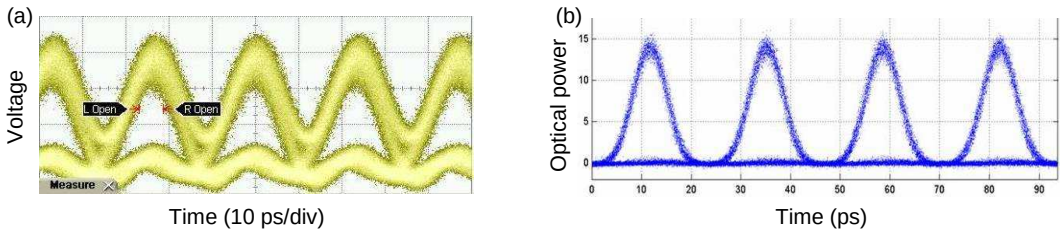

Figure 1.14: Example of eye-diagrams of a 42.7 Gb/s OOK RZ-33% signal: (a) electrical and (b) optical.

The observation of signal eye diagrams can provide a qualitative estimation of signal degradations such as intensity fluctuations, timing jitter and intersymbol interference. The lower the signal quality is, the more closed the eye diagram is. A quantitative estimation of the signal quality which can be deduced from the electrical eye diagrams is the signal extinction ratio (ER). ER is defined as

$$ER = \frac{I_1}{I_0} \tag{1-3}$$

where I_0 and I_1 are average values of the detected currents of the "0" and "1" levels, respectively as illustrated in Figure 1.13.

1.1.3.2 Quality factor

The signal quality can also be represented by a quality factor (Q-factor) which describes intensity fluctuations, timing jitter, and also the extinction ratio of a signal. The quality factor Q of the transmitted optical signal is defined as

$$Q = \frac{I_1 - I_0}{\sigma_1 + \sigma_0} \tag{1-4}$$

where σ_0^2 and σ_1^2 are the conditional probability variances of the detected voltages of bit "0" and bit "1", respectively. I_0, I_1, σ_0^2, and σ_1^2 are illustrated in Figure 1.13.

1.1.3.3 Optical signal-to-noise ratio

As mentioned in Section 1.1.2.2, during the propagation along transmission links, the optical signal is impaired by the accumulation of ASE noise. To quantify the ASE noise, the *optical signal-to-noise ratio* (OSNR) is used. The OSNR is defined as the ratio of the signal power to the noise power measured over a given spectral bandwidth and calculated by

$$OSNR = \frac{P_{signal}}{P_{noise}} \tag{1-5}$$

The OSNR is generally measured in the spectral domain. Figure 1.15 describes the principle of the OSNR measurement. Optical signal power and noise power are measured by using an optical spectrum analyser (OSA) in a spectral width B leading to the OSNR in dB/B. The unit of the OSNR is usually dB/0.1 nm.

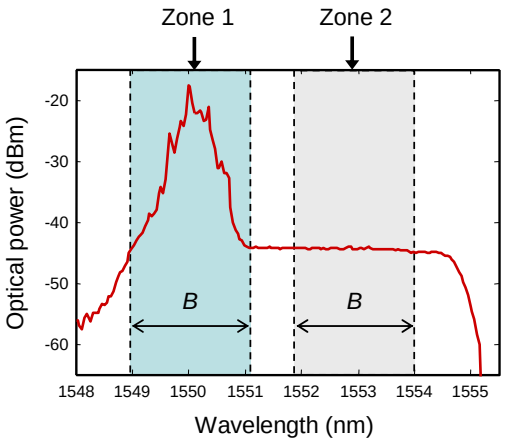

Figure 1.15: Example of measurement of OSNR.

The first measured optical power P_1 within the spectral width of B (zone 1) includes both signal and noise power contributions and thus corresponds to power of signal and noise. The second measurement within zone 2 (spectral width of B) gives an optical power P_2 corresponding to the noise power only. The OSNR is then expressed by

$$OSNR = \frac{P_1}{P_2} - 1. \tag{1-6}$$

1.1.3.4 Timing jitter

As mentioned in Section 1.1.2.3, in practice, the decision instant is determined by a clock-recovery circuit (see Figure 1.10). As the signal is naturally noisy, it can temporally fluctuate from bit to bit. Such fluctuations are called *timing jitter*. The Q-factor of the signal is degraded because fluctuations in time lead to additional fluctuations in amplitude of signal. This can be explained by the fact that, in theory, the signal must be sampled at the peak of the pulse. Fluctuations in time cause the pulse not to be sampled at the pulse center. The sampled value fluctuates by an amount that depends on the timing jitter Δt. Since Δt is a random variable, the fluctuation is also random. The Q-factor of signal is reduced as a result of such additional fluctuations.

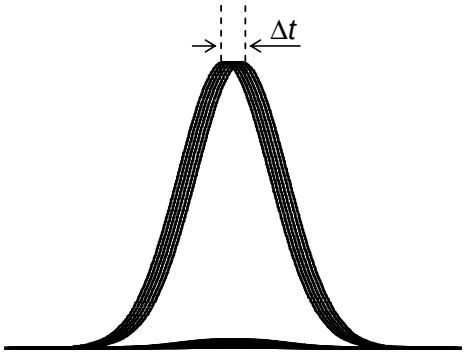

Figure 1.16: Illustration of timing jitter

As its name denotes, timing jitter is measured in units of seconds, normally it is ps or fs. Timing jitter is usually measured by using the phase detector method [26] or the relative timing jitter method [27].

1.1.3.5 Bit-error rate

Bit-error-rate (BER) is the ultimate criterion used to quantify the quality of an optical transmission and is related to the error probability, defined as the probability of incorrect identification of a bit by the decision circuit of the receiver. As described in Section 1.1.2.3, the receiver makes a decision on the presence of a symbol "1" or "0" depending on the received signal level at the decision instant. If the temporal and amplitude fluctuations are large, the current of a symbol "1" may be lower than the decision threshold and the current of a symbol "0" may exceed the threshold and the system therefore suffers errors.

At the receiver, the BER is measured by an error detector. It is calculated by dividing the number of bit errors by the total number of transmitted bits. For example, a BER of 2×10^{-9} corresponds to an average of 2 errors on one billion of transmitted bits. The error probability BER is defined by

$$BER = P(1)P(0|1) + P(0)P(1|0), \tag{1-7}$$

where $P(1)$ and $P(0)$ are the probabilities of "1" and "0" in the transmitted data stream, respectively, $P(0|1)$ is the probability of deciding "0" when "1" has been sent, and $P(1|0)$ is the probability of deciding "'1" when "0" has been sent.

Considering that the noise in optical transmission systems has a Gaussian distribution, the probabilities $P(1|0)$ and $P(0|1)$ therefore can be calculated by Gaussian statistics. In addition, the symbols "1" and "0" can be considered equally probable in actual data streams, the probabilities $P(1)$ and $P(0)$ are thus equal to 0.5. The BER can then be rewritten

$$BER = \frac{1}{2}\mathrm{erfc}\left(\frac{Q}{\sqrt{2}}\right) = \frac{1}{4}\left[\mathrm{erfc}\left(\frac{I_1 - I_{th}}{\sigma_1\sqrt{2}}\right) + \mathrm{erfc}\left(\frac{I_{th} - I_0}{\sigma_0\sqrt{2}}\right)\right], \tag{1-8}$$

where Q is the the Q-factor. I_1, I_0, and I_{th} are the photocurrents of "1", "0" symbols and threshold decision at a decision instant. σ_1^2 and σ_0^2 are the variances of probability density of "1" and "0", while erfc stands for the complementary error function, defined as

$$\mathrm{erfc}\,(x) \;=\; \frac{2}{\sqrt{\pi}}\int_x^{+\infty} \exp\left(-y^2\right) dy. \tag{1-9}$$

The measurement of BER depends on the value of the threshold decision I_{th}. The BER is minimum when the threshold decision is

$$I_{th} \;=\; \frac{I_1\sigma_1 + I_0\sigma_0}{\sigma_1 + \sigma_0}. \tag{1-10}$$

The minimum BER in this case is

$$BER_{min} \;=\; \frac{1}{2}\mathrm{erfc}\left[\frac{I_1 - I_0}{\sqrt{2}\,(\sigma_1 + \sigma_0)}\right]. \tag{1-11}$$

Most of optical transmission systems specify a BER of 10^{-9} as the operating requirement. A report on forward error correction codes (FEC) [28] allows a reduction of BER by a factor of 10 compared to the signal without FEC [29]. In laboratories, a transmission (without FEC) exhibiting a BER of 10^{-9} is considered to be reliable.

The system performance is commonly characterized by the measured BER as a function of the received average optical power at the receiver. These curves are known as the *receiver sensitivity curve*. The required optical power to obtain BER= 10^{-9} is defined as the receiver sensitivity. The measurement of BER is normally compared with the BER of the back-to-back (B2B) configuration (transmitter and receiver are connected directly without a transmission link) to assess the performance of a system or a device. Figure 1.17 describes two receiver sensitivity curves of BER (B2B and after transmission). The B2B curve is used as a reference.

In Figure 1.17, the additional power required in front of the receiver to obtain a BER of 10^{-9} is called the power penalty and it is usually used to quantify the signal degradations induced by the studied transmission. The inserted transmission links lead to different penalties on the receiver sensitivity. The example shows a power penalty of 3.5 dB at a BER of 10^{-9}.

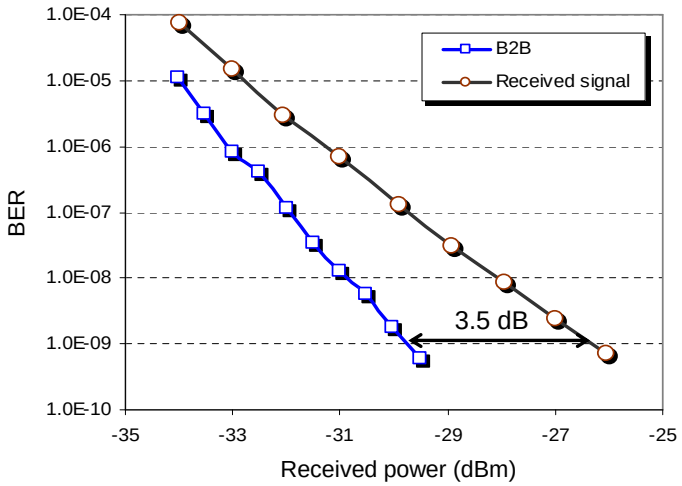

Figure 1.17: Example of BER measurement with a back-to-back (B2B) reference and power penalty.

1.2 Optical fibers

In an optical communication system, the optical fiber itself is one of the most important components. The transmission characteristics of the fiber play a major role in determining the performance of the entire system. An optical fiber is a dielectric medium which operates at optical frequencies. It is made of low-loss materials, usually fused silica glass of high chemical purity. An optical fiber confines electromagnetic energy of light and guides the light in a direction parallel to its axis. The light guiding process in optical fiber is based on the phenomenon of total internal reflection which has been known since 1842 [30].

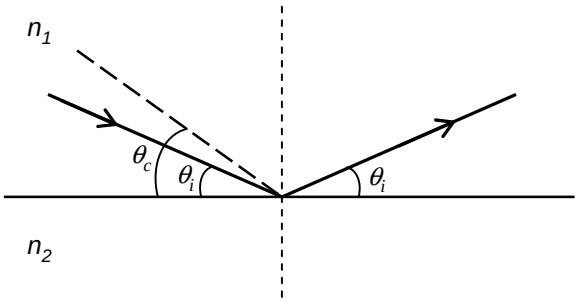

Figure 1.18: Reperesentation of the critical angle and total internal reflection.

Total internal reflection happens when a ray of light deriving from a medium which has a refractive index n_1 strikes the boundary with another medium of refractive index n_2 ($n_2 < n_1$) at an angle θ_i larger than a particular critical angle θ_c with respect to the normal to the surface (Figure 1.18). No light can pass through the boundary and all of the light is reflected.

1.2.1 Geometrical fiber description

An optical fiber in its simplest form consists of a cylindrical core of silica glass of refractive index n_1 surrounded by a cladding having a refractive index $n_2 < n_1$. An elastic plastic buffer normally encapsulates the fiber as seen in the schematic of a fiber structure in Figure 1.19.

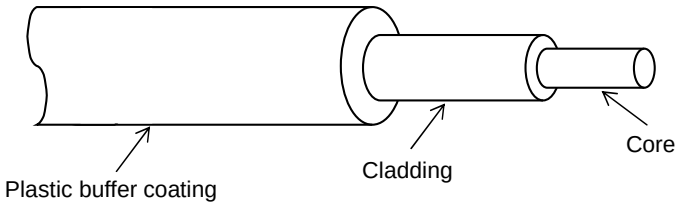

Figure 1.19: Schematic of a fiber structrure with core, cladding and elastic plastic buffer.

Variations in the refractive index of the core material give rise to the two commonly used fiber types. The first fiber type which has the property that the refractive index of the core is uniform throughout and undergoes an abrupt change at the core-cladding interface, is called a *step-index fiber*. In a different type of fiber, the refractive index of core is made to decrease gradually as a function of the radial distance from the center of the fiber. This is known as *graded-index fiber*. Figure 1.20 shows schematically the fiber cross section and the refractive index profile for two types of fibers.

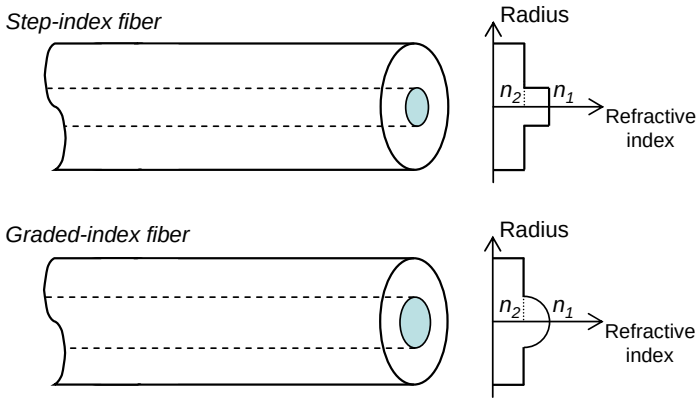

Figure 1.20: Refractive index profile for step-index and graded-index fibers.

The meridional ray propagating in an step-index fiber is illustrated in Figure 1.21. The incident ray goes into the fiber core from air with the refractive index n_0 at an angle θ_i with respect to the fiber axis. The ray bends toward the normal at an angle θ_r given by [31]

$$n_0 \, sin\theta_i = n_1 \, sin\theta_r, \tag{1-12}$$

where n_1 is the refractive index of the fiber core. It strikes the core-cladding interface at a angle ϕ. The condition that the total internal reflection occurs is the incident angle ϕ must

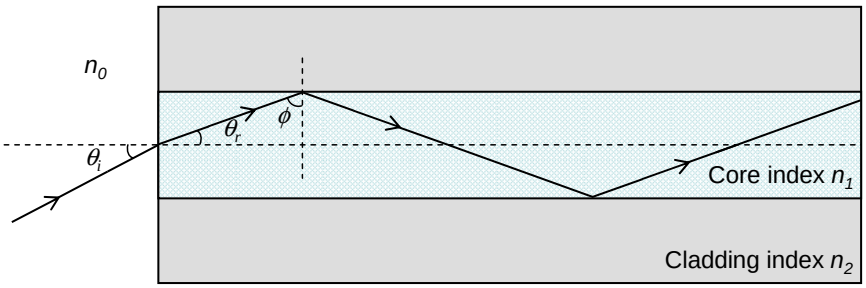

Figure 1.21: Optical ray representation of the propagation mechanism in a step-index fiber.

be greater than the critical angle ϕ_c, defined by [31]

$$sin\phi_c = n_2/n_1, \tag{1-13}$$

where n_2 is the cladding reflective index. The meridional ray then follows a zigzag path along the fiber core. Since such reflections occur throughout the fiber length, all rays with $\phi > \phi_c$ remain confined to the fiber core.

The condition of Eq. (1-13) can be related to the maximum incident angle $\theta_{i,max}$ through the relationship

$$n_0\, sin\theta_{i,max} = n_1\, sin\theta_{r,max} = n_1\, cos\phi_c = ({n_1}^2 - {n_2}^2)^{1/2}. \tag{1-14}$$

Eq. (1-14) also defines the *numerical aperture* (NA) of the step-index fiber for a meridional ray. It can be rewitten as

$$\text{NA} = n_0\, sin\theta_{i,max} = ({n_1}^2 - {n_2}^2)^{1/2} \simeq n_1\sqrt{2\Delta}, \tag{1-15}$$

where the parameter Δ is the core-cladding index difference and defined as $\Delta = (n_1 - n_2)/n_1$.

1.2.2 Propagation modes in optical fibers

The propagation of optical fields in fibers is governed by *Maxwell's equations*, which give the relationships between the electric and magnetic fields. In order to obtain solutions for *Maxwell's equations*, we assume that the optical fiber is a linear, isotropic dielectric material having no currents and free charges. Considering electromagnetic waves propagating along an optical fiber in a cylindrical coordinate system (r, ϕ, z) [31], as depicted in Fig. 1.22, the electric field vector $\mathbb{E}$ and the magnetic field vector $\mathbb{H}$ can be written as

$$\mathbb{E}(r, \phi, z, t) = \mathbf{E}(r, \phi)e^{j(\omega t - \beta z)}, \tag{1-16}$$

$$\mathbb{H}(r, \phi, z, t) = \mathbf{H}(r, \phi)e^{j(\omega t - \beta z)}, \tag{1-17}$$

where ω is the wave frequency, t is the time, β is the propagation constant, $\mathbf{E}(r,\phi)$ and $\mathbf{H}(r,\phi)$ are the transverse distribution of the electric field and the magnetic field respectively:

$$\mathbf{E} = \begin{pmatrix} E_r \\ E_\phi \\ E_z \end{pmatrix}, \tag{1-18}$$

$$\mathbf{H} = \begin{pmatrix} H_r \\ H_\phi \\ H_z \end{pmatrix}. \tag{1-19}$$

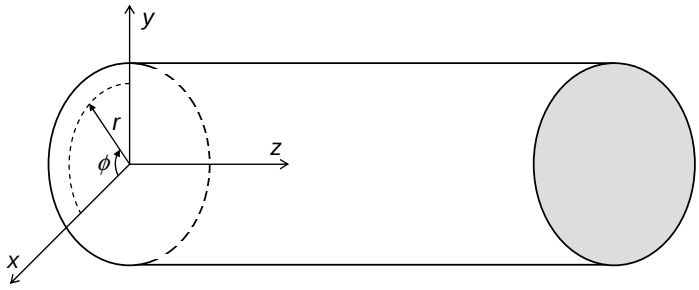

Figure 1.22: Cylindrical coordinate system used for analyzing electromagnetic wave propagation in an optical fiber.

The electromagnetic field that propagates along an optical fiber can be represented by guided modes (simply called *modes*). Each mode has a field distribution which forms a standing-wave pattern in the transverse direction [31]. The component E_z or H_z in Eqs. (1-18) and (1-19) are independent. They are however tied by the boundary conditions. In the case of $E_z = 0$, the modes are called *transverse electric* modes or briefly TE modes. When $H_z = 0$, they are called *transverse magnetic* or TM modes. In the case of both E_z and H_z are different from zero, the modes become *hybrid modes* HE or EH modes, which depends on whether H_z or E_z is dominant.

For an optical fiber with known parameters of the core radius a, and refractive indices n_1 and n_2, the field distribution $\mathbf{E}$ and the propagation constant β can be obtained numerically. The authorized propagation modes of an optical fiber are classified using to integers m and n. In the case of weakly guiding fibers [32] ($\Delta \ll 1$), the modes are degenerate and called *linearly polarized* (LP) modes. LP_{mn} modes are designated regardlesss of their TM, TE, EH, or HE field configuration [31]. In this case $E_z = H_z = 0$, and the field distribution $\mathbf{E}$ can be represented by a unique scalar function $\psi(r,\phi)$. This function can be analytically derived and is written as follows [33]:

$$\psi_{mn}(r,\varphi) = \begin{cases} \psi_0 J_m(\frac{p_{mn} r}{a}) \begin{cases} \cos m\varphi \\ \sin m\varphi \end{cases} & \text{if } r < a \\ \psi_0 \frac{J_m(p_{mn})}{K_m(q_{mn})} K_m(\frac{q_{mn} r}{a}) \begin{cases} \cos m\varphi \\ \sin m\varphi \end{cases} & \text{if } r > a \end{cases} \tag{1-20}$$

where ψ_0 is a arbitrary constant. The parameters p and q are defined by

$$p^2 = n_1^2 k_0^2 - \beta^2, \tag{1-21}$$

$$q^2 = \beta^2 - n_2^2 k_0^2, \tag{1-22}$$

where k_0 is the free-space propagation constant defined as $k_0 = \omega/c = 2\pi/\lambda$, in which c is the velocity of light, and λ is the wavelength of the optical field oscillating at the frequency ω. Figure 1.23 illustrates the transverse field distribution of several modes in a step-index fiber.

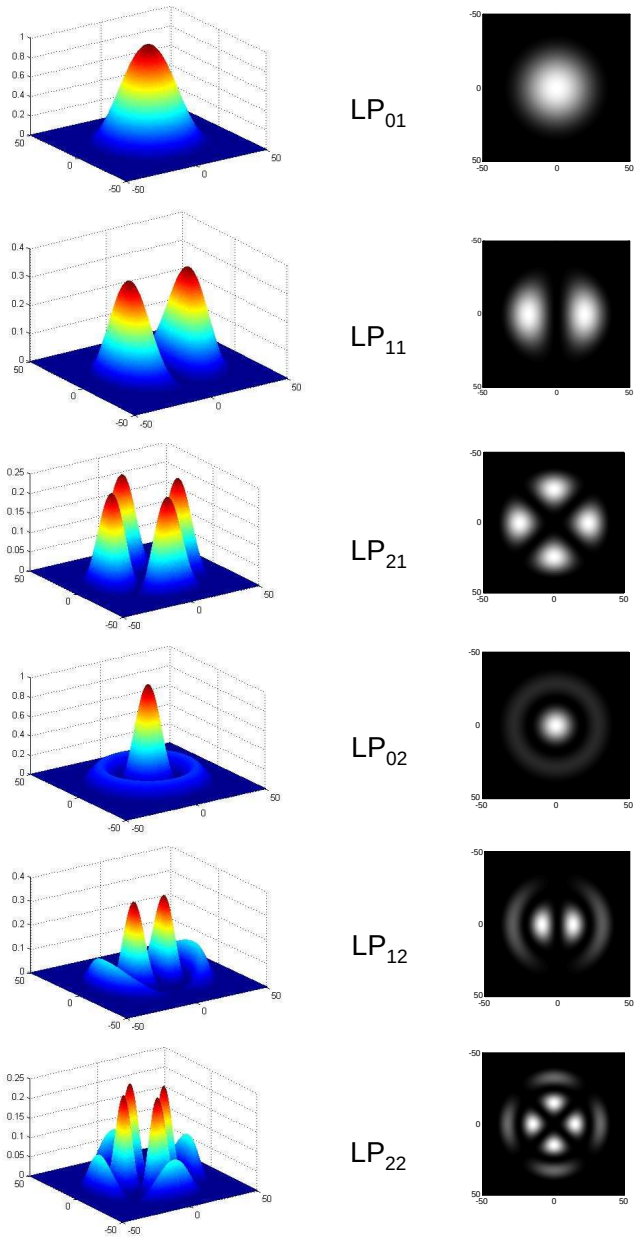

Figure 1.23: Intensity distribution of the first modes of a step-index fiber.

In order to determine the single-mode condition, it is useful to introduce the *cut-off conditions* which is the condition for which a mode is no longer bounded to the fiber core. An important parameter determining the cut-off condition is the *normalized frequency* V, defined by

$$V = k_0 a \sqrt{n_1^2 - n_2^2}. \tag{1-23}$$

The V-parameter decides how many modes a fiber can support. For more convenience, a *normalized propagation constant* b is defined as

$$b = \frac{\beta^2 - k^2 n_2^2}{k^2 \left(n_1^2 - n_2^2\right)}. \tag{1-24}$$

Note, that to ensure the modes can be guided in a fiber, the parameter b must be between 0 and 1, $(0 < b < 1)$. Figure 1.24 shows the dispersion relation of b as a function of V for few modes. This figure points out that a guided mode can exist only if the value of V exceeds a certain value. The fundamental mode LP_{01} has no cut-off frequency, it therefore always exists in a fiber.

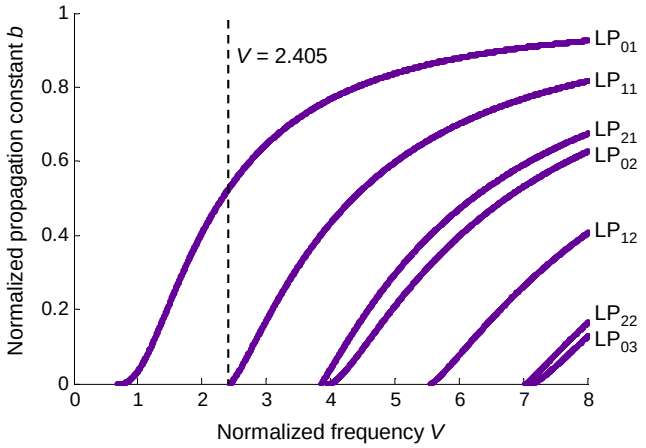

Figure 1.24: Propagation constant b as a function of V for a few of the low-order modes LP_{mn}. Cut-off condition shows single-mode propagation for $V < 2.405$.

Single-mode fiber

A single-mode fiber supports only the fundamental LP_{01} mode. The condition of a single-mode fiber is determined by the value of V at which the LP_{11} mode reaches the cut-off. By applying the cut-off condition $b = 0$, the smallest value of V is found to be 2.405. In other words, the single-mode condition is

$$V = ka\sqrt{n_1^2 - n_2^2} \leq 2.405. \tag{1-25}$$

However, a single mode fiber with a small V-parameter can not confine well the mode in the fiber core. For example, for $V = 1$, only 20% of the total mode power is confined in the core. This percentage increases to 75% for $V = 2$. For this reason, most of telecommunication single-mode fibers are designed to operate in the range $2 < V < 2.405$ [7].

Mode field diameter

For single-mode fibers, the *mode field diameter* (MFD) of the guiding mode is normally considered rather than the core radius a or the NA. The MFD can be calculated from the field distribution of the fundamental LP_{01} mode. The field distribution is normally approximated by a *Gaussian distribution*. This can be written as

$$E(r) = E_0 \exp(-r^2/w_0^2) \tag{1-26}$$

where E_0 is the field at zero radius, w_0 is called the mode field radius. The MFD is defined as $2w_0$. It is determined by fitting the exact distribution with a Gaussian function. Figure 1.25 shows an example of Gaussian approximation for a step-index fiber with $V = 2$.

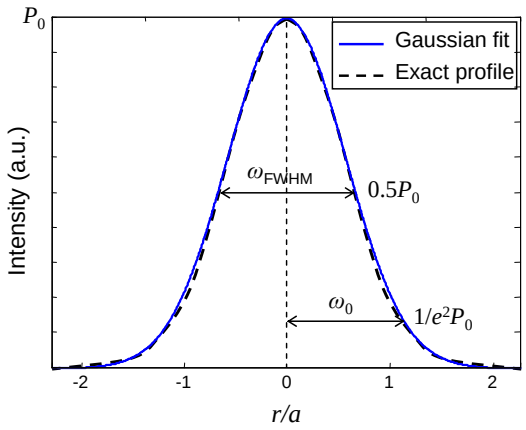

Figure 1.25: Example of Gaussian approximation for a step-index fiber with $V = 2$.

From the Gaussian distribution of the field, the mode field radius w_0 is determined to be the radius of the optical electric field distribution at $1/e$ point. It is equivalent to $1/e^2$-radius of the optical intensity (known as the half-width at $1/e^2$ intensity point).

The mode field radius w_0 can be determined from Marcuse's analytical approximation [34], accurate to within 1% for $1.2 < V < 2.4$:

$$\frac{w_0}{a} \approx 0.65 + 1.619V^{-3/2} + 2.879V^{-6}. \tag{1-27}$$

In optical fiber, another important parameter is the *effective mode area* A_{eff}, which determines how tightly light is confined in the fiber core. It is defined as

$$A_{eff} = \frac{2\pi\left(\int_0^\infty |E(r)|^2 r dr\right)^2}{\int_0^\infty |E(r)|^4 r dr} = \frac{2\pi\left(\int_0^\infty I(r) r dr\right)^2}{\int_0^\infty I(r)^2 r dr}, \tag{1-28}$$

where $E(r)$ is the electric field amplitude and $I(r)$ is the optical intensity of the fundamental mode field. As mentioned previously, in conventional step-index fibers, the mode field is well-approximated by a Gaussian function of radius w_0. In this case, the effective mode area can be simply expressed related to the mode field radius w_0

$$A_{eff} = \pi w_0^2. \tag{1-29}$$

It is useful to introduce another term also used to define the width of a beam. The full-width half-maximum (FWHM) is the diameter of beam at 50% intensity point. The FWHM is widely used in practice. For a Gaussian beam, the FWHM w_{FWHM} is related to w_0 by the relation:

$$w_{FWHM} = 2\sqrt{\ln 2}w_0 \simeq 1.665w_0. \tag{1-30}$$

1.2.3 Fiber losses

Understanding fiber losses is important in fiber optical communication systems. If P_{in} is the power launched at the input end of a fiber, the power P_{out} at the output end is given by:

$$P_{out} = P_{in}\exp(-\alpha L), \tag{1-31}$$

where α is the attenuation coefficient and L is the length of the fiber.

In practice, to describe the fiber loss, rather than using the attenuation coefficient α, it is preferable to use the ratio in dB, α (dB), of optical powers at the output and the input of fiber in a length unit of propagation:

$$\alpha(dB) = -\frac{10}{L}\log\frac{P_{out}}{P_{in}}. \tag{1-32}$$

The fiber losses α (dB) normally denotes one kilometre length of fiber. For a fiber, which has a high attenuation coefficient, it is usually denoted for a 1 m length. For example, the SMF28 Corning silica fiber has a fiber loss of 0.2 dB/km, the chalcogenide microstructured fiber published in Ref. [21] has a fiber loss of 15 dB/m.

Figure 1.26 presents the evolution of the attenuation coefficient of the fundamental mode in a standard silica SMF fiber as a function of the wavelength. Fiber losses may be

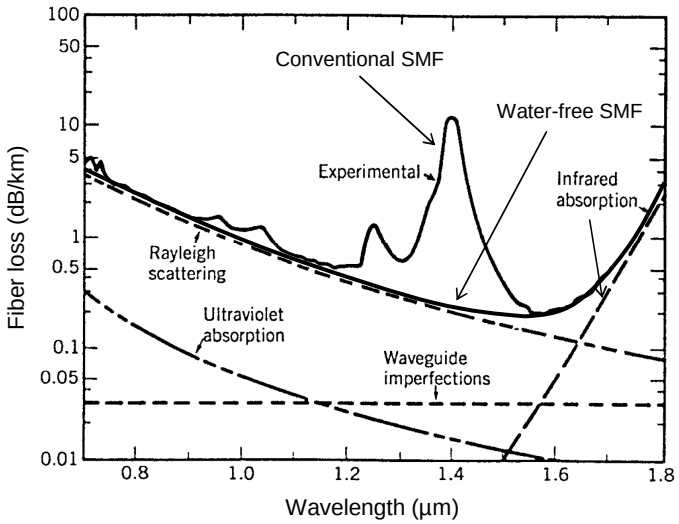

Figure 1.26: Loss spectrum of a standard single-mode fiber (after Ref. [7, 35]).

attributed to material absorption, Rayleigh scattering or fiber imperfections due to fabrication techniques. For conventional SMFs, the OH^- ion from water vapor in the glass leads to high absorption peaks at 1.24um and 1.38um. But now the elimination of water has almost completely removed the OH^- peaks as seen in Figure 1.26.

Deriving from the evolution of fiber losses as a function of wavelength, optical fiber communications typically operate in three wavelength regions. These three wavelength regions are known as the three telecommunication windows. The first window is around a wavelength 850 nm. The second telecom window utilizes wavelength around 1300 nm. The third telecom window, which is now widely used, locates at wavelengths around 1550 nm. The fiber loss of silica fibers at the third telecom window is about 0.2 dB/km. The second and the third telecom windows are further subdivided into the wavelength bands given in Table 1.1.

Table 1.1: Optical wavelength bands.

O band	original	1260 – 1360 nm
E band	extended	1360 – 1460 nm
S band	short wavelengths	1460 – 1530 nm
C band	conventional	1530 – 1565 nm
L band	long wavelengths	1565 – 1625 nm
U band	ultralong wavelengths	1625 – 1675 nm

Among those optical wavelength bands, the C band is widely used because of its lower losses and its match to the erbium resonance window. Our work, which is presented in the following chapters, concentrates on telecommunication signals located in C band. For a signal at a wavelength of 1550 nm, after propagating along 150 km SMF fiber, it is attenuated of 30 dB. It hence needs to be in-line amplified for further transmission. As mentioned in Section 1.1, erbium-doped fiber amplifiers (EDFAs) are commonly used for compensating attenuation losses. In fiber links, losses may also come from splices and connectors and are often treated as a part of the system losses. Microbending losses can also be included in the total losses.

1.2.4 Fiber dispersion

As mentioned in Section 1.2.2, the propagation constant β of the LP_{mn} modes of a fiber depends on ω for each mode. Figure 1.27 shows the propagation constant β for the LP_{01} fundamental mode as a function of the frequency ω and the wavelength λ.

We can see that the relationship between β and ω is not linear leading to chromatic dispersion D. It can be shown that the chromatic dispersion has two contributions: a material contribution D_M and a waveguide contribution D_W.

Figure 1.27 gives an example for only the fundamental mode. However, the propagation constant β is different for each LP_{mn} mode. Dispersion in a multimode fiber is called intermodal dispersion. Using single-mode fibers, we can avoid the intermodal dispersion.

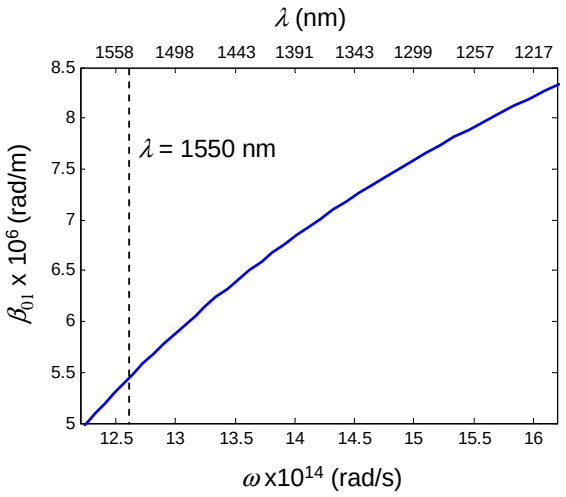

Figure 1.27: Propagation constant β of the fundamental mode as a function of the frequency ω and the wavelength λ.

Nevertheless, the waveguide dispersion and the material dispersion make the group velocity of the fundamental mode frequency dependent. This leads to different spectral components of the pulse travelling at slightly different group velocities. Thus the waveguide dispersion and the material dispersion contribute to *group-velocity dispersion* (GVD) or just simply *fiber dispersion*.

1.2.4.1 Group-velocity dispersion

By utilizing quasi-monochromatic approximation, the propagation constant $\beta(\omega)$ can be expanded in a Taylor series around the center carrier frequency ω_0 such as

$$\beta(\omega) = \beta_0 + (\omega - \omega_0)\beta_1 + \frac{1}{2}(\omega - \omega_0)^2\beta_2 + \frac{1}{6}(\omega - \omega_0)^3\beta_3 \ldots, \tag{1-33}$$

We introduce here a time delay τ_g and a group velocity v_g from the propagation constant β as following

$$\tau_g = \frac{d\beta}{d\omega} = \beta_1, \tag{1-34}$$

$$v_g = \frac{1}{\tau_g} = \left(\frac{d\beta}{d\omega}\right)^{-1}. \tag{1-35}$$

Since the group velocity v_g depends on frequency ω and pulses normally contain different spectral components, pulses are broadened during propagation. The magnitude of pulse broadening for a unit length (m) of fiber is given by

$$\Delta T = \frac{d\tau_g}{d\omega}\Delta\omega = \frac{d^2\beta}{d\omega^2}(\Delta\omega) = \beta_2\Delta\omega, \tag{1-36}$$

where $\Delta\omega$ is the spectral width of the pulse at the input of fiber. The parameter $\beta_2 = d^2\beta/d\omega^2$ is the group delay dispersion per unit length and called the GVD parameter or the

second-order dispersion. The basic unit of the GVD is s^2/m. An example of the GVD of a SMF silica fiber is -22 ps^2/km at 1550 nm.

In the wavelength unit scale, the pulse broadening is determined by

$$\Delta T = \frac{d\tau_g}{d\lambda}\Delta\lambda = D\Delta\lambda, \tag{1-37}$$

where λ is the center wavelength of pulse, $\lambda = 2\pi c/\omega$, where c is the speed of light in vacuum. $\Delta\lambda$ is bandwidth of pulse spectrum, which is defined as $\Delta\lambda = (\lambda^2/(2\pi c))\Delta\omega$. The parameter $D = d\tau_g/d\lambda$ is known as the fiber dispersion. It is related to β_2 by the relation

$$D = \frac{d\tau_g}{d\lambda} = -\frac{2\pi c}{\lambda_0^2}\beta_2 \tag{1-38}$$

The dispersion D is expressed in units of s/m^2, but is normally used in ps/km/nm. For the example of a SMF silica fiber, the dispersion D is 17 ps/km/nm at the wavelength of 1550 nm.

As mentioned above, the dispersion D is mostly constituted of the waveguide dispersion D_W and the material dispersion D_M, $D \approx D_W + D_M$. These two types of dispersion in a step-index fiber are given by the following equations [33]

$$D_W \simeq -\frac{\lambda}{4\pi^2 a^2 n_1 c}, \tag{1-39}$$

and

$$D_M \simeq -\frac{\lambda}{c}\frac{d^2 n_1}{d\lambda^2}, \tag{1-40}$$

where a is the radius of the fiber core and n_1 the refractive index of fiber core material. Figure 1.28 illustrates D_M, D_W, and their sum $D = D_M + D_W$, for a typical silica single-mode fiber. The material dispersion D_M varies from negative to positive values while the waveguide dispersion D_W is always negative in the spectral range between 1100 nm and 1700 nm. The zero-dispersion wavelength λ_{ZD}, where $D = 0$, of the fiber is 1310 nm.

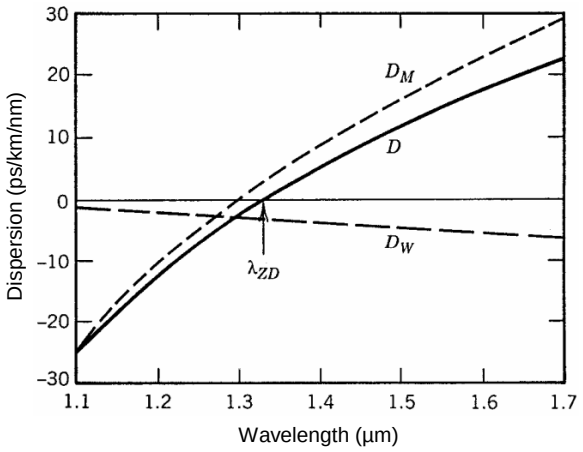

Figure 1.28: Total dispersion D and relative contributions of material dispersion D_M and waveguide dispersion D_W for a silica single-mode fiber (after Ref. [7]).

From Figure 1.28, the pulse broadening due to dispersion may be eliminated by operating at the zero-dispersion wavelength λ_{ZD}. However, the effects of dispersion do not disappear completely at $\lambda = \lambda_{ZD}$. The higher-order dispersion acts as a cause of pulse broadening. This feature can be understood by noting that the pulse spectrum normally contains different wavelengths and dispersion D cannot be zero at all those wavelengths. This means that the frequencies of a pulse have different values of dispersion. The parameter that describes the difference in dispersion as a function of wavelength is called the *dispersion slope* S. The higher-order dispersion are governed by the dispersion slope S, which is defined as $S = dD/d\lambda$. By using Eq. (1-38) the dispersion slope S can be written as

$$S = \left(2\pi c/\lambda^2\right)^2 \beta_3 + \left(4\pi c/\lambda^3\right) \beta_2, \tag{1-41}$$

where $\beta_3 = d^3\beta/d\omega^3$ is known as the *third-order dispersion*. In the wavelength vicinity of λ_{ZD}, the third-order dispersion β_3 may dominate the second-order dispersion. The influence of the third-order dispersion on 2R regeneration of a 160 Gb/s signal will be discussed in Chapter 2.

1.2.4.2 Polarization-mode dispersion

In principle, the polarization of the fundamental mode launched into a fiber whose core is perfectly cylindrical does not evolve along the fiber. Real fibers exhibit variation in the core along the fiber length leading to birefringence, with a fast mode and slow mode which have orthogonal and linear polarizations (Figure 1.29). The *fast axis* in this figure corresponds to the axis along which the mode index is smaller. The other axis is called the *slow axis*. The origin of birefringence in fibers can be an elliptical core, thermal elasticity, fiber-bending, fiber-twisting, fiber-winding, magnetic field or electric field.

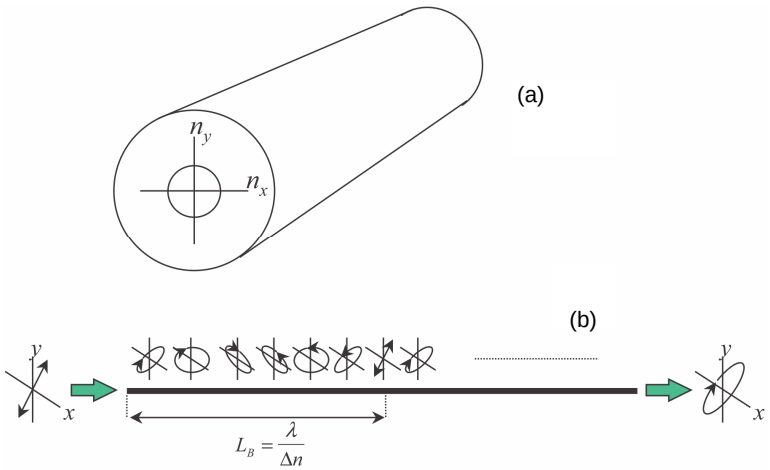

Figure 1.29: A birefringent fiber (a), evolution of the polarization-mode in a birefringent fiber (b).

The degree of modal birefringence B is defined as a difference in the mode indices of the orthogonally polarized fiber modes, $B = |n_x - n_y|$. Birefringence leads to a periodic

evolution of the launched polarisation state along the fiber, as seen in Figure 1.29. The initial polarisation state is restored after the beat length defined by $L_B = \lambda/B$. In an optical fiber, birefringence is not constant along the fiber but changes randomly, both in magnitude and direction, the polarization quickly becomes unpredictable. Typically, a SMF has a birefringence B of about 10^{-7}. It means that $L_B \sim 15$ m at a wavelength of 1550 nm.

As a result of birefringence, different frequency components of a pulse acquire different polarization states, leading in pulse broadening. This phenomenon is known as *polarization-mode dispersion* (PMD). The time group delay ΔT between two polarization components during pulse propagation in a fiber can be evaluated

$$\Delta T = |\tau_{gx} - \tau_{gy}| = \left| \frac{d\beta_x}{d\omega} - \frac{d\beta_y}{d\omega} \right| \simeq B/c, \tag{1-42}$$

where τ_{gx} and τ_{gy} are the time group delay, β_x and β_y the propagation constants of the two orthogonally polarized modes.

1.2.5 Fiber fabrication

For optical fiber fabrication, it is first necessary to prepare a preform with the desired design of refractive-index profile. For silica fiber fabrication, the preform is typically 1 m long and 2 cm in diameter and contains core and cladding layers with correct relative dimensions. The following stage is to apply a precision-feed mechanism that feeds the preform into a furnace at the proper speed to draw the preform into a fiber.

Several method that are used to make the preform are modified chemical-vapor deposition (MCVD), outside-vapor deposition (OVD), and vapor-axial deposition (VAD). Among those, MCVD method is widely used. The successive layers of SiO_2 are deposited on the inside of a fused silica tube. To ensure uniformity, a multiburner torch is moved back and forth across the tube length using an automatic translation stage. The refractive index of the cladding layers is controlled by adding fluorine to the tube. When a sufficient cladding thickness has been deposited, the core is formed by adding vapors to generate the dopants. These dopants determine the refractive index of the fiber core. When the core have been deposited, the torch temperature is raised to collapse the tube into a solid rod or preform.

The preform is then drawn into a fiber. It is fed into a furnace and heated to a temperature of about 2000°C. By using a precision-feed mechanism, the preform is then drawn into a fiber. By monitoring the light diffraction from a laser, the fiber diameter can be controlled. A polymer coating is applied to the fiber during the drawing process for protection.

In our work, we consider both silica fiber and chalcognide glasses fiber. Fabrication of chalcogenide glasses fibers also involve two stages: the preform preparation and the fiber drawing. Fabrication of chalcogenide fibers will be presented in Section 3.2.

1.3 Dispersion-tailored fiber

1.3.1 Dispersion-shifted fiber

As mention in Section 1.2.4, standard silica fibers exhibit zero chromatic dispersion wavelength λ_{ZD} around 1310 nm. For early optical fiber communications systems, these fibers were suitable because of the operational wavelength of 1310 nm. However, the C-band is now widely used. In this wavelength region, standard single-mode fibers exhibit an anomalous dispersion D of 17 ps/km/nm. This may cause significant dispersive pulse broadening, limiting the achievable transmission rates or distances. A new type of single-mode fiber was proposed to shift the zero dispersion wavelength λ_{ZD} to 1550 nm [36]. These fibers are, therefore, called dispersion-shifted fibers (DSF). Dispersion profile of a DSF fiber is shown in Figure 1.30 with comparison with a SMF fiber.

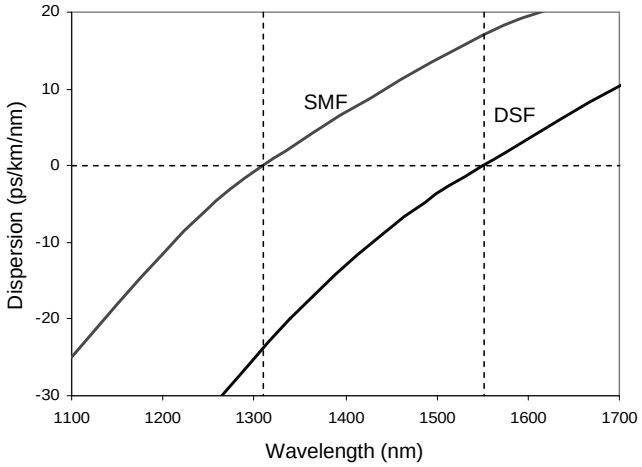

Figure 1.30: Dispersion profile of a DSF fiber.

The method to shift the zero dispersion wavelength λ_{ZD} is to govern the waveguide dispersion D_W so as to shift the zero dispersion wavelength into the 1550 nm region. This is achieved by modifying the refractive index profile of the core. Common index profiles of dispersion-shifted fibers have a triangular, trapezoidal or Gaussian shape.

1.3.2 Dispersion-compensating fiber

For compensating the dispersion of fiber after a long transmission distance in a SMF, a dispersion compensating fiber (DCF) [37] is used. The idea of using a DCF started since 1980 [37], however just after the advent of optical amplifier (1990s), when transmission link length was prolonged, the development of DCF accelerated.

The use of DCF provides an all-optical technique for compensating the fiber dispersion completely if the average optical power is kept low enough that the nonlinear effects inside optical fibers are negligible. A DCF is normally designed with normal dispersion around -100 ps/km/nm compared to the dispersion D of SMF of about 17 ps/km/nm at 1550 nm.

In other words, in a transmission link following 100 km of standard SMF fiber, 17 km of DCF is used. The total dispersion of a transmission link goes so to zero.

DCFs normally have a small core which tailors the dispersion. Some DCFs may have large dispersions D for using shorter DCF in a transmission link. A transmission over 1000 km at 40 Gb/s signal was demonstrated by a DCF of -420 ps/km/nm for dispersion compensation [38]. A DCF with dispersion D of -770 ps/km/nm was reported with the capacity of using only 1 km DCF to compensate the dispersion for a 40-km-long fiber link [39]. Because of its small core size, using DCF fiber should be considered carefully because of the nonlinear effects due to its high nonlinear coefficient.

1.3.3 Dense dispersion-managed fiber

In order to tailor fiber dispersion, dispersion-managed transmission links were introduced [40, 41]. A dispersion-managed link consists of several sections of single-mode fibers with opposite values of dispersion $\pm D$. With this design, fiber dispersion is locally large at value of $\pm D$, however the average dispersion, D_{avg}, is close to zero. Therefore, the influence of dispersion on pulse broadening is lessened. Figure 1.31 illustrate the dispersion profile map of a dispersion-managed fiber link.

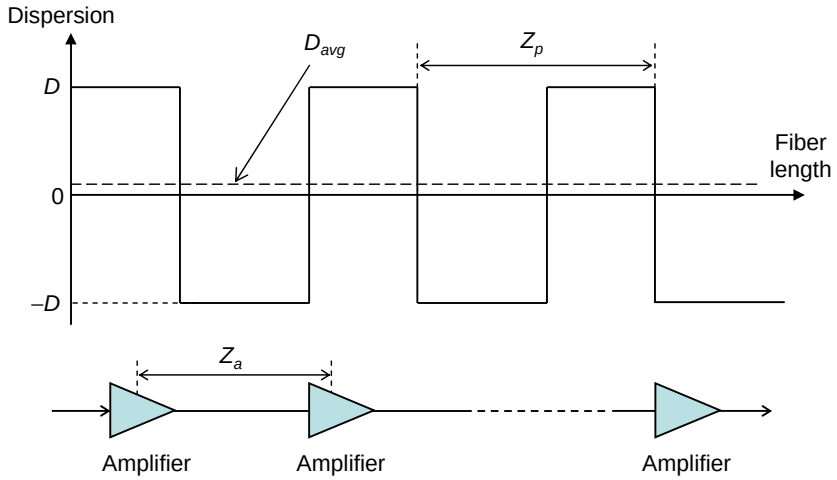

Figure 1.31: Dispersion profile map of a dispersion-managed fiber link as used in an amplified trasmission link.

Conventional dispersion-managed fiber link have a dispersion map period Z_p longer or equal to the amplifier spacing Z_a. Dispersion-managed fiber links can be formed by splicing together different fibers with opposite signs of dispersion [12] or they can be fabricated by slightly changing the core diameter of a single fiber during the drawing process [42].

However, conventional dispersion-managed link with long map periods lead to an increase of dispersion-managed soliton pulse energy, and hence to significant adjacent pulse overlap and interactions [43]. Therefore, they are not suitable to propagate pulses with bit rates larger than 40 Gb/s per channel, because of the large breathing and large power

enhancement factor of these dispersion-managed solitons [12]. To overcome this problem, dense dispersion-managed (DDM) fibers, which have a dispersion map period Z_p much shorter than the amplified spacing Z_a, were proposed [44, 45]. Demonstration of the use of DDM fibers in transmission at high bit-rate have been reported [12, 46]. Current technology allows the fabrication of DDM fibers with a short-period dispersion management map, as a fiber with alternating sign of dispersion can be manufactured in a continuous draw without splicing [46].

1.4 Nonlinear effects in optical fibers

Nonlinear effects rely on the response of bound electrons to an intense electromagnetic field. This causes the polarization $\mathbf{P}$ of the electric field $\mathbf{E}$ not to be linear:

$$\mathbf{P} = \epsilon_0 \left(\chi^{(1)}\mathbf{E} + \chi^{(2)} : \mathbf{EE} + \chi^{(3)} \vdots \mathbf{EEE} + \dots \right), \tag{1-43}$$

where ϵ_0 is the vacuum permittivity, $\chi^{(1)}$ is the linear susceptibility and $\chi^{(j)}$ $(j = 2, 3, \dots)$ is the jth order nonlinear susceptibility. In optical fibers, the second-order susceptibility $\chi^{(2)}$ can be ignored. This section considers the effects of the third-order susceptibility $\chi^{(3)}$.

The nonlinear effects governed by the third-order susceptibility $\chi^{(3)}$ can be elastic or inelastic. For elastic effects, there is no energy exchange between the optical field and the nonlinear medium. This corresponds to Kerr effect including self-phase modulation (SPM), cross-phase modulation (XPM), and four-wave mixing (FWM). When the optical field transfers part of its energy to the nonlinear medium, nonlinear effects fall into stimulated inelastic scattering such as stimulated Brillouin scattering (SBS) and stimulated Raman scattering (SRS).

1.4.1 Kerr effect

This section considers the Kerr effect in optical fiber. The Kerr effect results from the intensity dependence of the refractive index on the contribution of $\chi^{(3)}$.

1.4.1.1 Nonlinear Schrödinger Equation

In optical fibers, the propagation of an optical pulse along a distance z is described by the propagation equation [47]

$$\frac{\partial A}{\partial z} + \beta_1 \frac{\partial A}{\partial t} - i\frac{\beta_2}{2}\frac{\partial^2 A}{\partial t^2} + \frac{\alpha}{2}A = i\gamma|A|^2 A, \tag{1-44}$$

where A is the pulse slowly varying envelope, α is the fiber loss, $\beta_1 = \tau_g$ is the group delay, β_2 is the second-order dispersion, γ is the nonlinear coefficient given by

$$\gamma = \frac{2\pi n_2}{\lambda A_{eff}}, \tag{1-45}$$

with n_2 is the nonlinear refractive index, λ is the wavelength, and A_{eff} is the effective area of the fiber. By normalizing the time $T = t - \beta_1 z$, Eq. (1-44) becomes:

$$\frac{\partial A}{\partial z} - i\frac{\beta_2}{2}\frac{\partial^2 A}{\partial T^2} + \frac{\alpha}{2}A = i\gamma|A|^2 A. \tag{1-46}$$

Eq. (1-46) describes the basic effects during the propagation of an optical pulse in single-mode fibers and is referred to as the nonlinear Schrödinger equation (NLSE). Propagation of pulses depends on the fiber loss α, second-order dispersion β_2 and nonlinear coefficient γ. The NLSE is solved to investigate nonlinear propagation in fibers.

1.4.1.2 Self-phase modulation

As seen in the NLSE, propagation of pulses along a fiber depends on dispersion β_2 and nonlinear coefficient γ. When a pulse is launched into a fiber, both group-velocity dispersion (GVD) and self-phase modulation (SPM) act on it. It is useful to introduce here two lengths known as the dispersion length L_D and the nonlinear length L_{NL}:

$$L_D = \frac{T_0^2}{|\beta_2|}, \tag{1-47}$$

$$L_{NL} = \frac{1}{\gamma P_0}, \tag{1-48}$$

The relative magnitude of fiber length L compared to the dispersion length L_D and the nonlinear length L_{NL} allow us to classify four categories of pulse propagation behavior. When $L \ll L_{NL}$, and $L \ll L_D$, the pulse maintains its shape during propagation. When $L \ll L_{NL}$ but is comparable with L_D, only the dispersive effect creates pulse broadening (called GVD effect). When $L \ll L_D$ but is comparable with L_{NL}, only the nonlinear effect (known as SPM effect) plays a significant role during pulse propagation. When L is comparable to both L_D and L_{NL}, both dispersion and nonlinearity act together to make the pulse broaden along the fiber.

GVD effect

We first consider the case of only GVD acting during pulse propagation. It means that γ can be set to zero. Let us consider an unchirped Gaussian pulse, at $z = 0$, given by

$$A(0,T) = \sqrt{P_0}\exp\left(-\frac{T^2}{2T_0^2}\right), \tag{1-49}$$

where P_0 is the input peak power, T_0 is the half-width at $1/e^2$ intensity point. The Gaussian pulse, after a distance z, is given by [48]:

$$A(z,T) = \sqrt{P_0}\exp(-\alpha z/2)\frac{T_0}{\sqrt{T_0^2 - i\beta_2 z}}\exp\left[-\frac{T^2}{2\left(T_0^2 + i\beta_2 z\right)}\right]. \tag{1-50}$$

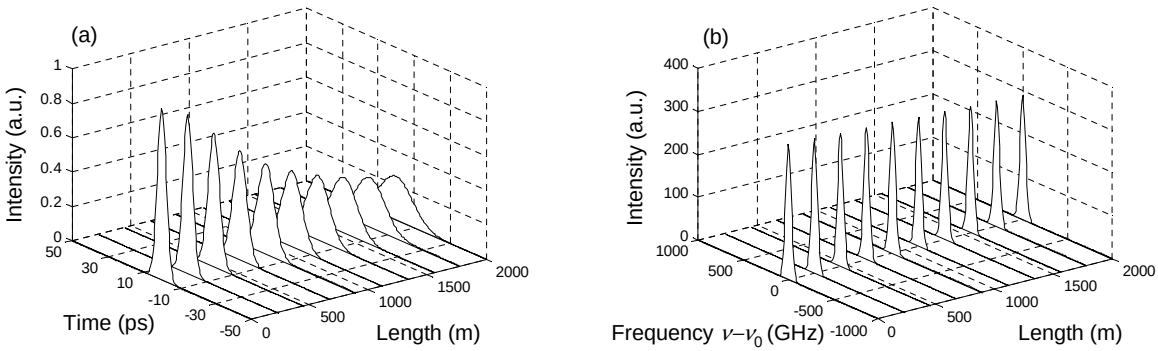

Figure 1.32: Evolution of pulse in (a) time domain and (b) in frequency domain in the case of only GVD ($\gamma = 0$). $T_{FWHM} = 6.25$ ps, $P_0 = 1$ W, fiber length $L = 2000$ m, fiber dispersion $D = 17$ ps/km/nm, $L_D = 580$ m.

At this distance, the pulse broadens to

$$T_1 = T_0\sqrt{1 + \left(\frac{z}{L_D}\right)^2}. \tag{1-51}$$

Note from Eq. (1-51) that the dispersion length L_D is the length after which the pulse width is increased by a factor $\sqrt{2}$. The GVD effect increases the pulse duration and reduces its amplitude. Figure 1.32 shows the evolution of a pulse with pulse duration $T_{FWHM} = 6.25$ ps, input peak power $P_0 = 1$ W after a 2000 m SMF with $D = 17$ ps/km/nm. In this case, effects of nonlinearity are ignored. We can see that the pulse duration is enlarged while the spectrum of the pulse does not change.

When a pulse propagates along a dispersive fiber, its instantaneous frequency varies in time. The instantaneous frequency ω_i then differs from the center frequency ω_0 by a quantity of $\delta\omega(t)$ in the time domain. The quantity $\delta\omega(t)$ is called *chirp*. For a Gaussian pulse, the chirp is calculated as [48]

$$\delta\omega(t) = \frac{2\mathrm{sgn}(\beta_2)(z/L_D)}{1 + (z/LD)^2}\frac{T}{T_0^2}. \tag{1-52}$$

SPM effect

The SPM affects an optical wave propagating along a fiber. This results from a change of refractive index leading to the time dependence of the nonlinear phase shift ϕ_{NL}. A temporally varying phase means that the instantaneous optical frequency differs across the pulse from its central value ω_0. This may broaden the pulse spectrum over its initial spectral width. Now we consider the case of only SPM acting during pulse propagation in the fiber. Eq. (1-46) with $\beta_2 = 0$ becomes

$$\frac{\partial A}{\partial z} = i\gamma|A|^2A. \tag{1-53}$$

This equation is solved to obtain [47]

$$A(z,T) = A(0,T)\exp(\alpha z/2)\exp\left[i\phi_{NL}(z,T)\right], \tag{1-54}$$

where $A(0,T)$ is the field amplitude at $z=0$, and the nonlinear phase shift is given by

$$\phi_{NL}(z,T) = \gamma \left|A(0,T)\right|^2 \frac{1-\exp(-\alpha z)}{\alpha}. \tag{1-55}$$

Knowing that $|A(0,0)|^2 = P_0$, the maximum phase shift ϕ_{NL} can be calculated as

$$\phi_{\max} = \frac{1-\exp(-\alpha z)}{\alpha L_{NL}} \simeq L_{eff}\gamma P_0, \tag{1-56}$$

where the effective length L_{eff} is given by

$$L_{eff} = \frac{1-\exp(-\alpha z)}{\alpha}. \tag{1-57}$$

Figure 1.33 illustrates the evolution of the effective length L_{eff} with respect to the fiber length L for a standard SMF. The maximum effective length of a fiber is given by $L_{eff\_max} = 1/\alpha$. With fiber loss α of 0.2 dB/km, the maximum effective length L_{eff_max} is 21.7 km. As seen in Figure 1.33, for $L \ll L_{eff\_max}$, the nonlinear effect due to SPM can be calculated by using, with a good approximation, $L_{eff} = L$. For $L > L_{eff\_max}$, the increase of L takes L_{eff} asymptotically to the maximum value of the effective length L_{eff_max}. As seen in Eq. (1-56), the maximum phase shift ϕ_{max} is proportional to the effective length L_{eff}. It reaches to a maximum value when the fiber length L is equal to the maximum effective length L_{eff_max}. To benefit from a maximum nonlinear effect, the fiber length L should be as long as the maximum effective length L_{eff_max}.

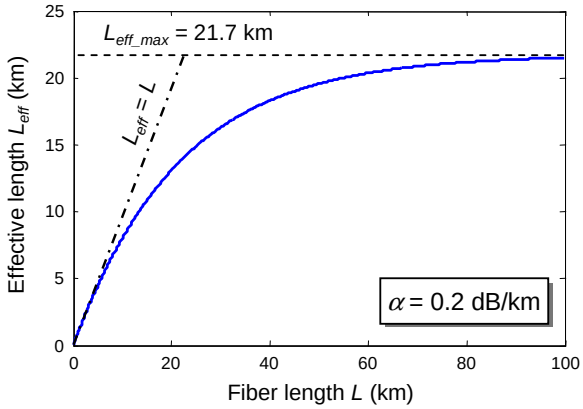

Figure 1.33: Effective length L_{eff} of a SMF as a function of fiber length L.

When only SPM effect act on the optical field, the chirp for a initially Gaussian pulse after propagation is given by

$$\delta\omega(t) = \frac{2}{T_0}\frac{L_{eff}}{L_{NL}}\frac{T}{T_0}\exp\left(-\frac{T^2}{T_0^2}\right). \tag{1-58}$$

Figure 1.34 shows the evolution of a pulse with a pulse duration $T_{FWHM} = 6.25$ ps and an input peak power $P_0 = 1$ W after 10 km of SMF with $\gamma = 1.3$ W^{-1}km^{-1}. In this

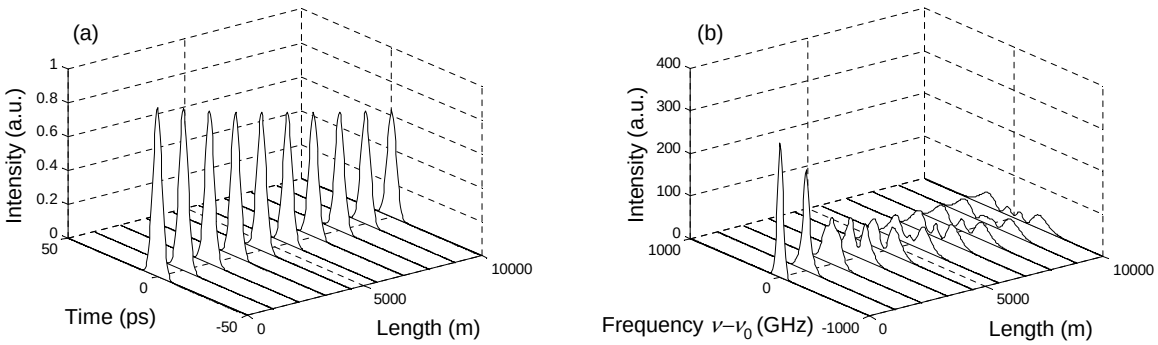

Figure 1.34: Evolution of a pulse in (a) the time domain and (b) in the frequency domain in the case of only SPM ($D = 0$). $T_{FWHM} = 6.25$ ps, $P_0 = 1$ W, fiber length $L = 10$ km, nonlinear coefficient $\gamma = 1.3$ W^{-1}km^{-1}, $L_{NL} = 769$ m.

case, the dispersion is ignored. We can see that the pulse maintains its shape in the time domain (Figure 1.34(a)) but its spectrum is enlarged and itself-modulated in phase as seen in Figure 1.34(b).

GVD and SPM

When both GVD and SPM act together in the propagation of pulses, the NLSE is numerically solved by using predictor-corrector split-step Fourier method [47]. The split-step Fourier method gives an approximate solution by assuming that the dispersive and nonlinear effects act independently on the propagation of the optical field over a small section of fiber (fiber length is divided into many sections).

In normal dispersion regime ($D < 0$), the combined effects of GVD and SPM lead to a broadening of the spectrum and of the duration of an initial Fourier-transform limited pulse. A quasi-linear chirp is accumulated during the propagation of the pulse. The pulse is no longer at the Fourier limit. It is possible to compensate for the chirp by using a DCF fiber or a Bragg grating. In Chapter 2, based on this type of GVD and SPM effects in a fiber, we numerically demonstrate the 2R regeneration of a 160 Gb/s signal.

Figure 1.35 shows the evolution of a pulse with pulse duration $T_{FWHM} = 6.25$ ps and input peak power $P_0 = 1$ W after a 1000 m highly nonlinear single-mode fiber with $D = -15$ ps/km/nm and $\gamma = 11$ W^{-1}km^{-1}. In this case, both dispersion and nonlinearity act together. We can see that the pulse shape in the time domain is broadened (Figure 1.35(a)). In the frequency domain, similar to the SPM-only case, the spectrum is enlarged and self-modulated in phase as seen in Figure 1.35(b).

In the anomalous dispersion regime ($D > 0$), the combined effects of GVD and SPM may lead to the generation of an optical wave called *a soliton*. An optical soliton is a pulse which undergoes periodic deformations of amplitude and spectrum during its propagation in a nonlinear and dispersive medium without attenuation. This stability is due to the mutual compensation of the dispersive effect and SPM effect. The temporal shape of a soliton is

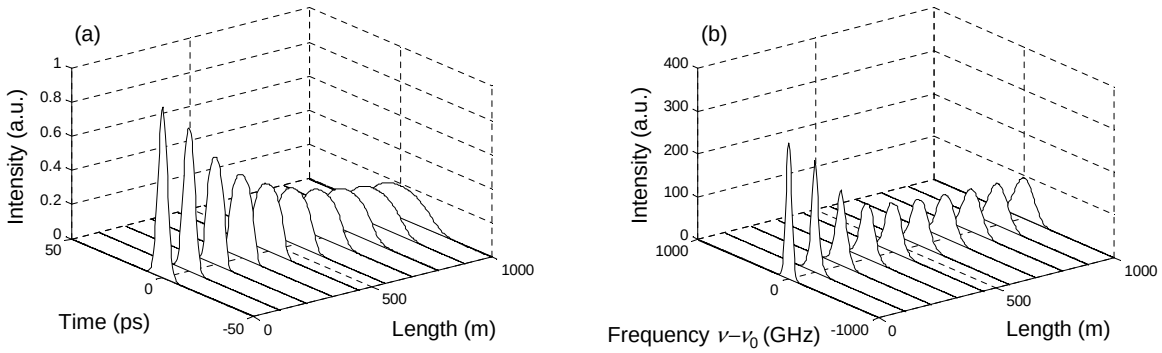

Figure 1.35: Evolution of pulse in (a) time domain and (b) in frequency domain in the case of both GVD and SPM. $T_{FWHM} = 6.25$ ps, $P_0 = 1$ W, fiber length $L = 1000$ m, dispersion $D = -15$ ps/km/nm, nonlinear coefficient $\gamma = 11$ W^{-1}km^{-1}, $L_D = 658$ m, $L_{NL} = 91$ m.

given by [48]

$$U(z,T) = \frac{1}{N}\mathrm{sech}\left(\frac{\mathrm{T}}{\mathrm{T_0}}\right)\exp\left(\mathrm{i}\frac{\mathrm{z}}{2\mathrm{L_D}}\right), \tag{1-59}$$

where N is the soliton order, which is defined as

$$N^2 = \frac{L_D}{L_{NL}} = \frac{\gamma P_0 T_0^2}{|\beta_2|}. \tag{1-60}$$

The first-order soliton ($N = 1$) is referred to as the fundamental soliton and its shape does not change on propagation. The soliton effect can be used in optical pulse compression [49], measurement of dispersion [50], or measurement of nonlinear coefficient [51].

1.4.1.3 Cross-phase modulation

As mentioned above, the SPM results from a change of refractive index leading to the time dependence of the nonlinear phase shift Φ_{NL} of a single wave propagation in optical fibers. When two or more waves propagate simultaneously in a fiber, each wave can change the refractive index. This change of refractive index influences the propagation of the different waves in the fiber. As a consequence, they interact with each other through the fiber nonlinearity. This introduces nonlinear coupling effects between the different waves, known as cross-phase modulation (XPM). XPM and also SPM are always accompanied together for a case of two optical fields of different wavelengths. The XPM may also come from the coupling between the two orthogonally polarized components of an optical field.

For two optical waves of frequencies ω_1 and ω_2 with their polarization identical along a fiber, the electrical field of the two waves can be written as

$$\mathbf{E}(r,t) = \frac{1}{2}\hat{x}\left[E_1\exp(i\omega_1 t) + E_2\exp(i\omega_2 t)\right] + \text{c.c.} \tag{1-61}$$

In the case of third-order susceptibility $\chi^{(3)}$, the nonlinear polarization P_{NL} can be

written as

$$\begin{aligned}\mathbf{P}_{NL}(r,t) = \tfrac{1}{2}\hat{x}\,\big[&P_{NL}(\omega_1)\mathrm{e}^{i\omega_1 t} + P_{NL}(\omega_2)\mathrm{e}^{i\omega_2 t}\\ &+P_{NL}(2\omega_1-\omega_2)\mathrm{e}^{i(2\omega_1-\omega_2)t}\\ &+P_{NL}(2\omega_2-\omega_1)\mathrm{e}^{i(2\omega_2-\omega_1)t}\\ &+P_{NL}(3\omega_1)\mathrm{e}^{i3\omega_1 t} + P_{NL}(3\omega_2)\mathrm{e}^{i3\omega 2t}\\ &+P_{NL}(2\omega_1+\omega_2)\mathrm{e}^{i(2\omega_1+\omega_2)t}\\ &+P_{NL}(2\omega_2+\omega_1)\mathrm{e}^{i(2\omega_2+\omega_1)t}\big] + c.c.\end{aligned} \tag{1-62}$$

The nonlinear polarization in Eq. (1-62) contains terms at new optical frequencies. These terms allow the creation of new waves in an optical fiber. The new frequencies and initial frequencies are illustrated in Figure 1.36. However, for new waves to be created in a fiber, several conditions must be met. The condition concerning phase-matching will be considered in detail in Section 1.4.1.4.

If frequencies ω_1 and ω_2 are close together, a group of new frequencies around the triple of initial frequencies ($\sim 3\omega_1$ and $\sim 3\omega_2$) can be generated as seen in zone B of Figure 1.36. For waves with frequencies far from each other, the phase matching condition is difficult to be met and thus the third-harmonic frequencies are not created or created with relatively small energy. The new frequencies in zone B are far from the initial band so that they can be ignored.

The nonlinear polarization also shows new frequencies at $2\omega_1-\omega_2$ and $2\omega_2-\omega_1$ around the initial frequencies ω_1 and ω_2 as seen in zone A in Figure 1.36. These waves correspond to the four-wave mixing (FWM) effect. The FWM effects also require the condition of phase matching. In this section, the condition for FWM is not considered so that the effect of FWM is negligible. The FWM effect will be discussed in detail in Section 1.4.1.4. In this section, only two terms of the nonlinear polarization $P_{NL}(\omega_1)$ and $P_{NL}(\omega_2)$ are considered. These two polarization can be written as

$$P_{NL}(\omega_1) = \chi_{eff}\left(|E_1|^2 + 2|E_2|^2\right)E_1, \tag{1-63}$$

$$P_{NL}(\omega_2) = \chi_{eff}\left(|E_2|^2 + 2|E_1|^2\right)E_2, \tag{1-64}$$

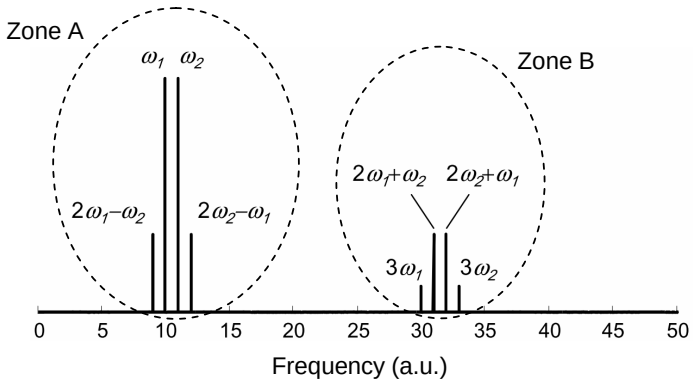

Figure 1.36: New frequencies created by XPM.

where

$$\chi_{eff} = \frac{3\epsilon_0}{4}\chi^{(3)}_{xxxx}. \tag{1-65}$$

When two waves E_1 and E_2 propagate in a fiber at different group velocities v_{g1} and v_{g2}, they may come out of the fiber at different time. The walk-off length L_W is defined as a fiber length over which two overlapping pulses (duration T_0) separate from each other by a time T_0 as a result of the group-velocity mismatch:

$$L_W = \frac{T_0}{v_{g1}^{-1} - v_{g2}^{-1}}. \tag{1-66}$$

Note that the group velocity v_g is deduced from the propagation constant β by the relation $v_g = (d\beta/d\omega)^{-1}$ (Eq. (1-35)), and by using an expansion of the propagation constant β in a Taylor series (Eq. (1-33)), we obtain:

$$v_{g1}^{-1} = \beta_1 + (\omega_1 - \omega_0)\beta_2, \tag{1-67}$$

$$v_{g2}^{-1} = \beta_1 + (\omega_2 - \omega_0)\beta_2. \tag{1-68}$$

The walk-off length is then expressed by

$$L_W = \frac{T_0}{\Delta\omega\beta_2}, \tag{1-69}$$

where $\Delta\omega$ is the difference in frequency between the two waves, $\Delta\omega = |\omega_1 - \omega_2|$. The walk-off length L_W is an important parameter in the case of two or more waves that simultaneously propagate along a fiber. Not only in XPM effect but also in FWM effect considered in the next section, the magnitude of nonlinear effects depends on the relation between fiber length L and walk-off length L_W.

1.4.1.4 Four-wave mixing

As discussed previously, the third-order susceptibility can include nonlinear interaction among four optical waves leading to four-wave mixing (FWM) or third-harmonic generation. In general, we can consider that a wave at frequency ω_4 is generated by the interaction of three waves at frequencies ω_1, ω_2, and ω_3. The electric field of four waves can be written as

$$\mathbf{E} = \frac{1}{2}\hat{x}\left[E_1 e^{i\omega_1 t - \beta_1 z} + E_2 e^{i\omega_2 t - \beta_2 z} + E_3 e^{i\omega_3 t - \beta_3 z} + E_4 e^{i\omega_4 t - \beta_4 z}\right] + \text{c.c.}, \tag{1-70}$$

where β_j and E_j are the propagation constant and the slowly varying envelope of the wave at frequency ω_j, respectively. The electric field contains 8 terms (4 terms and their 4 complex conjugates). The nonlinear polarization can be written as

$$\mathbf{P}_{NL} = \epsilon_0 \chi^{(3)} \vdots \mathbf{EEE}. \tag{1-71}$$

The nonlinear polarization thus contains 512 terms ($8\times8\times8$). Expanding the nonlinear polarization in the same way as the electric field E in order to retain only the terms oscillating at the initial frequencies, we obtain:

$$\mathbf{P}_{NL} = \frac{1}{2}\hat{x}\left[P_1 e^{(i\omega_1 t-\beta_1 z)} + P_2 e^{(i\omega_2 t-\beta_2 z)} + P_3 e^{(i\omega_3 t-\beta_3 z)} + P_4 e^{(i\omega_4 t-\beta_4 z)}\right] + \text{c.c.}, \tag{1-72}$$

where P_j ($j = 1$ to 4) consists of a large number of terms. For example, P_4 can be expressed as [47, 52]:

$$\begin{aligned} P_4 \;=\; & \tfrac{3\varepsilon_0}{4}\chi^{(3)}_{xxxx}\Big[|E_4|^2E_4 + 2\left(|E_1|^2+|E_2|^2+|E_3|^2\right)E_4 \\ & + 2E_1E_2E_3\exp(i\theta_+) + E_1E_2E_3^*\exp(i\theta_-) + ...\Big], \end{aligned} \tag{1-73}$$

where ε_0 is the vacuum permittivity, E_j ($j = 1$ to 4) is the electric field of the frequency ω_j, and θ_+ and θ_- are defined as:

$$\theta_+ = (\beta_1+\beta_2+\beta_3-\beta_4)z - (\omega_1+\omega_2+\omega_3-\omega_4)t, \tag{1-74}$$

$$\theta_- = (\beta_1+\beta_2-\beta_3-\beta_4)z - (\omega_1+\omega_2-\omega_3-\omega_4)t. \tag{1-75}$$

In Eq. (1-73), the first four terms containing E_4 are responsible for self-phase modulation (SPM) (first term) and cross-phase modulation (XPM) (3 following terms) respectively. The remaining terms result from the frequency combinations of all the four waves. The phase-matching between E_4 and P_4, which is governed by θ_+ and θ_-, determines how many frequency combinations are effective.

Typically, from Eq. (1-73), two schemes of FWM terms can be classified [5, 53]. The first term containing θ_+ corresponds to the case in which three photons (at frequencies ω_1, ω_2, and ω_3) transfer their energy to a new single photon at frequency $\omega_4 = \omega_1+\omega_2+\omega_3$ (Figure 1.37(a)). When the three waves are at the same frequency ($\omega_1 = \omega_2 = \omega_3$), this term is known the *third-harmonic generation* ($\omega_4 = 3\omega_1$). Note that the third-harmonic generation is a special type of FWM in which three frequencies coincide. The second term containing θ_- in Eq. (1-73) describes the case when a new wave ω_4 is generated from three waves in a relation

$$\omega_4 = \omega_1+\omega_2-\omega_3. \tag{1-76}$$

This case corresponds to the case of two pumps at ω_1 and ω_2 together with a signal at ω_3 and yields to a new "idler" wave at ω_4 (Figure 1.37(b)). In the case of two waves centered at the same frequency $\omega_1 = \omega_2$, the FWM is called *degenerate FWM*. It corresponds to the case of Figure 1.37(c) and the new "idler" frequency is

$$\omega_4 = 2\omega_1-\omega_3. \tag{1-77}$$

The term θ_- also describes the case of the interaction between two photons (ω_1 and ω_2) yielding two new photons (ω_3 and ω_4). In the case of $\omega_1 = \omega_2$, a strong pump wave at ω_1

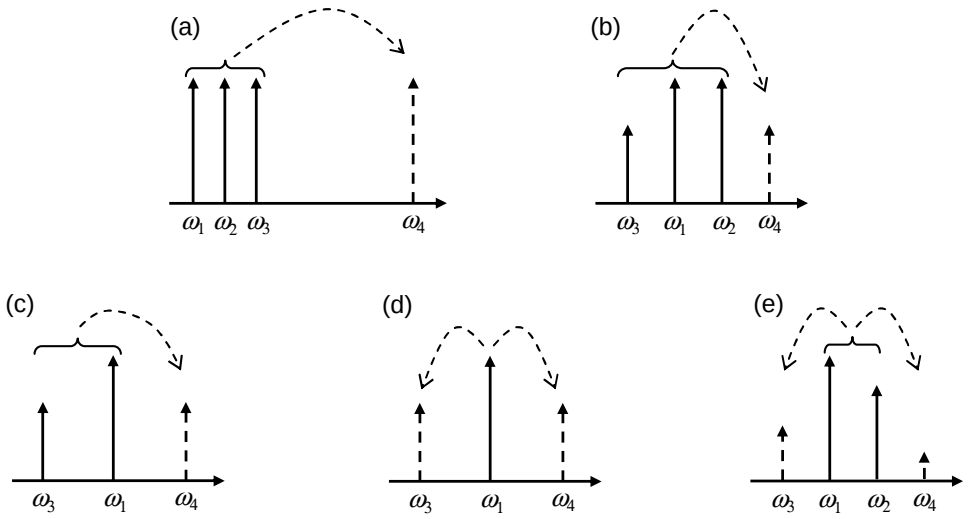

Figure 1.37: Five typical types of FWM.

creates two sidebands located symmetrically at frequencies ω_3 and ω_4. This type of FWM is also called *degenerate FWM* (Figure 1.37(d)). Both types of the degenerate FWM can also be called three-wave mixing as only three distinct frequencies are involved in the nonlinear process. However, the term three-wave mixing is generally reserved for the $\chi^{(2)}$ processes and not for $\chi^{(3)}$ processes. In the general case $\omega_1 \neq \omega_2$, we have *non-degenerate FWM*. This corresponds to the type of FWM described in Figure 1.37(e). The four waves are related in frequency as follows

$$\omega_3 + \omega_4 = \omega_1 + \omega_2. \tag{1-78}$$

In this case, two new waves at frequencies ω_3 and ω_4 are created simultaneously from two input waves ω_1 and ω_2. Our experiments in Chapter 3 and Chapter 4 fall in this type of FWM. Note that Figures 1.37(d) and 1.37(e), in which the idlers are generated from noise, are the spontaneous counterparts of Figures 1.37(c) and 1.37(b), respectively.

In general, the phase-matching requirement for FWM is $\Delta k = 0$, where

$$\begin{aligned} \Delta k &= \beta_3 + \beta_4 - \beta_1 - \beta_2 \\ &= (\tilde{n}_3\omega_3 + \tilde{n}_4\omega_4 - \tilde{n}_1\omega_1 - \tilde{n}_2\omega_2)/c, \end{aligned} \tag{1-79}$$

where $\tilde{n}_j$ ($j = 1$ to 4) is the effective mode index at the frequency ω_j.

The phase-matching Δk can also be written as the contribution of the linear mismatch Δk_L and the nonlinear mismatch Δk_{NL}:

$$\Delta k = \Delta k_L + \Delta k_{NL}. \tag{1-80}$$

The linear contribution Δk_L comes from dispersion and the nonlinear contribution Δk_{NL} depends on the nonlinear coefficient γ and the input peak powers. They are expressed as:

$$\Delta k_L = \beta_2 \Delta\omega^2, \tag{1-81}$$

$$\Delta k_{NL} = \gamma(P_1 + P_2), \tag{1-82}$$

where β_2 is the second-order dispersion, $\Delta\omega = \omega_2 - \omega_1$ is the frequency detuning, γ is the nonlinear coefficient, and P_1 and P_2 are input peak powers of the two input waves.

In a single-mode fiber, for phase-matching condition, three possibilities can be considered:

- Nearly phase-matching: in reality, a significant FWM can occur even if phase matching is not perfect to yield $\Delta k = 0$. The amount of tolerable wave-vector mismatch depends on how long the fiber is in comparison with the coherence length L_{coh}. Normally, Δk_L dominates Δk_{NL}. In this case, the coherence length is given by

$$L_{coh} = \frac{2\pi}{|\beta_2|\Delta\omega^2}. \tag{1-83}$$

  The coherence length indicate that significant FWM can occur when the fiber length satisfies the condition $L < L_{coh}$. This condition ($L < L_{coh}$) is known as the nearly phase-matching condition for FWM.

- Phase matching near the zero-dispersion wavelength: the linear contribution Δk_L near the zero-dispersion wavelength λ_{ZD} of the fiber is close to zero. Thus, the phase-matching condition is satisfied, provided that the nonlinear mismatch Δk_{NL} is kept close to zero. In other words, the phase-matching condition is satisfied in a limited range of power.

- Phase matching due to SPM: when the pump wavelength lies in the anomalous dispersion regime ($D > 0$) and deviates considerably from λ_{ZD}, the linear mismatch Δk_L is negative. Then, the nonlinear contribution Δk_{NL} is required to satisfy the condition $\Delta k = 0$. The corresponding frequency shift $\Delta\omega$ can be calculated by using the relation $\Delta k_L \approx \Delta k_{NL}$ and we obtain

$$\Delta\omega = \left[\frac{\gamma(P_1 + P_2)}{|\beta_2|}\right]^{1/2}, \tag{1-84}$$

  where P_1 and P_2 are the input peak powers of the two pumps. Thus, pump waves propagating in the anomalous dispersion regime can develop sidebands as a result of FWM that is phase-matched by the nonlinear process of SPM.

Figure 1.38 shows a schematic diagram for non-degenerate FWM simulation in an optical fiber. The two waves at frequencies ω_1 and ω_2, after propagating through a nonlinear medium, generate two new wave at frequencies ω_3 and ω_4 (named as anti-Stokes and Stokes waves or "idlers") as seen in Figure 1.39.

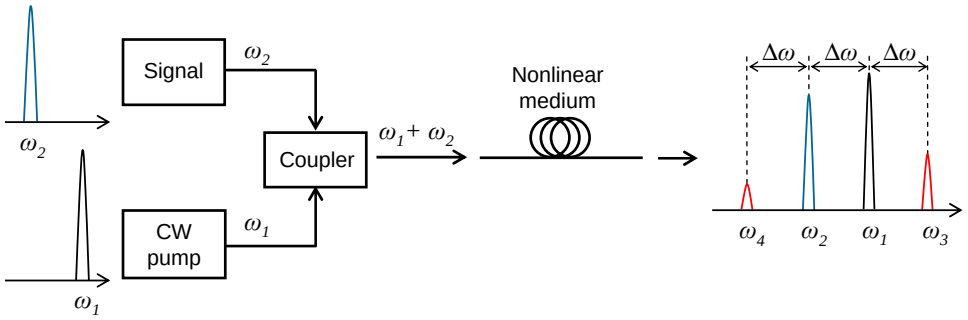

Figure 1.38: Theoretical schematic diagram for non-degenerate FWM generation.

Theoretical illustration of non-degenerate FWM is implemented for a signal at ω_1 (λ_1) and a continuous wave at ω_2 (λ_2). The NLSE is numerically solved for these two waves that propagate simultaneously in an optical fiber. A DSF fiber is taken for the simulation with $\alpha = 0.25$ dB/km, $\gamma = 2.6$ W^{-1}km^{-1}, fiber length $L = 2000$ m, the zero-dispersion wavelength $\lambda_{ZD} = 1555$ nm, and dispersion slope $S = 0.07$ ps/km/nm^2. Figure 1.39 illustrates the spectra at the input and the output of the fiber. The output spectrum shows Stokes and anti-Stokes frequencies appearing in symmetrical pairs ($\omega_4 = 2\omega_1 - \omega_2$ and $\omega_3 = 2\omega_2 - \omega_1$). We can also observe higher-order FWM waves due to different combinations of ω_1 and ω_2 ($\omega_6 = 3\omega_1 - 2\omega_2$, $\omega_5 = 3\omega_2 - 2\omega_1$ and so on). Practically, one can use an optical filter to extract out the converted signal at both Stokes or anti-Stokes side bands. The wavelength of the converted signal can be controlled by tuning the wavelength of the CW pump. In Figure 1.39, the λ_j ($j = 1, 2, \ldots$) corresponds to the frequency ω_j ($j = 1, 2, \ldots$).

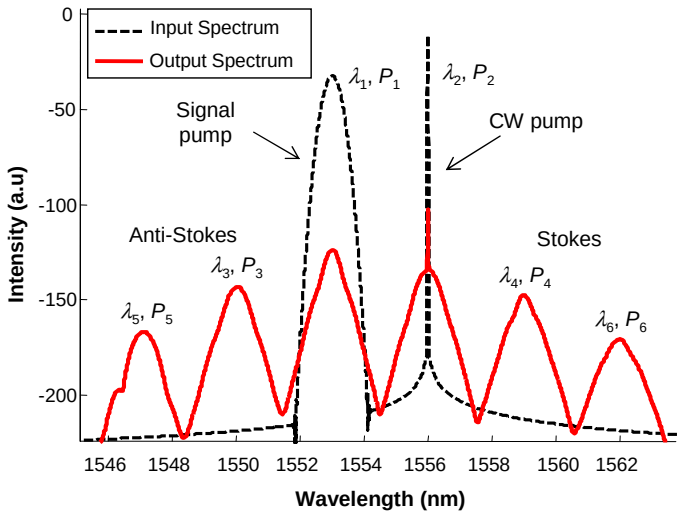

Figure 1.39: Theoretical spectra of FWM for modulated pump ω_1 and CW pump ω_2. The fiber parameters are fiber losses $\alpha = 0.25$ dB/km, the nonlinear coefficient $\gamma = 2.6$ W^{-1}km^{-1}, fiber length $L = 2000$ m, the zero-dispersion wavelength $\lambda_{ZD} = 1555$ nm, and dispersion slope $S = 0.07$ ps/km/nm^2.

To quantify the phase-matching for FWM, the phase-matching efficiency η_ϕ is defined as [54]

$$\eta_\phi = \frac{P_j(L,\Delta k)}{P_j(L,\Delta k=0)} = \left[\frac{\alpha^2}{\alpha^2+(\Delta k)^2}\right]\left[1+\frac{4\exp(-\alpha L)\sin^2(\Delta k L/2)}{(1-\exp(-\alpha L))^2}\right], \tag{1-85}$$

where α is the fiber loss, L is the fiber length, and P_j is peak power of the FWM wave λ_j ($j=3,\ 4$) (see Figure 1.39). It can be shown that the peak power P_3 of the stronger idler wave can be given by the relation [52]:

$$P_3 \ = \ \eta_\phi \gamma^2 P_1^2 P_2 L_{eff}^2 \exp(-\alpha L), \tag{1-86}$$

where γ is the nonlinear coefficient, and L_{eff} is the effective length. The peak power P_3 of the anti-Stokes wave λ_3 is proportional to the square of the input peak power of wave λ_1 and proportional to the input peak power of λ_2. In contrast, P_4 is proportional to P_1 and to the square of P_2. In wavelength conversion of an OOK signal with a continuous wave (CW), we can choose either λ_3 or λ_4 for the converted signal. The decision depends on which input peak power P_1 or P_2 is larger. However, for phase-modulated signals, the conversion has to preserve the phase of the signal. We, therefore, should select the wave that is proportional to the input data signal, not to the square of the input data signal. These issues will be discussed in Chapter 4.

FWM efficiency

To quantify the efficiency of FWM, we define the FWM efficiency as the ratio of the peak power of the idler at the output end of fiber to the input peak power. As an example for the idler P_3, two FWM efficiencies are possible: $\eta = P_3(L)/P_1(0)$ or $\eta = P_3(L)/P_2(0)$. In our work, for identity definition, FWM efficiency is defined as

$$\eta = \frac{P_3(L)}{P_2(0)}, \tag{1-87}$$

and for the wave λ_4, FWM efficiency is

$$\eta = \frac{P_4(L)}{P_1(0)}. \tag{1-88}$$

Wavelength conversion range

Figure 1.40 illustrates the FWM efficiency with respect to the wavelength detuning $\Delta\lambda$ between two input continuous waves, $\Delta\lambda = \lambda_2 - \lambda_2$. The fiber taken into the calculation is 10 m with a dispersion $D = -15$ ps/km/nm at 1550 nm. This theoretical curve is plotted from the definition of FWM efficiency in Eq. (1-87) and using Eq. (1-86). As seen in Figure 1.40, the FWM efficiency η varries with $\Delta\lambda$. The first point $\Delta\lambda_0$ for which the FWM efficiency is locally minimum is determined by $\sin^2(\Delta k L/2) = 0$ in Eq. (1-85). The value of $\Delta\omega$ that reduces $\sin^2(\Delta k L/2)$ to zero is:

$$\Delta\omega_0^2 = \frac{2\pi}{\beta_2 L}, \tag{1-89}$$

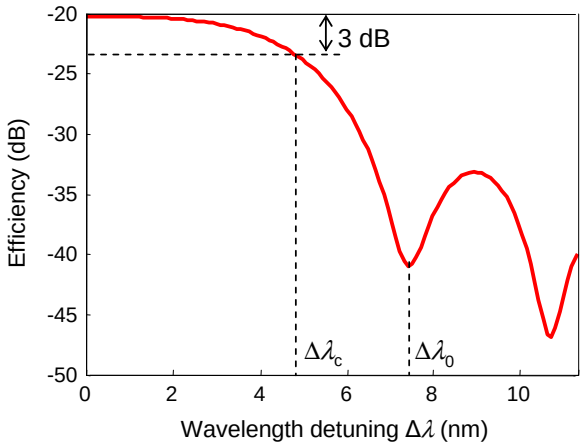

Figure 1.40: FWM efficiency with respect to wavelength detuning $\Delta\lambda$. Fiber length $L = 10$ m, dispersion $D = -15$ ps/km/nm at 1550 nm.

or in the wavelength domain:

$$\Delta\lambda_0 = \frac{\lambda_0}{\sqrt{cL\,|D|}}. \tag{1-90}$$

$\Delta\lambda_0$ is known as the *zero-efficiency detuning*. We define the *wavelength conversion range* $\Delta\lambda_c$ as the wavelength detuning $\Delta\lambda$ at which the FWM efficiency is reduced by a factor of 2 (3 dB) with respect to the maximum FWM efficiency (see Figure 1.40). By calculation, a good approximation of $\Delta\lambda_c$ is

$$\Delta\lambda_c = 0.67\Delta\lambda_0. \tag{1-91}$$

In WDM transmission systems, FWM can be detrimental and systems thus must be designed to reduce its impact. It is, however, a useful phenomenon in the domain of nonlinear all-optical signal processing. FWM can also be used for nonlinear characterization of fibers or waveguides (Section 3.3.4 and 3.3.5). In Chapter 3, FWM together with SPM are used to characterize chalcogenide fibers. Optical signal processing applications based on the FWM effect in chalcogenide fibers will be investigated in Chapter 4.

1.4.2 Raman scattering

As mentioned earlier, stimulated Raman scattering (SRS) and stimulated Brillouin scattering (SBS) occur when the optical field transfers part of its energy to the nonlinear medium. Generally, in SRS and SBS, a photon of the incident field is annihilated to create a new photon. A fundamental difference is that SBS in single-mode fibers occurs only in the backward direction whereas SRS can occur in both directions.

For the Raman effect, in any molecular medium, an incident photon transfers a small fraction of its power to another photon, whose frequency is downshifted by an amount determined by the vibrational modes of the medium. The pump photon is annihilated, and

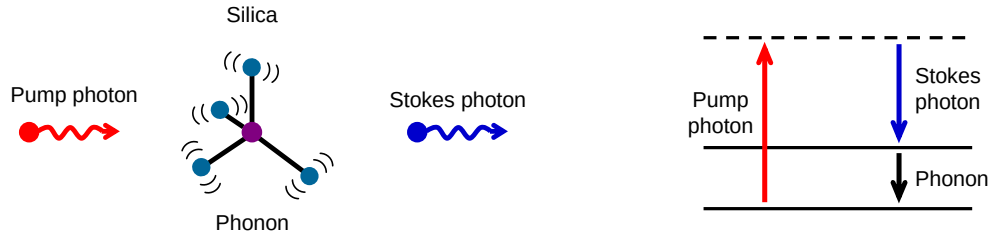

Figure 1.41: Schematic illustration of spontaneous Raman scattering in silica.

a new photon at a lower frequency and a phonon are created. The principle of the Raman effect can be seen in Figure 1.41.

The incident photon is often called the pump photon at frequency ν_p and the scattered photon is the Stokes photon at frequency ν_S. Usually a small portion of the pump photon is converted into a Stokes photon that is emitted in a random direction. This is known as *spontaneous Raman scattering*. For silica fibers, the difference in frequency (called the Raman shift) $\nu_p - \nu_s$ is around 13 THz. For a chalcogenide As_2Se_3 glass fiber, the Raman shift is about 7 THz [55].

When the pump photon flux is strong enough, the phenomenon of SRS, in which the Stokes wave from the Raman scattering grows rapidly during propagation, can be observed. This is known as Raman gain. The curve showing the Raman gain coefficient g_R (m/W) as a function of the frequency difference $\nu_p - \nu_s$ in a silica fiber with the pump at $\lambda_p = 1$ μm is shown in Figure 1.42.

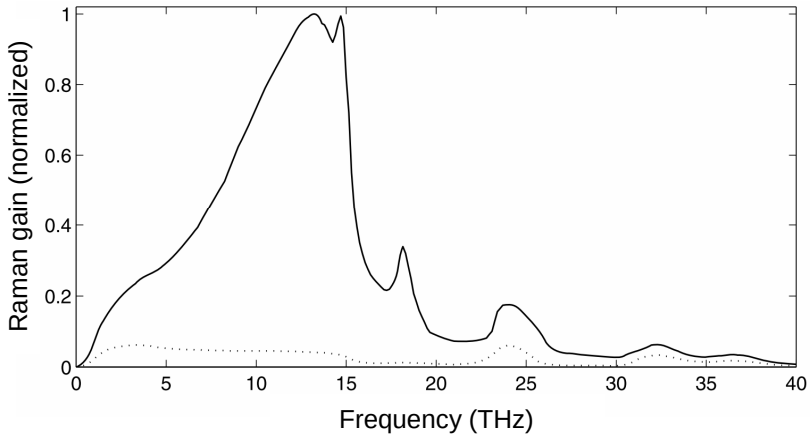

Figure 1.42: Normalized Raman gain for fused silica when the pump and Stokes waves are co-polarized (solid curve). The dotted curve shows the situation in which the pump and Stokes waves are orthogonally polarized (after Ref. [47]).

An important parameter in SRS is the Raman threshold. It is defined as the input pump power at which the Stokes power becomes equal to the pump power at the fiber output [56]. The condition is written as

$$P_s(L) = P_p(L) = P_0 \exp(-\alpha_p L), \tag{1-92}$$

where P_0 is the input pump power, α_p is fiber loss at the pump frequency, L is the fiber length. Assuming that $\alpha_s = \alpha_p$, the threshold condition becomes

$$P_{s0}^{eff} \exp(g_R P_0 L_{eff}/A_{eff}) = P_0, \tag{1-93}$$

where P_{s0}^{eff} depends on P_0, g_R is the Raman gain, L_{eff} is the effective length, and A_{eff} is the effective area. The solution of Equation 1-93 provides the critical input pump power P_0^{cr}, which is required to reach the Raman threshold. The critical input pump power P_0^{cr}, to a good approximation, is given by

$$\frac{g_R P_0^{cr} L_{eff}}{A_{eff}} \approx 16. \tag{1-94}$$

For an example, an optical fiber with fiber losses of 0.2 dB/km, fiber length L of 20 km, effective mode area of 50 μm^2, the Raman threshold is calculated to be 600 mW (28 dBm). In optical fiber communication systems, as optical powers are generally of the order of 10 mW, the Raman effect generally does not affect the transmission data.

Figure 1.43 illustrates an example of SRS spectrum in a chalcogenide AsSe fiber. The wavelength of the pump wave is 1547 nm. The Stokes shifted wave is observed around 1605 nm leading to a Stokes-shift of 58 nm. It is equivalent to 7 THz in the frequency domain.

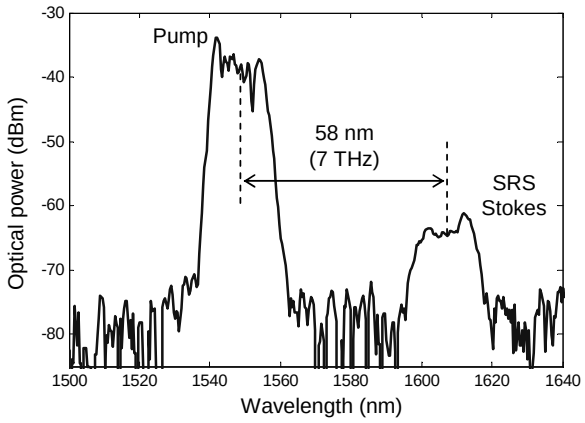

Figure 1.43: Experimental spectrum of SRS of a chalcogenide AsSe fiber with pump peak power of 3 W.

1.4.3 Brillouin scattering

Stimulated Brillouin scattering (SBS) is a nonlinear process that can occur in optical fibers. Input power levels for SBS is much lower than those needed for SRS. Similarly to SRS, SBS manifests itself through the generation of a Stokes wave whose frequency is shifted from that of the incident light by an amount set by the nonlinear medium. The SBS, however, differs from the Raman effect in both the physical principle of the generation of the Stokes wave and the magnitude of the frequency shift (11 GHz instead of 13 THz for Raman effect

in a silica fiber). The Stokes wave of SBS propagates only backward in contrast with SRS that can occur in both directions in an optical fiber.

The principle of the Brillouin effect can be seen in Figure 1.44. The process of SBS can be described classically as a nonlinear interaction between the pump and Stokes fields through an acoustic wave. The pump field generates an acoustic wave through the process of electrostriction. The acoustic wave in turn modulates the refractive index of the medium. This pump-induced index grating scatters the pump light through Bragg diffraction. Scattered light is downshifted in frequency as the Doppler shift associated with a grating moving at the acoustic velocity v_A ($v_A = 5.96$ km/s in silica). The Brillouin shift is given by

$$v_B = \frac{2n_p v_A}{\lambda_p}, \tag{1-95}$$

where λ_p is the wavelength of the pump and n_p is the effective mode index at the pump wavelength λ_p. For example, at the wavelength of 1550 nm and $n_p = 1.45$, the Brillouin shift v_B in silica is 11 GHz.

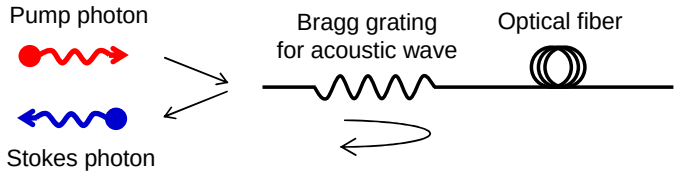

Figure 1.44: Stimulated Brillouin scattering in an optical fiber.

Similarly to the case of SRS, the growth of the Stokes wave is characterized by the Brillouin-gain spectrum $g_B(\nu)$. The Brillouin-gain spectrum for silica fibers can differ significantly from that of bulk silica because of the guided nature of optical modes and the presence of dopants in the fiber core. Figure 1.45 shows the gain spectra measured for three different fibers having different structures and different doping levels of germanium (GeO_2) in their cores. The bandwidth of the Brillouin gain is around 10 MHz in silica fibers.

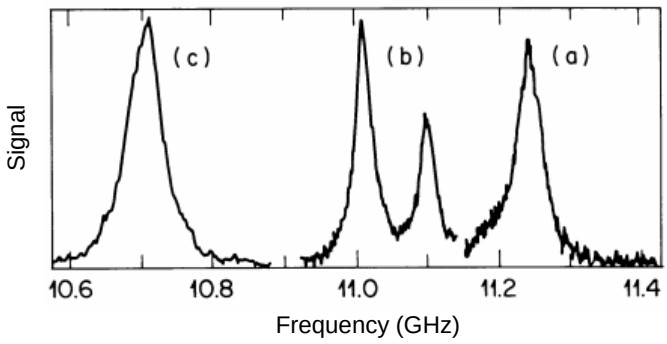

Figure 1.45: Brillouin-gain spectra of three fibers for $\lambda_p = 1525$ μm: (a) single-mode fiber, (b) depressed-cladding fiber, and (c) dispersion-shifted fiber (after Ref. [47]).

As for the Raman effect, it is possible to find an analytical solution for the Brillouin threshold value which corresponds to the value of the critical input pump power P_0^{cr} for

which the power of the Stokes wave is equal to the reflected power of the pump wave transmitted. The Brillouin threshold is found to occur at a critical pump power P_0^{cr} such that

$$g_B P_0^{cr} L_{eff}/A_{eff} \approx 21. \tag{1-96}$$

For example, for an optical fiber with fiber losses of 0.2 dB/km at the wavelength of 1550 nm, $A_{eff} = 50\ \mu m^2$, and $g_B = 5 \times 10^{-11}$ m/W, the critical input pump power P_0^{cr} is 1 mW. Compared with the P_0^{cr} of SRS, this value is dramatically smaller.

Figure 1.46 illustrates the SBS spectrum for a suspended-core chalcogenide fiber composed of AsSe. The pump is a continuous wave with a bandwidth of 70 kHz and a power of 150 mW. The peak observed at 1551.38 nm represents the Fresnel-reflected pump signal at the fiber input facet. The second peak, redshifted by 0.0636 nm (7.95 GHz) with respect to the pump signal, corresponds to the first-order Stokes Brillouin wave and the third peak is the back-reflected second-order Stokes Brillouin wave.

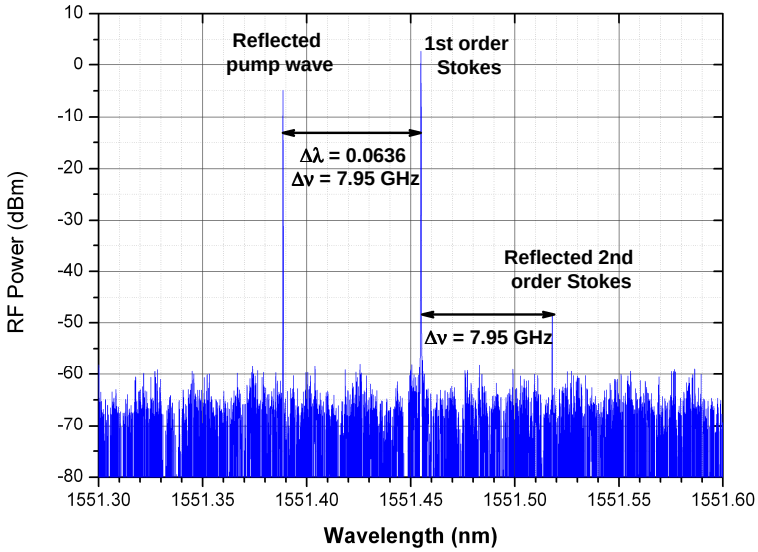

Figure 1.46: Optical spectrum of the backscattered light from AsSe fiber.

Stimulated Brillouin scattering is a nonlinear process that can occur in optical fibers at low input power levels. The SBS threshold depends not only on the material but also on the linewidth of the pump. A pump with a linewidth lower than the Brillouin bandwidth (10 MHz of silica) may lead to a low SBS threshold. The Brillouin threshold is considerably increased when the linewidth of the pump is largely wider than the Brillouin bandwidth. In practice, when the Brillouin effect is not desired, a narrow-linewidth CW wave can be modulated in order to enlarge its spectral width and increase the Brillouin threshold. However, for some reasons, if the CW wave is not allowed to be modulated, other solutions to suppress SBS must be found. Following this objective, an active research on how Brillouin can be suppressed in HNLF is carried out [57, 58].

In optical communication systems, SBS can limit the channel power and can degrade signal propagation. SBS is, however, useful for making fiber-based Brillouin lasers [59] and Brillouin amplifiers [60], which are now an active topic due to the trend of highly nonlinear optical fibers.

1.5 Nonlinear fibers

As seen in the previous section, the magnitude of the Kerr effect is proportional to the nonlinear coefficient γ, the input optical peak power P_0 and the fiber length L. In nonlinear fiber optics, when trying to make an optical signal processing device based on a nonlinear optical fiber, we need to decrease the optical powers as much as possible. Increasing the nonlinear coefficient allows a reduction of the optical power or required length or both at once. This makes optical systems more easily integrated, more compact and less expensive.

We recall here the formula for the nonlinear coefficient from Eq. (1-45):

$$\gamma = \frac{2\pi n_2}{\lambda A_{eff}}, \tag{1-97}$$

where n_2 is the nonlinear refractive index, λ is the wavelength, and A_{eff} the effective area. For example, for a standard SMF with a core diameter $2a = 8.4$ μm, a nonlinear refractive index $n_2 = 2.6\times10^{-20}$ m^2/W, and an effective area $A_{eff} = 80$ μm^2, the nonlinear coefficient γ at 1550 nm is 1.3 W^{-1}km^{-1}. To increase the nonlinear coefficient γ, one can act on the fiber core structure to reduce A_{eff} or on material to increase n_2.

- Fiber core structure: by decreasing the core diameter of the fiber, the effective mode area A_{eff} can be reduced. The nonlinear coefficient may be enhanced 10 times compared to a SMF. Recently, the advent of microstructured fibers allows further reduction of the core diameter [61]. These fibers, due to their particular structure, can confine the guided mode in dimensions slightly larger than the wavelength. By using a microstructured core, the nonlinear coefficient of a silica fiber can be increased nearly by a factor of 50 compared to a standard SMF [15]. In addition, these fibers can manage chromatic dispersion over a wide frequency range.

- Materials: doping silica glasses with some elements (GeO_2, Al_2O_2, F, etc.) or using other materials with higher nonlinear refractive index n_2 rather than silica allows the increase of the nonlinear coefficient. For example, in the literature, bismuth-oxide glasses [62, 63], lead silicate [64, 65], tellurite oxide [66, 67], silicon [68, 69] or chalcogenide glasses [18, 70] are extensively studied. Among them, chalcogenide glasses exhibit an ultra-high nonlinearity with n_2 which may be 500 times greater than silica [55]. A combination of a material with a high nonlinearity and a proper structure (microstructure for example) can lead to fibers with extremely nonlinear characteristics and dispersion tailoring.

Figure 1.47 shows a representation of the nonlinearity increase with material and waveguide structure. For a standard SMF, the nonlinear coefficient γ is around 1 W^{-1}km^{-1}. A highly nonlinear fiber (HNLF) is a step-index silica fiber with a smaller core diameter

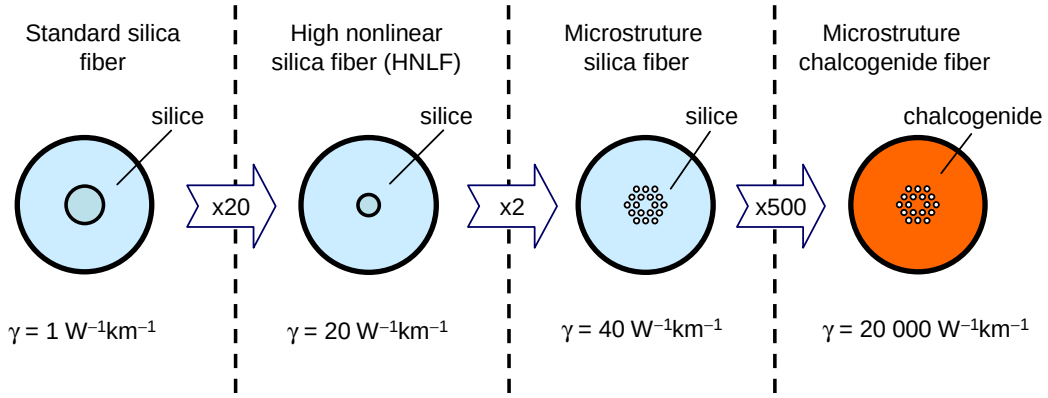

Figure 1.47: Nonlinear coefficient γ increases with the change of core structure and material.

and a highly doped silica glass. Its nonlinear coefficient γ may increase 20 times to about 20 $W^{-1}km^{-1}$. The core diameter of a silica fiber can be decreased more by using a microstructure. The nonlinear coefficient of a silica microstructured fiber may be a factor of 2 compared to the HNLF. A dramatic jump in the nonlinear coefficient can be achieved with chalcogenide glasses. As mentioned, chalcogenide glasses with 500 times higher nonlinear refractive index can lead to a nonlinear coefficient of the order 20 000 $W^{-1}km^{-1}$.

In the next sections, nonlinear step-index fibers and nonlinear microstructured fibers will be discussed.

1.5.1 Nonlinear step-index fibers

To have a small effective mode area A_{eff}, one need to reduce the core diameter of the fiber while maintaining the value of the V parameter to ensure a good confinement of light and singlemode propagation (i.e. $V > 2$ to confine about 75% of the power in the core and $V < 2.405$ to satisfy the condition of singlemode guidance). We recall here the formula for the V parameter from Eq. (1-25)

$$V = ka\sqrt{n_1^2 - n_2^2} = ka\mathrm{NA}. \tag{1-98}$$

The V parameter is proportional to the core diameter a of a fiber and numerical aperture NA. To reduce the core diameter of a fiber while conserving the value of the V parameter, the NA needs to be increased. In other words, the contrast between the refractive index of the core and the refractive index of the cladding needs to be increased.

In 1998, M. Onishi *et al.* reported a silica HNLF with high-concentration-GeO_2-doped core and fluorine-doped cladding to realize a high nonlinear coefficient of 20.4 $W^{-1}km^{-1}$ [71]. In 2006, T. Nakanishi *et al* reported a silica-based highly nonlinear fiber with a nonlinear coefficient of 30 $W^{-1}km^{-1}$ [72]. This was achieved by governing the refractive index profile with a GeO_2- doped core and a fluorine-doped depressed cladding. For larger increase in the value of the nonlinear coefficient of step index fibers, a greater increase of the core-cladding

index contrast is required. Both core-diameter and core-cladding index contrast are so far limited.

The nonlinearity of step-index fibers is increased by using other nonlinear materials rather than silica ($n_2 = 2.6 \times 10^{-20}$ m^2/W). The materials could be lead-silicate, bismuth glasses, chalcogenide glasses, etc. In 2010, A. Camerlingo *et al.* reported a W-type fiber based on lead-silicate with a commercial SF57 glass in the core. The nonlinear refractive index n_2 of about 10^{-19} m^2/W (for a commercial SF57 glass) [73] and a small core diameter of 1.6 μm lead to a nonlinear coefficient γ of 820 W^{-1}km^{-1} [65]. Bismuth-oxide (Bi_2O_3) has a nonlinear refractive index n_2 of the order of ten times the value of n_2 of silica [74]. In 2004, N. Sugimoto *et al.* reported a bismuth step-index fiber with a nonlinear coefficient of 1360 W^{-1}km^{-1} [75] and a fiber loss of 1.9 dB/m at 1310 nm. Chalcogenide glasses have higher nonlinear refractive index n_2 leading to higher nonlinear coefficient. For chalcogenide step index fibers, a typical example is reported in [76]. The composition is As_2Se_3 with a nonlinear refractive index $n_2 = 2.4 \times 10^{-17}$ m^2/W leads to a nonlinear coefficient of 2450 W^{-1}km^{-1}. The fiber loss is 1 dB/m.

1.5.2 Nonlinear microstructured fibers

Microstructured optical fibers (MOFs) are a new class of optical fibers having internal structure and light-guiding properties that are significantly different from conventional optical fibers. A cross-section of a microstructured fiber reveals micro-channels (air holes) that run the length of the fiber. The air holes can be made with diameters less than 1 μm. The diameter, the spacing (periodicity), and the configuration of the air holes can be modified to achieve fibers with unique characteristics.

The increase in the nonlinearity of fibers has been possible by the technological breakthrough of MOFs. MOFs are typically separated into two classes, defined by the way in which they guide light: *holey fibers* (HF) for a solid core fiber (Figure 1.48(a)) and *photonic band-gap fibers* for light guidance in a hollow core can be achieved via photonic band-gap effects (Figure 1.48(b)). For example, silica MOFs are composed entirely of silica, but the cladding contains a proportion of air that can be controlled. By increasing the proportion of air significantly, it is possible to greatly increase the index contrast between the core and the cladding. Therefore, the effective mode area A_{eff} of the fiber can be further reduced to increase the nonlinearity of the fiber.

If the MOFs are defined by the material which composes the fiber, they can be classified into two categories: silica MOFs and non-silica MOFs. For non-silica MOFs, there are various types such as chalcogenide MOFs (AsSe MOFs, GeAsSe MOFs, etc.), Bismuth-oxide MOFs, silicon MOFs, tellurite MOFs, lead-silicate MOFs, etc.

If the MOFs are classified by structure types, they can be "hexa" MOFs, grapefruit MOFs, "delta" MOFs, etc. The "hexa" structure MOFs in Figure 1.48(c) consist of hexagonal rings of air holes and the closest ring to the core consists of 6 air holes. The hexa MOFs are the

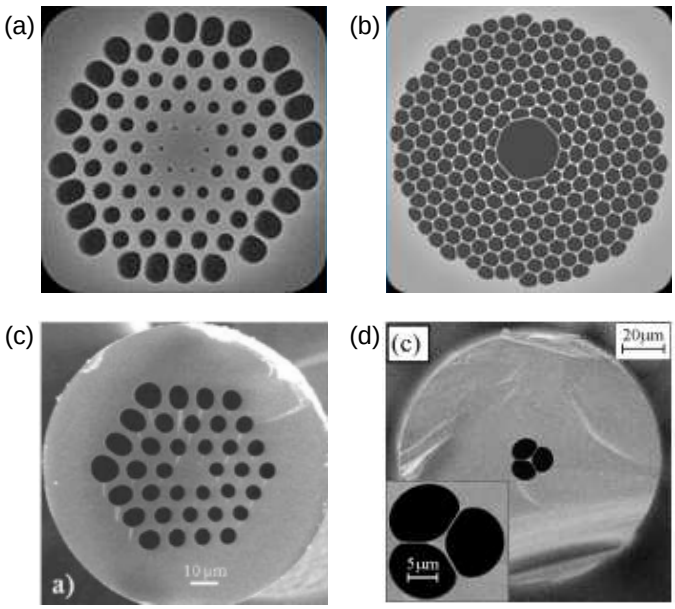

Figure 1.48: Several types of MOFs: (a) hexagonal microstructure, (b) hollow-core microstructure, (c) 3-ring microstructure, and (d) suspended-core microstructure.

most common MOFs. Depending on how many rings of air holes around the core, MOFs can be called as n-ring MOFs. For the example in Figure 1.48(c), is called a 3-ring MOF. The "delta" structure MOF in Figure 1.48(d) is also called a suspended-core MOF. These two types of MOFs will be further considered in Chapter 3 and Chapter 4.

There are some critical parameters in MOFs designing. Figure 1.49 shows the case of hexa MOFs with the key geometrical parameters: the air hole diameter d, the distance between two any adjacent air holes in the cladding Λ and the number of rings or air holes N_r (in the example, $N_r = 2$). These parameters determine the characteristics of MOFs such as fiber losses, fiber dispersion and also fiber nonlinearity. The condition of single-mode propagation is $d/\Lambda < 0.4$ for an infinite number of rings according to Ref. [61, 77].

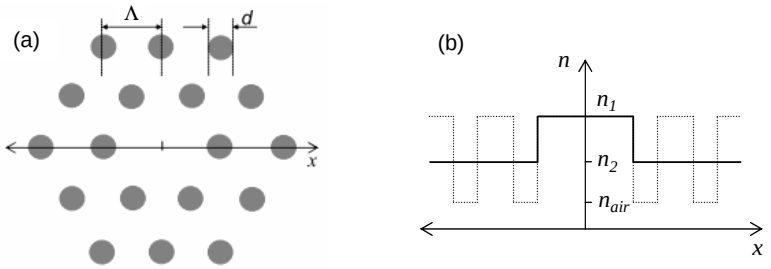

Figure 1.49: An example of MOF design with two-rings of air holes (a) and its refractive index profiles (b).

An example of a silica MOF is reported in [15]. The nonlinear coefficient of the fiber is 70 $W^{-1}km^{-1}$ and the fiber losses is 190 dB/km. Note that, this fiber has a effective mode area as small as 1.5 μm^2, which is close to the fundamental limitation for mode guidance

at 1550 nm in silica fibers [78]. Recently a lot of studies have been carried out on non-silica MOFs. Based on tellurite glasses, a hexa MOF was reported in 2009 with the nonlinear coefficient of 5700 $W^{-1}km^{-1}$ and fiber losses of 5 dB/m [79]. For chalcogenide glasses fiber, the first MOF was fabricated in 2000 [18]. Since then, many studies on chalcogenide MOFs have been reported [80, 81, 82]. To the best of our knowledge, by the time this thesis began, the highest nonlinear coefficient for MOFs, 15000 $W^{-1}km^{-1}$, was demonstrated by Foton in 2009 with a chalcogenide hexa 3-ring MOF [21].

1.6 All-optical signal processing

In conventional optical transmission systems, when an optical signal is processed (regeneration, add/drop, demultiplexing, switching...) transmitted optical signals are converted to electrical signals and then re-converted from electrical to optical for further transmission. This process is known as the optical-electrical-optical (O-E-O) conversion. It suffers some disadvantages such as limitation of about 50 GHz, power consumption, electromagnetic interference (EMI), and of course active processes. That makes the systems neither compact nor suitable for high bit rates. A solution is direct processing of optical signals. Figure 1.50 illustrates the difference between a conventional signal processing and all-optical signal processing, the example here is wavelength conversion.

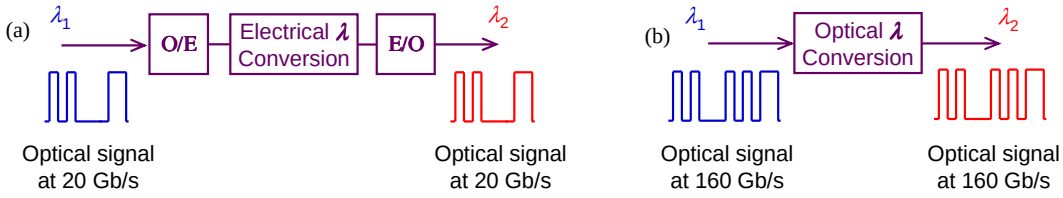

Figure 1.50: (a) Conventional wavelength conversion at 20 Gb/sand (b) all-optical wavelength conversion at 160 Gb/s.

All-optical signal processing has been and is still receiving a lot of attention all over the world because it can greatly increase the capacity of the optical networks by avoiding the O-E-O conversion process. All-optical signal processing is widely used in regeneration, wavelength conversion, format conversion, mux/demux, switching, sampling, etc.

To implement all-optical signal processing, nonlinear effects based operations seem to be good techniques. There exists a wide variety of photonic materials capable of providing all-optical nonlinear signal processing operations, including semiconductor optical amplifiers (SOAs), saturable absorbers (SAs), nonlinear fibers, nonlinear waveguides, etc. Fiber-based solutions have the advantage of being directly integrated with existing fiber networks and being passive operations. Silica-based highly nonlinear fibers (HNLFs), for the beginning, is the most interesting for the reason of well understood material and cost. However, one of the limitations of current HNLFs is a low power threshold of stimulated Brillouin scattering (SBS), which sets an upper limit on the amount of power launched into HNLFs.

Many other materials, including bismuth-oxide fiber (Bi-HNLF), tellurite-based fibers, silicon, lead-silicate, and chalcogenide fibers, and microstructured fibers have also shown great potential in miscellaneous all-optical signal processing applications.

Depending on the characteristics of these components, the nonlinear interaction $\chi^{(2)}$ or $\chi^{(3)}$ is exploited. Periodically poled lithium niobate (PPLN) waveguides, for example, take advantage of $\chi^{(2)}$ nonlinearity such as second-harmonic generation (SHG), difference-frequency generation (DFG), or sum-frequency generation (SFG). Fibers, nanowires, waveguides, and chips may utilize SPM, XPM, or FWM, Brillouin or Raman effects, which are caused by the $\chi^{(3)}$ nonlinearity.

In our work, three operations in all-optical signal processing are considered: regeneration, wavelength conversion, and demultiplexing. The use of silica-based fiber to demonstrate 160 Gb/s all-optical signal regeneration will be discussed in Chapter 2. This is enabled by exploiting the SPM effect in a silica fiber with dispersion tailoring. FWM effects in chalcogenide fibers allow us to implement all-optical signal wavelength conversion and all-optical signal demultiplexing at high bit rates. These will be dealt in Chapter 4.

1.7 Conclusion

This chapter has provided a basic understanding of optical transmission systems. It has supplied a foundation for the following chapters. All the fundamental concepts and definitions of concern in this thesis have been involved.

Fundamental notions of optical transmission systems with three key elements, including transmitters, optical fibers, and receivers, have been provided in the two first sections. Optical modulation types (ASK, FSK, PSK) and modulation formats (RZ, NRZ) have also been described in the first section. Geometric description, wave propagation, and physical mechanisms of optical fibers were dealt with in the second section. Section 1.3 described several types of fibers which tailor fiber dispersion for enhancing transmission capacity. The dispersion-managed fiber has been introduced with the aim of using it for 160 Gb/s regeneration, which will be discussed in Chapter 2.

The following sections of this chapter were devoted to nonlinear optics and introduction of all-optical signal processing. The nonlinear Schrödinger equation, Kerr effects, Raman effect and Brillouin effect are involved. The Kerr effect including effects such as self-phase modulation and four-wave mixing effects have been concentrated on. These nonlinear effects will be used in the following chapters for nonlinearly characterizing chalcogenide fibers as well as implementing photonic applications. An introduction of nonlinear fibers with their classification was also supplied.

This chapter also defined or determines terminologies which are used identically throught out the thesis. The following chapters will focus on our contributions with theoretical and experimental results.

Chapter 2

Study of 160 Gb/s 2R-Regeneration

All-optical signal regeneration is a solution for future high speed (>100 Gb/s) long distance optical fiber transmission systems. It supports not only high-bit-rate operations but also flexibility, compactness, low cost and low power consumption. All-optical regeneration may preferably be implemented by in-line regenerators which rely on fiber-based techniques. Different fiber-based all-optical approaches have been proposed to accomplish regeneration at high bit rates. They can be based on instantaneous nonlinear effects in fibers, such as self-phase modulation [83, 84], non-linear optical loop mirrors [85, 86], cross-phase modulation [87] or four-wave mixing [88, 89]. Amongst these fiber-based regeneration methods, the 2R-scheme proposed by Mamyshev in 1998 [83], which relies on SPM-induced spectral broadening in a normally dispersive fiber and offset filtering, is particularly attractive due to its relative simplicity and potential for low-cost implementation.

The aim of this chapter is to investigate the influence of high-order dispersion on 160 Gb/s regeneration. Based on this, dense dispersion-managed fiber designs are proposed to perform regeneration of 160 Gb/s signals. The principle and experimental demonstrations of Mamyshev 2R-regeneration are described in Section 2.1. Section 2.2 and Section 2.3 provide simple scale rules to calculate the parameters of a Mamyshev regenerator and a simulation model of 160 Gb/s regeneration with noise addition, respectively. The influence of high-order dispersion on regeneration at high bit-rate is analyzed in Section 2.4. To overcome the limitation caused by the high-order dispersion, Section 2.5 discusses fiber designs with dispersion tailoring. Section 2.6 is dedicated to theoretically demonstrating SPM-based 2R regeneration at 160 Gb/s by using dense dispersion-managed fibers.

2.1 Mamyshev 2R-Regeneration

2.1.1 2R regeneration

After propagating along a long distance in fibers, signals are degraded principally by nonlinear effect and noise from the amplification process. It needs to be regenerated for further transmission. There are three schemes of signal regeneration, such as reamplifying (1R), re-

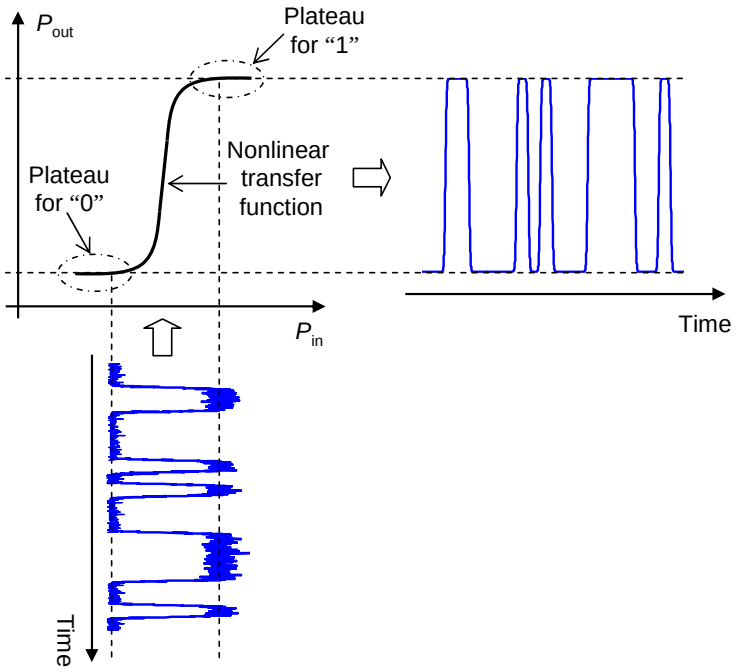

Figure 2.1: Principle of a 2R regeneration.

amplifying + reshaping (2R), and reamplifying + reshaping + retiming (3R). This chapter focuses on 2R regeneration. The principle of 2R regeneration is schematically depicted in Figure 2.1.

The aim of a 2R regenerator is to reduce intensity fluctuations of signals at “one” and “zero” levels. This requires output peak powers and input peak powers of signals to be in a relationship of letter “S” as seen in Figure 2.1. This function is known as a *nonlinear transfer function* or shortly *transfer function* (TF). On the other hand, one can use the TF of regenerators to assess the performance of regeneration. A good regenerator should have a TF with two plateaus which are for “one” level and “zero” level as described in Figure 2.1.

2.1.2 Principle of Mamyshev 2R regeneration

Exploiting the phenomenon of the spectral broadening of pulses due to self-phase modulation (SPM), Mamyshev introduced a simple and effective 2R regenerator in 1998 (known as a Mamyshev regenerator). The principle of this method is described in Figure 2.2. If optical pulses propagate along nonlinear mediums such as nonlinear fibers or nonlinear waveguides, the spectrum of the pulses is broadened due to the effect of SPM. For a Gaussian pulse train with a centre frequency at ν_0 and an initial spectral bandwidth (half-width at $1/e^2$ intensity point) of $\Delta\omega$, the spectral bandwidth of the pulses broadens, after a length L of a nonlinear medium, to become [83]:

$$\Delta\omega_{SPM} = \sqrt{2}\exp\left(\frac{1}{2}\right)\Delta\omega\gamma P_0 L, \tag{2-1}$$

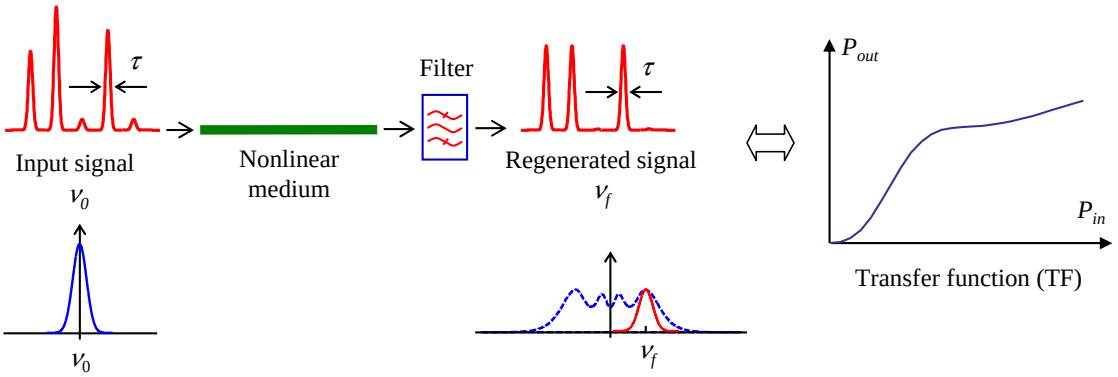

Figure 2.2: Schematic diagram of the SPM-based 2R Mamyshev regenerator and its corresponding transfer function.

where γ is the nonlinear coefficient, and P_0 the input peak power of the pulse (can be different for different pulses).

At the output of the nonlinear medium, an optical band-pass filter is used. The filter is not centered at the centre frequency of the input pulse but shifted by $\Delta\nu_{shift}$ to the frequency ν_f:

$$\nu_f = \nu_0 + \Delta\nu_{shift}. \tag{2-2}$$

It is obvious from Eq. (2-1) that, for a nonlinear medium with a given nonlinear coefficient γ and a length L, the magnitude of SPM-induced spectral broadening changes with the level of input peak power of the pulses. If the spectral broadening $\Delta\omega_{SPM}$ of the pulses is large enough, $\Delta\omega_{SPM} > \Delta\omega_{shift}$ ($\Delta\omega_{shift} = 2\pi\Delta\nu_{shift}$), then a part of the spectrum of the pulses passes through the filter. Otherwise, the pulses are rejected by the filter. The former case is that of high level pulses corresponding to bits of "ones" (marks), and the latter case corresponds to "zeros" (space). The TF shape exhibiting two plateaus allows noise reduction on both one and zero levels. By utilizing an output filter with the same shape and the same band-pass as the input pulses, one can regenerate the original signal. However, the frequency of the regenerated signal is shifted to the new frequency ν_f. To have wavelength-conversion-free regeneration, a bi-directional setup can be used as reported in reference [90] by Matsumoto.

2.1.3 Mamyshev's experiment

For the first experimental demonstration of SPM-based regenerations, Mamyshev used a fiber with a length of 8 km, an effective mode area A_{eff}=45 μm^2 and a negative dispersion $D = -2$ ps/km/nm at 1550 nm [83]. The 10 Gb/s on-off keying (OOK) return-to-zero (RZ) pulse stream signal with noise, whose partially closed eye diagram as seen in Figure 2.3(a), needs to be regenerated. This signal is injected into the fiber. At the output of the fiber, an optical band-pass filter with a bandwidth of $\nu_f/2 = 29$ GHz, and a filter frequency offset with respect to the input signal frequency of $\Delta\nu_{shift}/2 = 100$ GHz was used. The resultant

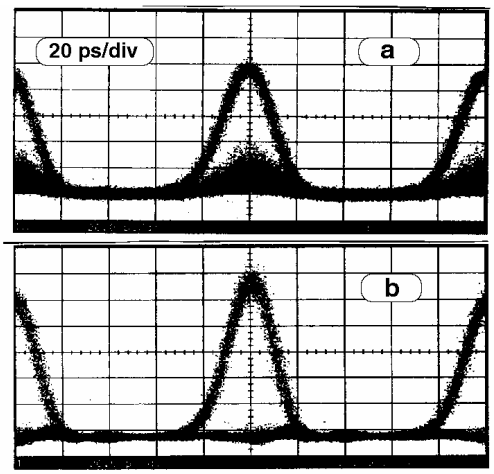

Figure 2.3: Eye diagrams of signal before (a) and after (b) of the Mamyshev regeneration (after Ref. [83]).

regeneration is demonstrated by the completely opened eye diagram of the signal at the output of the regenerator (Figure 2.3(b)).

2.1.4 Demonstrations of Mamyshev regenerations

Since the first introduction of SPM-based 2R-regeneration by Mamyshev in 1998, there have been many studies of this type of regeneration both experimentally and theoretically. These have concentrated on optimizing the parameters of Mamyshev regenerators, trying to use highly nonlinear fibers as well as combining with other techniques to improve the regenerators.

In 2002, with a combination of 2R Mamyshev regeneration and synchronous modulation after every 400 km in a recirculating loop, Raybon *et al.*, experimentally demonstrated transmission over 1 000 000 km for a 40 Gb/s 33% duty cycle signal [91]. With only 2R Mamyshev regeneration, the signal was regenerated at 5200 km but its eye diagram showed jitter. The eye diagram was clearer when the regenerator was combined with a synchronous modulation. The authors showed that there is no appreciable power penalty by a BER measurement for the regeneration.

In 2004, Her *et al.* proposed an optimization scheme to calculate the 2R Mamyshev regenerator parameters. Then, they experimentally demonstrated a regenerator with a silica fiber which had a length L of 2.5 km, dispersion $D = -0.7$ ps/km/nm, attenuation loss $\alpha = 0.6$ dB/km and a nonlinear coefficient $\gamma = 8.4$ $W^{-1}km^{-1}$. They obtained an improvement in the Q-factor of 1.5 dB when regenerating a 40 Gb/s signal with a temporal width T_{FWHM}=6.25 ps [92].

By utilizing highly nonlinear fiber based on bismuth-oxide, in 2006, Parmigiani *et al.* demonstrated regeneration for signals of 10 Gb/s and 40 Gb/s [93]. By using a high nonlinear coefficient γ of 1 100 $W^{-1}km^{-1}$, they obtained the advantage of decreasing the length of

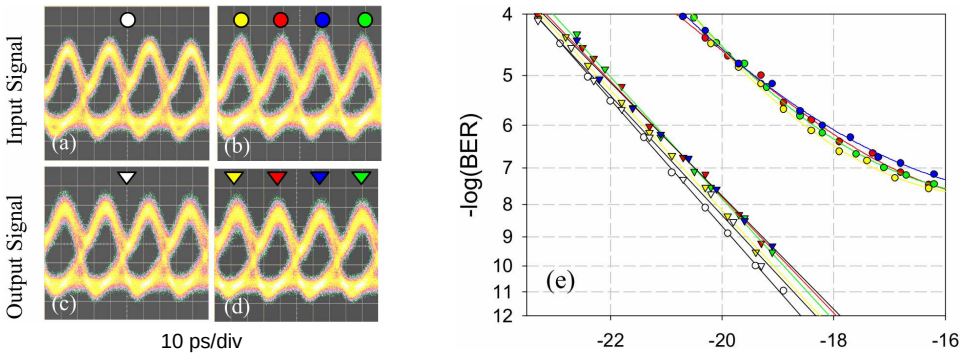

Figure 2.4: Eye diagrams of the input and output of the system at 40 Gb/s when no noise ((a) and (c)) or some amplitude noise ((b) and (d)) is induced. Corresponding BER measurements were also presented (e) (after Ref. [93]).

fiber down to 2 m. In the experiments, in order to boost the peak power, the temporal width of their input pulses was as short as 1.4 ps. However, the average power used in the experiments was still high at 31 dBm, the peak power being then 18.5 dB higher for the case of 10 Gb/s and 12.5 dB higher for the case of 40 Gb/s. The regenerated signal was obtained after the filter, whose centre wavelength is shifted by 3.9 nm with respect to the input signal. The authors showed an improvement in receiver sensitivity of 5 dB for 10 Gb/s signal and 2 dB for 40 Gb/s. Figure 2.4 shows eye diagrams of input and output signals of the regenerator and their corresponding BER measurements.

In 2006, Matsumoto reported all-optical 2R regeneration using SPM in a bidirectional fiber configuration [90]. Two fold regenerators showed wavelength-conversion-free regeneration. The signal was transmitted twice along the fiber in opposite directions and the second filter for the return signal has its center wavelength the same as the input signal. He showed that in these experiments, no penalty arose from the bidirectional transmission at 10 Gbit/s in the fiber, and the regenerator also improved the extinction ratio of the input signal. The schematic of the bidirectional configuration and its experimental extinction ratio measurement are shown in Figure 2.5.

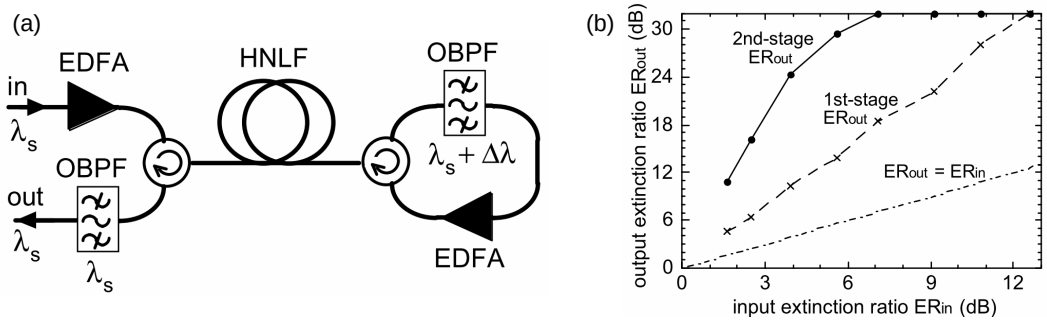

Figure 2.5: (a) Schematic of the wavelength-conversion-free 2R regenerator in bidirectional fiber configuration, and (b) extinction ratios of input and output signals after first-stage and second-stage regeneration (after Ref. [90]).

Following the trend of highly nonlinear fibers and waveguides made of chalcogenide glasses, many studies on chalcogenide components to carry out SPM-based 2R regeneration have been implemented. In 2005, L. B. Fu *et al.* investigated for the first time the feasibility of regeneration in a chalcogenide fiber. A fiber with a length of 2.8 m, a nonlinear coefficient γ of 1 200 $W^{-1}km^{-1}$ and a dispersion D of -504 ps/km/nm was used to test regeneration for a signal with 5.8 ps duration pulses [81]. It showed a possibility of a 40 Gb/s regeneration but with very high power needed (average power of 900 mW). In 2006, by using the same chalcogenide fiber, D. J. Moss *et al.* also reported on an experimental regeneration at 40 Gb/s. He reported nearly transform limited output pulses from a 2R all-optical regenerator in a single mode chalcogenide As_2Se_3 fiber. In the experiment, a longer fiber of 4.1 m was used.

In 2008, Provost *et al.* presented a theoretical study of simple scaling rules to optimize the design of 2R Mamyshev regenerators. They demonstrated an application of the rules to the design of a regenerator for a specific 160 Gb/s system [94]. In 2010, by utilizing 3 segments of fibers, they experimentally reported 40 Gb/s regeneration. They used two highly nonlinear fibers (HNLFs) with a nonlinear coefficient γ of 20 $W^{-1}km^{-1}$ and put a DCF fiber between them. They proved that the concept of dispersion and nonlinearity management can indeed be beneficial for regeneration [95].

In 2009, T.N Nguyen *et al.* from Foton laboratory numerically and experimentally demonstrated a double-stage 2R regenerator for 42.6 Gb/s RZ-33%. The first stage is a SPM-based pulse compressor and the second stage is a SPM-based Mamyshev regenerator. A 2R regenerator combining a pulse compressor showed a wavelength-transparent regeneration with a sensitivity-improvement of 5 dB and a 10 times maximum transmission distance improvement for a BER of 10^{-4} [96].

In 2011, C. Finot *et al.* reported an active Mamyshev regenerator with the implementation of an additional Raman gain. The authors evaluated the potential efficiency and advantages of the new active Mamyshev regenerator at 40 Gb/s. By combining Raman amplification, the working power of the regenerator was strongly reduced with a large improvement of the available output power [97]. Figure 2.6 shows the transfer functions for different pump powers and an examples of eye diagrams before and after the regenerator

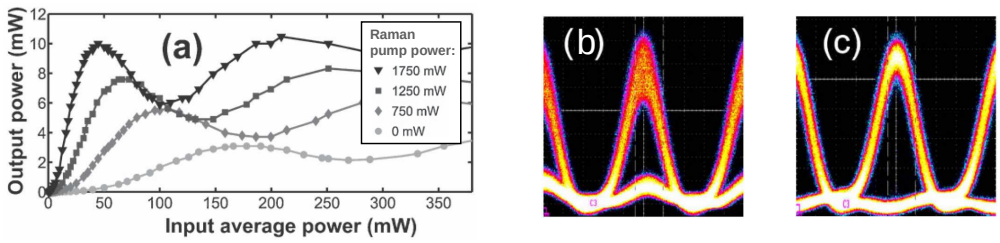

Figure 2.6: (a) Experimental measurements of the transfer function for various Raman pump levels; Eye diagrams of the 40 Gb/s RZ signal recorded before the regenerator (b) and after the regenerator for a pump power of 1750 mW (c) (after Ref. [97].)

for a pump power of 1750 mW.

Recently, by combining the use of a HNLF with a saturable absorber (SA), M. Gay *et al.* from Foton laboratory demonstrated a 170 Gb/s all-optical SPM-based 2R regenerator. The HNLF with an anomalous dispersion and a centering filter made a power limiter for high levels. The SA complemented this by rejecting the noise at low level, due to its reflection characteristic, leading to an enhanced extinction ratio. They showed the receiver sensitivity improvement using bit-error-rate assessment [98]. The experimental setup for the regenerator and its eye diagram observation are shown in Figure 2.7(a). The investigation of the receiver sensitivity with and without the regenerator is plotted in Figure 2.7(b).

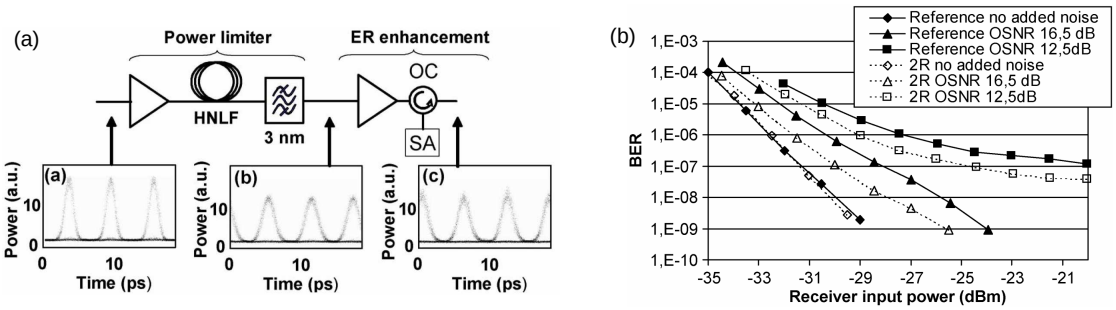

Figure 2.7: (a) Regeneration setup with a SA and its eye diagrams observation, and (b) Receiver sensitivity with and without the regenerator (after Ref. [98]).

2.2 Simple scale rules

Several simple rules have been proposed to design Mamyshev regenerators [94, 99]. This section describes the rules that are proposed in references [94, 99] to calculate parameters of the Mamyshev regeneration. The purpose of the rules is to obtain the S-shape transfer function (TF). As reported, to obtain a S-shape TF of a regenerator using an optical fiber with given parameters (fiber loss α, dispersion D, and nonlinear coefficient γ), a fiber length L and a frequency offset ΔF must be carefully chosen. To introduce the rules, it is useful to recall two length scales of the dispersion length L_D and the nonlinear length L_{NL} from Eqs. (1-47) and (1-48):

$$L_D = \frac{T_0^2}{|\beta_2|}, \qquad L_{NL} = \frac{1}{\gamma P_0}, \tag{2-3}$$

where T_0 is the pulse duration, β_2 the group-velocity dispersion, γ the nonlinear coefficient, and P_0 the peak power of pulse. From Ref. [94], the optimal length of fiber L for the regeneration is calculated as

$$L = L_D \sqrt{\frac{K_0}{N}}, \tag{2-4}$$

where, $K_0 = 0.382$ is the fitting constant that is proposed by the authors, and the parameter N is defined by

$$N^2 = \frac{L_D}{L_{NL}} = \frac{\gamma P_0 T_0^2}{|\beta_2|}. \tag{2-5}$$

The parameter N should be chosen between 5.5 and 23. The regenerator is critically dependent on not only the parameters of the fiber but also on the frequency offset of the output filter. There is a linear relationship between the optimal filter frequency detuning ΔF and the parameter N:

$$\Delta F \simeq (0.71N - 2.13)\, F_0, \tag{2-6}$$

where F_0 is half-bandwidth at $1/e$ intensity point of the input pulse spectrum.

Eq. (2-4) also shows that the design of the regeneration needs to consider both the fiber nonlinearity and fiber dispersion. By combining Eq. (2-3) and Eq. (2-4), it is seen that the square of the length L of fiber scales inversely as the square root of $\gamma\beta_2^3$

$$L^2 = \frac{K_0 T_0^3}{\sqrt{P_0}} \frac{1}{\sqrt{\gamma\beta_2^3}}. \tag{2-7}$$

This means that the length of fiber can be considerably reduced if we use a highly nonlinear and highly dispersive fiber. The fibers made of glasses such as chalcogenide glasses are of this type that may be able to implement regeneration.

Following the scale rules of L. Provost, T.N. Nguyen introduced two simple relations with a useful chart to calculate the appropriate set of parameters for a nonlinear fiber and a filter for regeneration at 40 Gb/s [99]. We then developed a chart for regeneration at 160 Gb/s. Figure 2.8 describes the relation between dispersion D, nonlinearity γ, length L of fibers, and also the power needed, for the case of a filter frequency detuning equal to 2.5 times the signal bandwidth and a pulse duration of 1.5 ps. Each point on the chart corresponds to a fiber of length L (right Y-axis), dispersion D (left Y-axis), and nonlinear coefficient γ (X-axis). The oblique lines are iso-power curves indicating the value of input power which is needed for regeneration.

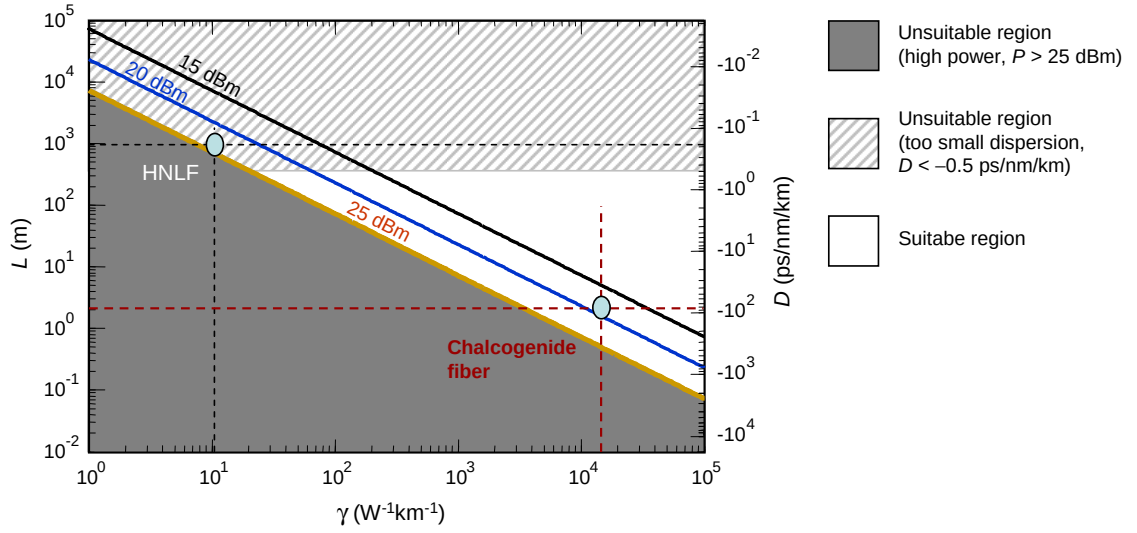

Figure 2.8: Proposed chart with two examples of fibers for designing a SPM-based 2R regenerator at 160 Gb/s.

The chart shows three regions in different colors and labels. The dark-gray region (under the oblique line of 25 dBm) is unsuitable region because a power higher than 25 dBm is required. The hatched-region (the uppermost region) is also an unsuitable because of a too small dispersion values ($|D| < 0.5$ ps/km/nm). Fibers falling in this region have a too small β_2, therefore the higher-order dispersion or dispersion slope must be considered and, as we will see in Section 2.4.2, it impairs the performance of the regenerator. The remaining region in white is the suitable region. Fibers falling in this region can be use to perform 160 Gb/s regenerators.

Two examples are marked in the chart. The first one is a commercial HNLF fiber from OFS with a nonlinear coefficient of 11.5 $W^{-1}km^{-1}$. If we use a fiber length of 1000 m, the dispersion of the fiber must be about -0.2 ps/km/nm. This small value is not easy to achieve precisely. If we increase the fiber length, a smaller dispersion is needed. We can decrease the fiber length to increase the value of dispersion, but this case falls into the unsuitable region of a too high required power. A higher nonlinear fiber is needed for reducing the power and also for increasing the dispersion to a possible range. For example if we use a chalcogenide fiber with a nonlinear coefficient γ of 15000 $W^{-1}km^{-1}$ (reported in [21]) with a length of 2 m, the dispersion of the fiber must be about -100 ps/km/nm to ensure a power of about 20 dBm. However, the dispersion of chalcogenide fibers is normally at larger values of hundreds of ps/km/nm [21, 81].

The chart shown in Figure 2.8 together with the scaling rules proposed by L. Provost will be used in the following sections to investigate 160 Gb/s regeneration.

2.3 Noise addition and simulation model

To investigate the performance of the regenerator, a simulation model is used. In this model, white Gaussian noise is added to the signal to simulate signal degradation similar to Ref. [100]. Figure 2.9 illustrates the schematic block diagram model for regeneration simulation. The calculation technique is based on the spectral representation of white noise. The white noise is an accumulation of amplified spontaneous emission (ASE) noise emitted by erbium-doped fiber amplifiers (EDFA).

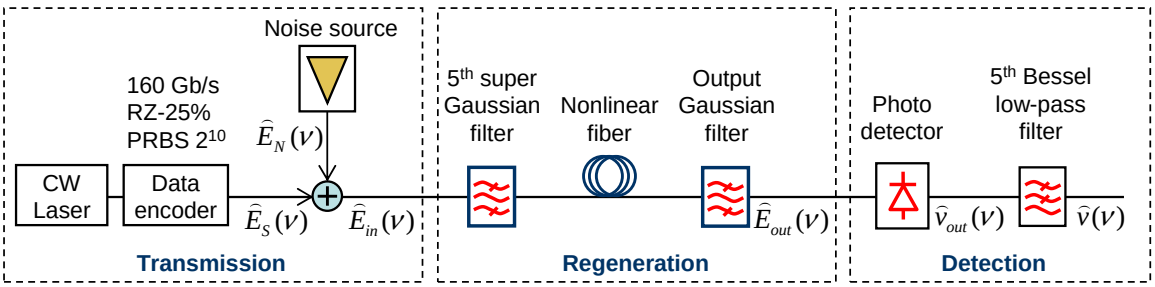

Figure 2.9: Schematic block diagram used for 2R regeneration simulation of a 160 Gb/s RZ-25% signal with a PRBS of 2^{10} bits.

The principle of the simulation model for 2R regeneration is outlined as follows. Let $E_S(t)$ be the function representing the magnitude of the electrical field of the optical signal in the time domain. The spectral representation $\widehat{E}_S(\nu)$ is numerically calculated from $E_S(t)$ by using the discrete Fourier transform (DFT):

$$\widehat{E}_S(\nu) = \frac{1}{\sqrt{N}} \sum_{k=-\frac{N}{2}}^{\frac{N}{2}-1} E_S\left(\frac{kT}{N}\right) \exp\left(-2i\pi \frac{kT}{N}\nu\right) \tag{2-8}$$

where N is the number of points dividing the temporal window T.

The spectral representation $\widehat{E}_N(\nu)$ of ASE noise is assumed to be similar to white Gaussian noise [7] and can be written, in the frequency domain, as

$$\widehat{E}_N(\nu) = A \exp\left(i\phi\left(\nu\right)\right) \tag{2-9}$$

where A is the magnitude of white noise. A is taken constant over a frequency range. The optical signal-to-noise ratio (OSNR) of signal with noise is set before injecting a signal with noise into the regenerator. The OSNR is applied to the whole frequency band and then multiplied with the mean value of intensity to form the magnitude A of noise. The OSNR will be varied to verify the performance of the regenerator qualitatively. The quantity $\phi(\nu)$ is a random phase uniformly distributed between $-\pi$ and π. This simple formulation allows us to take into account the incoherent nature of the spontaneous emission noise from optical amplifiers.

In the frequency domain, the signal arriving at the input optical band-pass filter can be written as

$$\widehat{E}_{in}(\nu) = \widehat{E}_S(\nu) + \widehat{E}_N(\nu) \tag{2-10}$$

The signal $\widehat{E}_{in}(\nu)$ is filtered by a flat-top fifth-order super-Gaussian filter before being launched into the fiber. The signal is then passed through the fiber and the output signal is obtained by solving the nonlinear Schrödinger equation (NLSE) by the split-step method [47]. It is then filtered by an output Gaussian filter which has the same bandwidth as the input signal but a frequency shift of ΔF.

Figure 2.10 illustrates an example of 160 Gb/s signal with and without ASE noise. The extinction ratio ER is set to 20 dB and for signal with noise the OSNR is set to be 30 dB/0.1 nm. The eye diagram and an example of pulse train with a pseudo random binary sequence (PRBS) of 2^{10} bits of the signal without ASE noise are shown in Figure 2.10(a) and Figure 2.10(b). Its spectrum is also shown in Figure 2.10(c). The eye diagram of the 160 Gb/s with white noise is presented in Figure 2.10(d) and an example of pulse train in Figure 2.10(e). The corresponding spectrum of noise-added signal is shown in Figure 2.10(f).

The signal $\widehat{E}_{out}(\nu)$ after the output filter is fed to the photodetector. The photodetector converts the optical intensity of the signal into a voltage $\hat{v}_{out}(\nu)$. Here, we ignore noise that is introduced by the detector. The finite bandwidth of the electronics is taken into account through a fifth-order Bessel low-pass filter. The Bessel filter has a frequency representative

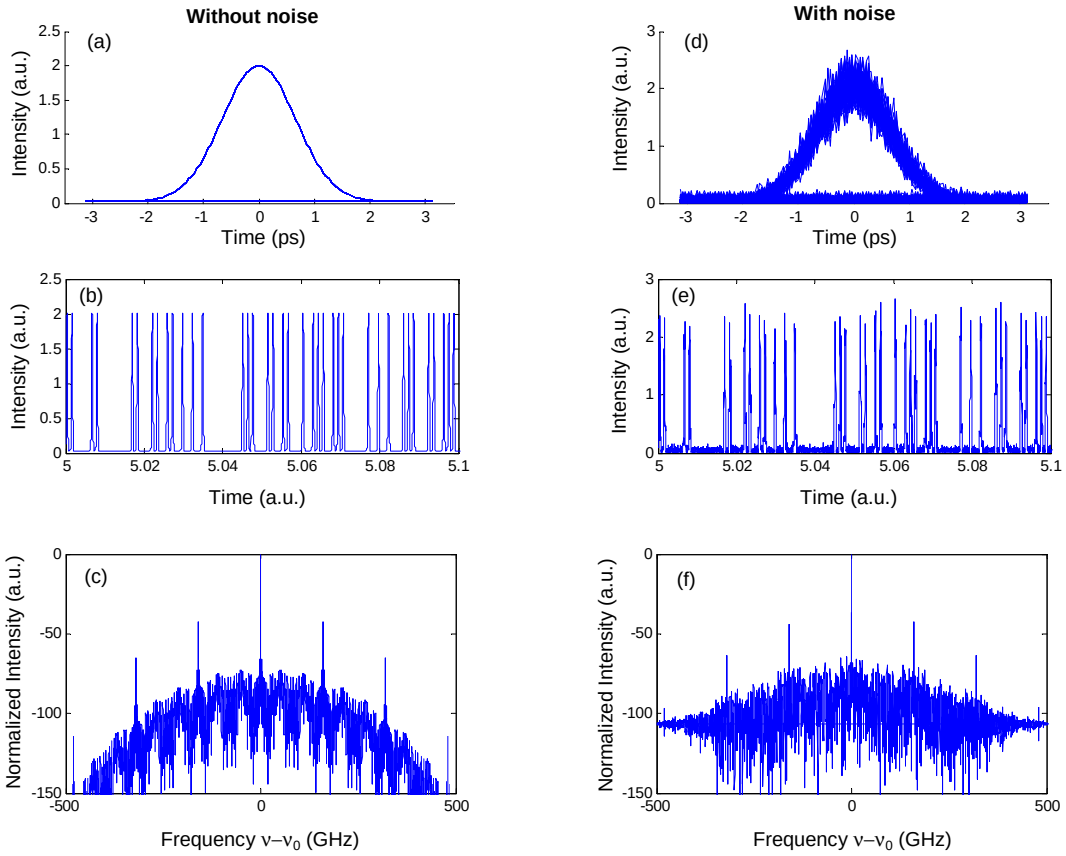

Figure 2.10: Example of a 160 Gb/s signal without noise and signal with noise for a case of OSNR = 30 dB/0.1 nm, ER = 20 dB. Without noise: (a) eye diagram,(b) example of PRBS of 2^7 pulse train, and (c) its corresponding spectrum. With added white-noise: (d) (a) eye diagram,(b) example of PRBS of 2^7 pulse train, and (c) its corresponding spectrum.

of $H(\nu)$ and its cut-off frequency is set depending on the bit-rate of signal needing to be regenerated. In the case of a 160 Gb/s signal, its cut-off frequency is 128 GHz. The voltage of the received signal can then be written in the frequency domain as

$$\hat{v}(\nu) = H(\nu)\hat{v}_{out}(\nu). \tag{2-11}$$

To observe the eye diagram of the regenerated signal, the voltage in the time-domain $v(t)$ is obtained by the inverse discrete Fourier transform (IDFT) of its representation in frequency $\hat{v}(\nu)$. The Q-factor is calculated for the input signal with noise, Q_1, and for the regenerated signal, Q_2. To assess the performance of the regenerator, the Q-factor improvement is defined as the ratio between the input Q-factor Q_1 and the regenerated Q-factor Q_2

$$Q_{IM} = Q_2 - Q_1, \ \text{(dB)}. \tag{2-12}$$

In the following sections, Q_{IM}, eye diagrams as well as the transfer functions (TF) are used to assess the performance of the regenerators.

2.4 Dispersion in high-bit rate regeneration

As mentioned in Section 2.1.2, the Mamyshev all-optical regenerator relies on the combined effects of SPM and normal dispersion in a fiber to induce a S-shape transfer function when an offset filter is placed after the fiber. To obtain an appropriate transfer function, the fiber length L, the value of the dispersion D and the nonlinear coefficient γ must be carefully chosen. At 40 Gb/s, for example, for standard or nonlinear fibers (γ in the range of 1 $W^{-1}km^{-1}$ and 20 $W^{-1}km^{-1}$ typically), the dispersion D must be around -1 ps/km/nm as calculated in Ref. [99]. At 160 Gbit/s, since the pulse duration is reduced to one-fourth it can be demonstrated that the value of dispersion has to be divided by a factor 16 with respect to the 40 Gb/s case, leading to a value of dispersion very close to zero. In this case, the signal experiences the effect of third-order dispersion β_3 that degrades the shape of the transfer function. This section considers the influence of third-order dispersion β_3 on 160 Gb/s regeneration in a single fiber.

The simulation model with noise addition described in the previous section is used for the investigation. The signal at 160 Gb/s is a pseudo random binary sequence (PRBS) of Gaussian transform-limited pulses of 2^{10} bits. The pulse duration (FWHM) is 1.5 ps, and centered at the wavelength of 1550 nm. The optical signal-to-noise ratio (OSNR) and extinction ratio (ER) are set at the input of the regeneration at 25 dB/0.1 nm and 20 dB, respectively.

2.4.1 Regeneration in a single fiber without higher-order dispersion

To investigate the Mamyshev 2R regeneration of a 160 Gb/s signal, three types of fibers are used in the numerical simulations. These fibers are: a dispersion-shifted fiber (DSF), a highly nonlinear fiber (HNLF), and an ultra-highly nonlinear fiber (a chalcogenide fiber). In regeneration simulations, propagation of signal along an optical fiber is obtain by numerically solving the nonlinear Schrödinger equation (NLSE), which is presented in Eq. (1-46). The split-step Fourier method described in Ref [47] is used to solve the NLSE.

DSF fiber

First the DSF is taken to be the fiber in the Mamyshev regenerator. The DSF has a nonlinear coefficient γ of 2.6 $W^{-1}km^{-1}$ and attenuation coefficient α of 0.25 dB/km. As discussed in Section 2.2, in order to use power as low as possible the fiber must be as long as possible because the length L of fiber is inversely proportional to the input peak power P_0 as in Eq. (2-7). The fiber length used is thus taken into account as long as the maximum effective length L_{eff_max}. In the case of a DSF fiber, the maximum effective length L_{eff_max} is 16085 m. By utilizing the scaling rules and the chart (mentioned in Section 2.2), the dispersion D of the DSF fiber must be as small as -0.009 ps/km/nm to obtain the S-shape of the transfer function TF. With a group-velocity dispersion $D = -0.009$ ps/km/nm but without third-order dispersion β_3, regeneration of a 160 Gb/s signal can be carried out. In

the simulation, the third-order dispersion β_3 is set to be zero. The frequency offset ΔF is set to 706 GHz, which is equivalent to 2.5 times of the full-width at half maximum of the input pulse spectrum.

The pulse train of a 160 Gb/s signal, with noise, is injected into the DSF fiber. The OSNR and extinction ratio ER of signal with noise are varied to investigate the regenerator's performance. In the simulation, the OSNR is set to be 25 dB/0.1 nm and the extinction ratio ER is 20 dB. Figure 2.11(a) illustrates the pulse train at the input of the DSF fiber. It has a pulse width of 1.5 ps in the bit-time slot of 6.25 ps. After propagating along the DSF fiber, the pulse train of the signal is shown in Figure 2.11(b). Note that its pulse width is broadened and adjacent pulses are slightly overlapped. The regeneration of a 160 Gb/s signal without third-order dispersion β_3 is shown in Figure 2.11(c). The pulse train is completely regenerated.

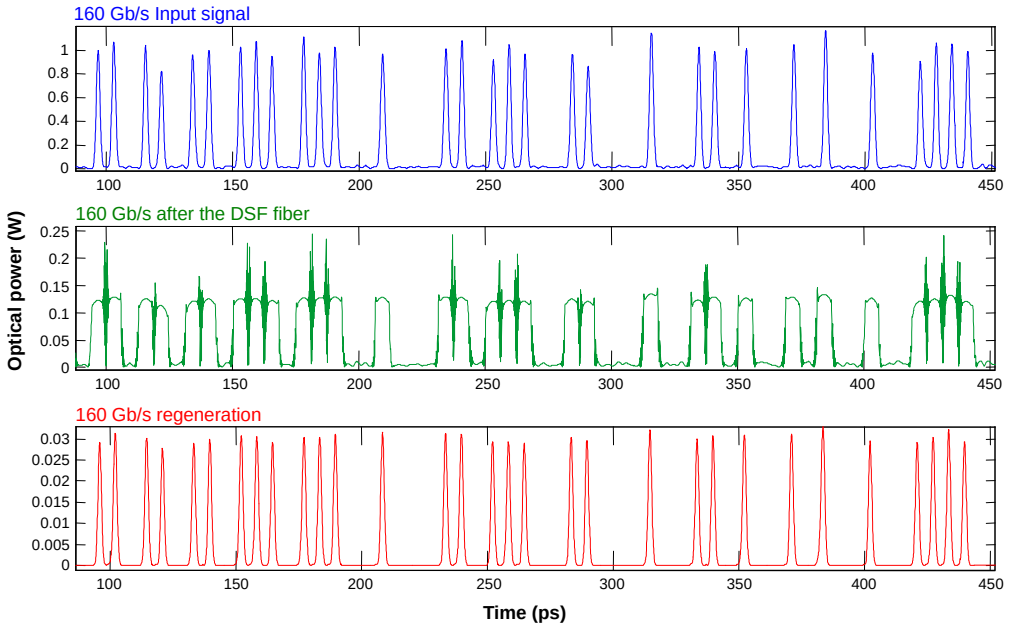

Figure 2.11: Examples of the 160 Gb/s pulse train signal (a) at the input (b) at the output of the DSF fiber, and (c) after the regeneration.

The transfer function (TF) of the regenerator is drawn in Figure 2.12. As defined in Section 2.1.1, the TF represents the dependence of the output peak power related to the input peak power. The vertical axis of the TF is on the right side of Figure 2.12. The TF shows a plateau around a value of the input peak power of 0.7 W. Together with the TF, the Q-factor improvement, Q_{IM} (defined in Section 2.3), is also calculated. Its vertical axis is on the left side of Figure 2.12. The Q_{IM} points out that the working position should be moved slightly higher than the input peak power calculated by the TF.

The choice of the working point of Mamyshev regenerators can be understood by referring to Ref. [101]. The effective optimal working point does not exactly correspond to the range

of powers at which the TF exhibits a plateau area. The working point should be moved to slightly higher power than the plateau power exhibited in the TF in order to minimise the timing jitter intrinsically induced by the regenerator and the amplitude jitter induced by the pulse-to-pulse overlapping [101].

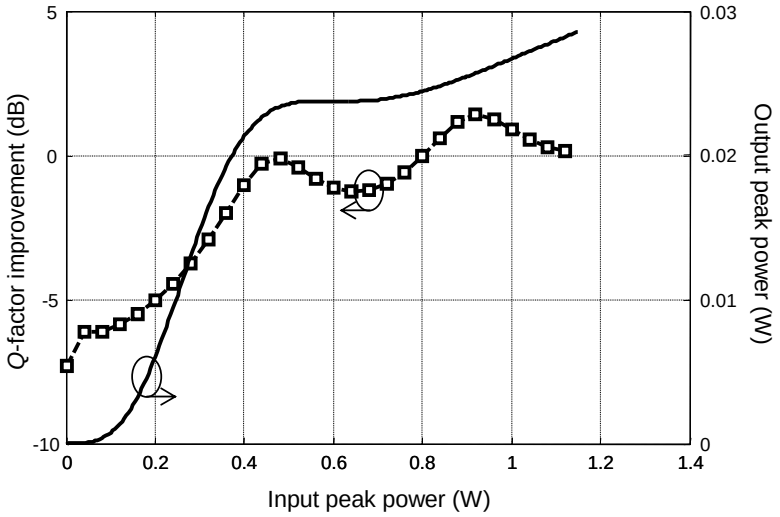

Figure 2.12: Q-factor improvement with respect to input peak power (the line with points and the left axis) and transfer function of the regeneration (the smooth line and the right axis) using a DSF.

At the working power of 0.95 W, a maximum Q_{IM} of 1.5 dB is obtained as seen in Figure 2.12. The peak power of 0.95 W corresponds to an average power of 114 mW (20.6 dBm).

Corresponding to the input peak power of 0.95 W, the eye diagram of the input signal and regenerated signal are illustrated in Figure 2.13(a) and Figure 2.13(b), respectively. By offset frequency filtering, noise at low levels is rejected. Noise at the "one" level is also slightly reduced. After the regeneration, the output eye diagram exhibits a higher extinction ratio (ER) compared to the input signal. The corresponding spectra of the 160 Gb/s signal at the input and after the regenerator are also presented in Figure 2.13(c) and Figure 2.13(d), respectively. The input spectrum shows noise. The regenerated spectrum presents a Gaussian shape which looks like the signal without noise as seen in Figure 2.10(c). Returning to the Figure 2.11 which is the case of an input peak power set at 0.95 W, we can see the regenerated pulse train in Figure 2.11(c). The signal is evidently regenerated based on SPM and filtering frequency offset at the output of the DSF fiber.

The numerical study on the DSF fiber without the appearance of third-order dispersion β_3 shows that 160 Gb/s regeneration can be done in a DSF fiber, if we can shift the dispersion to a value close to zero, such as -0.009 ps/km/nm.

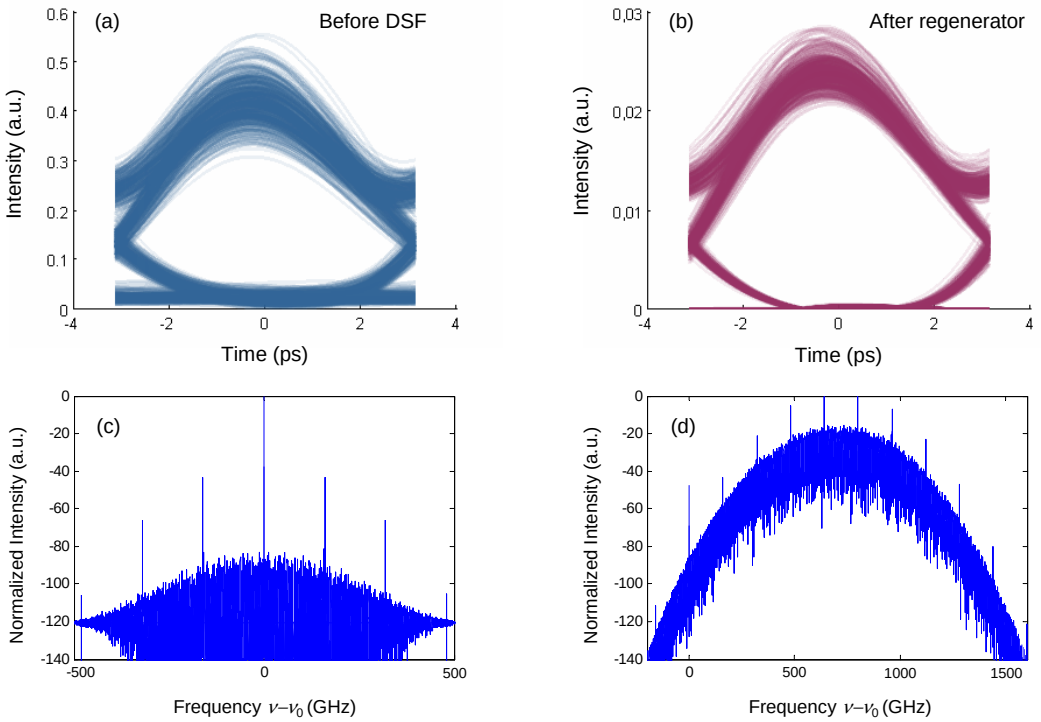

Figure 2.13: Eye diagrams of the 160 Gb/s signal at the input of the DSF fiber (a), and after regeneration (b). Spectra of the 160 Gb/s signal at the input of the DSF fiber (c), and after regeneration (d).

HNLF fiber

The theoretical investigation of 160 Gb/s regeneration is now carried out with a highly nonlinear fiber (HNLF). The HNLF, made of silica, has a nonlinearity γ=11 $W^{-1}km^{-1}$ and attenuation losses α=0.6 dB/km. To reduce the input power, the length of fiber used in the simulation is equal to the maximum effective length L_{eff_max} and thus equal to 7218 m. The third-order dispersion β_3 is also set to zero. To have a S-shape of the transfer function (TF), the dispersion D of fiber is calculated to be -0.02 ps/km/nm. The OSNR here is also set to be 25 dB/0.1 nm and the extinction ratio (ER) is 20 dB as the previous investigation of a regeneration with the DSF.

Without third-order dispersion β_3, the transfer function exhibits a S-shape with two plateaus, for the "zero" and "one" levels as seen in Figure 2.14 (smooth curve). Its vertical axis is on the right side. The plateau at low input peak power ensures the elimination of noise at "zero" level. From the plateau for "one" level, the working point may be around 0.35 W of input peak power.

Together with the transfer function TF, the Q-factor improvement is also presented in the same Figure 2.14 (curve with points). The maximum Q_{IM} is about 1.5 dB with an input peak power of 0.5 W. The working point of the regenerator must then be about 0.5 W of input peak power. As discussed previously, this is similar to the case of the DSF fiber,

the maximum Q_{IM} is achieved at the point where the input peak power is slightly higher than the point of "one" level plateau of the TF. We note here that the use of a HNLF allows to decrease a required input power.

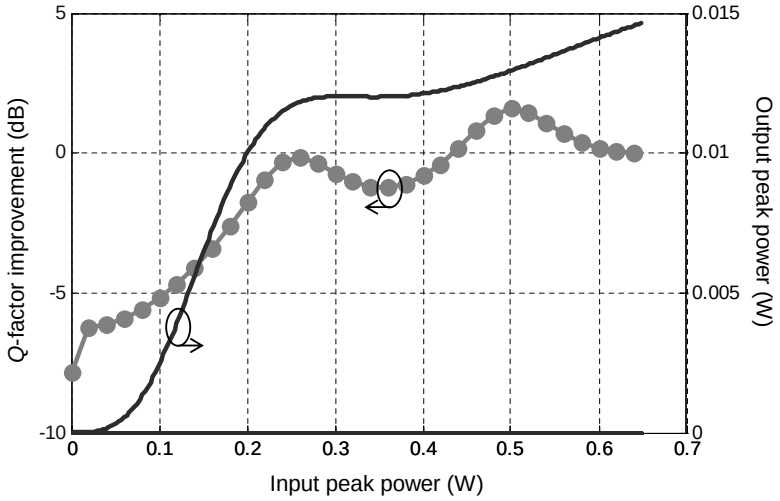

Figure 2.14: Q-factor improvement with respect to input peak power (the line with point and the left axis) and transfer function of the regeneration (the smooth line and the right axis) using a HNLF.

Figure 2.15 presents the pulse train of the 160 Gb/s signal with a pulse duration of 1.5 ps (FWHM) for the case of an input peak power $P_0 = 0.5$ W. The pulse train of the 160 Gb/s signal at the output of the HNLF fiber and after the regenerator are also presented in Figure 2.15(b) and Figure 2.15(c). The pulse train after the HNLF is shown in Figure 2.11(b). The signal is then filtered by a filter, whose center frequency is shifted from the signal of 706 GHz as previously, placed at the output of the HNLF. The pulse train of the regenerated signal is illustrated in Figure 2.15(c).

The eye diagrams of the 160 Gb/s input signal and the regenerated signal are illustrated in Figure 2.16. With 1.5 dB of Q-factor improvement, the regenerated eye diagram shows lower noise at "zero" and "one" levels. Like the previous case with the DSF, fluctuation at "one" level still appears. This can be understood by noting that the working point is slightly shifted to the higher input peak power where the transfer function TF is not in the flat region as discussed above with the DSF.

Similar to the case with the DSF fiber, 2R regeneration with a HNLF which has a low dispersion $D = -0.02$ ps/km/nm but without β_3, is demonstrated by both the transfer function TF and the Q-factor improvement. The S-shape TF of the regenerator exhibits two plateaus and the eye diagram quality has an improvement of Q_{IM}=1.5 dB.

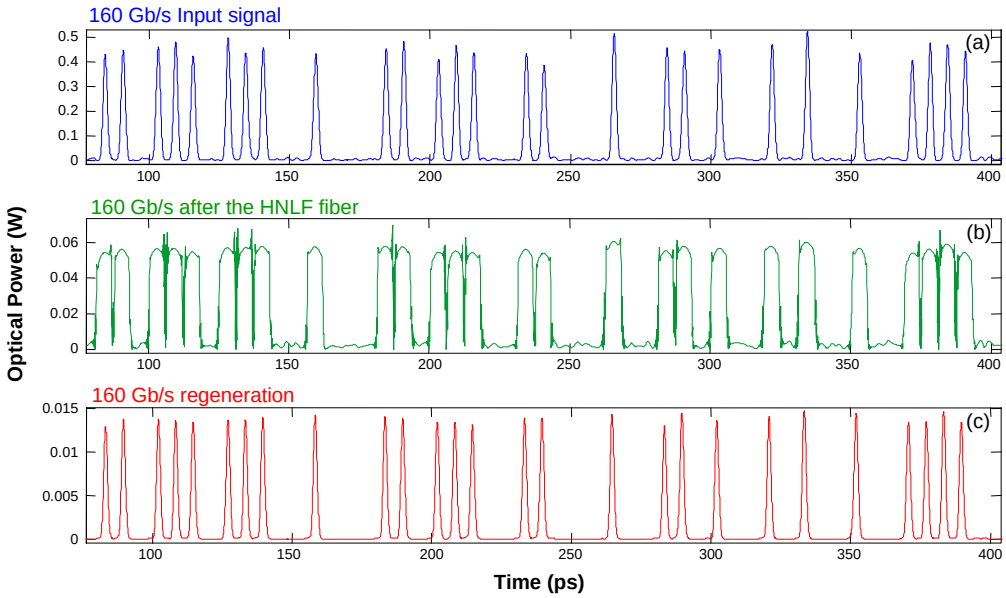

Figure 2.15: Examples of the 160 Gb/s pulse train signal (a) at the input (b) at the output of the HNLF fiber, and (c) after the regeneration.

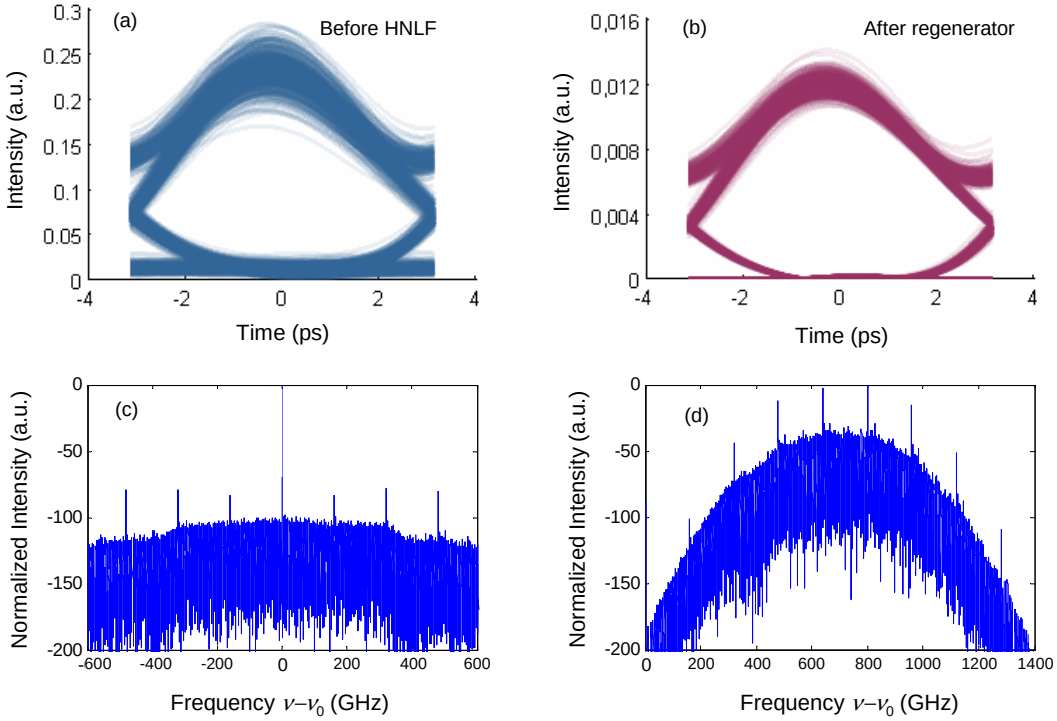

Figure 2.16: Eye diagrams of the 160 Gb/s signal at the input of the HNLF fiber (a), and after regeneration (b).

Chalcogenide fiber

Nowadays with the development of highly nonlinear fibers made of chalcogenide glasses, 2R regeneration with this type of fiber should be considered. This part investigates 2R regeneration with a chalcogenide glass fiber which has a nonlinear coefficient γ of 15 000 $W^{-1}km^{-1}$ (reported in [21]).

The fiber has an attenuation loss α of 0.8 dB/m, leading to an maximum effective length L_{eff_max}=5.4 m. In the simulation, the fiber length L is set to be equal to L_{eff_max} for input power reduction. Numerical calculations based on the required S-shape of the transfer function leads to the value of dispersion D needing to be -27.5 ps/km/nm. The third-order dispersion β_3 is set to zero in the numerical simulation.

Figure 2.17 presents the transfer function TF of the regenerator and the Q-factor improvement. The plateau of the TF occurs for an input peak power P_0 of 0.33 W. However, the maximum of Q_{IM} is obtained for a peak power P_0 of 0.5 W. The numerical simulations point out that the Q-factor is improved by 1.2 dB at $P_0 = 0.5$ W.

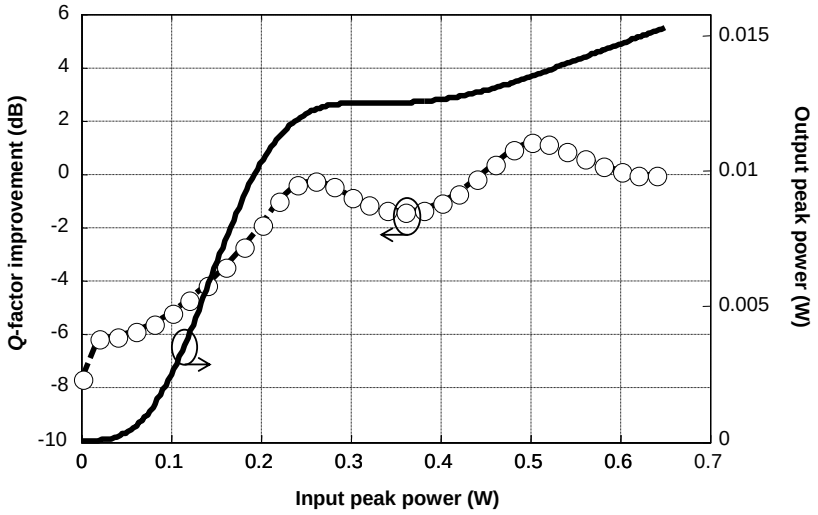

Figure 2.17: Q-factor improvement with respect to input peak power (the line with point and the left axis) and transfer function of the regeneration (the smooth line and the right axis) using a chalcogenide fiber.

The pulse train corresponding to the input peak power P_0 of 0.5 W is shown in Figure 2.18. The 160 Gb/s signal, with noise, is set at the input of the chalcogenide fiber to have 25 dB/0.1 nm of OSNR and 20 dB of extinction ratio ER. A sample of pulse train is seen in Figure 2.18(a). The pulse train after 5.4 m of chalcogenide fiber is shown in Figure 2.18(b) and the regenerated one is in Figure 2.18(c).

The eye diagrams of the 160 Gb/s input signal and the regenerated one are also presented in Figure 2.19. In the same way as in the case of DSF fiber and HNLF fiber, the regenerated eye diagram has a better extinction ratio compared to the eye diagram of the input signal. Noise on "zeros" as well as on "ones" is reduced giving a more opened eye.

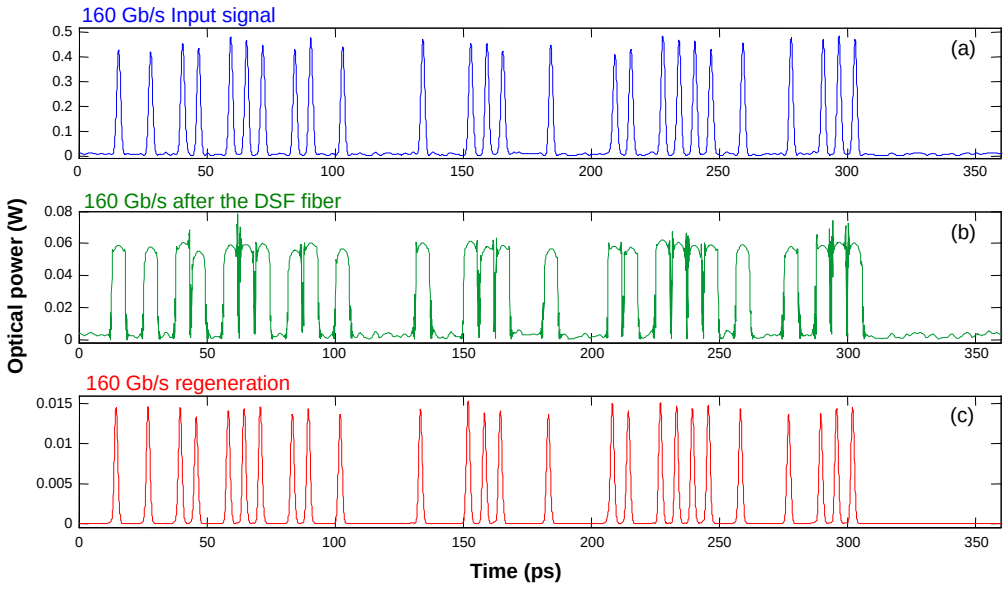

Figure 2.18: Examples of the 160 Gb/s pulse train signal (a) at the input (b) at the output of the chalcogenide fiber, and (c) after the regeneration.

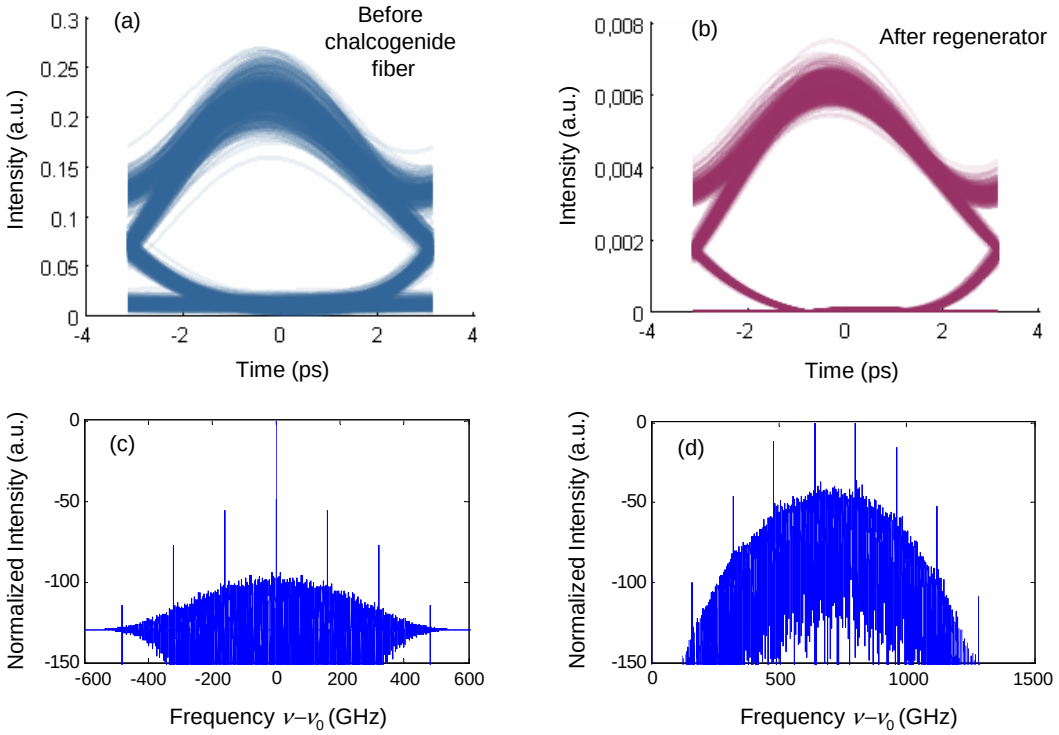

Figure 2.19: Eye diagrams of the 160 Gb/s signal at the input of the chalcogenide fiber (a), and after regeneration (b). Corresponding spectra of the 160 Gb/s signal at the input of the chalcogenide fiber (c), and after regeneration (d).

In conclusion for this section, numerical simulations were used to investigate the SPM-based 2R regeneration with three types of fibers. They demonstrate regeneration at 160 Gb/s in case of zero β_3. If β_3 is ignored, to fulfil the 2R regenerator the dispersion of the fibers must have small values: -0.009 ps/km/nm for the DSF fiber, -0.02 ps/km/nm for the HNLF fiber, and -27.5 ps/km/nm for the chalcogenide fiber. These small dispersion values may lead to the fact that the third-order dispersion may dominate over the dispersive effects. Indeed, the spectrum of a signal includes not just a single wavelength but a range of several nanometers. Dispersion at each wavelength is different due to dispersion slope. The third-order dispersion β_3 or dispersion slope S becomes important and must be considered. In the next section, 2R regeneration at 160 Gb/s is investigated in the case of the third-order dispersion β_3.

2.4.2 Regeneration in a single fiber with higher-order dispersion

This section investigates SPM-based 2R regeneration when the third-order dispersion β_3 is taken into account. The same three fibers (DSF, HNLF, and chalcogenide fiber) are again used in the numerical simulations with the third-order dispersion β_3. Depending on the value of the dispersion slope S of each fiber, the value of the third-order dispersion is different. The third-order dispersion is calculated by using Eq. (1-41) and can be expressed by

$$\beta_3 = \left(S - \frac{4\pi c}{\lambda^3}\beta_2\right)\left(\frac{\lambda^2}{2\pi c}\right)^2, \tag{2-13}$$

where c is the light velocity, and λ is the wavelength. For the case of the DSF, the dispersion slope is $S = 0.07$ ps/km/nm^2 at 1550 nm [7], the third-order dispersion β_3 is thus 0.1 ps^3/km. A HNLF has a dispersion slope of $S = 0.025$ ps/km/nm^2 [11] giving a value of the third-order dispersion $\beta_3 = 0.05$ ps^3/km. For a chalcogenide fiber, the third-order dispersion of $\beta_3 = 4.8$ ps^3/km with a dispersion slope of $S = 3$ ps/km/nm^2 at 1550 nm is taken from Ref. [81].

The simulations show that neither the transfer functions (TFs) of the regenerator nor the Q-factor improvement Q_{IM} of eye diagrams for all of the three fibers are suitable to carry out the regeneration of a 160 Gb/s signal. Figure 2.20 illustrates the TF and Q_{IM} for (a) the DSF fiber, (b) the HNLF fiber, and (c) the chalcogenide fiber. The TF curves of the three fibers do not have the S-shape with plateaus, which is required for regeneration. For the Q_{IM}, they are all negative indicating that the signal is degraded and not regenerated.

This is clearly not the same as the case of the regeneration in the absence of β_3. The signal after propagating along the fibers with β_3 is degraded. For the example of the regenerator with the DSF fiber, no value of the input peak power gives a positive Q_{IM}. Figure 2.21 shows the pulse train of the 160 Gb/s signal (a) at the input of the DSF fiber, (b) after the DSF fiber, and (c) after the output filter of the regenerator. We can see that the signal is strongly degraded after the DSF fiber due to the third-order dispersion β_3 despite

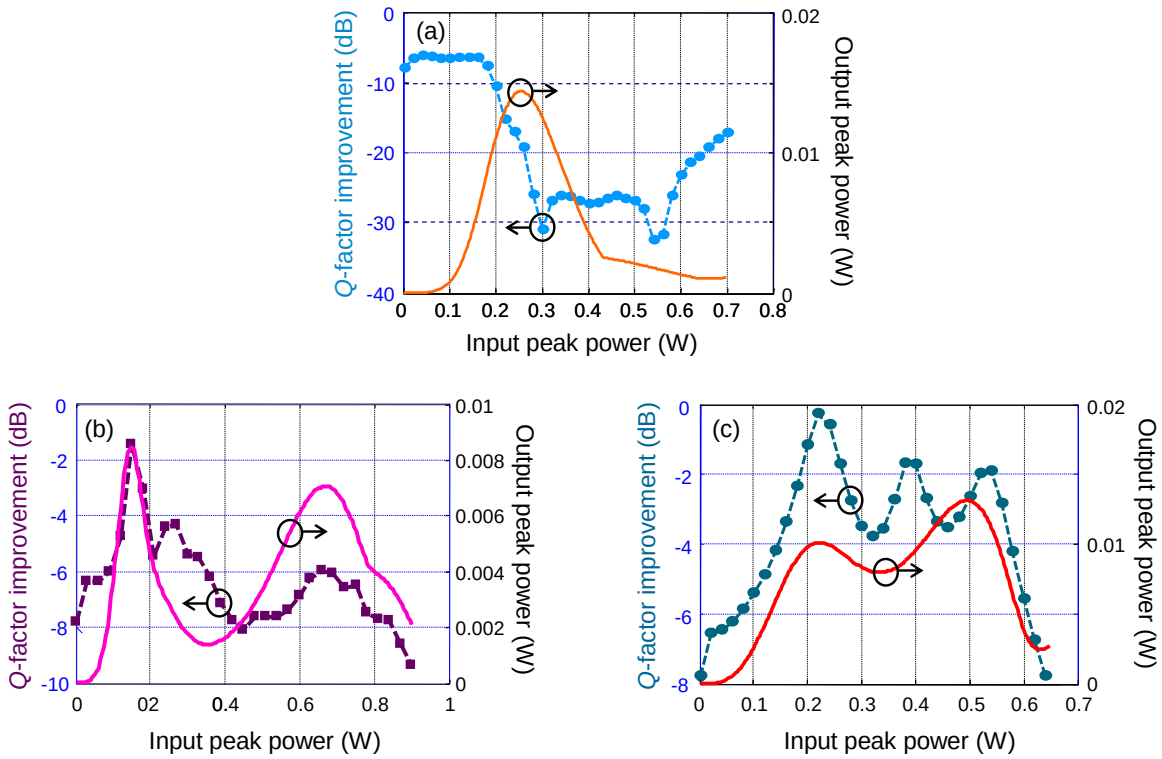

Figure 2.20: Q_{IM} with respect to input peak power (the line with points and the left axis) and transfer function of the regeneration (the line and the right axis) for three types of fibers with β_3: (a) the DSF, (b) the HNLF, and (c) the chalcogenide fiber.

the group-velocity dispersion β_2 being close to zero (Figure 2.21(b)). The signal after the offset filter, shown in Figure 2.21(c), is strongly degraded.

Figure 2.22 shows an example of eye diagrams of the 160 Gb/s signal at the input of the DSF and at the output of the output filter. The output eye diagram (Figure 2.22(d)) is completely degraded. This corresponds to the pulse train of Figure 2.21(c).

The same problem occurs in SPM-based 2R regenerators using the HNLF fiber and the chalcogenide fiber due to influence of the third-order dispersion β_3. In other words, we have found that it is so far impossible to implement a 160 Gb/s signal SPM-based regeneration in a single fiber.

To avoid the influence of β_3, one can use fibers with higher dispersion or fibers with a small dispersion but with a dispersion slope $S = 0$. For the former, this, however, leads to a need for a high nonlinear coefficient as seen in the chart of Figure 2.8. If dispersion of chalcogenide fibers, normally at large value (hundreds of ps/km/nm), can be reduced (to a value of, for example, -100 ps/km/nm), chalcogenide glasses fibers can be good a choice for studying 2R regeneration at high bit-rate. For the latter, the dispersion of the fiber must be small and at a precise value, and the third-order dispersion $\beta_3 = 0$. This means the dispersion slope S must be zero to ensure the same dispersion for a range of wavelengths.

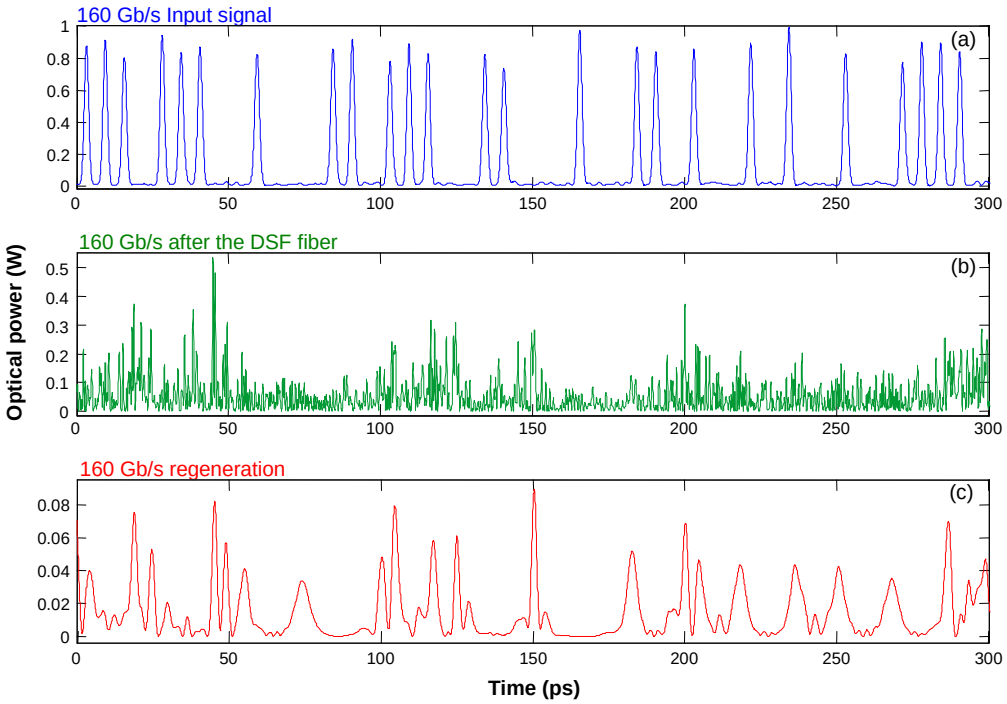

Figure 2.21: Examples of the 160 Gb/s pulse train signal in the case of β_3 existing (a) at the input (b) at the output of the DSF fiber, and (c) after the output filter.

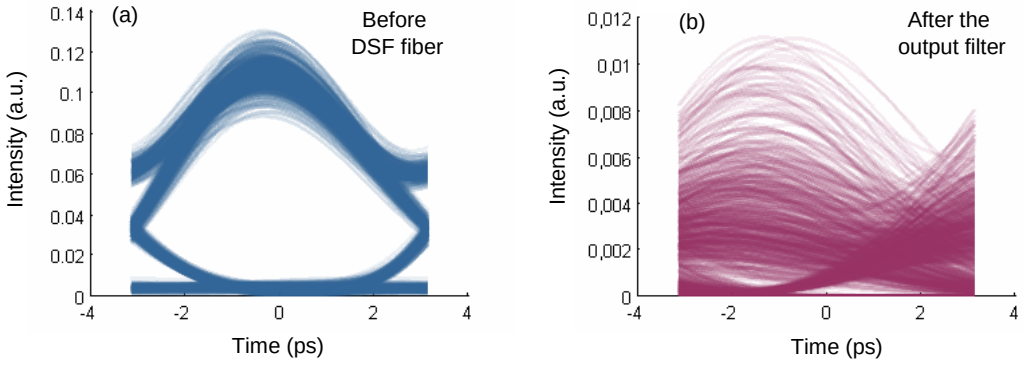

Figure 2.22: Examples of eye diagrams of the 160 Gb/s signal in the case of β_3 existing (a) the input (b) after the output filter for the input peak power $P_0 = 0.25$ W.

However, such a fiber with a value of β_2 close to zero and constant over a wide range of wavelengths is difficult to realize.

To overcome the influence of β_3, one could think about a fiber which has an average dispersion close to zero but with a β_2 that locally dominates the β_3. In the following sections, we propose the use of a dense dispersion-managed (DDM) fiber [102] to perform 160 Gb/s regeneration. Firstly, the next section provides the overview of DDM fibers and our designs of DDM fibers in order to use them in a 160 Gb/s regeneration.

2.5 Dense dispersion-managed fiber

Dispersion-managed optical transmission links were introduced to increase the capacity of optical transmission systems [103, 104, 105]. The idea of dispersion-managed transmission links is the use of several segments of fiber with different lengths and opposite signs of dispersion to compensate each other. It leads to an average dispersion D_{avg} close to zero. Basically, the dispersion management technique utilizes a fiber with a periodic dispersion map. Each periodic map is built up by two types of fiber which are generally different in length and opposite in dispersion sign. As mentioned in Section 1.3.3, the map length of conventional dispersion-managed transmission links is greater than or equal to the amplifier span of the fiber transmission system. These conventional dispersion-managed transmission links are unsuitable for propagation of pulses with bit rates above 40 Gb/s in each channel [103]. In 1999, Liang *et al.* proposed a dense dispersion-managed (DDM) fiber, whose dispersion map length is shorter than the amplifier span, to perform pulse transmission at 80 Gb/s [13]. Then 160 Gb/s transmission using DDM fibers were theoretically simulated [105, 106] and experimentally demonstrated [12], and higher bit rate transmission was also demonstrated [107, 108].

In order to avoid the problem of pulse distortion due to third-order dispersion at 160 Gb/s (as discussed in Section 2.4), we propose to use a DDM fiber to perform the in-line SPM-based 2R regeneration of a 160 Gb/s signal instead of DSF, HNLF, or chalcogenide fibers. The DDM fiber consists of several portions of fibers with opposite but equal values of dispersion $\pm D$. With a DDM fiber the average dispersion D_{avg} is close to zero but locally, the group-velocity dispersion dominates the third-order dispersion. The periodic dispersion maps of the DDM fibers are as short as several hundred of meters up to several kilometers. The numerical simulations vary the DDM fiber parameters to ensure the fiber's parameters are not awkward for manufacturing. These DDM fibers can be made by splicing different fibers with opposite sign of dispersion [109] or they can be fabricated by slightly changing the core diameter of a single fiber during the drawing process [42]. The current fiber fabrication technology can fabricate a short-period dispersion management by a continuous draw without splicing and their dispersion map period can be as short as hundreds of meters [46, 110].

The schematic representation of a DDM fiber is illustrated in Figure 2.23(a). The fiber of length L is divided in N_s sections. Each section has a dispersive sign that differs from its adjacent sections. As shown in Figure 2.23(b), the value of dispersion of each section alters the dispersive sign between D and $-D$. The dispersion of the fiber is then equal to the average dispersion D_{avg}.

In order to obtain the expected S-shape transfer function of the SPM-based 2R regenerator, the average dispersion D_{avg} of the DDM fiber must be negative and close to zero accordingly to the scaling rules presented in Section 2.2. An example of DDM fiber design with dispersion profile is illustrated in Figure 2.24. The length of the normal dispersion sec-

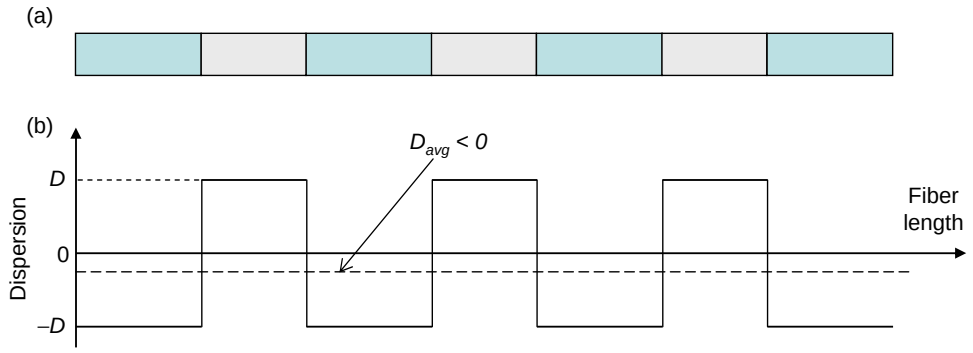

Figure 2.23: (a) Schematic representation of a DDM fiber and (b) its dispersion profile map.

tions is equal to L_1 and the length of the anomalous dispersion sections is L_2. A transition section of length L_{TF} where the dispersion changes gradually from $-D$ to D is also taken into account. The length L_{TF} is designed to be about 10% of the length of a section. The DDM fiber is composed of several periodic sections of L_1 and L_2.

To ensure a negative value for the average dispersion D_{avg}, the first and the last section of DDM fiber are designed in the normal dispersion regime ($D < 0$) as seen in Figure 2.24. The total length of the normal dispersion sections is then:

$$L_{1T} = \frac{(N_s + 1)L_1}{2}, \tag{2-14}$$

and the total length of the anomalous dispersion sections is:

$$L_{2T} = \frac{(N_s - 1)L_2}{2}. \tag{2-15}$$

The total length of the transition sections is:

$$L_{TF-T} = (N_s - 1)L_{TF}. \tag{2-16}$$

The total length of the fiber is then calculated by:

$$L = L_{1T} + L_{2T} + L_{TF-T}. \tag{2-17}$$

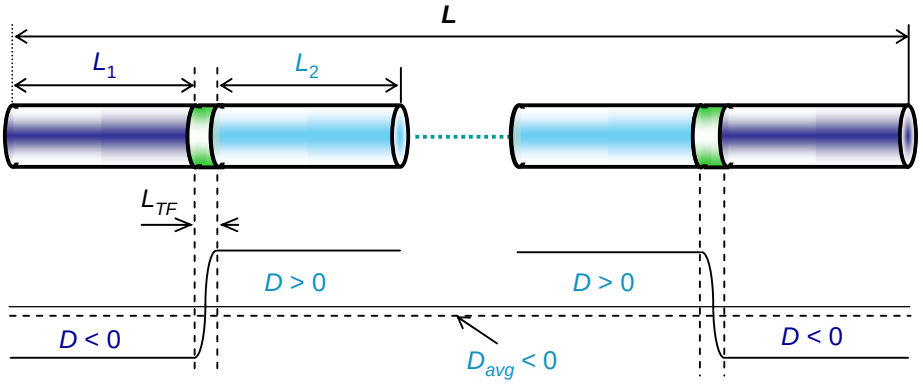

Figure 2.24: A DDM fiber with transition parts L_{TF} and its dispersion profile.

The total dispersion of the fiber is then figured out by summing dispersion of the normal dispersion sections and the anomalous dispersion sections. The average dispersion D_{avg} of fiber is then given by

$$D_{avg} = \frac{D(L_{2T} - L_{1T})}{L} = \frac{D[(N_s + 1)(L_1 - L_2) + 2L_2]}{2L}. \quad (2\text{-}18)$$

A control of the dispersion can be obtained by changing either the values of L_1 and L_2 or the number of sections N_s. It is useful to introduce the ratio r of length between the negative dispersion sections L_{1T} and the total length L, $r = L_{1T}/L$. The total length L, the ratio r, the length of each section L_1, L_2, the number of section N_s, and the value of the dispersion D are critical parameters for DDM fibers. They will be used to describe the DDM fibers as well as used in the numerical simulation to perform 160 Gb/s signal regeneration.

2.6 2R regeneration of 160 Gb/s signals

This section discusses the results concerning the simulation of DDM fiber-based 2R regeneration of 160 Gb/s signals. The DDM fibers are designed with different values of the absolute dispersion D. The transfer function TF and the Q-factor improvement, Q_{IM}, are used to investigate the use of DDM fibers in the 2R regeneration. As previously, signal propagation along a DDM fiber is simulated by solving the nonlinear Schrödinger equation (Eq. (1-46)) by using the split-step Fourier method [47].

2.6.1 DDM fiber parameters

For the first calculation, an absolute dispersion $|D|$ is set to 1 ps/km/nm. The fiber length L is varied but does not exceed the effective length L_{eff}. To control the average dispersion, the ratio r is changed in the range 50% to 100%. This range of r ensures that the total length L_{1T} of the normal dispersion sections is greater than the total length L_{2T} of the anomalous dispersion sections. In other words, the average dispersion D_{avg} is sure to be negative. The fiber losses α of all sections are set to be 0.27 dB/km. The nonlinear coefficient γ is 3.2 $W^{-1}km^{-1}$. The third-order dispersion β_3 of all fiber sections is set to 0.1 ps^3/km. All these characteristics are similar to those of fibers which have already been fabricated [6, 111]. Several examples of DDM fibers that are simulated for 160 Gb/s signal regeneration are given in Table 2.1.

Numerical simulations are also done with absolute dispersions $|D|$ set to be 2, 3, 4, and 5 ps/km/nm. Table 2.2 presents some examples of the DDM fibers which can be used to perform the regeneration of 160 Gb/s signals. For each value of the absolute dispersion $|D|$, the fiber length L, the ratio r, and the number of sections N_s are varied to find sets of parameters that implement the regeneration. Transfer functions TFs and Q-factor improvement Q_{IM} are both used to verify the performance of DDM fibers in 2R regeneration.

In the next section, the use of DDM fibers in 2R regeneration of a 160 Gb/s signal will be demonstrated.

Table 2.1: Parameters of new design DDM fibers for $|D| = 1$.

Fiber name	L (m)	L_1 (m)	L_2 (m)	r (%)	$\|D\|$ (ps/km/nm)	N_s	D_{avg} (ps/km/nm)
DDM 1	1 612	172	187	53.5	1	9	−0.066
DDM 2	1 612	139	155	51.8	1	11	−0.036
DDM 3	1 612	117	132	50.7	1	13	−0.014
DDM 4	2 073	156	163	52.8	1	13	−0.056
DDM 5	2 073	134	143	51.7	1	15	−0.034

Table 2.2: Parameters of new DDM fibers for $|D| > 1$.

Fiber name	L (m)	L_1 (m)	L_2 (m)	r (%)	$\|D\|$ (ps/km/nm)	N_s	D_{avg} (ps/km/nm)
DDM 6	2 985	216	246	50.6	2	13	−0.024
DDM 7	13 589	707	725	52	3	19	−0.012
DDM 8	14 050	857	609	61	4	13	−0.088
DDM 9	16 085	60	58	51	5	273	−0.1

2.6.2 Regeneration of 160 Gb/s signal

In this section, the ability of DDM fibers to be used as the nonlinear fiber of the Mamyshev regeneration of a 160 Gb/s signal are demonstrated through numerical simulations. The 160 Gb/s signal is a pulse train of 1.5 ps with a PRBS of 2^{10} bits. The OSNR and the ER is set to be 25 dB/0.1 nm and 20 dB, respectively. At the output of the DDM fiber, a frequency offset filter, whose center frequency is shifted from the input signal by 706 GHz, is used to filter signal.

All the fibers with the parameters described in the previous section are tested by numerical simulations and the performance of the regenerator is verified by the transfer function TF and the Q-factor improvement. Here, the results of the fiber DDM1 are chosen for presentation. Figure 2.25 illustrates the transfer function together with the evolution of the Q-factor improvement, Q_{IM}, as a function of the input peak power. It clearly shows a maximum Q_{IM} of 3.2 dB associated with an adequate transfer function with a plateau around the input peak power of 1.15 W. This peak power is equivalent to 138 mW (21 dBm) of average power.

Signal noise, for the "one" and the "zero" levels, is also consider in the simulation. Figure 2.26 represents the noise reduction coefficients for the "ones" and the "zeros" as a function of the input power. These coefficients are defined as the ratio between the standard deviation of intensity distribution of the "one" level or "zero" level at the output and the corresponding standard deviation at the input of the regenerator. We see that noise for both "one" and

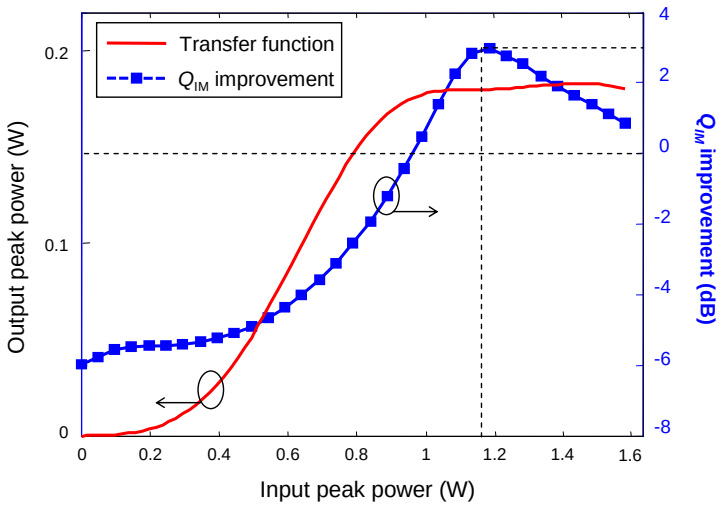

Figure 2.25: Transfer function TF and Q_{IM} improvement as a function of input peak power of the regenerator using the DDM1 fiber.

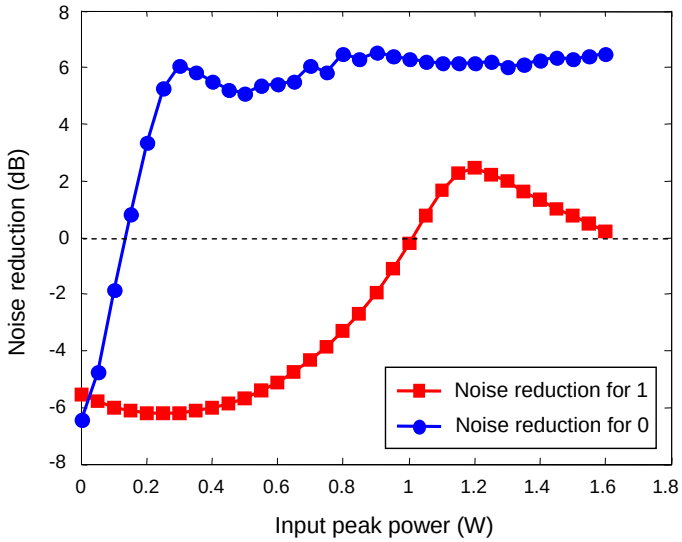

Figure 2.26: Noise reduction for the "one" and the "zero" levels as a function of input peak power of the regenerator using the DDM1 fiber.

"zero" levels can be reduced by a factor 2.6 dB and 6.2 dB, respectively. Noise at "zeros", after the regenerator, is reduced by about 6 dB in a large range of input peak power (from 0.4 W to 1.65 W), and noise at "ones" is reduced by a maximum value of 2.6 dB at a input peak power of 1.2 W.

The quality of the regenerated signal is shown by the pulse train and eye diagrams. The pulse trains of the 160 Gb/s signal at the input, after propagating along the DDM1 fiber and after the regenerator are illustrated in Figure 2.27(a), (b), and (c), respectively. Figures 2.28(a) and Figure 2.28(b) show the eye diagrams of the 160 Gb/s signal at the input and at the output of the regenerator, respectively. The regenerated eye diagram shows a

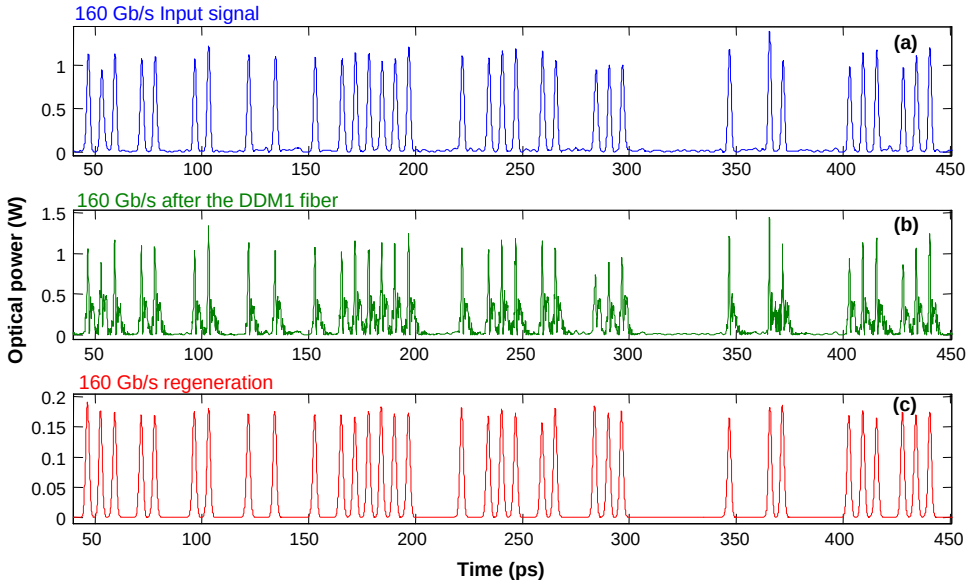

Figure 2.27: Examples of the 160 Gb/s pulse train signal (a) at the input (b) at the output of the DDM1 fiber, and (c) after the regeneration.

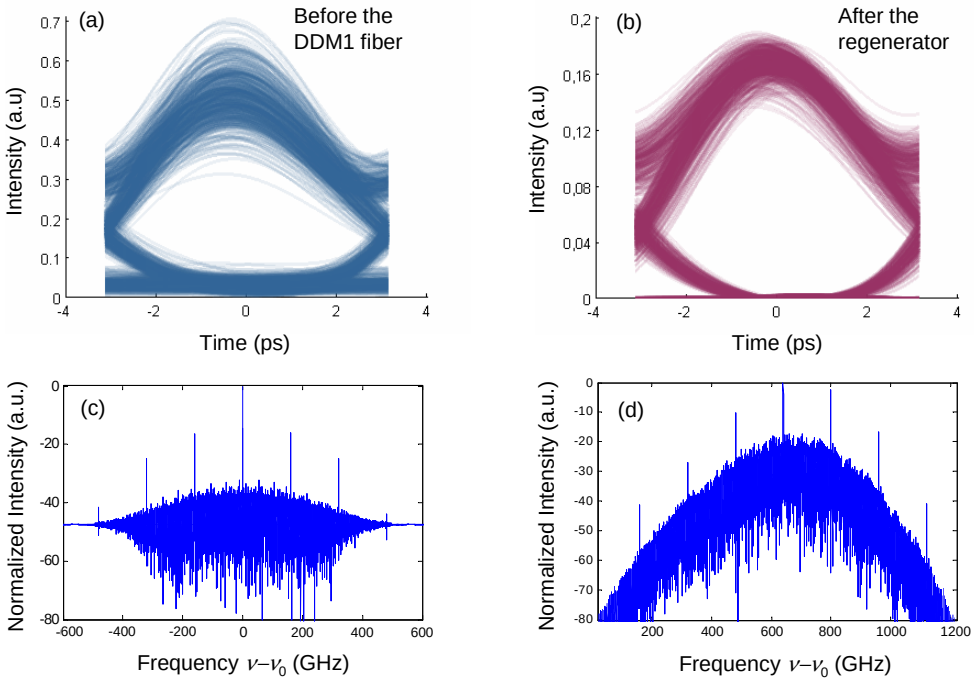

Figure 2.28: Eye diagrams of a 160 Gb/s signal before (a) and after (b) the regenerator using the DDM1 fiber. Spectra of a 160 Gb/s signal before (c) and after (d) the regenerator using the DDM1 fiber.

slight timing-jitter. It however has lower noise at both "zero" and "one" levels leading to a more open eye diagram compared to the input one.

With DDM fibers, the average dispersion of fiber is ensured close to zero while the dis-

persion of each section has large values. The second-order dispersion thus locally dominates the third-order dispersion leading to an avoidance of the influence of β_3. This is satisfactory for performing 160 Gb/s regeneration.

We have also investigated the performance of the regenerator when the parameters of the DDM fiber are changed. Doing this work ensures that the parameters of the DDM fiber are not too crucial so as to allow the fiber to be manufactured. Firstly, the ratio r, which not only accounts for the lengths of segments but also determines the average dispersion D_{avg} of the fiber, is varied.

Figure 2.29 represents the transfer function of the regenerator when the ratio r varies from 52.7% to 53.9%. On the other hand, the length of the normal dispersion section L_1 is variable in a range of 4 m (8% of the section length). The length of the anomalous dispersion section can also be varied in range of 8%. Figure 2.29 shows that, in this range, the transfer functions are still suitable for regeneration of 160 Gb/s signal.

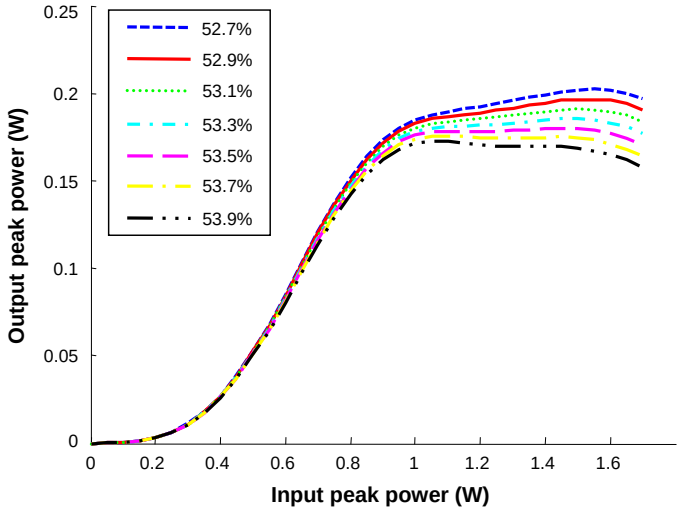

Figure 2.29: Transfer function TF of a 160 Gb/s regenerator using the DDM1 fiber for different values of r.

The ratio r is varied in the same range from 52.7% to 53.9% to investigate the Q-factor improvement and the noise reduction. Figures 2.30 represents Q_{IM} as a function of the input peak power. For all the values of the ratio r, the maximum Q-factor improvement is always greater than 2.5 dB (see inset of Figure 2.30).

Figure 2.31 illustrates the noise reduction of the "one" level of the regenerated signal with respect to the input signal for the same range of r variation. The result shows that the noise reduction is greater than 1.8 dB. For "zero" level, noise reduction by more than 4.5 dB is also numerically demonstrated.

The variation of the absolute dispersion $|D|$ is also considered. This step ensures that the dispersion tailoring during the fabrication process is not too critical. We examine the effect of the absolute dispersion $|D|$ changing in the range of $\pm 5\%$ around 1 ps/km/nm. Figure 2.32 shows that when the absolute dispersion $|D|$ changes in the range between

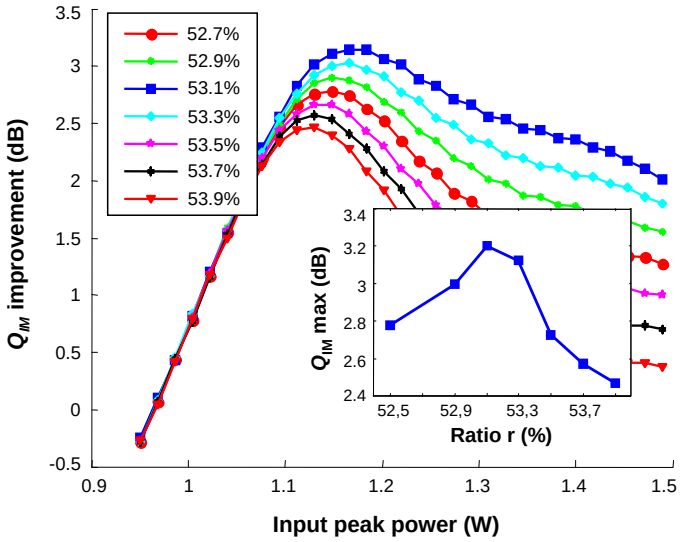

Figure 2.30: The Q-factor improvement Q_{IM} as a function of input peak power of a 160 Gb/s regenerator using the DDM1 fiber for different values of r.

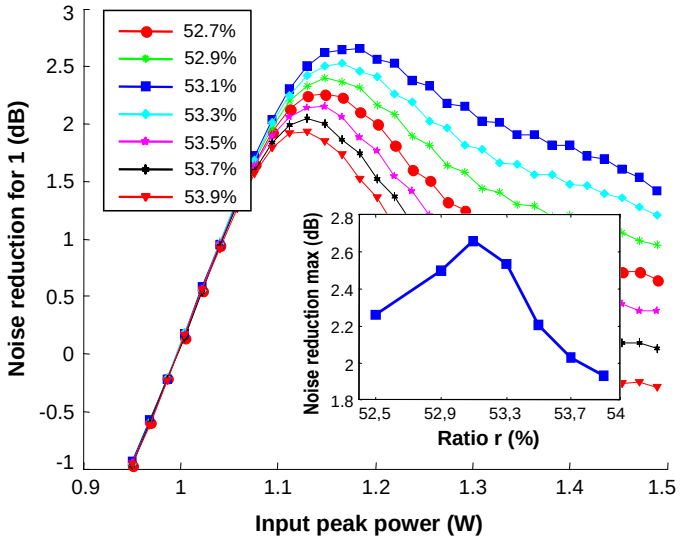

Figure 2.31: Noise reduction for "one" level as a function of input peak power of a 160 Gb/s regenerator using the DDM1 fiber for different values of r.

0.95 ps/km/nm and 1.05 ps/km/nm the transfer function of the regenerator is not much affected.

The same procedures are done with the other DDM fibers and similar results are obtained. For example, Figure 2.33(a) illustrates the transfer function and the Q-factor improvement of a 160 Gb/s regenerator using the DDM3 fiber with $|D| = 1$. For this case the frequency offset ΔF of the output filter is 564 GHz (twice the F_{FWHM} of the input signal). The maximum $Q_{IM} = 2.6$ dB is obtained at the input peak power of 0.95 W. This power corresponds to an average power of 114 mW (20.6 dBm). Similar to the case of using the DDM1 fiber, the working point is in the plateau of the TF. Figure 2.33(b) and

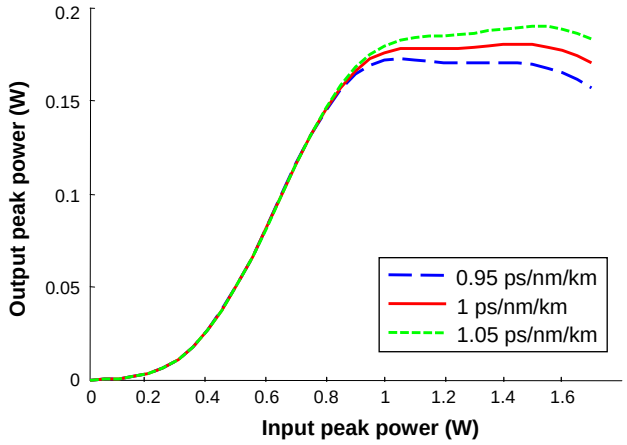

Figure 2.32: Transfer funtions of a 160 Gb/s regenerator using the DDM1 fiber for different values in the vicinity of the absolute dispersion $|D| = 1$.

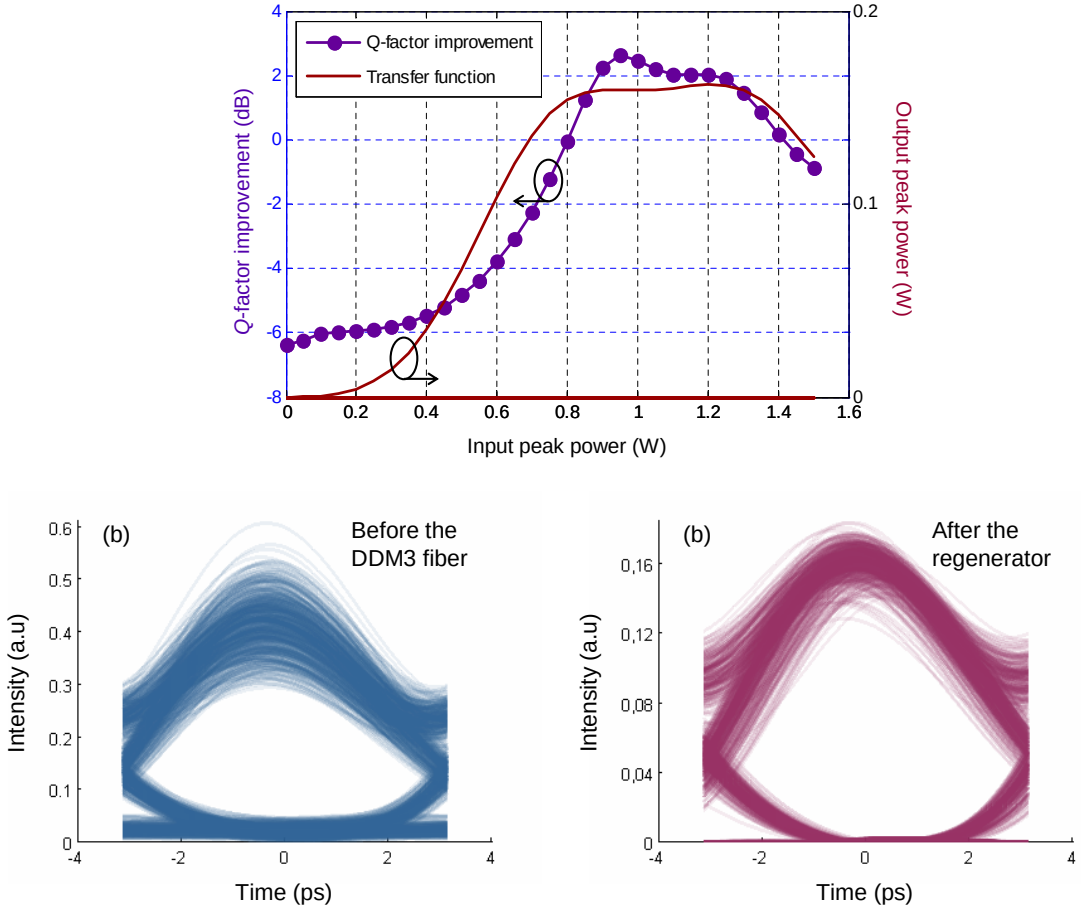

Figure 2.33: (a) Q-factor improvement and transfer function of a 160 Gb/s regenerator using the DDM3 fiber. Eye diagram of (b) the input and (b) after the regenerator using the DDM3 fiber.

Figure 2.33(c) show the eye diagrams of the input and the regenerated 160 Gb/s signal, respectively. Compared to the input eye diagram, fluctuations at both "one" and "zero"

levels are reduced leading to the regenerated eye diagram being more open.

From these studies, we conclude that variations of the parameters of the DDM fibers in a reasonable range do not degrade the performance of the regenerator much. This point is important for the fabrication of DDM fibers fabrication which are designed for SPM-based optical regeneration at 160 Gb/s.

2.7 Conclusion

In this chapter, we have shown that the group-velocity dispersion and the third-order dispersion both critically influence the performance of Mamyshev regenerators when using a high bit-rate signal. We have theoretically demonstrated that a dense dispersion-managed fiber can be used as the appropriate nonlinear fiber for a Mamyshev regenerator at 160 Gb/s. This fiber offers the advantage of limiting the influence of the third-order dispersion β_3 while maintaining average group-velocity dispersion, D_{avg}, negative and close to zero. For suitably chosen sets of parameters, we have shown that the Q-factor improvement of the regenerator can reach the value of 3.2 dB. The parameter variations studied are compatible with fiber fabrication. The demonstration of using DDM fibers in Mamyshev regenerators was presented in *the European Conference on Lasers and Electro-Optics* (CLEO/Europe) in Munich, Germany in 2011.

The DDM fibers take advantage of ease of implementation of silica fibers. However, it has a low nonlinear coefficient, γ, therefore we need a long fiber to increase the product nonlinearity-length (γL). The power used in 160 Gb/s regeneration is still high as about 1 W of peak power. Nowadays, the trend of ultra-highly nonlinear fibers made of chalcogenide glasses have been paving the way for the use of chalcogenide glasses fibers in all-optical signal processing at high bit rate. The following chapters are devoted to introducing chalcogenide glass fibers (Chapter 3) and the use of chalcogenide glass fibers for all-optical signal processing (Chapter 4).

Chapter 3

Nonlinear Chalcogenide fibers

For the past two decades, nonlinear fiber optics has been an active topic drawing much attention. Many studies to increase nonlinearity of optical fibers have been carried out. The fiber nonlinearity can be increased by decreasing the core diameter with the use of microstructured fibers or by using higher nonlinear materials than silica. This chapter deals with microstructured nonlinear optical fibers made of chalcogenide glasses.

The chapter starts first with the state of the art of nonlinear fibers with an emphasis on chalcogenide fibers. Section 3.2 introduces the fabrication method that is used to draw the chalcogenide fibers. Section 3.3 deals with the characterization methods, which are used to characterize linearly and nonlinearly chalcogenide fibers. Section 3.4 is devoted to presenting the optical characterization of chalcogenide MOFs with their characteristics and discussion on them. The last section summarizes the results.

3.1 State of the art

Nonlinear optical fibers represent a good choice for use in nonlinear optical signal processing. The first highly nonlinear fiber (HNLF) with relatively low attenuation was developed by Nippon Telegraph and Telephone Corporation (NTT) in 1986 [8]. Commercial HNLFs made of silica proposed by OFS (USA) and Sumitomo Electric Lightwave (Japan) are now widely used in optical systems and in laboratories. These fibers have a nonlinear coefficient γ between 10 $W^{-1}km^{-1}$ and 20 $W^{-1}km^{-1}$. Their nonlinear coefficient is not so high, but these fibers have very low loss (< 1 dB/km). The nonlinearity can thus be enhanced by using fiber lengths of hundreds of meters.

As mentioned in Chapter 1, the nonlinear coefficient γ of fibers is given by

$$\gamma = \frac{2\pi n_2}{\lambda A_{eff}}, \tag{3-1}$$

in which n_2 is the nonlinear refractive index of the material, A_{eff} is the effective mode area of the fiber, and λ is the wavelength.

As discussed in Section 1.5, to boost the nonlinear coefficient γ, we need either to increase the nonlinear refractive index n_2 or to decrease the effective mode area A_{eff}.

In the case of increasing n_2, among several proposed materials (see in Section 1.5), chalcogenide glasses have attracted much interest due to the fact that they have interesting optical properties such as high nonlinearity, fast response and infrared transparency, which can be used for photonics applications. Chalcogenide glasses can be transparent from the visible region (sulfur based glass) up to the mid infrared (25 μm for telluride glasses) [112]. Chalcogenide glasses include major compositions which are constituted from one or more of the chalcogen elements in Group 6a of the periodic table (sulphur - S, selenium - Se and tellurium - Te) and some other elements such as Arsenic - As, Germanium - Ge, Antimony - Sb, Gallium - Ga, or Indium - In. For tailoring thermal, mechanical and optical properties of chalcogenide glasses, other elements such as P, I, Cl, Br, Cd, Ba, Si, or Tl can be added. Chalcogenide glasses exhibit strong nonlinearity. The nonlinear refractive index n_2 of sulfur based glasses is over 100 times higher than in silica and even 500 times higher for selenium and tellurium based glasses [113, 114, 115]. For highly nonlinear fibers, chalcogenide glasses are a good choice compared with the other materials.

In the case of decreasing A_{eff}, one needs to diminish the core diameter of guiding components. There are several structures that allow the reduction of the core diameter such as microstructured fibers [18, 116], waveguides [117], tapers [118], or nanowires [119]. Microstructured fibers offer an advantage of not only a small core diameter but also a long fabrication-possible length leading to a high magnitude of the product γL. This helps to reduce the optical power when used in telecommunication systems. A combination of chalcogenide glasses (highly nonlinear materials) and microstructured fibers (small core and long possible length) leads to an active branch of nonlinear fibers optics for photonics applications. Our work concentrates on *chalcogenide microstructured fibers* (MOF).

Research on the optical nonlinearity of chalcogenide glasses started from 1953 [120]. Then, in 1965 the first ever chalcogenide fiber was successfully demonstrated [17]. With the new trend of MOFs, in the year of 2000, the first chalcogenide MOF [18] with the composition of GaLaS was introduced by T. Monro from the ORC (Optoelectronics Research Centre, UK). However, no light guidance was observed. In 2006, the NRL (Naval Research Laboratory, USA) and the PERFOS/EVC collaboration fabricated chalcogenide MOFs in which light guidance could be observed [55, 121]. Since then, several chalcogenide MOFs of different glass compositions have been demonstrated to exacerbate the Kerr nonlinearity as well as to reduce the attenuation losses and dispersion [122, 123, 124, 125].

For qualitative assessment of nonlinear fibers, we propose the use of a figure of merit (FOM). It is defined as the product of the nonlinear coefficient γ and the effective length of fiber L_{eff} :

$$FOM = \gamma L_{eff}. \tag{3-2}$$

As mentioned in Section 1.5, the maximum effective length of the fiber L_{eff_max} is $1/\alpha$, where α is the fiber loss. We therefore have the maximum figure of merit FOM_{max} of a

fiber given by

$$FOM_{max} = \gamma/\alpha. \tag{3-3}$$

For example, a commercial Corning SMF28 fiber with an attenuation loss of 0.2 dB/km and a nonlinear coefficient γ of 1.3 $W^{-1}km^{-1}$ has a FOM_{max} of 26 W^{-1}. An HNLF, with a nonlinear coefficient of 30 $W^{-1}km^{-1}$ and an attenuation loss of 0.9 dB/km may have a maximum figure of merit FOM_{max} of 145 W^{-1}, provided that the whole effective length (4.8 km in this case) can be used. However, in order to reduce zero wavelength dispersion fluctuation and Brillouin effect, the length of HNLFs used in practice is generally below 1 km, reducing their FOM below 29 W^{-1}.

In 2005, CorActive (Canada), an optical fiber manufacturer, offered chalcogenide step-index single-mode fibers with a nonlinear coefficient of approximately 1200 $W^{-1}km^{-1}$ for the As_2Se_3 glass composition [126, 127]. The fibers have an attenuation loss of about 1 dB/m, the FOM_{max} of these fibers is thus 5 W^{-1}. Despite the high value of the nonlinear coefficient, the FOM_{max} of this fiber is less than the previous ones because the loss is much increased than the nonlinearity. Moreover, with the AsSe composition, the dispersion of fibers is as high as -550 ps/km/nm at 1550 nm [128]. This high dispersion limits the four-wave mixing wavelength conversion range λ_c, which is defined in Section 1.4.1.4. From then, various solutions have been proposed to both increase the FOM of fibers based on chalcogenide glasses and decrease their dispersion.

In 2007, the CUDOS laboratory (Australia) strove to make a small core fiber in order to reduce the effective mode area to increase the nonlinearity. By tapering, the size of fiber is significantly reduced. This process produces a nanowire. Researchers at CUDOS demonstrated a nonlinear coefficient of 93400 $W^{-1}km^{-1}$ and a dispersion of -280 ps/km/nm [119]. The FOM_{max} of the nanowire is as high as 101 W^{-1}. However, possible lengths of nanowires are limited by a few decimeters, which limit their performance in terms of nonlinear efficiency. For the 93400 $W^{-1}km^{-1}$ nanowire, the length of the waist is only 3 cm leading to a FOM of only 2.8 W^{-1}. This requires relatively high powers for applications. For wavelength conversion at 40 Gb/s, the required optical power is 180 mW [118] for a optical bandwidth conversion of more than 30 nm.

Another solution taken by the CUDOS laboratory is the realization of waveguides of chalcogenide glasses. While exacerbating the nonlinearity by keeping the effective mode area of around several μm^2, waveguide technology allows strong integration in photonics systems. Their applications have been demonstrated in Ref. [117, 129]. Like nanowires, the waveguide is again limited in length (a few centimeters), leading to a high optical power of 400 mW [117] but the optical bandwidth is significant (>30 nm). With a nonlinearity of 10 000 $W^{-1}km^{-1}$ and a real waveguide length of 7 cm, the FOM of these waveguides is 0.7 W^{-1}.

Recently, R. Ahmad and M. Rochette have presented As_2Se_3 microwires coated with poly-methyl meth-acrylate (PMMA) which allowed the production of optical degenerate FWM with a wavelength conversion range as broad as 190 nm and FWM efficiency as

high as 21 dB at peak input power levels as low as 70 mW [130]. This was enable with a high nonlinear coefficient of the microwire $\gamma = 97000$ W^{-1}km^{-1}. With an actual length of the component of 10 cm, the FOM is 9.7 W^{-1}. The authors have also reported the use of an As_2Se_3 chalcogenide microwire coated with a layer of PMMA cladding to perform optical parametric oscillation (OPO) [131]. OPO allows simultaneous oscillation at two wavelengths: at a Stokes and anti-Stokes wavelength shifts of +53 nm and −50 nm with respect to the pump laser at 1552 nm with a peak power threshold of 21.6 dBm.

From 2004, the three partners PERFOS of Photonics Bretagne (PB), Equipe Verres et Céramiques (EVC), and Foton have been collaborating in order to pursue the high nonlinearity of chalcogenide MOFs. MOFs provide a key to significantly decrease the core diameter of fibers compared with standard fibers and also to give a chance of tailoring chromatic dispersion to have a wider optical conversion range. With a few years of research, PERFOS and EVC (chalcogenide fiber manufacturers) have achieved a higher quality of chalcogenide glass and a more stable fabrication method for chalcogenide MOFs. Thanks to a casting method with a preform by moulding [112], they were able to demonstrate in 2009 a record of a high nonlinear coefficient of 15000 W^{-1}km^{-1} [21]. The fiber loss of 15 dB/m gave the FOM_{max} of only 4.3 W^{-1}

Figure 3.1 shows the FOM_{max} of some highly nonlinear devices as a function of the nonlinear refractive index of their material. For silica fibers, though the nonlinear refractive index n_2 is low ($\sim 2.6 \times 10^{-20}$ m^2/W) they have high FOM_{max} due to low fiber losses. The HNLF of OFS has a FOM_{max} of 82 W^{-1}. The SMF Sumitomo fiber has a high FOM_{max} at 145 W^{-1}. A Bismuth-oxide fiber with $n_2 \sim 3.2 \times 10^{-19}$ m^2/W has a FOM_{max} of 1.43 W^{-1} [132]. A lead silicate fiber with $n_2 \sim 4.1 \times 10^{-19}$ m^2/W has a FOM_{max} of 3.5 W^{-1} [133]. The AsS waveguide with $n_2 \sim 2.5 \times 10^{-18}$ m^2/W has a FOM_{max} of 7.1 W^{-1} [117]. Using chalcogenide glasses, which has a high nonlinear refractive index ($n_2 \sim 1.3 \times 10^{-17}$ m^2/W), an AsSe nanowire with a FOM_{max} of 101 W^{-1} [119], an AsSe step-index fiber with a FOM_{max} of 3.4 W^{-1} [81], and an AsSe MOF with a FOM_{max} of 4.5 W^{-1} [21] have been reported. In 2012, a report on AsSe microwire with PMMA coating gave a FOM_{max} 9.7 W^{-1} [130]. Also in 2012, with a high nonlinear material $n_2 \sim 7 \times 10^{-17}$ m^2/W, a silicon waveguide was reported with FOM_{max} of 37 W^{-1} [190]. By the time this thesis began (2009), we believe that the highest value of FOM of optical fibers is 145 W^{-1}, which belongs to the Sumitomo SMF [134].

Chalcogenide glasses possess an advantage of nonlinearity. The nonlinear coefficient γ may be 15000 W^{-1}km^{-1} for a chalcogenide MOF, 10000 W^{-1}km^{-1} for a chalcogenide waveguide, even 97000 W^{-1}km^{-1} for a chalcogenide microwire. However, these components have not high FOM due to either high attenuation coefficients or short actual lengths. This requires high optical powers to be able to carry out the applications. FOM can be increased by using chalcogenide MOFs because of their possible lengths. Nevertheless, chalcogenide MOFs have a restriction of chromatic dispersion. A high value of dispersion restricts the optical wavelength conversion range. For that reason, in order to use chalcogenide MOFs in

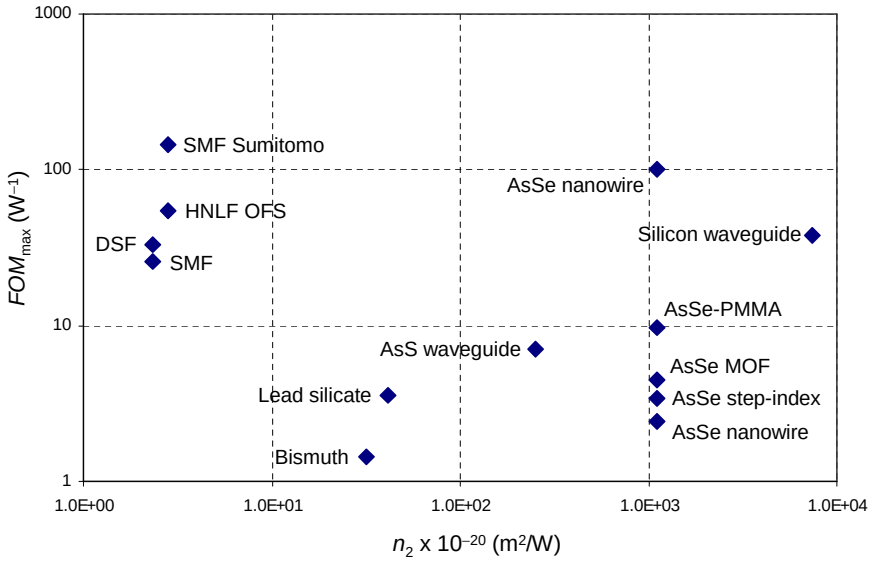

Figure 3.1: Figure of merits of highly nonlinear fibers

telecommunication applications, one needs to use chalcogenide MOFs with lower attenuation losses and lower dispersion.

3.2 Fabrication of chalcogenide fibers

In this section, methods to fabricate chalcogenide MOF fibers are described. The common method to realize MOFs is the stack and draw technique which is widely used to make silica MOFs [61] and chalcogenide MOFs [18, 55, 122, 135]. Some of the first chalcogenide MOFs were limited in ability of light guidance and attenuation losses. The chalcogenide MOFs fabricated before 2006 suffered high losses ($>$ 25 dB/m [121]). They could not be used to investigate applications. Before beginning my thesis, the lowest optical losses recorded so far for selenium-based MOFs were 13 dB/m at 1.55 μm [136] and about 9 dB/m at 3.39 μm [122]. In 2008, L. Brilland *et al.* proved that most of the optical losses were due to inhomogeneities at the interfaces between capillaries [137]. They found that the transmission was greatly improved by using a fiber design including interstitial holes. By utilizing this technique, the lowest losses obtained were 3 dB/m at 1550 nm for selenium-based glasses [137]. These results have shown that the stack and draw method seems not to be well suited to the fabrication of low loss chalcogenide MOFs. The challenge was to improve the fabrication method for chalcogenide MOFs.

In 2010, Q. Coulombier *et al.* introduced a new method [112] that permits the realization of chalcogenide MOFs of several types, included fibers with suspended-core or several rings of holes designs. The method is based on casting glass. It allows a considerable increase of the transmission as inhomogeneities at the interfaces are greatly reduced.

The principle of the method can be understood as follows (Figure 3.2). Preforms are

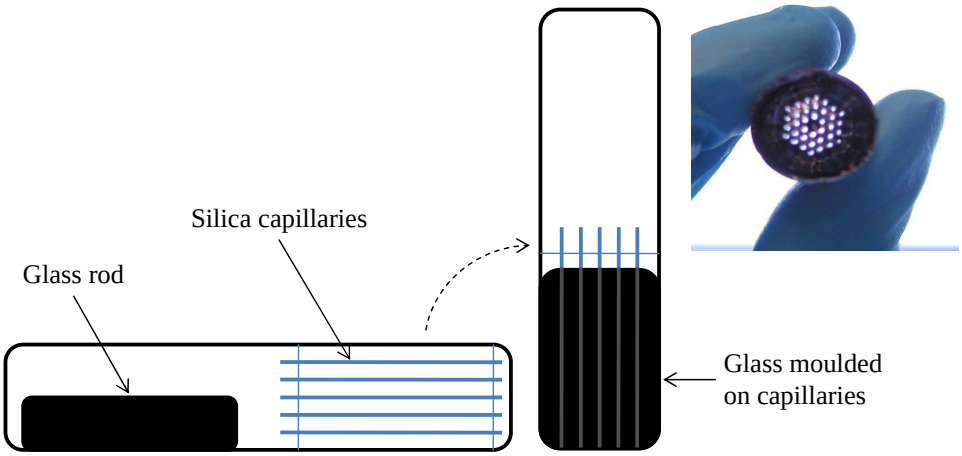

Figure 3.2: Scheme of the silica mould. The glass is poured into the mould which is then removed by a HF treatment. The resulting preform is shown on the right picture.

fabricated from chalcogenide glass rods and a mould. The glass rods are prepared and purified with the usual sealed silica tube method. For example of the As_2Se_3 glass, it is purified using oxygen and hydrogen getters. The mould is entirely made of silica capillaries. How the silica capillaries thread in the mould determine the structure of the fibers. They can be designed in silica hexagonal guides or suspended-core guides. The glass rod is heated to become liquid enough to flow into the silica mould. When the glass has set in the mould, the tube is quenched in air and annealed. The silica structure is then removed with hydrofluoric acid to obtain the chalcogenide glass preform. The fiber, finally, is drawn from the preform.

Here is an example of fabrication of a chalcogenide hexagonal fiber [112]. A preform is prepared from a As_2Se_3 glass rod. The silica guides are slices of a silica microstructured preform. The hole diameter is 610 μm and the pitch is 1350 μm. The silica slices are fused in a silica tube (16 mm inner diameter, 5 cm between the slices) which is closed afterwards. This arrangement allows the glass and the capillaries to resist to the mechanical stress induced by air quenching. Initially, the silica capillaries have an outer diameter of 600 μm and an inner diameter of approximately 490 μm. The diameter of the capillaries is reduced in a hydrofluoric acid (HF) bath to reach the outer diameter of 510 μm. The As_2Se_3 glass rod is placed above the mould, heated to 420°C for one hour and poured into the mould in 5 minutes. It stays in the vertical position for 15 minutes. The full mould is then quenched in air for four minutes before being annealed at 180°C for one hour. After the silica tube is removed with a diamond tool, the structured As_2Se_3 preform is then treated with 40% concentrated HF in order to remove the silica capillaries stuck in the glass. After staying in the bath for one hour, the preform is rinsed with distilled water and dried with an argon purge. Chalcogenide MOF is then drawn from the preform. A chalcogenide glass preform is held vertically and the lower end is heated until a glass drop appears. This falls down under gravitational forces forming a chalcogenide fiber which is then reeled on a drum in a rotary motion. At the same time, the preform is moved down, feeding the drawing furnace.

For a given feed speed of the preform, the diameter of the fiber is controlled by the drum speed. A narrow (5 mm width) drawing furnace is used to decrease the time during which the glass is in the critical high-temperature zone. A gas flow of 2.5 L/min creates an inert atmosphere around the preform. During fiber drawing, the hole diameters are adjusted by applying pressure in the preform holes.

The most important parameters of the method are the size of the capillaries and the glass temperature during the pouring process. First, if capillaries are too thin, they break during the moulding process. Conversely, if they are thicker than 15 μm, they create an important mechanical stress due to the difference between the thermal expansion of silica and As_2Se_3 [138], inducing glass breakage. Secondly, the viscosity of the glass must be well chosen for the moulding process. The glass is flowing into the cast with a low viscosity. Indeed, if the viscosity of the glass is too high, the glass does not flow into the mould, or it does not fill it. The temperature used to heat the glass rod depends on the materials. In the case of As_2Se_3 glass, the flowing temperature is around 420°C.

This casting method allows us to obtain various chalcogenide MOFs geometries. Figure 3.3 shows some examples of scanning electron microscope (SEM) images of chalcogenide MOFs fabricated by the casting method. Indeed, the fibers can have 3 rings of holes (Figure 3.3(a) and (b) or a suspended core (Figure 3.3(c)). The effective mode area can be controlled from 2 μm^2 to 300 μm^2. fibers with a very small core (core diameter of ~2 μm) can be obtained to enhance the nonlinear properties of the chalcogenide glass. Power delivery can also be considered with large core fibers (core diameter of 20 μm). The fiber can be either multimode or single mode, depending on the core size and the arrangement, the number and the size of the holes [139]. The geometry is controlled and chosen to realize the desired optical functions. In the case of small core chalcogenide MOFs (Figure 3.3(b)), a 2 mm diameter cane is first stretched from a microstructured preform. This cane is then inserted in a cladding made by a rotational casting method and is drawn into a fiber having a 2 μm core diameter [136]. Conversely, the large core fiber (core diameter of 13 μm) with a cladding made of 3 rings of holes (3.3(a)) is fabricated in one step such as the suspended core fiber (core diameter of 4 μm) (3.3(c)). In the last case (Figure 3.3(c)), only 3 capillaries are used in the mould and the size of the holes is adjusted during the drawing.

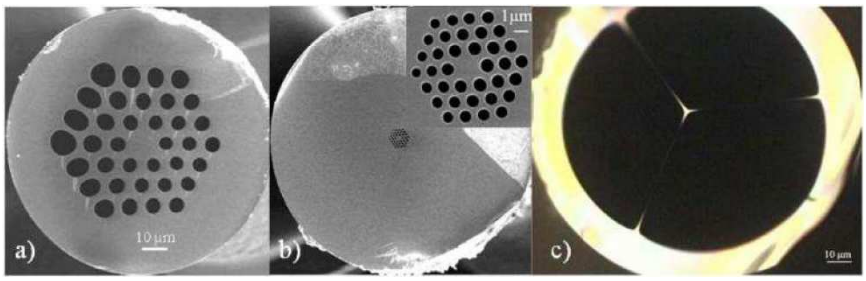

Figure 3.3: a) SEM picture of a large core fiber (13 μm). b) SEM picture of a small core fiber (2 μm). c) Optical microscopy picture of a suspended core fiber (4 μm)

3.3 Fiber characterization methods

This section is devoted to describing methods which are used to characterize the chalcogenide MOFs. Characterizations of attenuation losses, effective mode area, guiding modes, dispersion and nonlinear coefficient of fibers are considered.

3.3.1 Fiber losses

The loss of chalcogenide MOFs is one of the most critical parameters. It plays an important role in the implementation of telecommunication applications, performance assessment and optical system design. As mentioned in section 3.2, the high values of the attenuation coefficient α of chalcogenide MOFs restrict the applicability of fibers. It becomes an important parameter that needs to be accurately considered. Measurement of the attenuation coefficient of chalcogenide MOFs also helps to characterize the dispersion, the nonlinear coefficient with accuracy.

To measure the attenuation coefficient of fibers, several techniques have been proposed such as cut-back [140, 141], optical time domain reflectometry [142, 143], light scattering measurement [144, 145], using a dummy fiber [146], based on Brillouin or Raman scattering [56, 147]. Among those techniques, cut-back and optical time domain reflectometry (OTDR) are commonly used thanks to their simplicity and accuracy. With OTDR technique, the optical fiber must be long enough (hundreds of meters or more). Chalcogenide MOFs with losses of the order of few dB/m are not possible in such length. Hence, the cut-back technique is more suitable for chalcogenide MOFs. We use this technique to characterize the fiber losses of chalcogenide MOFs. The cut-back technique is briefly described in the following part. A non-destructive technique will be also used and described hereafter.

Cut-back technique

In the beginning, the cutback technique was widely used to measure the attenuation of optical fibers. The technique supposes that the fiber loss is linear and uniform. It measures fiber transmission losses at different lengths by cutting back the fiber. The fiber losses are then obtained from a serial power measurement for different lengths of fibers. It is illustrated in Figure 3.4. If P_{in} is the power launched at the input end of a fiber of length L, the output power P_{out} is given by

$$P_{out} = P_{in} \exp(-\alpha L) \tag{3-4}$$

Obviously, from Eq. (3-4), we only need a couple of values P_{in} and P_{out} to deduce the attenuation loss α of a fiber when the length L of the fiber is known. However, in practice, coupling losses and reflection losses at each end of the fiber under test may be unknown. It thus needs to take some more measurements. The cutback method measures different output powers at different fiber length. The total power launched into the fiber is kept

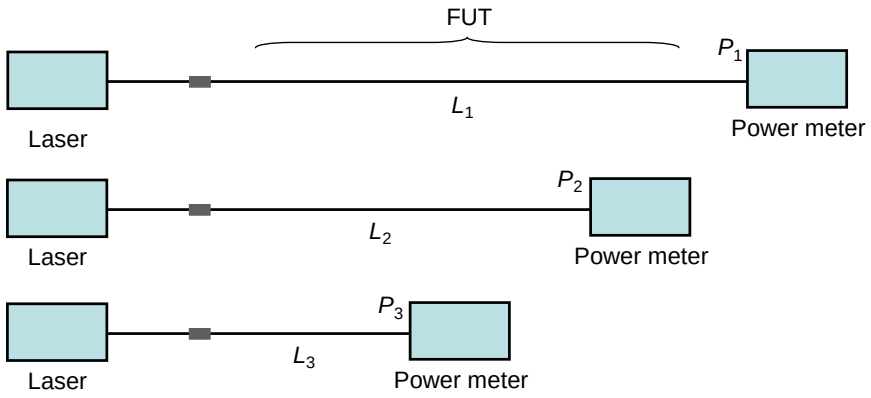

Figure 3.4: Illustration of the cutback technique to measure fiber losses.

unchanged, the output powers P_1, P_2, and P_3 are measured for different fiber lengths L_1, L_2, and L_3, respectively (see in Figure 3.4). The attenuation coefficient α of the fiber can then be interpolated. Figure 3.5 shows an example of fiber loss interpolation from a series of measured data for a chalcogenide fiber. The measured loss is 2.2 dB/m in this case.

The cut-back method can also measure the coupling losses. Power $P(0)$ launched into the fiber can also be interpolated from the measurement. The coupling loss, α_c, is easily obtain by a difference between the input power P_{in} and the launched power $P(0)$:

$$\alpha_c = P_{in} - P(0) \tag{3-5}$$

For the example of Figure 3.5, the values $P_{in} = 0.8$ dBm and $P(0) = -3.4$ dBm lead to a coupling loss α_c of 4.2 dB. Note that, this coupling loss includes losses due to Fresnel reflection.

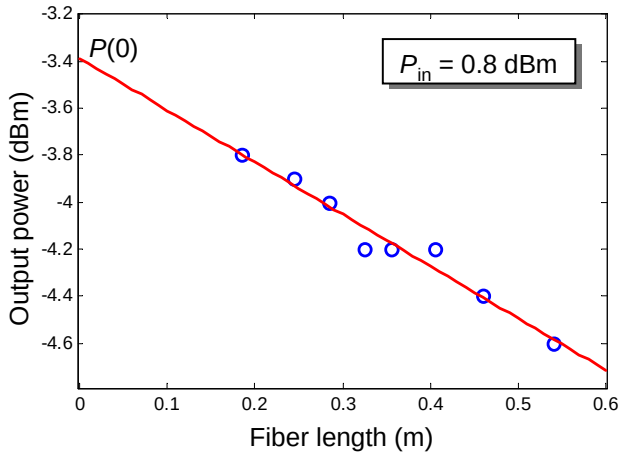

Figure 3.5: Example of the cutback technique to measure fiber losses and coupling losses

New non-destructive technique

The cut-back technique is a useful and simple technique to measure the attenuation coefficient of fibers. However, it is a destructive technique and the fiber under test (FUT)

is damaged. In order to develop a method that can preserve the fiber and be simple to use, T. N. Nguyen *et al.* from Foton laboratory has proposed a new method which can measure the attenuation coefficient of fibers as well as of waveguides [148]. Here, we are just considering the case of fibers. The technique is based on the principle that the linear losses of single-mode fibers are unchanged whatever the extremity where the light comes from.

The setup of the technique is described in Figure 3.6, in which the FUT is the CD segment. Two coupling fibers AB and EF are used to couple light into and out of the FUT. α_{ij} is named for the losses between point i (i =A, B, C, D, E) and point j (j =B, C, D, E, F). The coupling loss between fiber AB and the extremity C of the FUT is α_{BC}. The coupling loss between fiber EF and the extremity D of the FUT is α_{DE}. We suppose that the coupling loss between two guided structures is independent with the direction of light. That means that the coupling loss α_{BC} (light from B to C) and the coupling loss α_{CB} (light from C to B) are identical. Similarly, the coupling loss α_{DE} (light from D to E) and the coupling loss α_{ED} (light from E to D) are the same. This hypothesis is reasonable for single-mode propagation which is generally required for most applications. The aim of our loss measurement procedure is to identify α_{BC}, α_{CD} and α_{DE}.

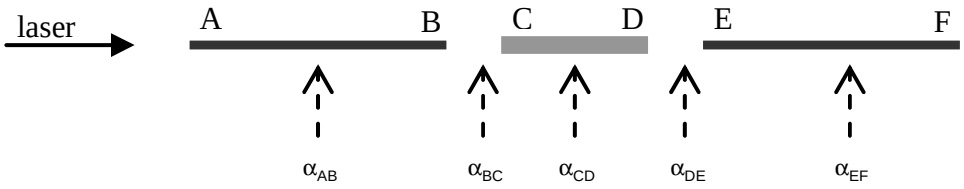

Figure 3.6: Principle of the new loss measurement technique. CD is the FUT, AB and EF are the coupling fibers.

It is straightforward to establish the three following equations with 3 variables (α_{BC}, α_{CD} and α_{DE}):

$$\alpha_{BC} + \alpha_{CD} + \alpha_{DE} = \alpha_{BE} = \alpha_{AF} - \alpha_{AB} - \alpha_{EF}, \tag{3-6}$$

$$\alpha_{BC} + \alpha_{CD} = \alpha_{BD} = \alpha_{AD} - \alpha_{AB}, \tag{3-7}$$

$$\alpha_{CD} + \alpha_{DE} = \alpha_{CE} = \alpha_{CF} - \alpha_{EF}. \tag{3-8}$$

From Eqs. (3-6) and (3-7), the output coupling loss α_{DE} can be found as

$$\alpha_{DE} = \alpha_{AF} - \alpha_{EF} - \alpha_{AD}. \tag{3-9}$$

From Eqs. (3-6) and (3-8), the input coupling loss is also given by

$$\alpha_{BC} = \alpha_{AF} - \alpha_{AB} - \alpha_{CF}. \tag{3-10}$$

By replacing α_{DE} and α_{BC} in Eq. (3-6), the guiding losses of the FUT is obtained:

$$\alpha_{CD} = \alpha_{AF} - \alpha_{AB} - \alpha_{EF} - \alpha_{BC} - \alpha_{DE} \tag{3-11}$$

The three unknown values α_{BC}, α_{CD}, and α_{DE} can thus be deduced provided that we can measure the loss parameters α_{AF}, α_{AB}, α_{EF}, α_{AD}, and α_{CF}. Figure 3.7 describes the procedure to deduce these values from the experiment. In our laboratory, to measure the light power, an integrated sphere powermeter with suitable photodetector is used. The light source is a laser diode which emits light at a power of P_0 at a wavelength λ.

	Description	Setup	Measured power	Identifiable value
1	Inject light source in the injecting fiber	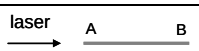	P_B^+	α_{AB}
2	Make an optimized coupling between injecting fibers and FUT		P_D^+	α_{AD}
3	Make an optimized coupling between injecting fibers and FUT (optimisation condition maybe consist in achieving the maximum transmission). Light direction from A to F	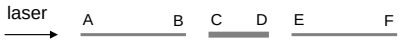	P_0, P_F^+	α_{AF}
4	Remake an optimized coupling between injecting fibers and FUT but change the direction of injected light. Make sure that α_{AF} is the same as in step 3		P_0, P_A^-	α_{FA} (should be identical to α_{AF} in step 3)
5	Take out the injecting fiber AB		P_C^-	α_{FC} (supposed to be equal to α_{CF})
6	Take out the DUT-CD		P_E^-	α_{EF}

Figure 3.7: Procedure of the new fiber loss measurement method.

3.3.2 Measurement of effective mode area

Measurement of the effective mode area is essential for fiber characterization. The effective mode area A_{eff} described in Section 1.2.2 determines how tightly light is confined in the core of the fiber. For a Gaussian beam, it is defined as $A_{eff} = \pi w_0^2$, in which w_0 is the *mode field radius*. Knowledge of A_{eff} helps to optimize the light coupling efficiency in fibers. For chalcogenide MOFs, the measurement of A_{eff} is also important due to the fact that the nonlinear coefficient is higher in fibers with smaller values of A_{eff}. For the measurement of A_{eff} [149], two common techniques can be used such as the *near-field measurement technique* and the *far-field measurement technique*.

Near-field measurement technique

The near-field technique is based on the important point that the distribution of the optical field inside the fiber is exactly equivalent to the optical field distribution on the

surface at the output end of the fiber. Since the cross-section dimension of fibers is really small especially with chalcogenide MOFs, it is impossible to measure the optical field distribution directly. A microscope objective is usually used just after the fiber to zoom in the image. The magnification of the objective depends on the core dimension of fibers. It usually should be 20× to 100×. Figure 3.8 illustrates the near-field measurement setup.

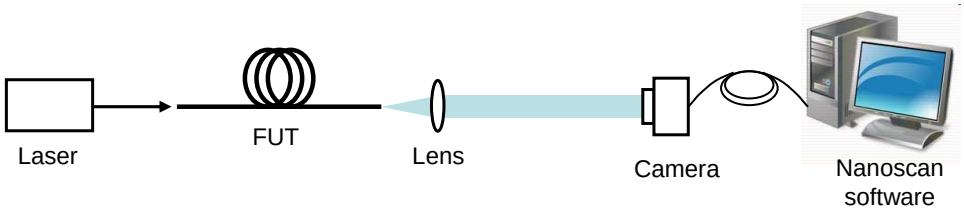

Figure 3.8: Near-field measurement setup

The accuracy of the near-field measurement depends on the magnification of the image. The image should have enough sampling points. However, the more image is magnified the more power is needed. For example, if an objective lens 20× is used, it means the image at the output of fiber under test is magnified 20×. The power density at camera is 400× lower than that of the fiber output. The power budget at the input thus needs more, about 26 dB. Since the light is diffracted at the output of fiber under test, the numerical aperture of the objective lens must be large enough. Deriving from the Rayleigh criterion, the numerical aperture of the objective lens NA must be greater than $0.61\lambda/d$ [150], in which d is the distance between two adjacently separated points that can be resolved.

Figure 3.9 illustrates examples of the measured near-field profile for a SMF fiber, in which Figure 3.9(a) is the near-field image and Figure 3.9(b) and (c) are the near-field profiles of X-axis and Y-axis respectively. The measurement gives the mode field diameter (MDF) to be 10.4 μm at 1550 nm.

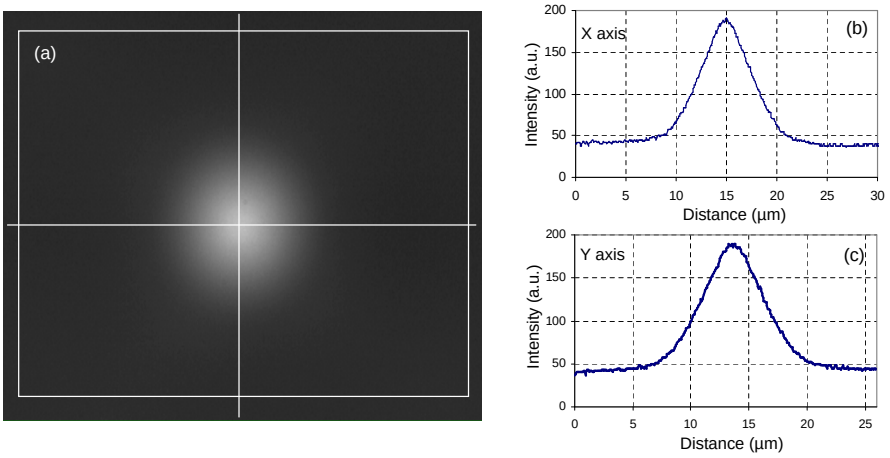

Figure 3.9: Examples of the measured near-field profile: (a) near-field image, the near-field profile in (b) the horizontal and (c) the vertical directions.

Recently, the development of digital image processing technology in camera photodetector allows us to observe and to measure real-time near-field images. It also helps to control input powers and also optimize the focus of the objective lens. However, the near-field measurement is not accurate for fibers with high numerical apertures because of limitation of the objective lens. One should use the far-field measurement technique.

Far-field measurement technique

The principle of far-field measurement is described in Figure 3.10. At the output of the FUT, a detector head is used to measure the power at a distance R. The detector head rotates around the output end of the FUT with an angle θ from $-80°$ to $80°$. In our measurement, a standard multimode fiber (type of 62.5/125) is used for the detector head.

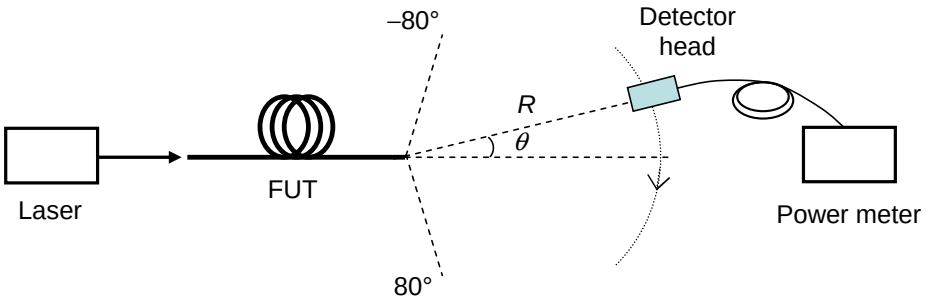

Figure 3.10: Principle of far-field measurement

The measurement should be implemented with a wide rotation range of the detector head to have a more accurate far-field power distribution pattern. From the far-field power distribution pattern measured, the near-field distribution can be easily obtained by an inverse Hankel transform [149]. As the name "far-field" suggests, it requires the detector head to be far from the output end of the FUT, $R \gg w_0^2/\lambda$ [149].

In our laboratory, the far-field technique is preferred to measure the effective mode area of fibers, especially for chalcogenide MOFs which will be described in section 3.4. Figure 3.11 shows an example of far-field measurement for a SMF fiber. Figure 3.11(a) illustrates the far-

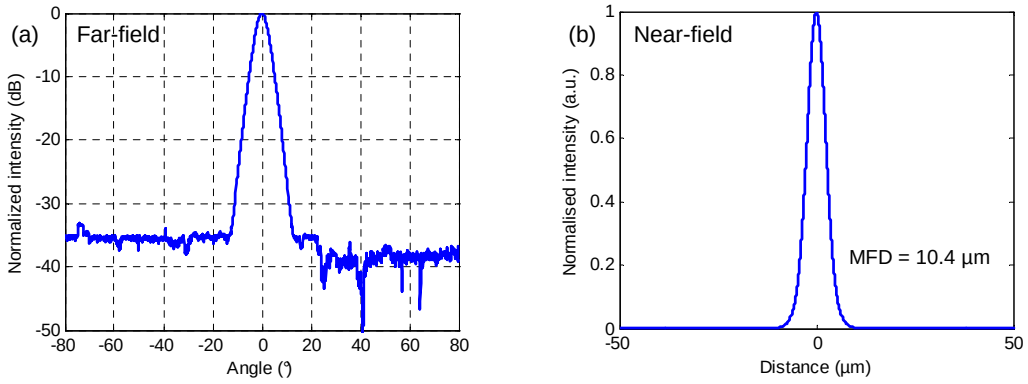

Figure 3.11: Examples of the far-field distribution measurement.

field power distribution measurement and Figure 3.11(b) plots the near-field profiles deduced from the far-field profile. The measurement gives the MFD of a SMF to be 10.4 μm. This result is similar to the measurement by the near-field technique.

3.3.3 Fiber modes scanning

Deriving from the S^2 imaging method which was proposed by Nicholson [151], S. Blin *et al.* from Foton laboratory has developed an alternative S^2 method to perform mode analysis of fibers [152]. Instead of a broad-band laser source and a 2D-scanning system, a tunable continuous wave (CW) laser and a camera are used. The method is simpler than the method of Nicholson because it allows us to vary only the wavelength of the optical laser rather than spatial scanning.

In a multi-mode optical fiber, each mode propagates at its own group velocity. They undergo a phase-shift along the fiber length L. The phase-shift between two modes can be written as $\Delta\varphi = 2\pi\Delta n_g L/\lambda$, in which Δn_g is the group index difference of the two modes. Therefore, at each position (x,y) of the fiber output plane interferences occur. By scanning the wavelength of the laser, one can observe interference fringes with a period of $\Delta\lambda = \lambda^2/(\Delta n_g L)$. The intensity of both modes at this position (x, y) can be retrieved by measuring the contrast of the 2-modes interference pattern. If other modes propagate in the fiber, interference will also occur but with different periods as long as Δn_g differs. Thus, analysis of the interference pattern at each point is facilitated by using Fourier analysis. Figure 3.12 gives an example of output spectra with interference and its Fourier transformation. Each peak in the Fourier domain corresponds to the beating between modes. In Figure 3.12, 3 beating frequencies correspond to 4 modes.

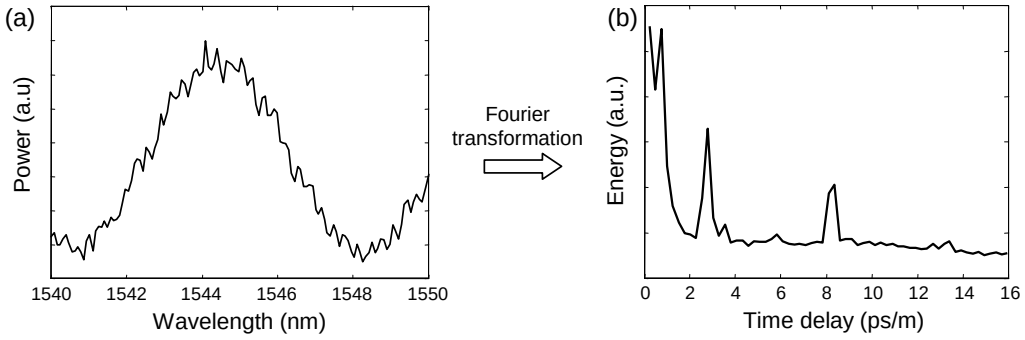

Figure 3.12: Principle of the alternative S^2 method: (a) the scanning interference spectrum, and (b) its Fourier transformation.

Figure 3.13 shows the experimental setup of the method. The tunable optical source is a commercial C-band external-cavity laser. It emits a continuous wave whose wavelength is swept in the desired range. Light propagates in a standard SMF fiber before injection into the fiber-under-test (FUT). An 80× microscope objective is used for magnification of the near-field images at the FUT output. Images are captured using a camera which returns

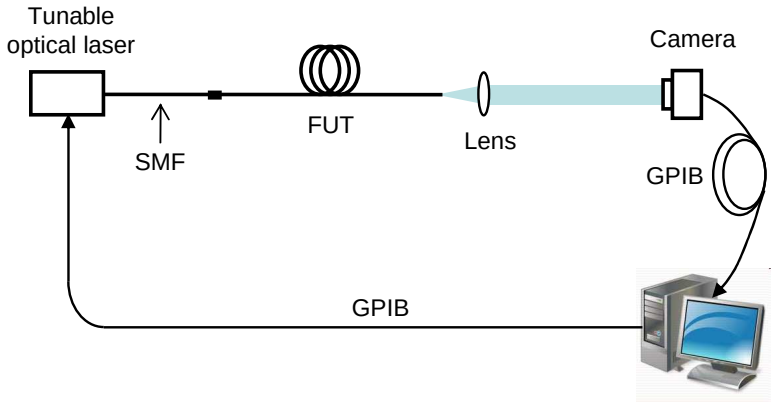

Figure 3.13: Modal decomposition principle and experimental setup.

one 8-bits 200×200-points image per primary color. The data acquisition is experimentally stored and analyzed by a computer. The computer controls the laser and collects data via GPIB ports.

Figure 3.14 illustrates an example of the mode profiles measured for a multimode fiber. The multimode fiber used under test is 4 m long. Its core and external diameters are 25 μm and 250 μm respectively. The experiment shows that the fiber supports 4 dominant modes as seen in Figure 3.14(a). The profiles of those 4 modes are also presented in Figure 3.14(b). In theory, from the equation of the normalized frequency, $V = (2\pi/\lambda)a\mathrm{NA}$, the V parameter of the fiber is calculated to be 5.06. This value also theoretically gives 4 guided modes which agrees with the experimental results.

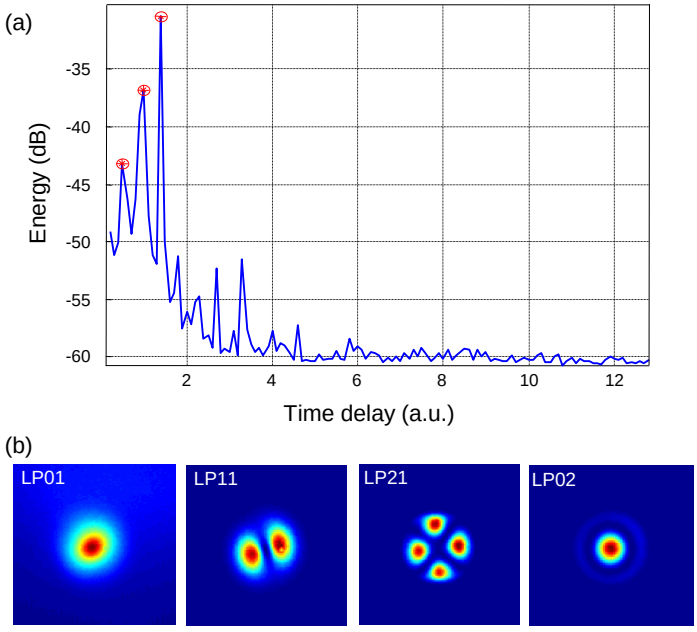

Figure 3.14: An example of using the alternative S^2 technique for a 4 m long multimode fiber with the core diameter of 25 μm.

3.3.4 Nonlinear coefficient

There are several techniques to measure the nonlinear coefficient γ of fibers. They are based on nonlinear Kerr effects such as SPM [153], XPM [154, 155], FWM [156] or based on interferometric methods [157]. Among the nonlinear effects, SPM-induced spectral broadening is simple to implement. SPM-based techniques can also simultaneously measure the chromatic dispersion of fibers [158]. The SPM-based technique is founded on the calculation of the nonlinear phase-shift $\Delta\phi$ of pulses between the output and the input of the FUT. The schematic setup used to measure the nonlinear coefficient of fibers is shown in Figure 3.15.

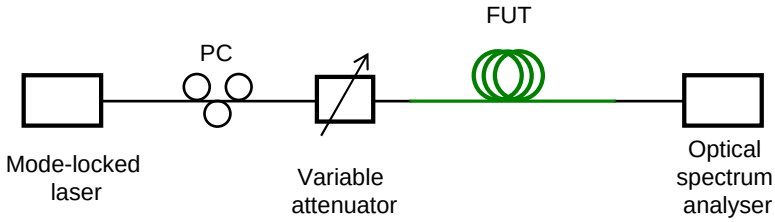

Figure 3.15: Experimental setup of SPM-based nonlinear coefficient measurement.

SPM-induced spectral broadening is measured with various values of the nonlinear phase shift by varying the input peak powers. To have the broadened SPM-spectra large enough, a mode-locked fiber laser (MLFL) with a low repetition rate should be used. Polarization optimization is obtained by using a polarization controller (PC) before the FUT. At the output of the FUT, spectra of SPM-induced pulses are observed on an optical spectrum analyser (OSA). These spectra are matched with the simulation to calculate the nonlinear coefficient and the dispersion of the FUT. The accuracy of the SPM-based technique depends on the quality of the input pulse and the output measured spectra. Using our mode-locked laser with some uncertainties concerning the initial chirp this technique gives rather a rough estimation of γ and D than an accurate measurement. This SPM-based technique is used to implement nonlinear characterization for our chalcogenide MOFs, which will be presented in the section 3.4.

Figure 3.16 shows an example of spectral measurement for 1 m chalcogenide fiber with a input peak power $P_0 = 1.1$ W. By matching the measured spectra with the simulated spectra of pulses at the output of the chalcogenide fiber, the nonlinear coefficient γ is estimated to be 11000 $\mathrm{W^{-1}km^{-1}}$ and dispersion D to be -500 ps/km/nm.

3.3.5 Dispersion

As mentioned above, based on SPM-induced spectral broadening, the nonlinear coefficient and the dispersion of the FUTs can be simultaneously estimated. In addition, the nonlinear coefficient and the dispersion of fibers can be obtained by using another nonlinear Kerr effect: four-wave mixing (FWM). Particularly, FWM-based technique is useful for the dispersion measurement. There are also other techniques to measure the dispersion of fibers [159,

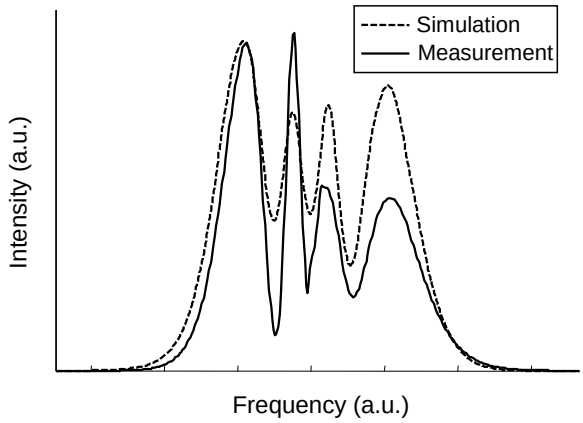

Figure 3.16: An example of simulated and measured SPM spectra for a 1 m chalcogenide fiber with input peak power $P_0 = 0.9$ W.

160, 161]. For chalcogenide MOFs, we prefer to use the FWM-based technique due to its simplicity and efficiency especially for high values of dispersion and high nonlinearity of chalcogenide fibers. This section considers the FWM-based technique to measure the dispersion of fibers.

The experimental setup of FWM-based technique is described in Figure 3.17(a). Two CW lasers are used. They are refered as the pump waves 1 and 2 at wavelengths λ_1 and λ_2, respectively. They are coupled by a 3-dB coupler before being injected into the FUT. During propagation along the fiber, due to the nonlinearity two new idler waves appear at λ_3 and λ_4 as seen in Figure 3.17(b) (mentioned in Section 1.4.1.4). At the output of the FUT, the power of one FWM idler wave is measured by an optical spectrum analyser. We use the definition of FWM efficiency, which is defined in Section 1.4.1.4, as the ratio between the idler peak power $P_3(L)$ at the output of the FUT and the input peak power $P_2(0)$ of pump 2, $\eta = P_3(L)/P_2(0)$.

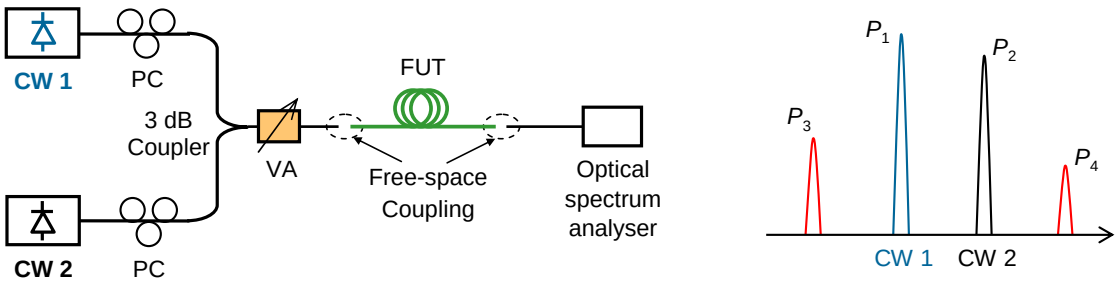

Figure 3.17: Experimental setup of FWM-based fiber dispersion measurement (a), and the spectrum at the output of the FUT (b).

The wavelength of pump 1 is fixed at λ_1, while wavelength of pump 2 λ_2 is varied. Figure 3.18 illustrates the efficiency for different wavelength detunings $\Delta\lambda$ between the two pumps. As mentioned in Section 1.4.1.4, the zero-efficiency detuning $\Delta\lambda_0$ is the first point for which the FWM efficiency is minimum. From this point, the value of dispersion is easily

figured out. The dispersion D of the fiber can be obtained from the measured value of the zero-efficiency detuning $\Delta\lambda_0$ by the relation that can be re-written from Eq. (1-90):

$$|D| = \frac{\lambda_0^2}{cL\Delta\lambda_0^2}. \tag{3-12}$$

The example in Figure 3.18 is measurement of dispersion for the chalcogenide fiber, whose dispersion was estimated by SPM-based technique. The chalcogenide with a length $L = 1$ m, measurement wavelength around 1550 nm, and a measured $\Delta\lambda_0 = 4$ nm gives a dispersion $D = -500$ ps/km/nm. This confirms the value of dispersion which was previously estimated by SPM-based technique. For nonlinear characterization of the chalcogenide fibers, we use both the SPM-based technique and the FWM-based technique.

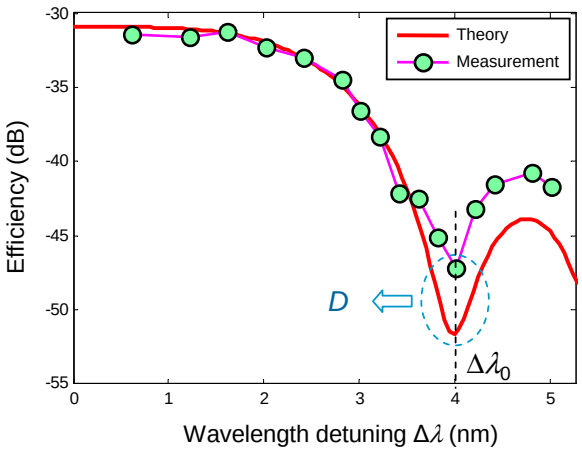

Figure 3.18: An example of simulation and measured FWM efficiencies.

3.4 Characterization of chalcogenide microstructured fibers

In Section 3.3 above, methods and techniques that are used to characterize chalcogenide MOFs have been described. The present section is now devoted to presenting some of chalcogenide MOFs with their characteristics. These chalcogenide MOFs are fabricated by the casting method (mentioned in Section 3.2) by PERFOS and EVC. Foton laboratory is in charge of fiber characterization. From 2010, our collaboration has yielded four chalcogenide fibers with different structures and with three compositions of glasses: $As_{38}Se_{62}$, $Ge_{11.5}As_{24}Se_{64.5}$, and $Ge_{10}As_{22}Se_{68}$. For simpler, henceforth, these compositions will be named AsSe or GeAsSe. The AsSe MOFs fabricated in 2010 and in 2011 both are suspended-core microstructures but with different core diameters. In 2011, a GeAsSe fiber with a hexagonal 3-rings structure was fabricated. The GeAsSe MOF fabricated in 2012 has also a hexagonal 3-rings structure but with a reduction of the core diameter. These four fibers will be characterized and presented in the next sections.

3.4.1 AsSe suspended-core fiber - 2010

In the year 2009, in the framework of a collaboration between PERFOS, EVC and Foton, a highly nonlinear As_2Se_3 MOF with a structure of 3-hexagonal-rings was presented [21]. The nonlinear coefficient γ was 15000 $W^{-1}km^{-1}$. However, the attenuation loss was high (around 15 dB/m), due to the many disadvantages of the "stack-and-draw" fabrication method concerning the optical qualities of microstructured optical fibers. The alternative fabrication technique (casting method) [112] allows us to overcome the problems of the "stack-and-draw" technique and thus reduce the attenuation loss of fibers. It also allows the development of various fiber designs. Typically, the suspended-core structure made of three holes around a solid core is a solution to reduce the core diameter and losses of fiber. The nonlinear coefficient γ is hence enhanced.

This section presents a chalcogenide suspended-core fiber fabricated by the casting method in 2010. The composition of the glass is $As_{38}Se_{62}$. A high purity AsSe glass is heated to around 450°C and flowed into a silica mould made of silica capillaries. These are then removed at ambient temperature by applying a hydrofluoric solution. The chalcogenide fiber has a suspended-core structure which contains 3 holes around a solid core. The fiber and its cross-section image is shown in Figure 3.19. The core diameter ϕ_C of the fiber, defined in Figure 3.19, is as small as 2 μm. The length of the fiber is 3 m. This fiber will henceforth be named the *AsSe2010* fiber.

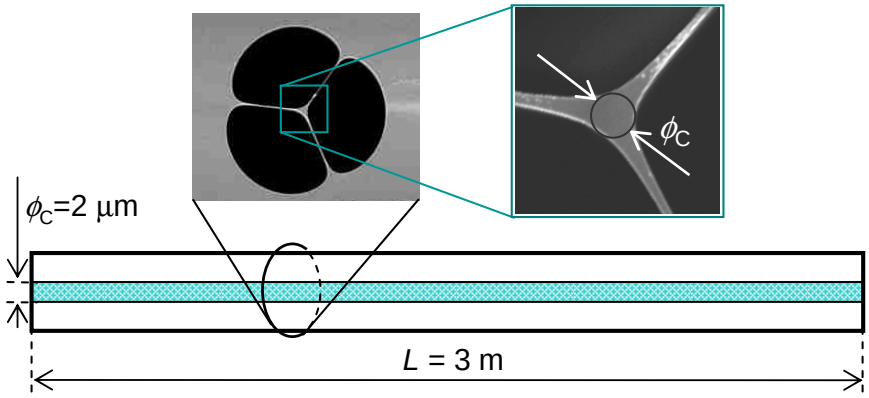

Figure 3.19: The suspended-core AsSe2010 fiber and its cross-section image.

3.4.1.1 Linear characterizations

Effective mode area measurement

The knowledge of the effective mode area is important because it allows us to choose the optical fibers for coupling. Firstly, near field images of the intensity distribution at the output of the AsSe2010 fiber are recorded on a camera using a high-numerical-aperture microscope objective. In this experiment, the coupling is performed using a standard SMF. Figure 3.20 shows a near-field image of the AsSe2010 fiber.

Figure 3.20: Near-field image of intensity distribution of the AsSe2010 fiber.

Since the fiber core diameter is small (around 2 μm), the far field method is required to measure the effective mode area and the mode diameter of the beam exactly. A standard multimode fiber (MMF) (62.5/125) is used to detect the signal out of the chalcogenide fiber. It rotates around the chalcogenide fiber at a fixed long distance from the output end of the chalcogenide fiber from $-80°$ to $80°$. The inverse Hankel transform is used to calculate the mode effective area from far-field distribution data as mentioned in Section 3.3.2. Figure 3.21 presents the far-field distribution measurement of the chalcogenide fiber. The far-field distribution is shown in Figure 3.21(a) and its near-field distribution transform is given in Figure 3.21(b). This near-field distribution gives the value of the effective mode area. The A_{eff} of the AsSe2010 fiber is measured to be 1.7 ± 0.1 μm^2. We believe that this is one of the smallest values reported in chalcogenide MOFs so far. This value is equivalent to a value of MFD of 1.4 μm if we assume a Gaussian shape.

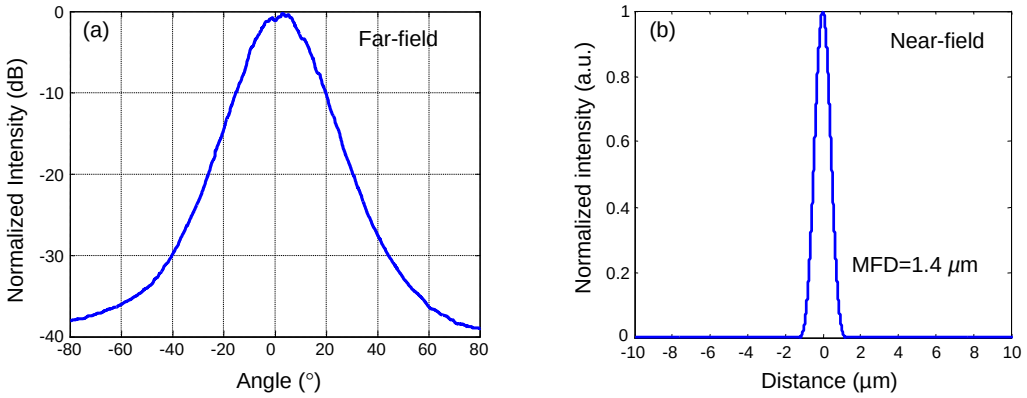

Figure 3.21: (a) far-field distribution measurement of AsSe2010 fiber, and (b) its near-field distribution by inverse Hankel transform.

Fiber loss and coupling loss

The fiber losses are measured by the cut-back technique at the wavelength 1550 nm (Section 3.3.1). As mentioned above, this technique is one of the most suitable techniques

to measure fiber losses for such a short length of fiber (several meters). The fiber that is used for coupling light into the chalcogenide fiber is a high-numerical-aperture (HNA) fiber with a MFD of 3.2 μm. The power P_{in} is measured at the output of the HNA fiber to be 8.6 dBm.

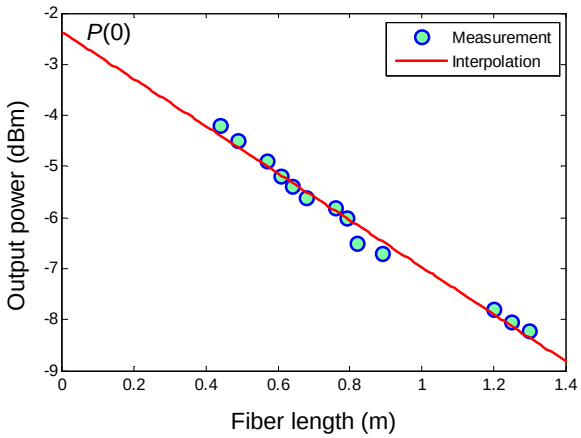

Figure 3.22: Fiber loss measurement using cut-back technique

The power at the output of the AsSe2010 fiber is measured as a function of the length of the fiber. The initial fiber with a length of 1.3 m is cut several times down to 0.44 m (Figure 3.22). From the measured data, the fiber loss is calculated by a linear interpolation. The linear fit in Figure 3.22 gives the value of the fiber losses of 4.6 dB/m. It shows a large improvement compared to that of the previous AsSe fiber (15 dB/m) fabricated in 2009 by the "stack-and-draw" technique [21].

By using the cut-back method, the output power $P(0)$ at the length of zero ($L = 0$) can be interpolated. In this measurement, $P(0)$ is deduced to be -2.4 dBm. As mentioned in Section 3.3.1, we can obtain the coupling loss α_c at the input of the chalcogenide fiber. α_c is calculated to be 10 dB. This value also includes the Fresnel reflection losses due to free-space coupling and difference in refractive indices between two fibers. Indeed, when a light passes normally from one medium with the refractive index n_1 to another medium with the refractive index n_2, the Fresnel reflection is given by

$$R_F = \frac{(n_1 - n_2)^2}{(n_1 + n_2)^2}. \tag{3-13}$$

In this case, the refractive index of air n_1 is approximately 1, and the refractive index of the chalcogenide AsSe material n_2 is 2.815. The loss of Fresnel reflection is calculated to be 1.1 dB.

Fiber guiding

The number of modes propagating in the AsSe2010 fiber is investigated by using the modal analysis technique mentioned in section 3.3.3. The near field images are magnified by a 80× microscope objective with a tunable continuous-wave laser source. The wavelength

sweeps from 1545 nm to 1555.24 nm with 1024 steps and the spectral intensity due to interference between different modes is then retrieved. The number of modes is extracted by investigating peaks of the Fourier transformation of the measured optical spectra. The length of the fiber is 1.5 m.

Figure 3.23(a) describes the Fourier transformation of data acquisition. The fiber is found to be multimode as several peaks appears as in Figure 3.23(a). Some example of modes are shown in Figure 3.23(b). This result is in accordance with the simulation results (Figure 3.23(c)), which has been performed by L. Provino from PERFOS.

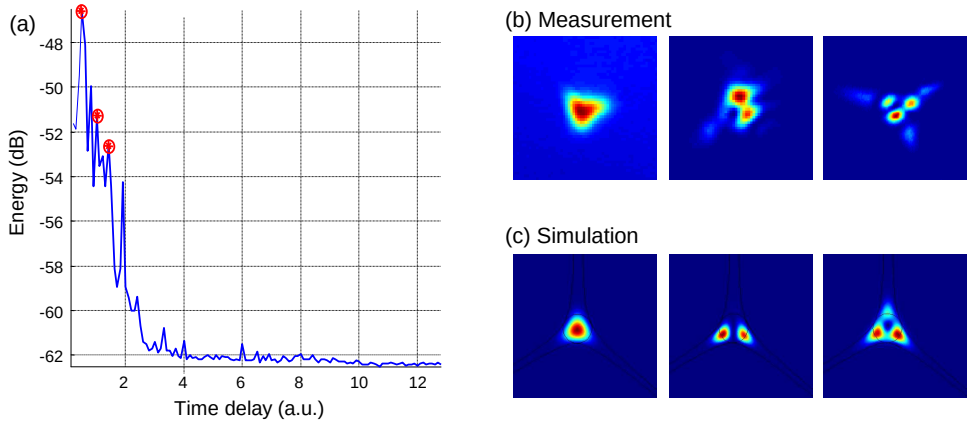

Figure 3.23: The Fourier transformation of data acquisition (a), and examples of modes of the AsSe2010 fiber: (b) measurement and (c) simulation.

3.4.1.2 Nonlinear characterizations

Self-phase modulation

Self-phase modulation (SPM) is an interesting manifestation of the intensity dependence of the refractive index in nonlinear fibers. SPM leads to spectral broadening of optical pulses. Because the broadened spectrum of an optical pulse propagating in the fiber is the combined effect of self-phase modulation (SPM) and group velocity dispersion (GVD), the nonlinear coefficient γ and the dispersion D can be evaluated by comparing broadened spectra between simulation and experiment as mentioned in Section 3.3. The SPM-based experimental setup is shown in Figure 3.24.

The incident signal is a train of Gaussian pulses of 8 ps produced by a commercially available mode-locked erbium-doped fiber laser (MLFL) operating at 1550 nm. The MLFL used here works at a low repetition rate of 19.3 MHz to boost the pulsed peak power. The signal is passed through a polarization controller (PC) to ensure that there is not any unexpected polarization effects during the nonlinear propagation. The length of the AsSe fiber used in the SPM experiment is 63 cm. High-numerical-aperture (HNA) fibers with a mode diameter of 3.2 μm are used to couple signal into and out of the AsSe fiber. SPM spectral broadening is recorded by use of an optical spectrum analyser (OSA).

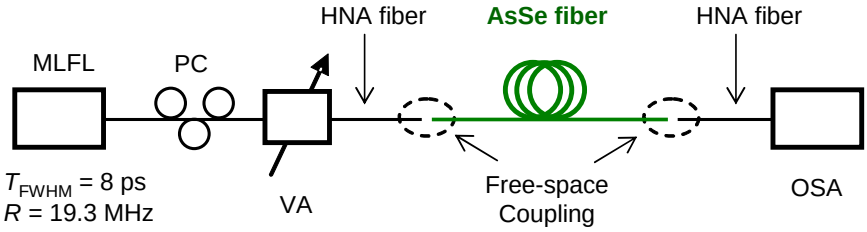

Figure 3.24: Experimental setup of SPM-based measurement. MLFL: mode-locked fiber laser. VA: variable optical attenuator. PC: polarization controller. OSA: optical spectrum analyser. HNA: High numerical aperture.

The input power is varied by adjusting the variable optical attenuator (VA). Typical SPM behaviours with spectral broadening accompanied by an oscillatory structure are observed at different input peak powers P_0 (Figure 3.25). A good agreement between simulated and experimental broadening spectra is obtained with a value of γ of 31 000 $\mathrm{W^{-1}km^{-1}}$ and a dispersion D of -820 ps/km/nm. We see from Figure 3.25 that the simulated and the experimental spectra are somewhat different. This may be caused by the imperfect Gaussian shape and initial chirp of input pulses. At the time of the measurement, to the best of my knowledge, the value of γ of 31 000 $\mathrm{W^{-1}km^{-1}}$ was the highest nonlinear coefficient reported in microstructured optical fibers. The FOM_{max} of the AsSe2010 fiber is 29.3 $\mathrm{W^{-1}}$. Knowing the effective mode area of fiber and using Eq. (3-1), the corresponding nonlinear refractive index n_2 is calculated to be 1.3×10^{-17} $\mathrm{m^2/W}$. The nonlinearity of the AsSe glass is 500 times greater than that of silica ($n_2 = 2.6 \times 10^{-20}$ $\mathrm{m^2/W}$).

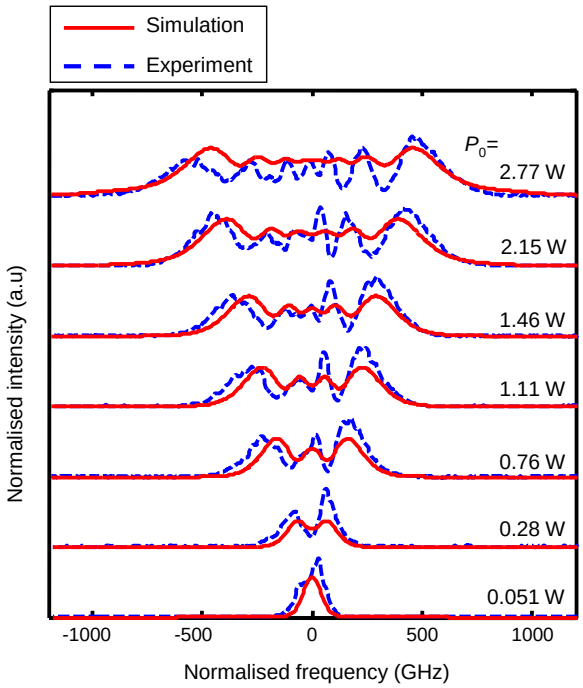

Figure 3.25: SPM-induced spectra broadening. P_0: input peak power.

Four-wave mixing

This section considers the four-wave mixing (FWM) effect in the AsSe2010 fiber. FWM resulting from the interaction between two pumps is considered [47]. In some particular cases, the two pumps can be defined as a pump and a signal depending on the type of applications [162]. Utilizing the FWM effects, all-optical signal processing such as regeneration [89], wavelength conversion [163, 164], time-division demultiplexing [165, 129] can be carried out. Using the AsSe2010 fiber, FWM experiment with a 10 GHz pump and a CW pump is implemented. Based on the FWM experiment, dispersion of the fiber is also measured. The experimental setup of FWM characterization is illustrated in Figure 3.26.

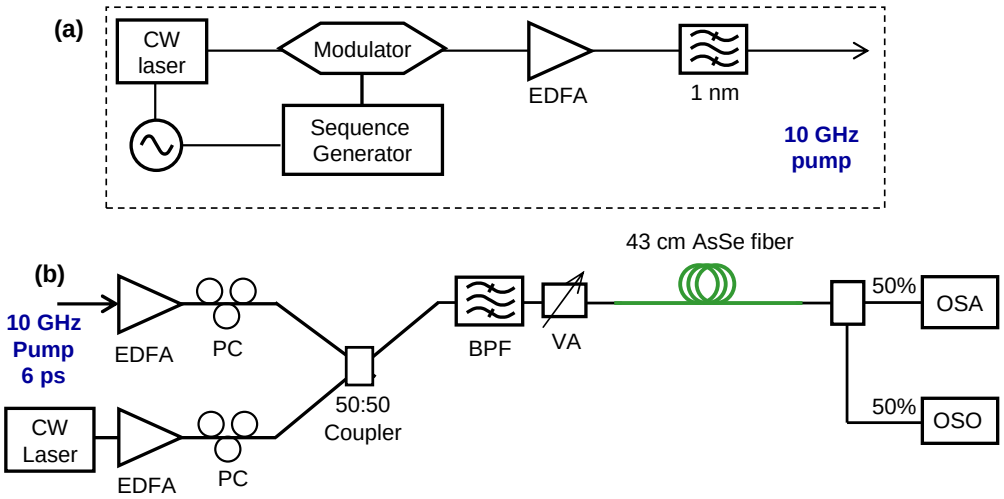

Figure 3.26: (a) Setup of 10 GHz generation and (b) experimental setup of FWM characterization. MZI: modulation March-Zender. PC: polarization controller. EDFA: erbium-doped fiber amplifier. BPF: band-pass filter. OSA: Optical spectral analyzer. OSO: optical sampling oscilloscope.

Figure 3.26(a) describes the setup of the 10 GHz pump generation. The 10 GHz optical clock signal is generated by a Mach-Zehnder modulator from a CW laser and a 10 GHz electrical clock. The optical clock signal has a pulse width of 1.5 ps with a time-bandwidth-product (TBP) of 0.35 centered at a wavelength of 1553 nm. This pulsed pump is then amplified and filtered by using an erbium-doped fiber amplifier (EDFA) and a bandwidth optical filter (BPF) of 3 nm.

Figure 3.26(b) illustrates the experimental setup of the FWM characterization of the AsSe2010 fiber. The second CW pump source is a tunable laser. The continuous and pulsed pumps are then amplified with EDFAs and combined with a coupler with polarization states aligned via polarization controllers. A 5 nm band-pass filter is used at the input of the AsSe fiber to eliminate the noise caused by the EDFAs for the FWM viewing. At the output of the 5 nm filter, the pump pulsewidth is 8 ps and its average power is 7.7 mW. The average power of the CW pump is set to 14 mW. To couple signals into and out of the AsSe fiber, Gradhyp microlensed fibers [166] with a mode field diameter of 3 μm are used. However,

the coupling loss suffered at each end of the fiber is around 10 dB (including 1.1 dB losses of Fresnel reflection) due to the small mode field diameter of 1.4 μm of the AsSe MOF. It is similar to the case of using HNA fiber for coupling.

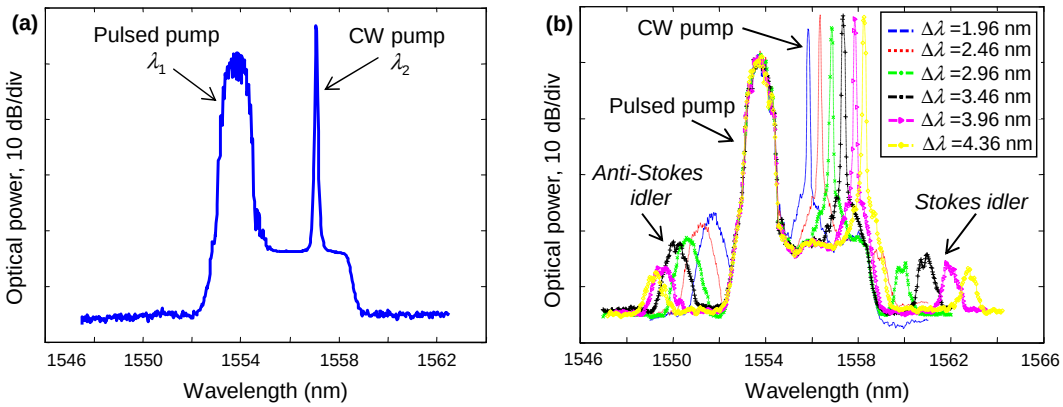

Figure 3.27: (a) Input spectra of CW and pulsed pumps and (b) output spectra of the chalcogenide fiber.

An example of the input optical spectrum and optical spectra at the output of the fiber at different wavelengths of the CW pump are shown in Figure 3.27. At the output of the AsSe fiber, FWM-waves appear as symmetrical pairs as a function of the wavelength detuning $\Delta\lambda = \lambda_2 - \lambda_1$ (see in Figure 3.27(b)). It means that the two pump waves at the corresponding frequencies ν_1 and ν_2 create two sidebands located symmetrically at frequencies ν_3 and ν_4 such that $\nu_3 + \nu_4 = \nu_1 + \nu_2$ [47].

Theoretically, we recall here the formula used to calculate the peak power of the anti-Stokes idler from Eq (1-86):

$$P_3 = \eta_\phi \gamma^2 P_1^2 P_2 \exp(-\alpha L) \left\{ \frac{[1 - \exp(-\alpha L)]^2}{\alpha^2} \right\}, \tag{3-14}$$

where γ is the nonlinear coefficient, P_1 and P_2 are the input peak powers for the pulsed and CW pumps respectively, L is the fiber length, α is the fiber loss, and n_ϕ is the phase-matching efficiency which is a function of the phase mismatch vector Δk and given in Eq. (1-85).

In the experiment, the anti-Stokes band located next to the pulsed pump is preferable to study since the peak power of the pulse is much larger than the average power of the CW one. A 3 nm filter is located at the output of the AsSe fiber to filter the anti-Stokes idler. FWM temporal traces are investigated by using an optical sampling oscilloscope (OSO) with a time resolution of 1 ps. Time-resolved traces of the FWM anti-Stokes idler for 8 ps input pulses are shown in Figure 3.28. When the CW pump is OFF, the FWM idler is not present (light black trace). As both pumps are ON, the FWM idler appears (heavy black trace) with a pulsewidth of 6.2 ps. It can be understood from Eq. (3-14) that the peak power $P_3(L)$ of the anti-Stokes idler is proportional to the square of the input pulsed peak power $P_1(0)$.

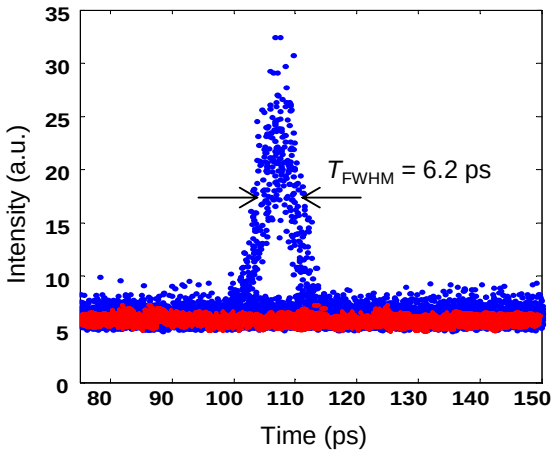

Figure 3.28: Time-resolved trace of the FWM idler for a 10 GHz with 8 ps input pulses.

This leads to a reduction of the pulse duration of the anti-Stokes idler by a factor $\sqrt{2}$. The input pulse duration is 8 ps, the anti-Stokes idler pulse duration theoretically calculated to be 5.7 ps, which is close to the experimental value of 6.2 ps.

To investigate the FWM conversion efficiency, we use the definition of the FWM efficiency given in Section 1.4.1.4, as the ratio between the collected peak power $P_3(L)$ of the idler wave at the output of the AsSe fiber and the CW power $P_2(0)$ at the input of the AsSe fiber (Section 1.4.1.4):

$$\eta = P_3(L)/P_2(0), \tag{3-15}$$

To maintain phase-matching, the length of the fiber should be shorter than the coherence length, L_{coh}. As mentioned in Section 1.4.1.4, the coherence length can be given by

$$L_{coh} = \frac{2\pi}{|\beta_2|\Delta\omega^2}, \tag{3-16}$$

where β_2 is the second-order dispersion, and $\Delta\omega$ is the frequency detuning $\Delta\omega = \omega_1 - \omega_2$. In the FWM experiment, the length of the AsSe2010 fiber is 43 cm. It is suitable for efficient FWM generation since the coherence length of the fiber given by Eq. (3-16) is 61 cm for a dispersion D of -820 ps/km/nm (calculated by SPM-based technique above) and a detuning of $\Delta\lambda = 4$ nm.

Figure 3.29 presents the experimental and theoretical FWM efficiencies with respect to wavelength detuning $\Delta\lambda$. The theoretical efficiency is calculated by using Eqs. (3-14) and (3-15) with values of the nonlinear coefficient γ of 31000 $W^{-1}km^{-1}$ and the dispersion D of -820 ps/km/nm estimated above by SPM-technique.

As mentioned in Section 3.3.5, from the zero-efficiency detuning $\Delta\lambda_0 = 4.8$ nm, the value of the dispersion $D = -820$ ps/km/nm is easily extracted by using Eq. (3-12). A good agreement between the calculated and measured FWM efficiencies is shown in Figure 3.29

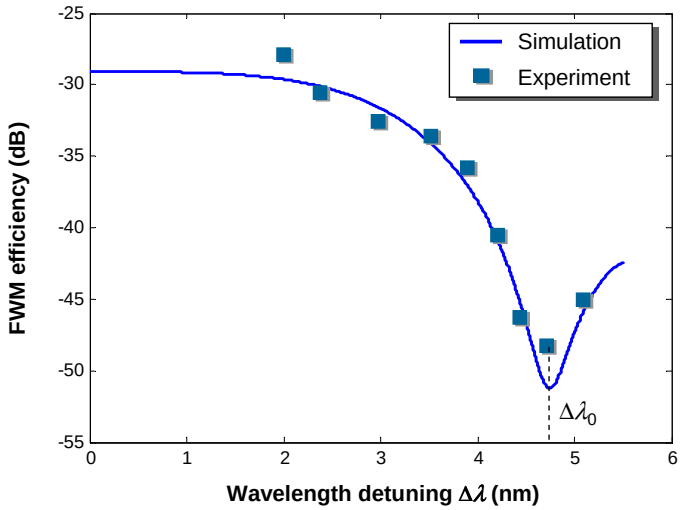

Figure 3.29: FWM efficiency with respect to the wavelength detuning $\Delta\lambda$.

confirming the value of the nonlinearity and the dispersion of the AsSe2010 fiber. The FWM characterization shows a FWM efficiency of -27 dB with about 20 mW of total average power (including 10.2 dBm of pulsed pump and 9.8 dBm of CW pump) at the fiber input and a detuning $\Delta\lambda$ of 1.96 nm. This is much better compared to the FWM efficiency of -40 dB with 60 mW average input power obtained for photonic crystal waveguides [167].

3.4.1.3 Conclusion

With the aim of improving the nonlinear coefficient of MOFs, for the first time, PERFOS and EVC succeeded in fabricating a suspended-core chalcogenide fiber. The core diameter of the AsSe2010 fiber is as small as 2 μm leading to a record value of the nonlinear coefficient γ of 31000 $W^{-1}km^{-1}$ (by the year 2010, the nonlinear coefficient of MOF was recorded with a γ of 15000 $W^{-1}km^{-1}$ [21]). Nevertheless, high antenuation losses α of 4.6 dB/m and coupling losses (10 dB per facet) lead to high input powers. This limits the use of the fiber for telecommunication systems. In addition, a high dispersion D of -820 ps/km/nm makes a wavelength conversion range $\Delta\lambda_c$ of only 3 nm. Furthermore, the fiber has been experimentally demonstrated to be a multimode fiber. This restricts feasibilities for high-bit-rate applications. The fiber characterizations was presented in *the ECOC conference* in 2010 in Torino, Italy [168] and the nonlinear demonstration was reported in *IEEE Photonics Technology Letters* Vol. 22 (24) in 2010 [169]. Table 3.1 summaries the characteristics and parameters of the AsSe2010 fiber.

Table 3.1: Characterization of the AsSe2010 MOF.

Name	γ ($W^{-1}km^{-1}$)	α (dB/m)	D (ps/km/nm)	FOM_{max} (W^{-1})	Propagation	Publications
AsSe2010	31000	4.6	-820	29.3	multi-mode	ECOC2010 [168], IEEE PTL [169]

To use this type of MOF for telecommunications applications with a power compatibility, one need to think about firstly a reduction of the fiber losses as well as coupling losses. Besides, the dispersion of fiber also need to be decreased in order to increase the wavelength conversion range $\Delta\lambda_c$.

3.4.2 AsSe suspended-core fiber - 2011

In the previous section, our first chalcogenide AsSe suspended-core fiber, AsSe2010, with the Kerr nonlinearity of 31000 $W^{-1}km^{-1}$ was presented. The AsSe2010 fiber suffers high fiber losses and high coupling losses. These limitations make the fiber difficult for implementing applications. By improving the quality of chalcogenide AsSe glass with the expectation of reducing the fiber loss, a new suspended-core fiber was fabricated early in 2011 (named the *AsSe2011* fiber). The composition of the chalcogenide glass is $As_{38}Se_{62}$. During the fabrication process, the core diameter of the AsSe2011 fiber was drawn as small as possible to enhance the nonlinear coefficient. For the first time, the core diameter of our fiber was drawn as small as 1.13 μm with an external diameter ϕ_F of 62 μm. The fiber also contains 3 holes around a solid core as seen on the cross-section image of Figure 3.30.

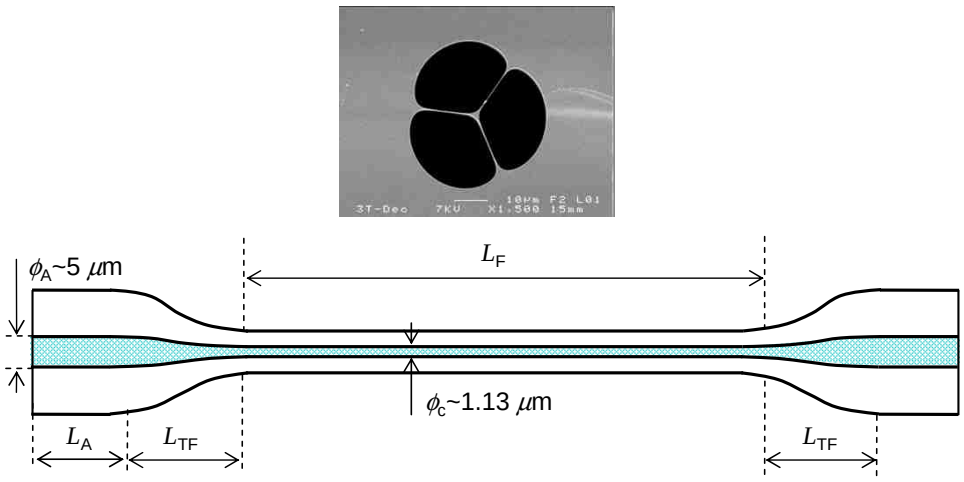

Figure 3.30: Suspended-core chalcogenide fiber with mode adaptation ends. Where L_F, L_A, L_{TF}: length of fiber, length of adaptation mode sections and length of taper sections, respectively; ϕ_C, ϕ_A: core diameters of fiber and adaptation mode sections, respectively.

The core size of the fiber is reduced to boost the nonlinearity. However, it makes it difficult to inject signals into and out of a such a very small core diameter. In order to limit the coupling losses, the fiber is preserved with large input and output ends during the fabrication process. Mode adaptation sections at each end of the 1 m long fiber is shown in Figure 3.30. The length of mode adaptation sections L_A are 5 cm and the length of the taper L_{TF} is around 10 cm. For both mode-adapted facets of the fiber, the core diameter and the external diameter are 5 μm and 280 μm, respectively.

3.4.2.1 Linear characterizations

Effective mode area measurement

To characterize the effective mode area of this fiber, the mode adaptation taper at the output end of the fiber is cut out. There remains now only the mode adaptation section at the input for coupling and the length of the fiber is 1 m. In the near-field measurement, a microscope objective 100× with a high NA of 0.95 is used to magnify the image at the fiber output facet. Figure 3.31 shows the near-field distribution of the fiber. A microlensed fiber [166] with a mode field diameter of 5.2 μm is used to couple the signal into the AsSe fiber.

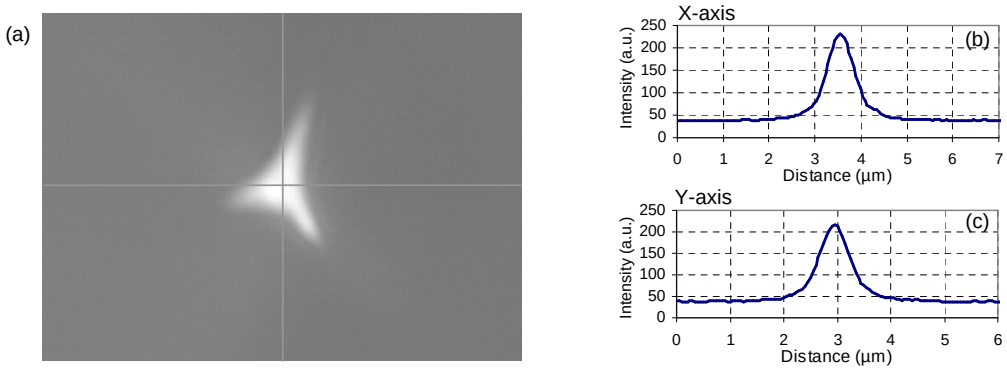

Figure 3.31: Near-field distribution of the AsSe2011 fiber: (a) near-field image, (b) the horizontal and (c) the vertical distributions.

The near-field intensity profiles in the horizontal and vertical directions of the AsSe2011 fiber are illustrated in Figure 3.31. The intensity distribution is nearly Gaussian for both horizontal (X-axis) and vertical (Y-axis) directions as seen in Figure 3.31. The near-field measurement gives a MFD of the fiber around 1.2 μm.

The far-field measurement is also implemented to confirm the value of the MFD measured by the near-field method. Figure 3.32(a) illustrates the far-field profiles and Figure 3.32(b)

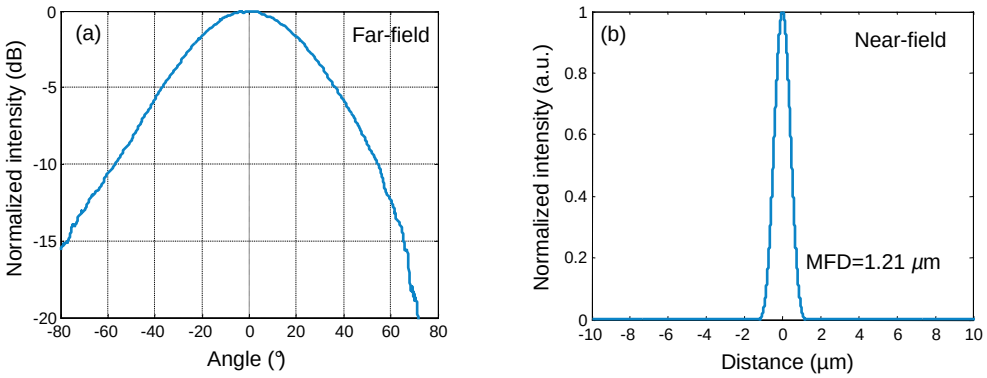

Figure 3.32: (a) Normalized far-field intensity profiles and (b) near-field profiles transformation of the AsSe2011 fiber.

presents the near-field transformation profiles from far-field of the AsSe2011 fiber. It shows an effective mode area A_{eff} is 1.15 ± 0.1 μm^2. This value is equivalent to the mode field diameter of 1.2 μm. Assuming a Gaussian shape, this is so far one of the smallest values reported in the field of microstructured optical fibers.

Fiber loss and coupling loss

To measure the fiber loss of the AsSe2011 fiber, the cut-back technique is once more used. The fiber is first truncated at the output end, while maintaining the input mode-adaptation end to couple power into the fiber. The output power is measured for different lengths of the fiber. The attenuation loss is implemented at the wavelength 1550 nm. The fiber is cut from 0.95 m down to 0.18 m. The powers are measured by a integrated sphere power meter. The experimental data are fitted as shown in Figure 3.33. The fiber losses are found to be 0.9 dB/m. This is a large improvement compared to that of the previous AsSe2010 fiber with 4.6 dB/m.

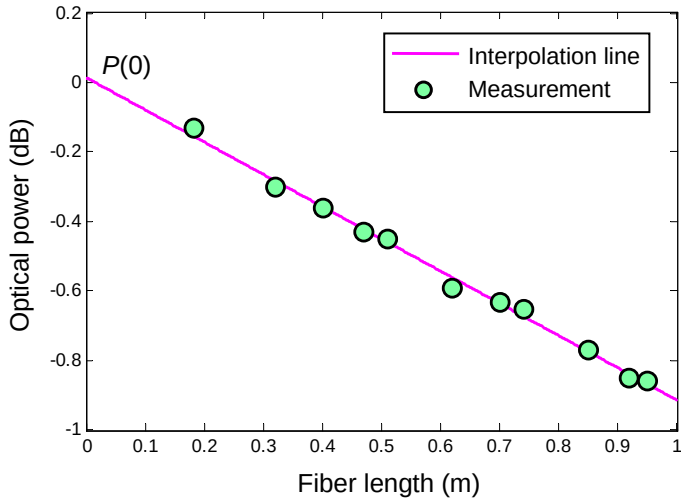

Figure 3.33: Cut-back measurement of the AsSe2011 fiber.

This value of 0.9 dB/m is the attenuation loss of the small-core section of the fiber. In order to measure the total loss of the fiber (including the coupling loss), we used the initial fiber with the two mode adaptation sections. Microlensed fibers with a mode field diameter of 5.2 μm are used to couple the signal in and out the fiber. The dimension of the mode field diameter is close to the core diameter of the input and output mode-adaptation ends of the fibers (~ 5 μm). Mode adaptation between the microlensed fiber and the AsSe2011 fiber is illustrated in Figure 3.34

The total insertion loss, between the output of the microlensed fiber used to couple signal in and the output of the AsSe2011 fiber, is measured to be 4.2 dB. As measured above, the fiber losses is 0.9 dB/m, this means that the propagation losses in a 1.26 m total length is less than 1.1 dB (0.9×1.26). Taking into account 1.1 dB of loss of Fresnel reflection

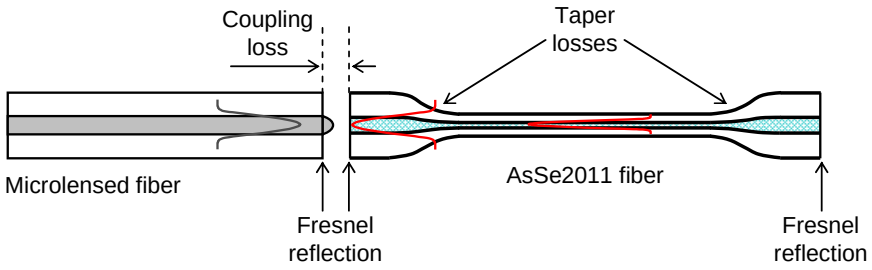

Figure 3.34: Mode adaptation between the microlensed fiber and the AsSe2011 fiber.

at the output of the AsSe fiber and 1.1 dB of propagation losses, the coupling loss at the input of the AsSe2011 fiber and the taper loss are evaluated to be 2 dB. It agrees with the measurement using the cut-back technique. Indeed, the insertion loss at the input can be obtained from the input power $P_{in} = 2$ dBm (output power of the microlensed fiber) and the output power $P(0) \sim 0$ dBm at the length $L = 0$ which is interpolated as seen in Figure 3.33. Deducting the losses due to Fresnel reflection at the input, the coupling loss is then estimated to be less than 0.9 dB (including taper losses). With the advantage of mode-adaptation tapers, the coupling losses get better compared to the non-taper chalcogenide suspended-core AsSe2010 fiber which is measured to be 10 dB.

Fiber guiding

The alternative S^2 image technique is used to implement modal analysis for the AsSe fiber-2011. A continuous-wave signal emitted by a tunable laser is injected into the AsSe fiber by a single-mode microlensed fiber with a mode field diameter of 5.2 μm. At the output of the fiber a microscope objective lens with high numerical aperture $NA = 0.95$ is used. Since the core diameter of the AsSe fiber is very small, the microscope objective with a magnification of 100× is used.

Figure 3.35 illustrates the relative energy between modes with respect to the time delay. The fundamental mode has no time delay and a normalized energy of 0 dBm. with respect to the time delay. The result shows the fiber is multimode. Although the energy of the other modes is low compared to the energy of the fundametal mode, they can degrade the signal propagating along the fiber. For further understanding of how the other modes interact with each other and how they impair the signal, a broadband source is injected into the fiber. Figure 3.36 shows the spectrum of the broadband source at the output of the AsSe fiber. The modulation that occurs on the output spectrum is the interference pattern due to the superposition of modes. The contrast of the interference pattern depends on the relative energies between modes, while the period of interference changes with the length of fiber.

In order to see if the multimode behaviour of the fiber is a problem for telecommunication applications, we have propagated different kinds of telecommunication signals through the fiber. An eye diagram is used for the qualitative analysis of signal propagation in the AsSe2011 fiber. Firstly, a 40 GHz clock signal is passed through the AsSe fiber. At the out-

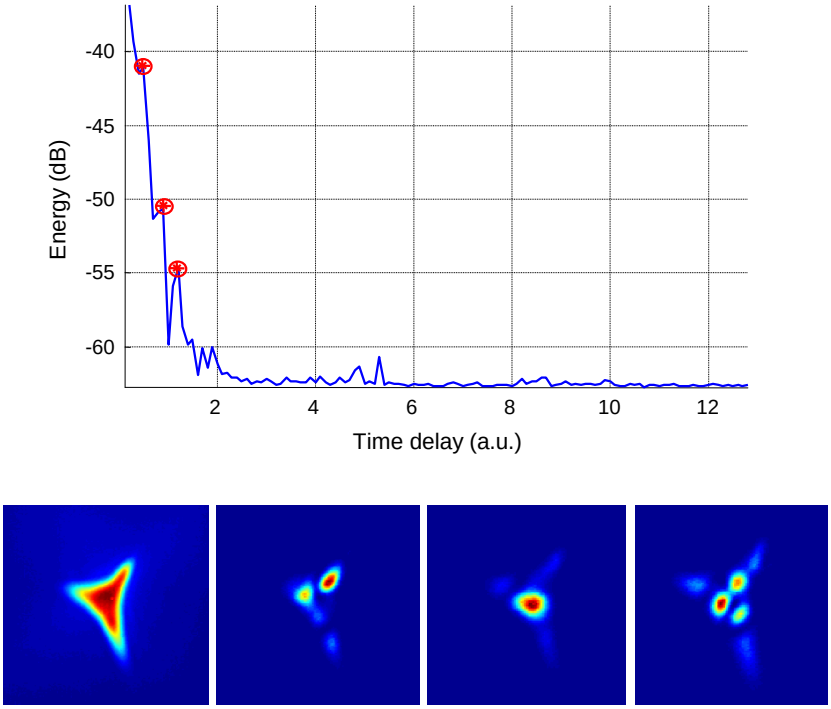

Figure 3.35: Modal analysis and modal images of the AsSe2011 fiber.

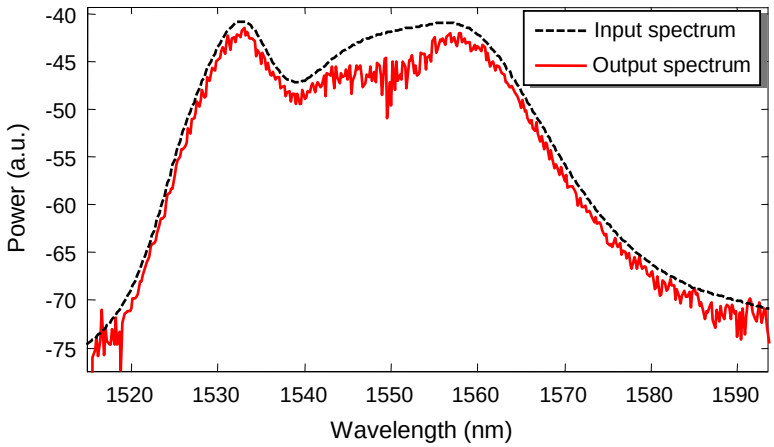

Figure 3.36: Broadband spectra at the input and at the output of the AsSe2011 fiber.

put, the eye diagram is observed on an optical sampling oscilloscope (OSO). Figure 3.37(a) shows the eye diagram of the 40 GHz clock signal at the output of the AsSe fiber. Noise appears on the eye diagram but is negligible. The eye diagram is open. A 40 Gb/s non-return-to-zero (NRZ) signal and a return-to-zero (RZ) signal with a duty-cycle of 33% are also used to verify the ability of data signal propagation in the AsSe2011 fiber. At the output, the OSO is also used to observe the eye diagram. Figure 3.37(c) illustrates the eye diagram of the output signal for the RZ case at 40 Gb/s. It is degraded and the eye diagram is almost closed. Referring to the back-to-back (B2B) case for the 40 Gb/s RZ signal with

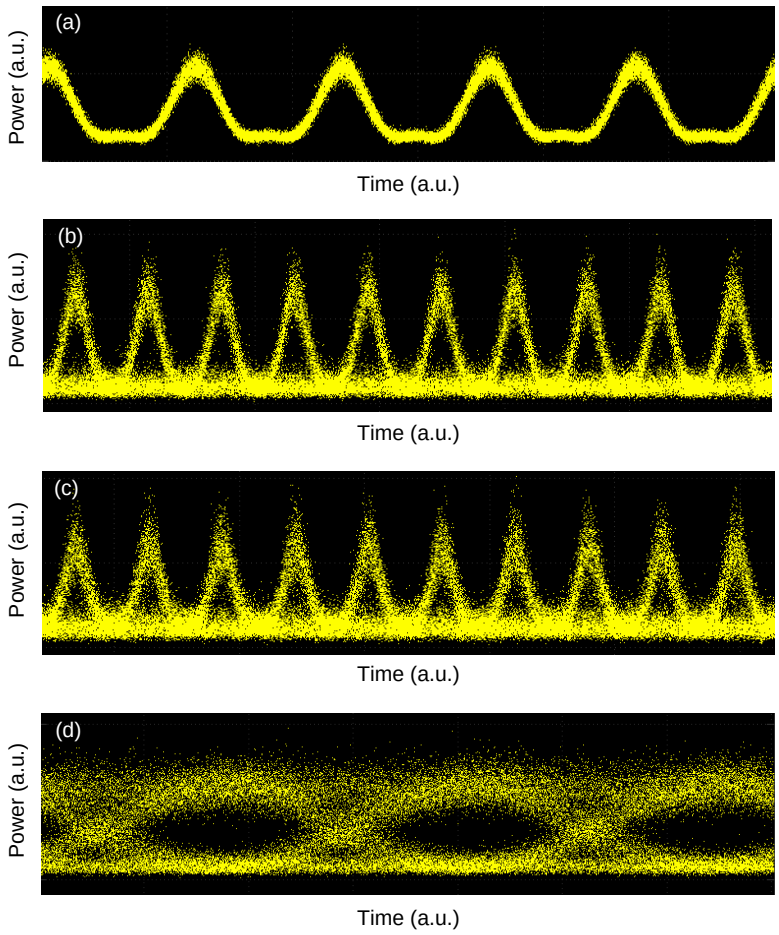

Figure 3.37: Eye diagrams of several types of optical signal passing through the AsSe2011 fiber: (a) 40 GHz clock, (b) 40 Gb/s RZ-33% (B2B), (c) 40 Gb/s RZ-33%, and (d) 40 Gb/s NRZ.

the same power reaching to OSO, the eye diagram is clearly opened (Figure 3.37(b)). The same problem occurs in the NRZ case, the eye diagram in Figure 3.37(d) is also degraded.

For several types of investigated signals, only the clock signal still preserves its quality after propagating through the AsSe fiber. The other modulated signals are considerably impaired. This can be understood if we refer to the spectra of the clock signal and the data signal. For the clock signal, the spectrum is modulated more deeply than the data signal as seen in Figure 3.38. After propagating through the fiber, the interference between modes make the spectra of the clock signal and the data signal changed. With a clock signal spectrum, the peaks may change in magnitude. This does not affect the clock signal much in the time domain. However, with a data signal spectrum, the change in magnitude affect the spectrum more dramatically and leads to impairments. This problem of multimode behaviour of the fiber should be resolved in order to use the fibers for telecommunication applications.

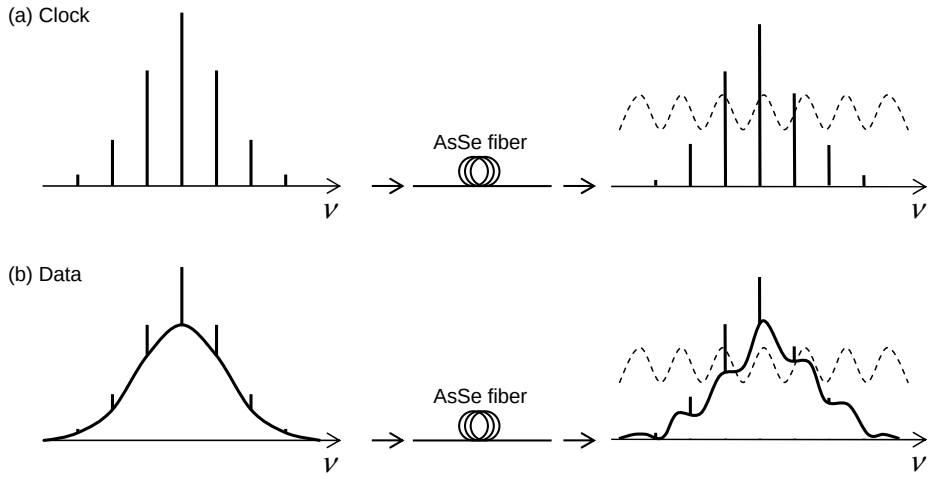

Figure 3.38: Spectra of clock and data signals at the input and output of the AsSe2011 fiber are changed due to multimode behaviour.

3.4.2.2 Nonlinear characterizations

Self-phase modulation

The experimental setup for SPM measurement is the same as the setup used for the AsSe2010 fiber (see Figure 3.15). The HNA fibers in the previous SPM experimental setup are replaced by microlensed fibers with a mode field diameter of 5.2 μm. As mentioned above, the coupling losses using microlensed fibers with the tapered suspended-core fiber is considerably reduced. This helps observing SPM broadened spectra more easily with lower needed power. The input pulsed signal generated by a MLFL at 1550 nm is a pulse train of 8 ps and a repetition rate of 19.3 MHz. An OSA is used at the output of the AsSe fiber to analyze SPM-broadening spectra for the different input powers.

Figure 3.39 illustrates the broadened SPM spectra at the output of the chalcogenide fiber with different input peak powers (line curve). The number of peaks of SPM spectra observed increases gradually when increasing the input peak power from 0.04 W to 1.47 W. Comparing to the SPM spectral broadening of the AsSe2010 fiber, we obtained here more broadened spectra. By solving the nonlinear Schrödinger equation, numerical simulations have been performed. Figure 3.39 shows the simulation and experimental data to be in good agreement with the number of SPM peaks related to input peak powers. The amplitude of spectra-broadening is somewhat different. Similar to the AsSe2010 fiber, the imperfect Gaussian and initial chirp of input pulses may cause the differences. From comparison of the simulation and experiment, a nonlinear coefficient of 46000 $W^{-1}km^{-1}$ and a dispersion D of -400 ps/km/nm are obtained. To the best of our knowledge, this is so far the highest nonlinear coefficient reported for microstructured fibers. The AsSe2011 fiber with a high nonlinear coefficient and a low loss leads to a FOM_{max} of 222 W^{-1}. We believe that this is the first fiber whose the FOM_{max} exceeds the FOM_{max} of 145 W^{-1} of the Sumitomo HNLF.

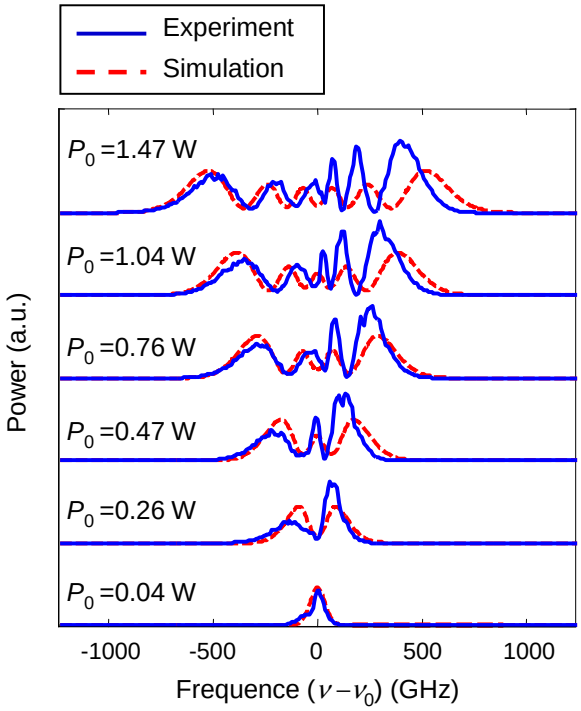

Figure 3.39: SPM-induced spectra broadening at the output of AsSe2011 fiber

Four-wave mixing

This section presents the FWM-based wavelength conversion of high-repetition-rate clock signals at 10 GHz to confirm the value of the nonlinear coefficient and the dispersion of the AsSe2011 fiber. The experimental setup for FWM characterization is shown in Figure 3.40. The in-and-out free-space coupling with the mode-adapted ends of the fiber is also performed by using microlensed fibers with a mode diameter of 5.2 μm.

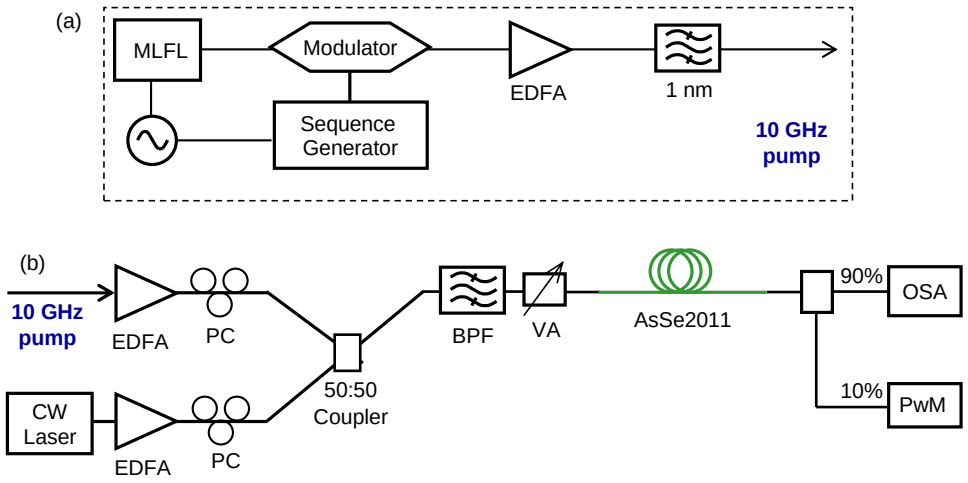

Figure 3.40: Block diagram of pulse stream generation of 10 GHz signal and setup of FWM measurement.

The generation of a 10 GHz clock signal and the setup of FWM characterization are similar to the setup used for the AsSe2010 fiber. Here, we recall the principles in Figure 3.40. A 10 GHz pump signal is generated from a mode-locked fiber laser emitting 1.5 ps pulses with a time-bandwidth product (TBP) of 0.35 centered at a wavelength of 1552.7 nm. This pump source is then amplified by an erbium-doped-fiber amplifier (EDFA) and filtered by a band-pass optical filter (BPF) of 1 nm (Figure 3.40(a)). The second pump source is a continuous-wave (CW) tunable laser amplified by a second EDFA. After amplifiers, both pulsed and CW pumps pass through polarization controllers (PC) and are combined with a 3 dB coupler. The coupled signal is then filtered by a BPF of 5 nm to reject the amplified spontaneous emission (ASE) noise of EDFAs. After the BPF, the pulse width of the 10 GHz pump source is 8.3 ps and the average power of the CW source is set to 8.1 mW.

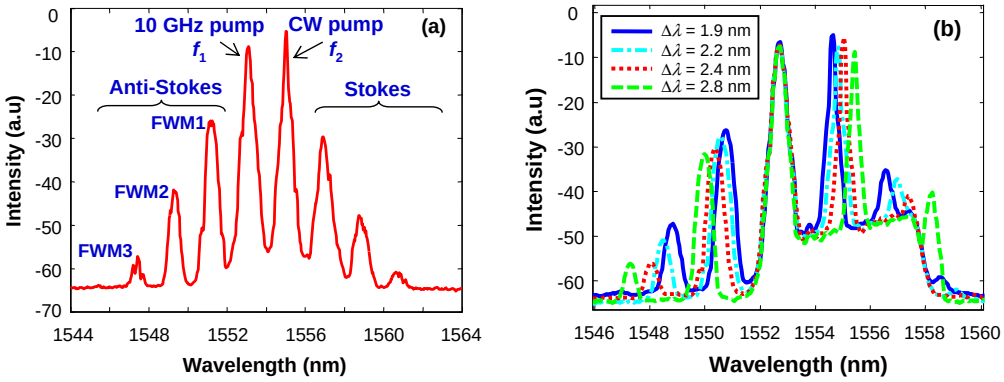

Figure 3.41: Optical spectra of 10 GHz signal at the output of the AsSe2011 fiber (a), and with various wavelengths of continuous-wave pump (b).

At the output of the AsSe2011 fiber, FWM Stokes idler and anti-Stokes idler waves appear in symmetrical pairs. The same definition of the FWM efficiency as in Section 3.4.1.2 is used to measure the conversion efficiency. It is the ratio between the collected peak power of an idler wave at the output of the fiber and the CW power at the input of the fiber. Efficiency of the first-order FWM at 10 GHz is measured to be -5.6 dB with a total average power at the input of AsSe fiber of only 17 mW and a detuning of 1.8 nm. This efficiency is much improved compared to the value of -27 dB with 20 mW of total average input power (10.2 dBm of pulsed pump and 9.8 dBm of CW pump) obtained with the previous AsSe2010 fiber (in Section 3.4.1.2). An improvement of 21 dB of the FWM efficiency is then obtained with the new AsSe2011 fiber even if the total input power is lower. Furthermore, second-order and third-order FWM waves are also measured with efficiencies of -21 dB and -37 dB respectively. Figure 3.41(a) plots the spectrum of the two input pumps and the cascade FWM waves up to the third order. The output spectra for different wavelength detuning $\Delta\lambda$ are illustrated in Figure 3.41(b).

Once again, based on FWM efficiency, the value of the nonlinear coefficient γ and the dispersion D can be measured. Figure 3.42 illustrates the FWM efficiencies of the experiment and the simulation. The first minimum point of FWM efficiency $\Delta\lambda_0 = 4.5$ nm figures out

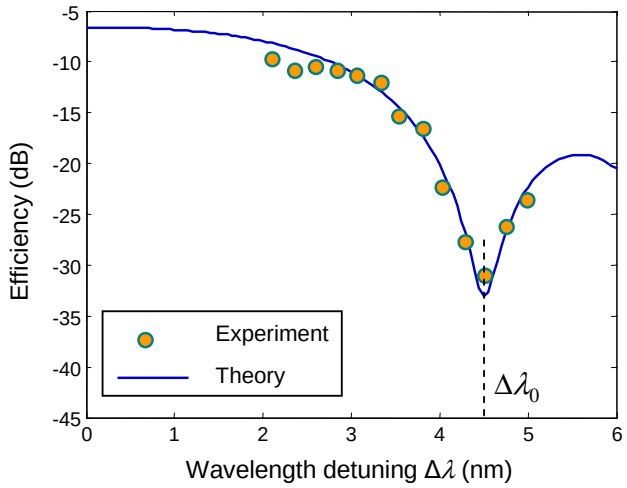

Figure 3.42: Efficiency of the first-order FWM related to wavelength detuning $\Delta\lambda$

the value of dispersion D to be -400 ps/km/nm. The simulated and measured efficiencies are in a good agreement for a nonlinear coefficient $\gamma = 46\ 000\ \mathrm{W^{-1}km^{-1}}$. These values confirm the previous evaluation by SPM experiments.

Stimulated Raman scattering

The high nonlinearity of the AsSe2011 fiber offers considerable potential to exploit nonlinear effects. By using the same setup as in SPM measurement, stimulated Raman scattering is also observed in only 50 cm of fiber. The same MLFL emits a 8 ps Gaussian pulse train at a repetition rate of 19.3 MHz at the wavelength 1547 nm. The polarization controller is adjusted to have maximum power of stimulated Raman scattering waves.

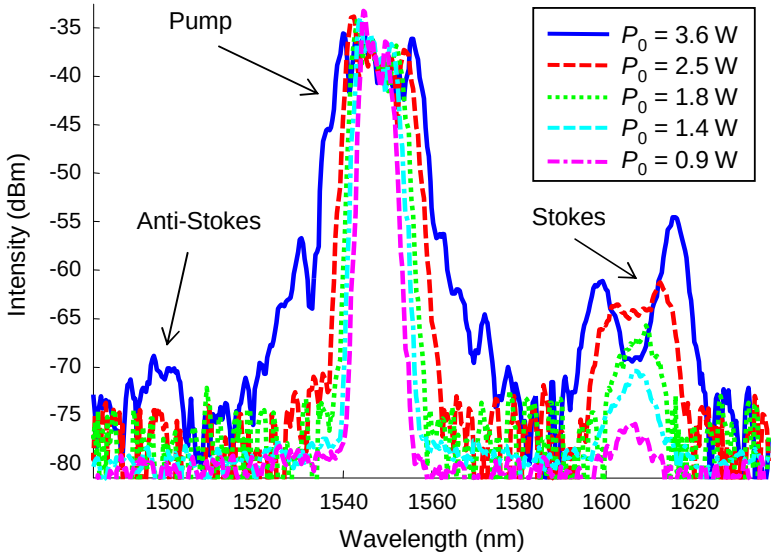

Figure 3.43: Spectra at the output of AsSe fiber for different input power with the SRS at frequency shift of 7 THz without seed signal.

At the output of the fiber, spectra are captured by an OSA for different input peak powers. The Stokes and anti-Stokes Raman spectra are observed around 1607 nm and 1493 nm, respectively (Figure 3.43). The Raman Stokes shift is measured to be 60 nm and anti-Stokes shift is 54 nm. They are equivalent to 230 cm^{-1} or 7 THz in other unit scales. This value agrees with the previous publications [55, 170]. A Raman 3-dB-bandwidth of 30 nm is measured. The Raman gain of this fiber has not been measured. However, referring to the same chalcogenide suspended-core AsSe fiber with a larger core diameter of 3.5 μm, the Raman gain coefficient is reported as 1.6×10^{-11} m/W at the pump wavelength of 1995 nm [170].

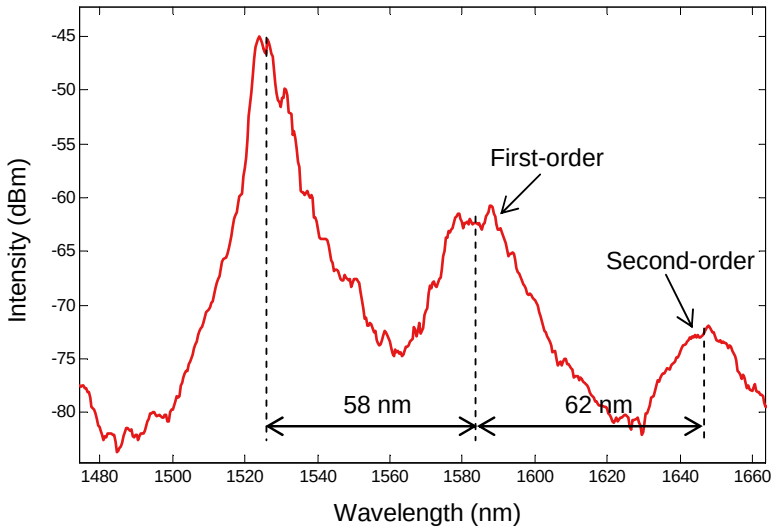

Figure 3.44: Cascaded Raman spectrum in a 1 m AsSe suspended-core fiber.

The Raman experiment was also implemented in a 1 m long AsSe suspended-core fiber. Two cascaded Raman wavelength shifts can be observed in the spectrum at the output of the fiber as shown in Figure 3.44. The peak power of the input pulses launched into the fiber is 4 W. The input pulse centered at the wavelength 1526 nm scatters the Stokes waves at the wavelengths of 1584 nm and 1646 nm respectively.

3.4.2.3 Conclusion

The suspended-core chalcogenide fiber fabricated in 2011 has led to a new record for the nonlinear coefficient for chalcogenide MOFs. This fiber with a nonlinear coefficient γ of 46000 $W^{-1}km^{-1}$ and fiber losses α of 0.9 dB/m has a FOM_{max} of 222 W^{-1}. Up to now, we think that this fiber is the first one having a FOM_{max} that exceeds the FOM_{max} of 145 W^{-1} of the silica HNLF (Sumitomo fiber [134]). The characterizations of the AsSe2011 fiber have been presented in *the ECOC conference* in 2011 [171]. The communication has been selected to be one of the eight finalists of the ECOC *Best Student Paper Award* by the technical program committee. The fiber is also reported in *Optics Express* in 2011 (OSA Optics Express, Vol. 19 (26), 2011) [70].

The AsSe2011 fiber with a suspended-core structure is still a multimode fiber. It could not preserve the quality of data signal propagating inside the fiber. The theoretical studies performed by L. Provino from PERFOS point out that one might overcome this problem by using a fiber with a microstructure of 3 or more rings of holes around the fiber core. Another limitation of the fiber is the value of dispersion of −400 ps/km/nm. It allows the wavelength conversion range $\Delta\lambda_c$ to be just about 3 nm. Table 3.2 summaries the characteristics and parameters of the AsSe2011 fiber.

Table 3.2: Characterization of the *AsSe2011* MOF fiber

Name	γ ($W^{-1}km^{-1}$)	α (dB/m)	D (ps/km/nm)	FOM_{max} (W^{-1})	Propagation	Publications
AsSe2011	46000	0.9	−400	222	multimode	ECOC2011 [171], Opt. Express [70]

3.4.3 GeAsSe microstructured fiber - 2011

3.4.3.1 Linear characterization

The suspended-core structure of chalcogenide fibers allows the reduction of the core diameter of fibers leading to ultra-high nonlinear coefficients ($\gamma = 31\,000$ $W^{-1}km^{-1}$ for the AsSe2010 fiber and $\gamma = 46\,000$ $W^{-1}km^{-1}$ for the AsSe2011 fiber). However, these fibers are multimode fibers, and optical signals are degraded after propagating through the fibers.

With the expectation of singlemode propagation, a fiber with three-rings of holes around a solid core was proposed. The composition of the chalcogenide glass is $Ge_{11.5}As_{24}Se_{64.5}$. Germanium is added to the previous composition of AsSe. The nonlinear refractive index n_2 of the GeAsSe glass is estimated to be between 400 times and 500 times greater than fused silica. The addition of Germanium slightly reduces the nonlinearity of glass, but it makes the composition more stable and more tolerant to higher powers.

As with previous fibers, in order to enhance the fiber nonlinear coefficient γ, the fiber is drawn with a core diameter as small as possible. For facilitating the coupling, the input and output ends of the fiber are still drawn with a larger core diameter ϕ_{CA} of 4.75 μm, while the main section of the fiber is drawn with a smaller core diameter. The first GeAsSe fiber with a 3-rings structure was fabricated in 2011. We will name it the *GeAsSe2011* fiber. Similar to the AsSe2011, the GeAsSe2011 fiber with the tapering process offers the advantage of a highly-nonlinear section and mode-adaptation sections to facilitate coupling. Figure 3.45 describes the GeAsSe2011 fiber with geometrical parameters and its cross-section image. The length L_F of the nonlinear section of the fiber is 1 m and its external diameter ϕ_F is 58 μm. The external diameter ϕ_{FA} of the mode-adaptation sections is 125 μm. The length L_A of the mode-adaptation sections is 10 cm, and the length L_{TF} of the tapers is around 3 cm. The total length of the fiber is then 1.26 m.

Near-field image of the GeAsSe2011 fiber is shown in Figure 3.46. A microscope objective

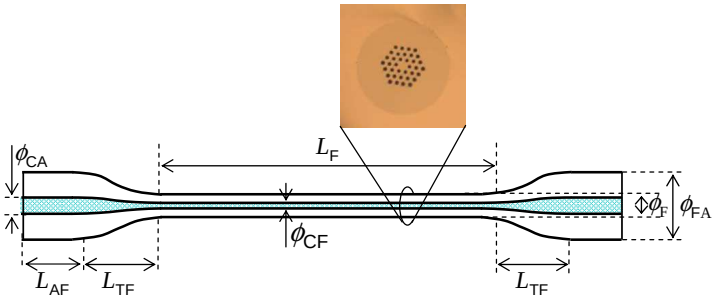

L_F (cm)	L_{TF} (cm)	L_A (cm)	ϕ_{FA} (μm)	ϕ_F (μm)	ϕ_{CA} (μm)	ϕ_{CF} (μm)
100	3	10	125	58	~4.75	~2.2

Figure 3.45: Chalcogenide GeAsSe microstructured fiber with mode-adaptation sections at two ends.

100× is used to magnify the image for digital camera monitoring. The near-field image shows a circle-shape light-spot. It is different from suspended-core fibers which have a near-field image in triangle shape (Figure 3.31).

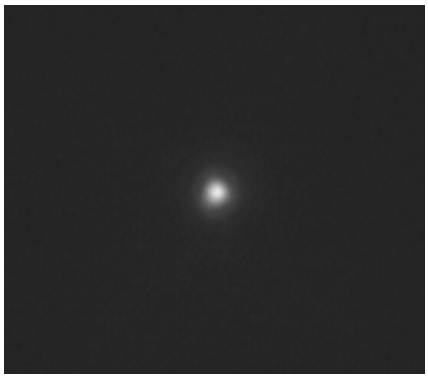

Figure 3.46: Near-field image of the GeAsSe2011 fiber.

Injection in the GeAsSe fiber is performed by using a microlensed fiber with a mode field diameter of 4.8 μm. This diameter is very close to the input and output core diameters (ϕ_{CA} = 4.75 μm) of the fiber. Two equivalent diameters allows us to limit the coupling losses. The non-destructive method (see in Section 3.3.1) is used to measure the fiber losses and coupling losses of the fiber. The ratio between the power at the output of the injected microlensed fiber and the power at the output of the chalcogenide GeAsSe fiber is measured to be 6.6 dB at 1550 nm. This value includes the losses due to Fresnel reflections of 1 dB per facet (the refractive index of the GeAsSe glass $n = 2.635$). The fiber losses is evaluated to be 2.5 dB/m. It means the propagation losses is about 3.2 dB (1.26 m×2.5 dB/m). The additional losses of 1.4 dB are probably due to coupling losses and taper losses at the input end of the GeAsSe fiber.

The measurement by using the alternative S^2 modal technique (mentioned in Sec-

tion 3.3.3) shows the GeAsSe2011 fiber is a singlemode fiber as seen in Figure 3.47. It agrees well with the simulation which was performed by L. Provino from PERFOS. The simulation points out that with a hexagonal 3-rings of holes structure, the fiber behaves as a single mode fiber. To confirm the ability of singlemode propagation, telecommunication signals at 42.7 Gb/s and 170 Gb/s were passed through the fiber and the eye diagrams were observed by OSO. Different from suspended-core fibers presented previously, the quality of both signals is preserved after propagating along the GeAsSe fiber. We will further discuss the applications of this fiber in Chapter 4.

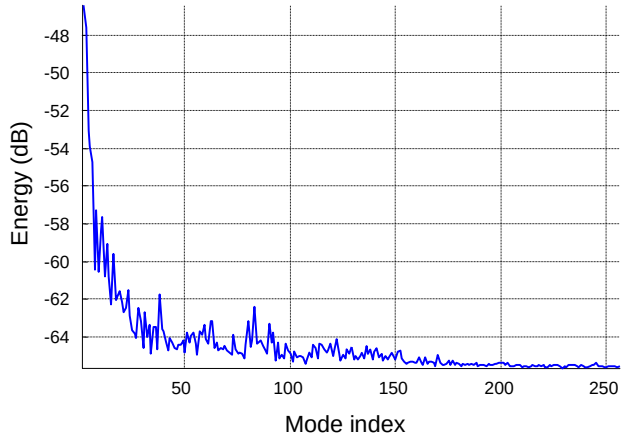

Figure 3.47: The Fourier transformation of data acquisition using the alternative S^2 method for the GeAsSe2011 fiber.

3.4.3.2 Nonlinear characterization

Measurement of γ and D

The nonlinear coefficient γ and the dispersion D are also measured by the SPM-based technique and re-confirmed by the FWM-based technique. For the SPM-based technique, SPM-induced spectra broadening has been observed by using a mode-locked laser emitting Gaussian pulses of 8 ps at 1550 nm with a repetition rate of 19.3 MHz. The experimental setup is the same as in Figure 3.24 (section 3.4.1.2), in which the HNA fibers are replaced by microlensed fibers with a mode field diameter of 4.8 μm.

Figure 3.48(a) shows an example of the experimental and the simulated spectra of SPM for an input peak power of 1.18 W. Good agreement between simulated spectrum and experimental SPM-broadened spectrum has been obtained for a nonlinear coefficient γ of 11000 $W^{-1}km^{-1}$ and a group-velocity dispersion D of -500 ps/km/nm. The nonlinear coefficient of the GeAsSe2011 fiber is not as high as the previous AsSe fibers because its core diameter is greater than core diameter of the previous ones. The nonlinear refractive index n_2 of the GeAsSe glass of 1.05×10^{-17} (about 400 times greater than silica) is also less than n_2 of the AsSe glass, which is 500 times greater than silica. The FOM_{max} of the GeAsSe2011 fiber is 19.6 W^{-1}.

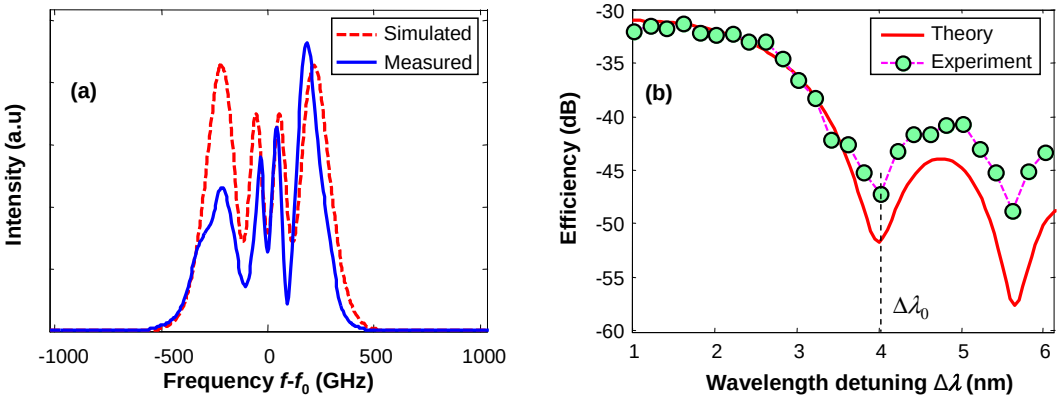

Figure 3.48: (a) SPM spectra at the output of the GeAsSe2011 fiber with the input peak power P_0 of 1.18 W, and (b) FWM efficiencies of two CW signals related to wavelength detuning $\Delta\lambda$.

The FWM-based technique is used to confirm the values of the nonlinear coefficient and the dispersion of the fiber. Two continuous-wave (CW) signals are used in the FWM characterization. Figure 3.48(b) illustrates the calculated and measured efficiencies. The total power of the two CW lasers used in experiment is 15.3 dBm, in which the power of one laser is 7.6 dBm and the power of the second is 14.6 dBm. The wavelength detuning $\Delta\lambda_0$ of 4 nm in the measurement gives the value of the dispersion $D = -500$ ps/km/nm as measured by SPM-based technique.

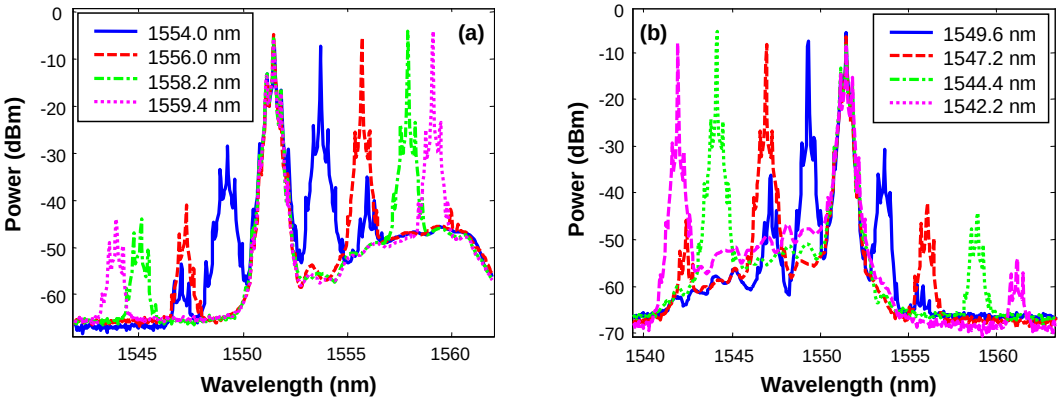

Figure 3.49: FWM spectra for different wavelength of CW waves at (a) redshifted and (b) blueshifted sideband. $\lambda_{42.7\ Gb/s} = 1551.5$ nm is fixed.

FWM characterizations using the GeAsSe2011 fiber are also implemented for a 42.7 Gb/s RZ-33% signal and a CW wave. Figure 3.49 presents the spectra at the output of GeAsSe fiber. The wavelength of the 42.7 Gb/s signal is fixed at 1551.5 nm. The CW wave is detuned from the data signal by the detuning $\Delta\lambda$. Figure 3.49(a) illustrates the FWM spectra at the output of the GeAsSe fiber for the CW pump located at the red-shift sideband, and Figure 3.49(b) is for the case of CW pump at the blue-shift sideband. The idler waves are

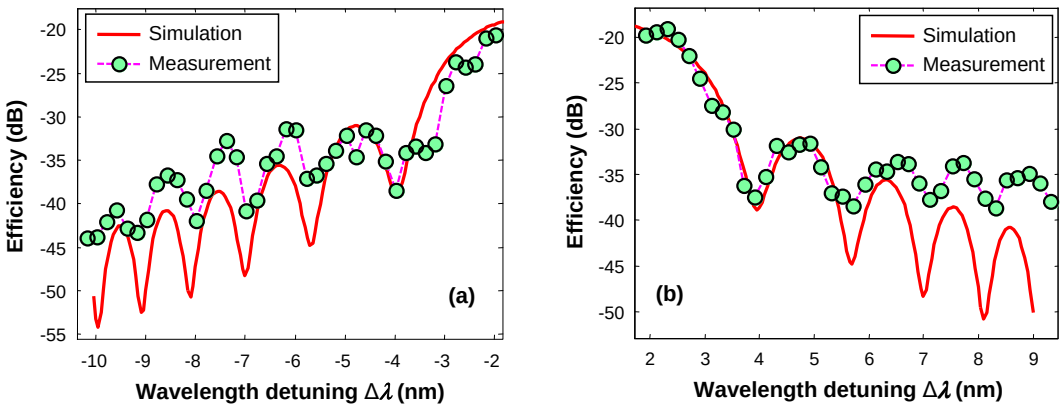

Figure 3.50: FWM efficiencies of idler in both cases of CW waves location: (a) redshifted and (b) blueshifted sideband.

observed at the opposite sideband in both cases.

Figure 3.50 presents the FWM efficiency of the idler wave with respect to wavelength detuning $\Delta\lambda$. The total average input power is 55 mW with a CW power of 21 mW. The theoretical and measured efficiencies also correspond to a nonlinear coefficient γ of 11 000 $W^{-1}km^{-1}$ and a dispersion D of -500 ps/km/nm. The wavelength detuning $\Delta\lambda$ is varied from 1.8 nm up to 9.5 nm at each side of the signal wavelength. This measurement also shows that the wavelength conversion range $\Delta\lambda_c$ of the fiber is around 3 nm for each sideband. This means that the fiber can be used to perform wavelength conversions with a conversion in wavelength of 6 nm when the CW signal is working as a pump. It is suitable not only for intensity-modulated OOK signal but also for phase-modulated signals (QPSK, DQPSK, etc.) which is discussed in Chapter 4.

Measurement of Brillouin threshold

Stimulated Brillouin scattering (SBS) has been investigated in the GeAsSe2011 fiber. Figure 3.51 illustrates the experimental setup. A tunable laser, having a spectral linewidth of 70 KHz, is used as the pump. This pump is amplified by an EDFA and injected into the

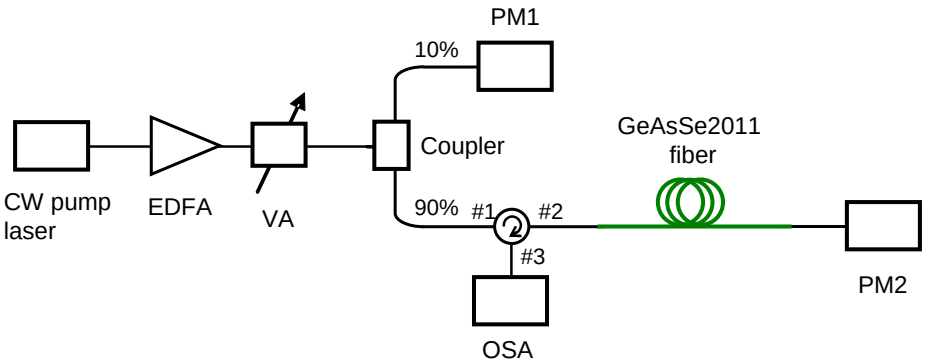

Figure 3.51: Experiment setup pour SBS measurement for the GeAsSe2011 fiber.

fiber via the port 2 of an optical circulator. A variable attenuator (VA) and a 90/10 coupler are inserted to allow the variation and monitoring of the power injected in the chalcogenide fiber. Two power-meters, PM1 and PM2, are used to monitor respectively the injected power and the transmitted power in the fiber. For different launched powers, the intensity of the backscattered Stokes component, collected at the port 3, is analyzed using a Brillouin optical spectrum analyzer (BOSA) with a resolution of 10 MHz.

Figure 3.52 shows the optical spectrum of the backscattered signal obtained on port 3 of the circulator. The peak at 1549.90 nm is the Fresnel-reflected pump signal. The second peak at 1549.958 nm, redshifted by 0.058 nm (7.25 GHz) with respect to the pump signal, corresponds to the Stokes Brillouin component generated in the chalcogenide fiber.

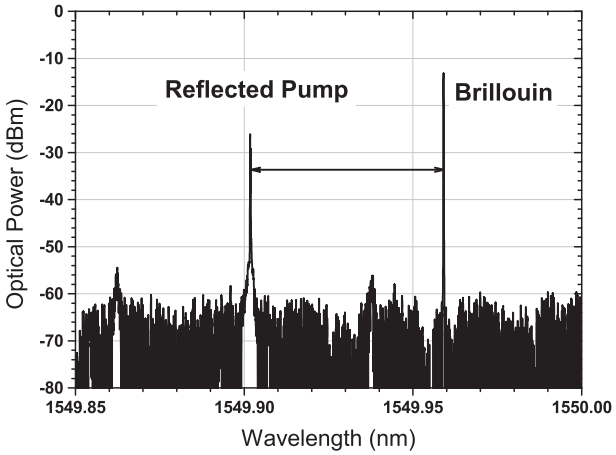

Figure 3.52: Example of optical spectrum of SBS in the GeAsSe2011 fiber.

In order to determine the SBS threshold power and the Brillouin gain coefficient g_B, the backscattered power of the Stokes component for different injected powers is plotted in

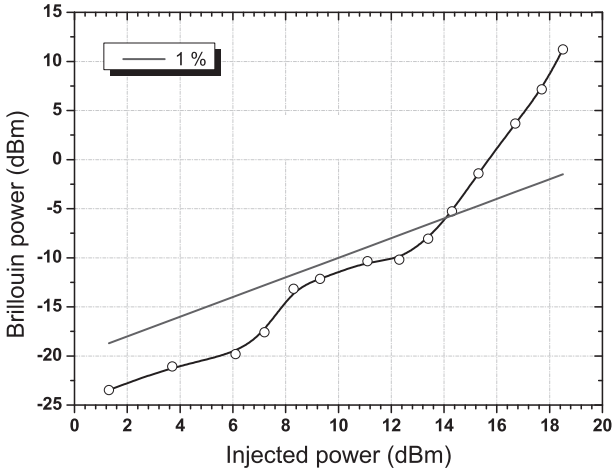

Figure 3.53: Deduction of the Brillouin gain coefficient using the measured Brillouin threshold power of the GeAsSe2011 fiber.

Figure 3.53. The SBS threshold power is defined as the input power for which the Stokes power is equal to 1% the input power [56]. A threshold value of 14 dBm (25 mW) is measured for the GeAsSe2011 fiber. The Brillouin gain g_B, calculated from the SBS threshold power using the small-signal steady-state theory of SBS [47], is found to be 2.6×10^{-9} m/W.

SBS is the phenomenon in which the reflected light increases rapidly when high power input light of narrow linewidth is launched into an optical fiber. In FWM experiment, which normally use a CW pump, SBS limits the pump power. The measurement of SBS for the GeAsSe2011 fiber confirms that, if the power of a narrow linewidth signal launched into the fiber is less than or equal to 14 dBm, the SBS can be negligible.

3.4.3.3 Conclusion

The GeAsSe2011 fiber has solved the problem of multimode propagation of suspended-core chalcogenide fibers. This fiber allows the propagation of data signals (at 42.7 Gb/s and 170.8 Gb/s). The characterization of the GeAsSe2011 fiber has been presented in *the OFC conference* in Los Angeles, CA in 2012 [172], and published in *Optics Letters* Vol. 37 (22) in 2012 [173]. Table 3.3 summarizes the characteristics and parameters of the GeAsSe2011 fiber.

Table 3.3: Characteristics of the GeAsSe2011 MOF fiber.

Name	γ ($W^{-1}km^{-1}$)	α (dB/m)	D (ps/km/nm)	FOM_{max} (W^{-1})	Propagation	Publications
GeAsSe2011	11000	2.5	−500	19.6	single-mode	OFC2012 [172], Opt. Lett. [173]

The GeAsSe2011 fiber has a nonlinear coefficient γ of 11000$W^{-1}km^{-1}$. Its singlemode behaviour offers a prospect for implementing all-optical signal processing in telecommunication systems which is considered in Chapter 4. The fiber still has a limitation of high dispersion. It limits the wavelength conversion range $\Delta\lambda_c$ of about 3 nm. Therefore, if applicable the use of this fiber is limited to signals with bit rates lower than 85 Gb/s.

3.4.4 GeAsSe microstructured fiber - 2012

At the beginning of 2012, other GeAsSe microstructured fibers were fabricated. A higher quality GeAsSe glass allows the reduction of the attenuation losses of the fiber. The composition of the chalcogenide glass is $Ge_{10}As_{22}Se_{68}$. To pursue the high nonlinearity as well as tailoring the dispersion, the fiber was drawn with a smaller core diameter. A 3-ring fiber with a core diameter of only 1.38 μm has then been realized. The fiber with its geometrical parameters and its cross-section image is shown in Figure 3.54. This fiber is named the *GeAsSe2012* fiber.

Linear and nonlinear characterizations are carried out with the same procedures as the GeAsSe2011 fiber. By utilizing the non-destructive method, the fiber loss is measured to be

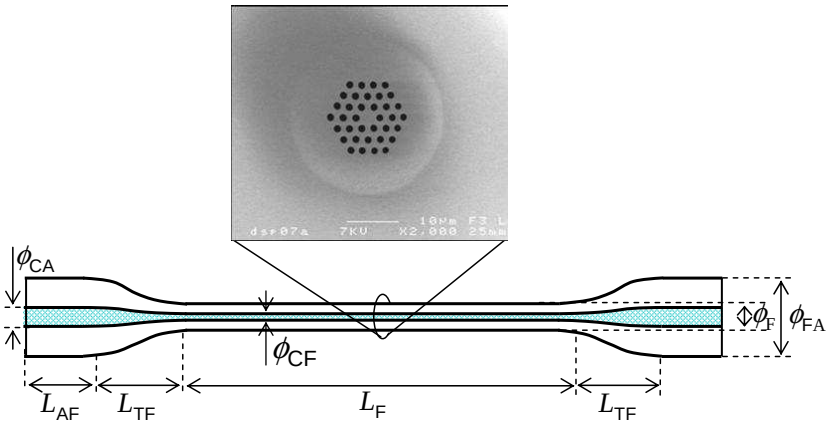

L_F (cm)	L_{TF} (cm)	L_A (cm)	ϕ_{FA} (μm)	ϕ_F (μm)	ϕ_{CA} (μm)	ϕ_{CF} (μm)
30	3	10	124	48	~3.2	~1.38

Figure 3.54: The GeAsSe microstructured GeAsSe2012 fiber.

0.9 dB/m. Similar to the GeAsSe2011 fiber, the structure of 3-rings of holes with a smaller core diameter ensures singlemode propagation. The core diameter of the fiber is 1.38 μm leading to a nonlinear coefficient γ of 25000 $W^{-1}km^{-1}$ and a group-velocity dispersion D of -310 ps/km/nm. These values have been evaluated by the SPM-based technique. The value of the nonlinear coefficient and the dispersion are also measured by FWM efficiency. Both techniques, the SPM-based technique and the FWM-based technique, give the same results. The FOM_{max} of the GeAsSe2012 fiber is 118 W^{-1}.

Two fibers with the same parameters have been drawn with shorter lengths than the previous fiber. One is 50 cm long and the other is 30 cm. This allows us to have a larger FWM conversion bandwidth as well as a shorter walk-off length. Experimental measurement as well as theoretical calculation using Eqs (1-90) and (1-91) give a wavelength conversion range of 4.8 nm and 6.2 nm for the 50 cm and the 30 cm GeAsSe2012 fibers, respectively.

The walk-off length is a key parameter in FWM-based time domain demultiplexing which will be discussed in Section 4.3. As mentioned in Section 1.4.1.3, for the case of two pulses of width T_0 propagating together in the fiber with a wavelength difference of $\Delta\lambda$, the walk-off length L_w can be written as

$$L_w = \frac{T_0}{\Delta\lambda\,|D|}, \tag{3-17}$$

where D is the dispersion of the fiber. For example, with the GeAsSe fibers, for the case of $T_0 = 3$ ps, $D = -310$ ps/km/nm and $\Delta\lambda = 5$ nm, the length of fiber should be less than $L_w = 2$ m.

These two fibers will be used to implement all-optical signal processing for 170 Gb/s signal wavelength conversion (in Section 4.2.4) and 170 Gb/s signal demultiplexing (in

Section 4.3.3). These fibers have been presented at *the ECOC conference* in Amsterdam, Netherlands in 2012 [174] and published in *Electronics Letters* vol. 49, no. 2 [175]. Table 3.4 summaries the characteristics and parameters of the two GeAsSe2012 fibers.

Table 3.4: Characteristics of the GeAsSe2012 fibers.

Name	L (cm)	γ ($W^{-1}km^{-1}$)	D (ps/km/nm)	FOM_{max} (W^{-1})	Propagation	Publications
GeAsSe2012	50	25000	−310	118	single-mode	ECOC2012 [174]
GeAsSe2012	30	25000	−310	118	single-mode	Electron. Lett. [175]

3.5 Conclusion

In this chapter, we have presented the characterizations of highly nonlinear chalcogenide fibers which have been fabricated by PERFOS and EVC. Table 3.5 presents our four chalcogenide microstructured fibers with their characterization.

Table 3.5: Characterization of chalcogenide microstructured fibers.

Chalcogenide MOF	Nonlinear coefficient γ ($W^{-1}km^{-1}$)	Fiber losses α (dB/m)	FOM_{max} (W^{-1})	Dispersion D (ps/km/nm)	Propagation
AsSe2010[168]	31000	4.6	29.3	−820	multimode
AsSe2011[171]	46000	0.9	222	−400	multimode
GeAsSe2011[172]	11000	2.5	19.6	−500	singlemode
GeAsSe2012[174]	25000	0.9	118	−310	singlemode

As time goes by, the quality of our chalcogenide MOF fibers have been improved. In 2009, the chalcogenide As_2Se_3 fiber had a FOM_{max} of only 4.3 W^{-1} (γ=15000 $W^{-1}km^{-1}$ and $\alpha = 15$ dB/m) [21]. In 2010, we reported an AsSe suspended-core fiber with a record of nonlinearity so far for MOFs. The nonlinear coefficient γ=31 000 $W^{-1}km^{-1}$ and the fiber loss $\alpha = 4.6$ dB/m give a FOM_{max} of 29.3 W^{-1} [169]. The suspended-core fiber fabricated in 2011 goes even further with a FOM_{max} of 222 W^{-1}. This fiber also achieved a new record for microstructured fibers with a nonlinear coefficient γ of 46000 $W^{-1}km^{-1}$ [171]. However, these fibers were multimode fibers. Telecommunications signals are degraded when propagating along these fibers.

In 2011, a microstructured fiber with 3-rings of holes was fabricated. The composition of the chalcogenide glass was GeAsSe. This fiber allows singlemode propagation. The FOM_{max} of the fiber is 19.6 W^{-1} for the nonlinear coefficient γ of 11000 $W^{-1}km^{-1}$ and fiber loss of 2.5 dB/m [172]. Other microstructured fibers in the composition of GeAsSe were then fabricated in 2012. With a core diameter as small as 1.38 μm leading to nonlinear

coefficient of 25000 $W^{-1}km^{-1}$ and fiber loss of only 0.9 dB/m, the FOM_{max} is 118 W^{-1} [174]. These two GeAsSe fibers with their characterizations are suitable to perform all-optical signal processing.

In the next chapter, all-optical signal processing utilizing these chalcogenide fibers will be presented. Wavelength conversion and time-division signal demultiplexing by exploiting the FWM effects in such highly nonlinear fibers will be discussed. The results as well as the limitations in the experiment are considered in details.

Chapter 4

All-optical signal processing in chalcogenide fibers

In the previous chapter, characterizations of highly nonlinear chalcogenide fibers were presented. Since the ultimate aim of this work is telecommunication applications, the chalcogenide glass fibers are now tested experimentally. This chapter presents our results on FWM-based all-optical nonlinear signal processing, in which wavelength conversion and time division multiplexing are considered. Section 4.1 gives a brief review of the state of the art of all-optical nonlinear signal processing. Sections 4.2 and 4.3 are respectively devoted to presenting FWM-based wavelength conversion and time-division demultiplexing using microstructured chalcogenide fibers.

4.1 All-optical signal processing

All-optical signal processing is one of the key technologies for future telecommunication networks requiring high-bit-rate data signals. The limitation of electrical bandwidth makes electrical components unsuitable for use for high-bit-rate signals above 40 GHz. All-optical signal processing can not only increase the capacity but can also avoid the optical-electrical-optical (O/E/O) conversion process. It thus reduces the power consumption allowing more compact components and improving the system stability. There are many different elemental functions in all-optical signal processing such as wavelength conversion, regeneration, time-division demultiplexing, logical operation, format conversion, sampling, buffering, etc. With the trend of nonlinear components (fibers, waveguides, semiconductors optical amplifiers (SOAs), saturable absorbers (SAs), etc.), all-optical signal processing, based on nonlinear efffects such as wavelength conversion [117, 176, 177], demultiplexing [162, 129], and regeneration [83, 81], has been receiving more and more attention. All-optical signal regeneration has already been discussed in Chapter 2. The following sections of this chapter consider all-optical wavelength conversion and all-optical time-division demultiplexing.

All-optical wavelength conversion could play a useful role in the future optical net-

works with their requirement for wavelength flexibility. Several schemes have been proposed to demonstrate all-optical wavelength conversion. They may be implemented by using SOAs [178, 179], SAs [180, 181], waveguides [182, 183], fibers [184, 185], etc. Among them, fiber-based wavelength conversion is one of the more attractive candidates because of its passive operation, high efficiency, and fast time response.

In the past two decades, a lot of studies on chalcogenide glasses components have been done to exploit their nonlinearity in photonic applications. In particular, highly-nonlinear fibers made of chalcogenide glasses are potential prospectives for high-bit-rate all-optical signal processing in general and wavelength conversion in particular. FWM-based wavelength conversion utilizing chalcogenide glasses components have been demonstrated. The first report of wavelength conversion at 10 Gb/s RZ with pulse duration of 7 ps in a 1 m long chalcogenide AsSe fiber was presented by V. G. Ta'eed *et al.* [186]. The chalcogenide AsSe fiber used had a nonlinear coefficient γ of 1200 $W^{-1}km^{-1}$ and a dispersion D of -560 ps/km/nm. The total average power was 90 mW and it suffered 1.4 dB of power penalty. In 2008, L. B. Fu *et al.* reported 40 Gb/s RZ wavelength conversion in a tapered chalcogenide fiber with the nonlinear coefficient γ of 2500 $W^{-1}km^{-1}$. With the limitation of being only 16 cm long, it required a total average power of 180 mW [118]. In 2010, M. D. Pelusi *et al.* successfully demonstrated 40 Gb/s DPSK wavelength conversion in a chalcogenide AsS waveguide. Restriction in the length of the waveguide led to a total average power of 400 mW [117]. By utilizing a short segment of chalcogenide AsSe fiber, in 2011 C.-S. Brès *et al.* reported a wavelength conversion at 8 GHz repetition rate for 1.4 ps pulses train [163]. With only 2.5 cm of fiber length, the total power used was more than 350 mW. Recently, R. Ahmad and M. Rochette demonstrated chalcogenide AsSe microwire wavelength conversion with total power as low as 70 mW and a large wavelength conversion range of 190 nm [130].

In 2011, by combining several types of optical fibers N. Verscheure and C. Finot have demonstrated wavelength conversion using triangular pulses generated in a normally dispersive fiber [187]. In 2010, A. Camerlingo *et al.* reported a highly nonlinear W-type fiber made of lead-silicate glass, which allowed FWM-based wavelength conversion operating at 1550 nm [188]. In 2011, based on a silicon platform, H. Hu *et al.* demonstrated wavelength conversion of a 640 Gb/s RZ-DPSK signal in a silicon photonic chip [189]. Although, the experiment obtained a minimum BER of only 10^{-5}, this was a significant result and offered the promise of high speed signal proccessing on silicon photonic chips. In 2012, K. Y. Wang and A. C. Foster also reported wavelength conversion in a hydrogenated amorphous silicon (a-Si:H) waveguide at telecommunication data rates (10 GHz) [190]. The maximum conversion bandwidth was 150 nm. In 2012, also based on a silicon platform, N. Ophir *et al.* reported a large wavelength conversion of 272 nm of a 10 Gb/s data signal using a silicon nanowaveguide [191]. The experiment had a 0.4 dB power penalty.

All-optical signal demultiplexing also plays an important role in high-bit-rate optical networks. To achieve high speed transmission at a single wavelength with a bit rate beyond

the limit of the electrical processing, optical time-division multiplexing (OTDM) of the transmitter signal is implemented [192]. At high-bit-rate, OTDM may involve multiplexing optical signal from 10 Gb/s to 40 Gb/s [193], 40 Gb/s to 160 Gb/s [194], 4 channels of 160 Gb/s to 640 Gb/s [195], 64 channels of 10 Gb/s to 640 Gb/s [196], etc. At the receiver, it is necessary to extract a tributary channel at a lower bit-rate for photodetection and bit-error-rate (BER) measurement. The opposite process, time-division demultiplexing, is used. For demultiplexing OTDM signals at a high bit rate, several all-optical schemes have been proposed using fibers [197, 198], waveguides [162, 129], SOAs [195], nonlinear optical loop mirrors [199, 200], electro-optical modulators [201], etc. fibers and waveguides offer a potential for ultrafast operation owing to the femtosecond response time of the Kerr nonlinearity. However, with waveguides, there is a need of high power due to a component length of just several centimeters [162]; with standard HNLFs, it requires long fibers to compensate the low nonlinearity [202]. For non-silica fibers, demultiplexing of a 160 Gb/s signal down to 10 Gb/s was demonstrated in 1.08 m of Bismuth-oxide fiber [203]. A large dispersion ($D = -310$ ps/km/nm) of the fiber limited the wavelength conversion range $\Delta\lambda_c$ to about 3 nm. In 2011, A. Camerlingo demonstrated the use of a 2.2 m sample of lead-silicate fiber in a 160 Gb/s-to-40Gb/s FWM-based demultiplexing experiment [204]. A nonlinear coefficient of 820 $W^{-1}km^{-1}$ and a fiber loss of 2.1 dB/m led to a total power of about 160 mW. Given the progress in chalcogenide glasses fiber fabrication, the nonlinear coefficient has now become high enough to use fiber lengths of 1 m or less. Chalcogenide glasses fibers, hence, have the potential to implement all-optical signal demultiplexing for high bit-rate signals.

Obviously, the greater the nonlinearity of the fibers the greater the efficiency of all-optical signal processing. Microstructured chalcogenide glasses fibers in general and suspended-core in particular have been reported with high nonlinear coefficient γ [171, 172] allowing photonics applications with acceptable input powers (less than 100 mW). Besides, chalcogenide tapers or chalcogenide wires are also good prospects in terms of nonlinearity. However, their possible length is limited due to their fabrication techniques and characteristics. With all the reasons above, chalcogenide microstructured fibers are one of the better candidates for all-optical signal processing but they are limited by high dispersion. Together with the results of all-optical wavelength conversion and time-division demultiplexing in chalcogenide glasses microstructured fibers, this problem will be discussed in detail in the following sections.

4.2 FWM-based wavelength conversion

This section is devoted to presenting our results concerning FWM-based wavelength conversion. Telecommunication signals with two modulation formats (OOK and DQPSK) at bit-rates of 42.7 Gb/s, 56 Gb/s, 85.4 Gb/s and 170.8 Gb/s are considered. In this section, we present and discuss some experimental results using highly-nonlinear chalcogenide fibers.

4.2.1 42.7 GHz clock signal wavelength conversion

In this section, wavelength conversion of an optical clock signal at 42.7 GHz based on FWM with a CW pump is experimentally presented. In the experiment, the chalcogenide AsSe2011 fiber with the nonlinear coefficient γ of 46 000 $W^{-1}km^{-1}$ is used.

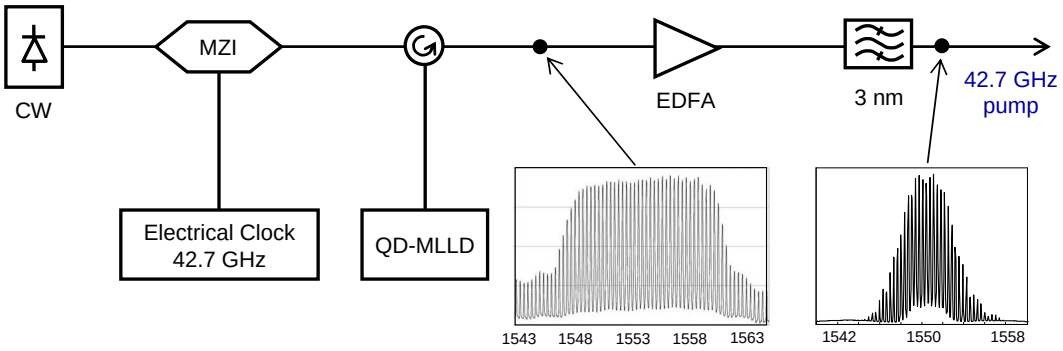

Figure 4.1: Generation of 42.7 GHz clock signal.

The schematic setup to generate a modulated optical clock signal at 42.7 GHz is illustrated in Figure 4.1. Firstly, a 42.7 GHz optical clock signal is generated at the wavelength of 1535 nm from a CW laser by a $LiNbO_3$ Mach-Zehnder modulator (MZ) and a 42.7 GHz electrical clock signal. The 1535 nm optical clock is then injected into the cavity of a quantum-dash actively mode-locked laser (QD-MLLD) through an optical circulator to generate a broadband clock signal. At the output of the optical circulator, a 42.7 GHz optical clock centered at 1553 nm with a 13 nm bandwidth at 10 dB intensity points is obtained (see the spectum in the inset of Figure 4.1) [205]. This optical signal is amplified by an EDFA and then filtered by a 3 nm tunable optical band-pass filter (OBPF) centered at 1550 nm for the FWM experiment. By tuning the centered wavelength of the OBPF, we can choose the wavelength of a 42.7 GHz clock signal around 1553 nm for FWM experiments.

Figure 4.2 shows the eye diagram of the 42.7 GHz signal after the 3 nm filter. After the 3 nm filter, the pulse duration is 3 ps. This signal continues to be filtered by a programable filter centered at 1550 nm to narrow its spectrum for FWM experiment. The pulse duration after this filter is 4.5 ps.

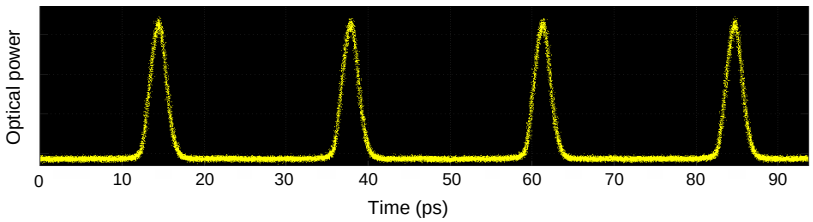

Figure 4.2: Eye diagram of the 42.7 GHz clock signal after the 3 nm filter.

The experimental setup for 42.7 GHz optical signal wavelength conversion is shown in Figure 4.3. The 42.7 GHz optical signal works as a pulse source cooperating with a CW

pump. Both pulse and CW signals are amplified by EDFAs and matched in polarization by using polarization controllers (PCs). They are then combined by a 3 dB coupler. The combined signal is then passed through a 5 nm OBPF to reject the amplified spontaneous emission ASE noise of the EDFAs. The optical pulse signal before launching into the AsSe fiber has a pulse width of 4.5 ps. To couple signals into and out of the AsSe fiber, free-space coupling is performed using microlensed fibers with a mode field diameter of 5.2 μm as mentioned in Section 3.4.2. The total insertion loss between the output of the injecting microlensed fiber and the output of the AsSe fiber is measured, for this experiment, to be 4.7 dB, which includes Fresnel reflection of 1.1 dB at each end of the fiber and propagation losses of 1.1 dB (see Section 3.4.2.1).

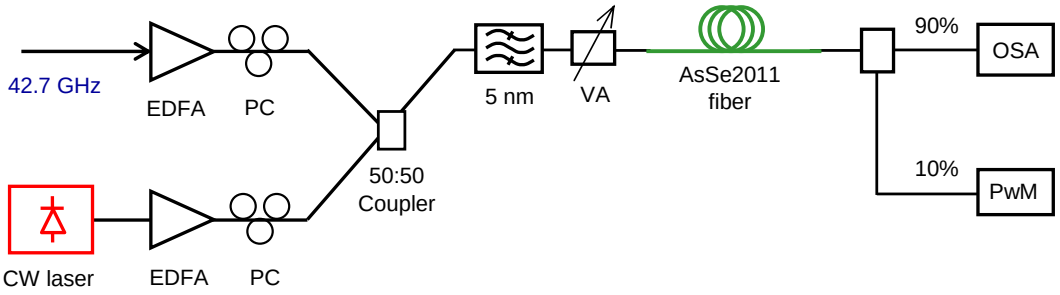

Figure 4.3: Experimental setup of 42.7 GHz wavelength conversion.

The total average power at the output of the variable attenuator (VA) is measured to be 15 dBm (31.6 mW) with a CW power of 11.4 dBm (13.7 mW). Taking into account 2.5 dB of insertion losses at the input, the total average power launched into the AsSe fiber is 12.5 dBm (17.2 mW). This value is compatible with usual powers in telecommunications systems. Note also that with these relatively low values of optical powers, two-photon absorption, that usually occurs in AsSe glasses, is not visible in our case.

Figure 4.4(a) plots the total spectrum just before the AsSe fiber. There are only two bands, those of the clock signal and of the CW pump without FWM peaks. After the AsSe fiber, the output spectrum exhibits strong FWM peaks (Figure 4.4(b)) with both first and second-order peaks visible. To assess the performance of the conversion, the definition of the FWM efficiency, defined in Section 1.4.1.4, is used. It is the ratio between the collected peak power of the anti-Stokes wave at the output of the AsSe fiber and the CW power injected in the AsSe fiber. Figure 4.5 depicts the measured FWM efficiency and its theoretical curve for the first-order FWM. The FWM efficiency calculation is carried out by using an analytical formula for the peak power P_3 (Eq. (3-14)). The measured efficiency and theoretical efficiency are in a good agreement. At the wavelength detuning $\Delta\lambda$ of 6.1 nm, a FWM efficiency of -17.5 dB is achieved. When the detuning $\Delta\lambda$ increases to 7.3 nm, we still have a FWM efficiency of -18.5 dB. The second-order FWM is obtained with an efficiency of -36 dB.

The AsSe2011 fiber with the nonlinear coefficient γ of 46000 $W^{-1}km^{-1}$ allows a reduction

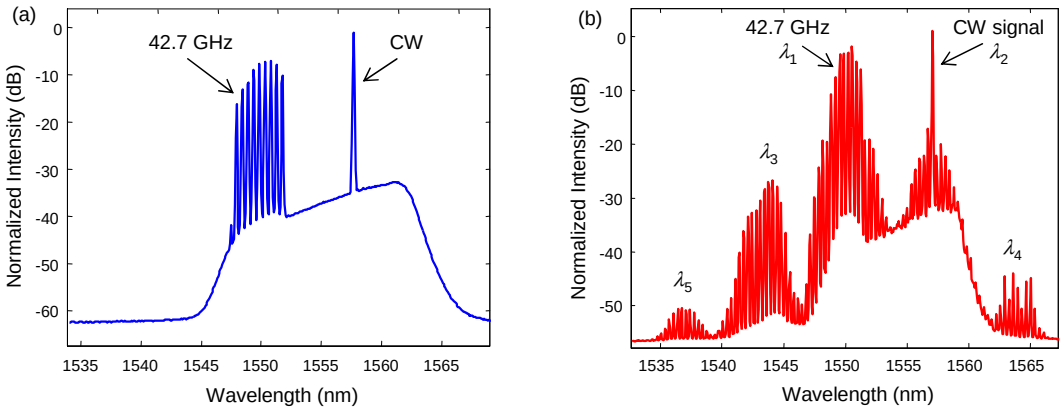

Figure 4.4: (a) Spectrum of combined CW signal and 42.7 GHz pump at the input of the AsSe2011 fiber; (b) Spectrum at the output of the fiber with FWM signal up to second order.

of the launched power compared to other FWM-based wavelength converters [117, 118]. This makes it compatible in power with telecommunication systems. However, as mentioned in Section 3.4.2.1 this suspended-core structure exhibits a multimode behaviour. This leads to eye diagram degradation when working with optical data signals rather than with optical clock signals, as discussed in Section 3.4.2.1. These observations lead to the conclusion that the fiber is not suitable for telecommunication uses and further work is needed in order to obtain suitable fibers. One possible solution is to use microstructured chalcogenide fibers with 3 or 4 rings of holes. The use of the fibers will be considered in the next sections.

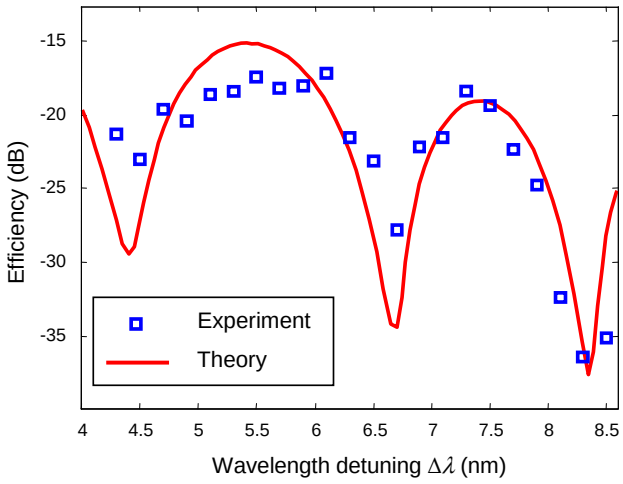

Figure 4.5: Efficiency of the first-order FWM with respect to the wavelength detuning $\Delta\lambda$.

4.2.2 42.7 Gb/s OOK signal wavelength conversion

In the previous section, wavelength conversion of a 42.7 GHz optical clock signal was demonstrated in a chalcogenide suspended-core fiber. However, the fiber behaves as a multimode

fiber and could not be used for modulated optical data signal (see the characterization in Section 3.4.2.1). By taking advantage of the 3 rings of air holes microstructure, chalcogenide fibers can exhibit single-mode propagation. In this section, wavelength conversion of a modulated optical data signal at 42.7 Gb/s in a 1 m long chalcogenide fiber will be considered. The fiber used is the GeAsSe2011 fiber presented in Section 3.4.3. Its Kerr nonlinearity is 11000 $W^{-1}km^{-1}$ and its dispersion D is -500 ps/km/nm.

The 42.7 Gb/s generation is schematically illustrated in Figure 4.6. It is similar to the case of 42.7 GHz optical clock signal generation except for the second MZI for data modulation. A CW laser is modulated with a 42.7 GHz electrical clock signal by a $LiNbO_3$ Mach-Zehnder modulator (MZI). After injection into the cavity of a quantum-dash actively mode-locked laser (QD-MLLD) through an optical circulator, the 42.7 GHz optical clock signal at the wavelength of 1553 nm clock is obtained. It is amplified by an EDFA and filtered by a 3.5 nm Gaussian filter before being injected into the second MZI. The second MZI modulates the 42.7 Gb/s optical clock signal with a PRBS of $2^{31}-1$ pattern length to generate a 42.7 Gb/s on-off-keying (OOK) RZ 33% duty cycle data signal. The 33% duty cycle leads to a difference of 7.5 dB between the peak power and the average power. The signal is then filtered by a 1 nm OBPF. After the filter, it has a pulse duration of 8.3 ps and is centered at the wavelength of 1553 nm. The eye diagram of this signal is shown in Figure 4.9(a).

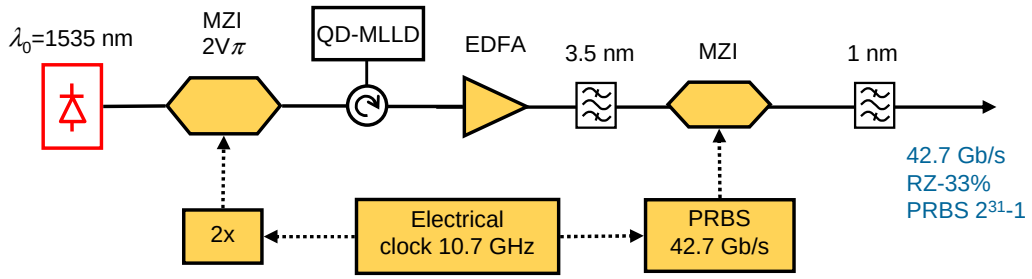

Figure 4.6: Generation of 42.7 Gb/s OOK signal.

Figure 4.7 illustrates the experimental setup for FWM-based 42.7 Gb/s OOK signal wavelength conversion. The 42.7 Gb/s OOK signal and a CW pump are amplified by EDFAs. They both pass through polarization controllers (PCs) and are then combined with a 3 dB coupler. The coupled signal is then filtered by an OBPF of 5 nm to reject the amplified spontaneous emission noise (ASE) of EDFAs. The power launched into the chalcogenide fiber is adjusted by a variable attenuator (VA). As described in Section 3.4.3, microlensed fibers are used to couple signals into and out of the chalcogenide mode-adapted fiber. The converted signal is filtered by a 1 nm filter then amplified before detection.

The CW pump wavelength can be tuned to set the wavelength of the converted signal. Figure 4.8 shows an example of the output spectrum for a wavelength detuning $\Delta\lambda$ of 2.6 nm with respect to the data signal. The spectrum clearly exhibits first-order and second-order idler waves. In this case, the total average power at the output of the injected microlensed

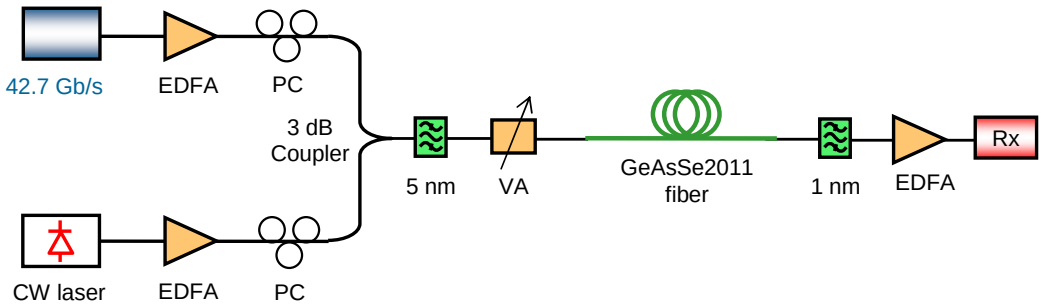

Figure 4.7: Experimental setup for FWM-based 42.7 Gb/s OOK wavelength conversion.

fiber is 17.5 dBm (56 mW) with a CW power of 13.4 dBm (21.5 mW). By taking into account injection losses at the input of the GeAsSe2011 fiber of around 2.4 dB (calculated in Section 3.4.3), the total average power launched into the nonlinear section of the GeAsSe2011 fiber is estimated at 15.1 dBm (32 mW). With this power, at a wavelength detuning $\Delta\lambda$ of 2.6 nm, the FWM conversion efficiency of the first-order anti-Stokes idler wave is found to be -22 dB (using the same definition of FWM efficiency as in Section 4.2.1).

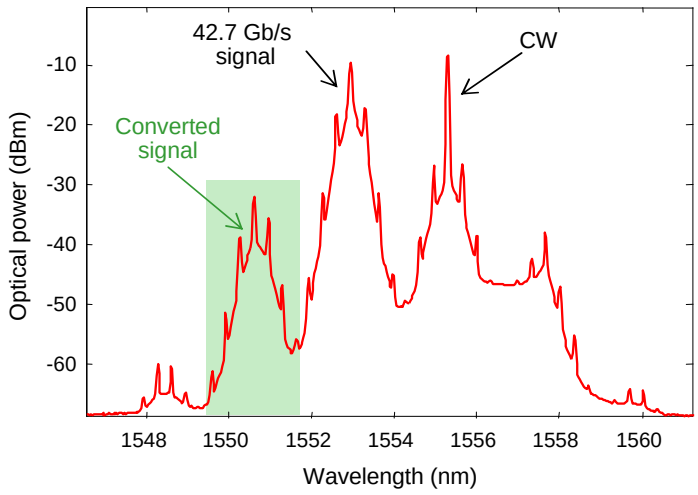

Figure 4.8: Four-wave mixing spectrum at the output of the GeAsSe2011 fiber.

To analyse the anti-Stokes converted signal, a 1 nm OBPF centered at 1550.4 nm is used. After the filter, the converted signal is measured to be -25 dBm. The filtered signal is then amplified by an EDFA before detection. Figure 4.9(a) and 4.9(b) illustrate the eye diagrams of the original 42.7 Gb/s signal and the 42.7 Gb/s converted signal, respectively. Note that in Figure 4.9(b) the optical signal-to-noise ratio (OSNR) is much lower than the case of Figure 4.9(a) due to less available power for the 42.7 Gb/s converted signal. The pulse duration of the converted signal is measured to be 5.9 ps. It agrees well with the theory that the converted pulses are compressed by a factor of $\sqrt{2}$ from the original pulse of duration 8.3 ps. This is due to the fact that the anti-Stokes signal is proportional to the square of the original 42.7 Gb/s signal power (see Eq. (3-14)).

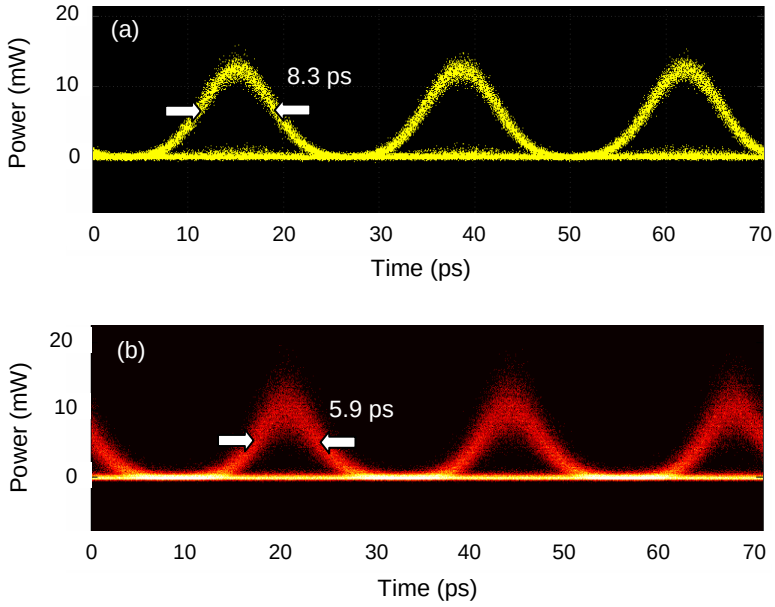

Figure 4.9: Eye diagrams of (a) the 42.7 Gb/s original signal at 1553 nm and (b) the converted signal at 1550.4 nm.

To assess the performance of the wavelength conversion, the bit-error rate (BER) is measured for a 42.7 Gb/s PRBS of $2^{31}-1$ pattern length as a function of the receiver input power. Since the BER testing system directly operates for 10 Gb/s signal, the converted signal is electrical time-division demultiplexed to 10.67 Gb/s for BER measurement. Figure 4.10 shows the evolution of the BER measurement for the back-to-back (B2B) case and for the converted 42.7 Gb/s signal case. Compared to the B2B reference, there is no power penalty for the received power lower than −34 dBm. For powers higher than −34 dBm, the measurement shows a negligible power penalty. At a BER of 10^{-9}, a penalty of 0.4 dB is

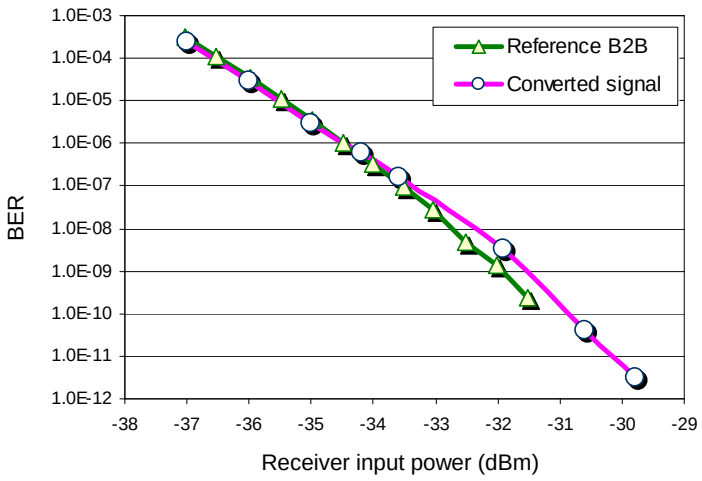

Figure 4.10: BER measurement of the converted signal and B2B with respect to receiver input power for a 42.7 Gb/s signal in the GeAsSe2011 fiber.

found. This small penalty can be due to the low OSNR of the converted signal. With power higher than −30 dBm, error free wavelength conversion is achieved.

The GeAsSe2011 fiber has successfully demonstrated 42.7 Gb/s OOK wavelength conversion. To the best of our knowledge, this result is the first demonstration of wavelength conversion for a 42.7 Gb/s OOK signal in a chalcogenide MOF with a total power of only 56 mW. As reviewed, 40 Gb/s-RZ wavelength conversion in a tapered chalcogenide fiber required a total average power of 180 mW [118]. By using a chalcogenide waveguide, 40 Gb/s DPSK wavelength conversion was also reported but with a total average power of 400 mW [117]. However, the wavelength conversion range $\Delta\lambda_c$ of about 3 nm (see the FWM efficiency curves in Figure 3.48(b)) is not large enough for spectrum bandwidth of signals higher than 80 Gb/s. This is attributed to the high dispersion of −500 ps/km/nm of the fiber. The dispersion needs to be reduced for further applications, as we will see in Section 4.3. In the following section, the present fiber is used in a wavelength conversion experiment for another modulation format.

4.2.3 56 Gb/s DQPSK signal wavelength conversion

After achieving error free wavelength conversion for an OOK RZ-33% signal at 42.7 Gb/s, we continued to investigate the wavelength conversion for another type of modulation. The same GeAsSe2011 fiber with a nonlinear coefficient of 11 000 $W^{-1}km^{-1}$ is used for a 56 Gb/s differential quadrature phase shift keying (DQPSK) wavelength conversion.

The experimental setup for a 56 Gb/s DQPSK generation [206] is shown in Figure 4.11. The DQPSK signal is generated by a nested Mach-Zehnder modulator (MZI) from a distributed feedback (DFB) laser and two data channels (I and Q) of 28 Gb/s with $2^{15}-1$ bit length PRBS. The second MZI is sinusoidally modulated at 28 GHz to convert 28 Gbaud non-return-to-zero (NRZ) DQPSK to 50% RZ DQPSK. The signal is then filtered by a 1 nm 3-dB bandwidth filter.

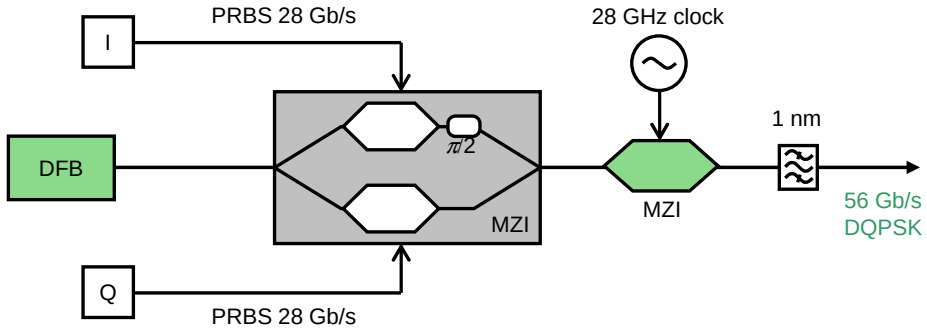

Figure 4.11: Generation of 56 Gb/s DQPSK signal. DFB: Distributed-feed back laser. I and Q: channels for DQPSK modulation. MZI: Mach-Zehnder Interferometer modulator

The experimental setup for the 56 Gb/s DQPSK wavelength conversion is the same as for the 42.7 Gb/s OOK signal. For easy recall, it is re-presented in Figure 4.12. The wavelength

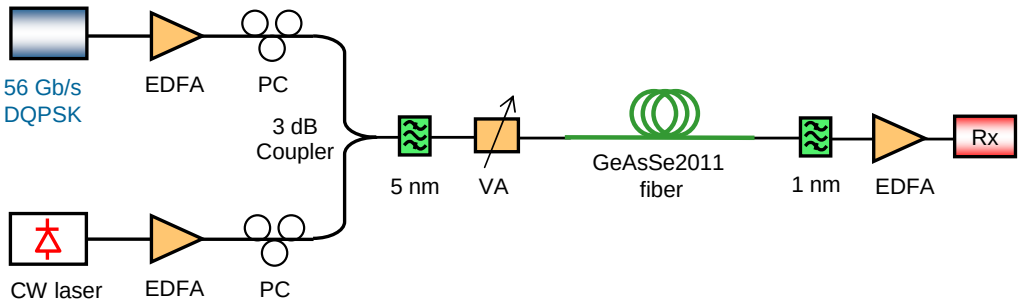

Figure 4.12: Experimental setup of a 56 Gb/s DQPSK signal wavelength conversion.

of the DQPSK signal is centered at 1556.2 nm. The CW pump wavelength can be tuned to choose the wavelength of the converted signal. In the experiment, the wavelength of the CW pump is set to 1557.8 nm leading to a detuning $\Delta\lambda$ of 1.6 nm between the signal and the pump.

An example of optical spectrum at the output of the GeAsSe2011 fiber is shown in Figure 4.13. It exhibits FWM waves shifted by multiples of $\Delta\omega$ ($\Delta\omega = 2\pi c\Delta\lambda/\lambda_0^2$) on both sides of the initial waves. Contrary to OOK wavelength conversion, DQPSK wavelength conversion should preserve the phase of the signal. The converted signal must then be the one proportional to the input signal, not to the square of the input signal (as discussed in Section 1.4.1.4). In our experiment, it corresponds to the wave close to the CW pump, centered at 1559.4 nm. At the output of the GeAsSe fiber, a 1 nm band-pass filter centered at 1559.4 nm is used to extract the converted signal. The total average power at the output of the VA is set to 16.5 dBm (45 mW), including a CW pump power of 13.7 dBm (24 mW). The power of the converted signal after the 1 nm filter is measured to be −22 dBm.

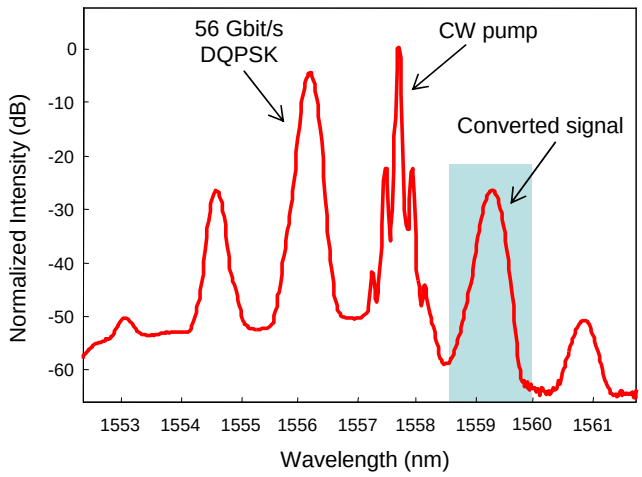

Figure 4.13: An example of spectrum at the output of the GeAsSe2011 fiber.

The schematic setup for BER analysis of 56 Gb/s DQPSK signal is shown in Figure 4.14. The 56 Gb/s DQPSK signal is demodulated into 4 optical channels. These 4 channels are

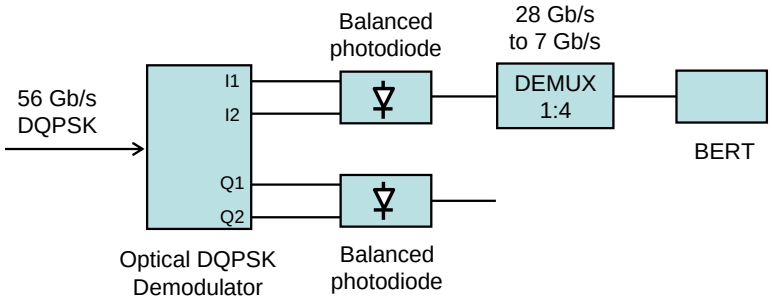

Figure 4.14: Schematic setup for BER measurement of 56 Gb/s DQPSK signal.

then detected by balanced photodiodes. Because the BER tester (BERT) only supports a signal rate lower than 12.5 GHz, the 28 Gb/s signal at the output of each photodiode is demultiplexed to 7 Gb/s signals.

Figure 4.15 shows BER measurements of the converted signal as a function of the power on the receiver. The B2B case is also represented as a reference. Error-free wavelength conversion of a 56 Gb/s DQPSK signal has then been demonstrated with a conversion shift of 3.2 nm (twice the wavelength detuning $\Delta\lambda$) and a total average power of 16.5 dBm (45 mW). A power penalty of about 1 dB for a BER of 10^{-9} is found. One possible reason for this may be nonlinear effects. This was experimentally investigated. DQPSK signal was propagated along the fiber and the BER was measured for different launched powers. This showed that the BER evolution did not depend on the launched powers and therefore nonlinear effects could not explain 1 dB penalty.

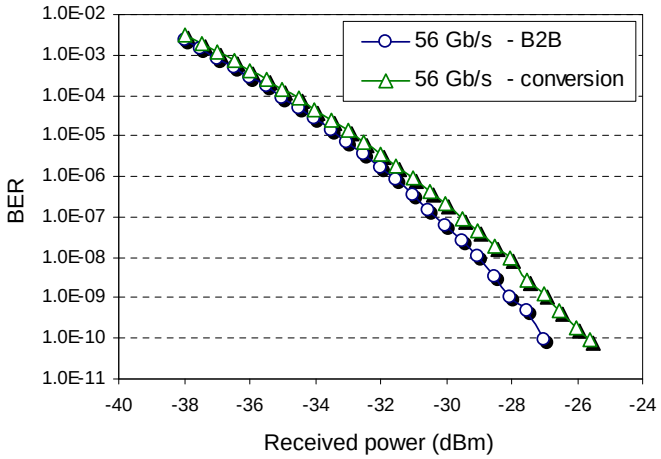

Figure 4.15: BER evolution of the converted 56 Gb/s signal and the B2B measurement.

Another possibility is the effect of noise. The BER of B2B for a launched power as low as the power of the converted signal (−22 dBm) was measured. This showed a power penalty as for the converted signal. It so can be understood if the power of the converted signal is not high enough. This causes a lower OSNR of the converted signal compared to the original DQPSK signal.

The 56 Gb/s DQPSK signal has a narrower spectral bandwidth than the previous 42.7 Gb/s OOK signal. The wavelength detuning $\Delta\lambda$, in the case of the DQPSK signal can thus be reduced to 1.6 nm (2.6 nm in the case of the OOK signal) in order to reduce the optical power. In the experiment, the total input power was only 45 mW. To the best of our knowledge, this is the first time a 56 Gb/s DQPSK wavelength conversion is demonstrated in a chalcogenide MOF with such a low power. However, as mentioned in the previous section, this fiber with a strong value of dispersion restricts the wavelength conversion range $\Delta\lambda_c$ to about 3 nm and does not allow processing signals with bit rates higher than 80 Gb/s.

4.2.4 170.8 Gb/s OOK signal wavelength conversion

The GeAsSe2011 fiber has a nonlinear coefficient of 11 000 $W^{-1}km^{-1}$ and a dispersion D of -500 ps/km/nm. This value of dispersion limits the wavelength conversion range $\Delta\lambda_c$ to about 3 nm. It is not large enough for the spectrum of a signal at a bit rate of 160 Gb/s, for example. A 160 Gb/s signal with a pulse duration of 3 ps has a spectral width at full width at half maximum (FWHM) larger than 2.5 nm. In theory, when the 160 Gb/s signal and a CW pump are injected into a nonlinear fiber with a suitable power, at the output we can observe two new waves (Stokes and anti-Stokes) due to FWM. Generally, one can choose the Stokes wave or anti-Stokes waves to be the wavelength-converted signal. However, in the case of FWM between a pulse signal and a CW pump, the peak power of the pulse signal is generally higher than the power of CW pump. Hence, the wave that is close to the pulse wave is chosen because its energy is higher than the wave close to the CW pump (as discussed in Section 1.4.1.4).

For the example of FWM between a 160 Gb/s signal and a CW pump in Figure 4.16, the energy of the anti-Stokes wave is proportional to the square of the peak power of the 160 Gb/s signal and the energy of the Stokes wave is proportional to square of the power of the CW pump. The peak power of the 160 Gb/s pulse signal is higher than its average power and also than the CW power, thus the energy of the anti-Stokes wave is higher than that of the Stokes wave. It would hence be preferable to take the anti-Stokes wave as the converted signal.

However, in the case of FWM with a 160 Gb/s signal and a CW signal, after the nonlinear medium, due to the XPM and FWM effects, the spectra of the four waves overlap each other as schematically shown in Figure 4.16. In this example, the spectrum surrounding the CW pump λ_2 induced by XPM will overlap the Stokes wave λ_4. The anti-Stokes wave λ_3 has a spectral width of about 3 nm as has the original 160 Gb/s signal λ_1. Their spectra also partly overlap. Hence, both the anti-Stokes wave λ_3 and Stokes wave λ_4 could not be filtered to be a converted signal. To overcome this problem to perform wavelength conversion for a 160 Gb/s signal or higher bit rate, the dispersion of the fiber needs to decrease in order to augment the wavelength conversion range. This should help the different waves not to overlap each other.

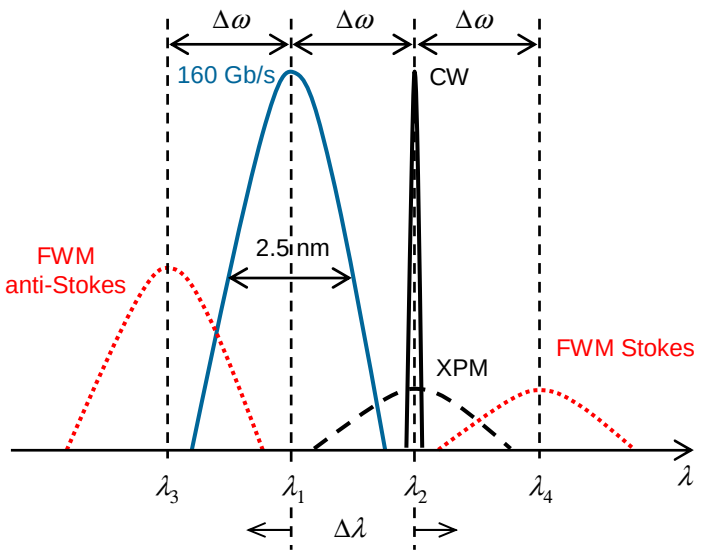

Figure 4.16: Illustration of spectral waves for FWM of 160 Gb/s and a CW signals.

This section now presents the wavelength conversion of a 170.8 Gb/s OOK RZ signal. As discussed above, a fiber with lower dispersion and higher Kerr nonlinearity should be used. The GeAsSe2012 fiber with a nonlinear coefficient γ of 25000 $W^{-1}km^{-1}$, and a dispersion D of -310 ps/km/nm is suitable for the experiment. The characterization of the fiber is described in Section 3.4.4. Taking into account the length of the fiber $L = 50$ cm, we have a zero-efficiency detuning $\Delta\lambda_0 = 7.2$ nm around a wavelength of 1550 nm (using Eq. (1-90)). The wavelength conversion range $\Delta\lambda_c$ is thus equal to about 5 nm. This value is large enough for the spectra of FWM waves and the input signals not to overlap each other. The experiment of a FWM-based wavelength conversion of a 170.8 Gb/s OOK signal is then implemented with a CW pump.

The 170.8 Gb/s OOK signal is generated as illustrated in Figure 4.17. The 42.7 GHz optical clock signal is generated at 1535 nm by by a $LiNbO_3$ Mach-Zehnder modulator (MZI) from a CW laser and a 42.7 GHz electrical clock signal. It is then injected into a QD-MLLD by a circulator. The QD-MLLD generates a 42.7 GHz optical clock signal with a bandwidth of 13 nm centered at 1555 nm. A 20-m-length SMF fiber is used at the output

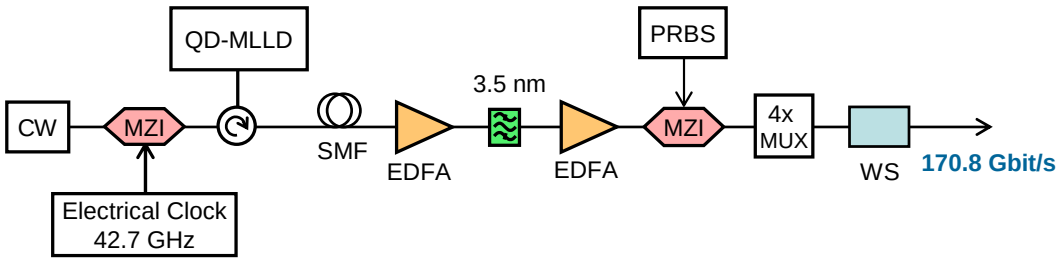

Figure 4.17: Generation of a 170.8 Gb/s OOK signal.

of the QD-MLLD to compensate for the chirp of the laser. The optical signal is amplified by an EDFA, then filtered by a 3.5 nm Gaussian filter and amplified again by another EDFA.

The second MZI is used to modulate the optical clock signal with a PRBS pattern of a length of $2^7 - 1$ bits. The 42.7 Gb/s is then time-division multiplexed by a multiplier $\times 4$ in order to create a 170.8 Gb/s signal. The signal is then passed through a programable optical filter (*Finisar waveshaper* - WS) which is programed to be the association of a Gaussian filter of 2 nm bandwidth at 3 dB intensity point (Figure 4.18(a)) and a 3 nm flat-top filter (Figure 4.18(b)). These two programed filters together produce a sharp-Gaussian filter as seen in Figure 4.18(c). This filter narrows the spectrum of the 170.8 Gb/s signal helping to put the 170. Gb/s signal and CW signal closer. The generated 170.8 Gb/s OOK signal is centered at a wavelength λ_0 of 1554.8 nm.

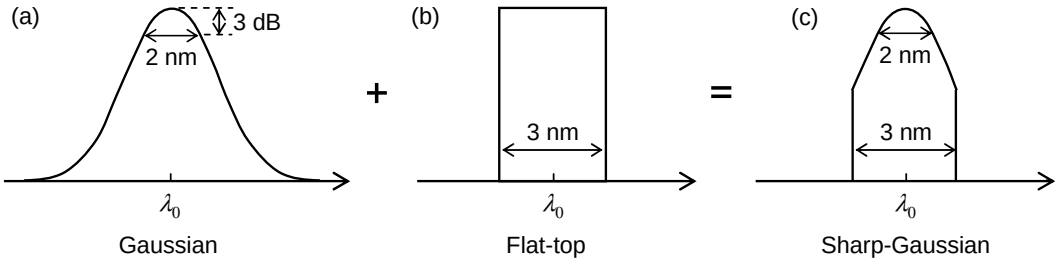

Figure 4.18: Two programed filters function by the waveshaper: a Gaussian filter (a) and a flat-top filter (b) produce a sharp-Gaussian filter (c).

Figure 4.19 illustrates the spectra of the 170.8 Gb/s OOK signal before and after the WS. Since the spectrum of the 170.8 Gb/s signal at the output of the 4×-MUX is large (Figure 4.19(a)), it is filtered by the sharp-Gaussian filter to have a suitable bandwidth (Figure 4.19(b)) for wavelength conversion. Before the WS, the pulse duration of the 170 Gb/s OOK signal is measured to be 1.2 ps. After the WS, the pulse duration is 2.5 ps. Eye diagrams of the 170.8 Gb/s OOK signal before and after the WS are shown in Figure 4.20.

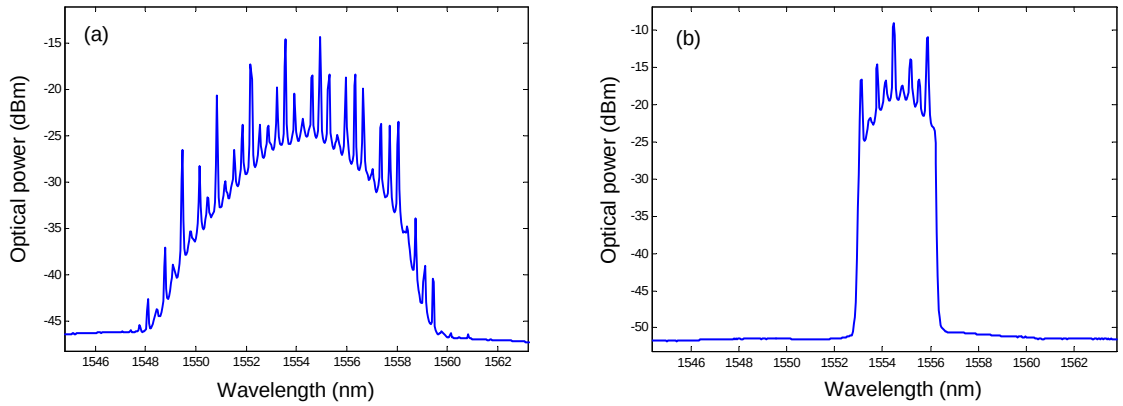

Figure 4.19: Spectra of the 170.8 Gb/s OOK signal (a) before and (b) after the waveshaper.

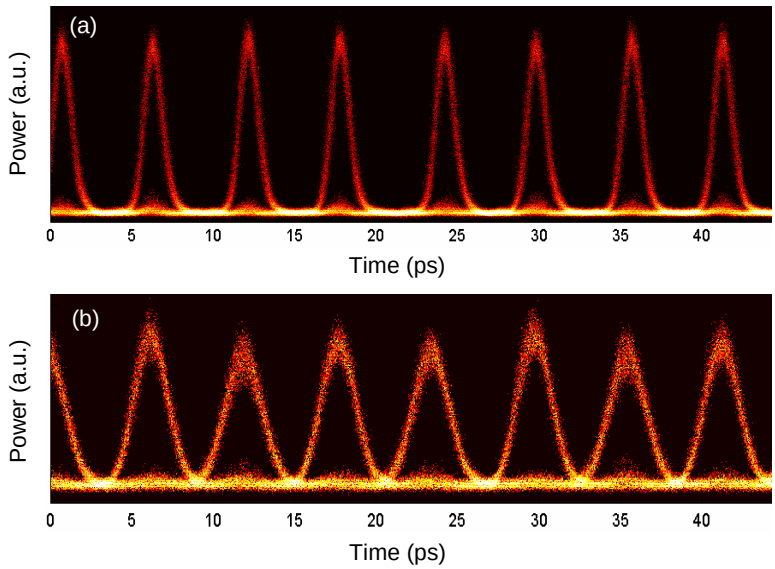

Figure 4.20: Eye diagrams of the 170.8 Gb/s OOK signal (a) before and (b) after the waveshaper.

The experimental setup for wavelength conversion is illustrated in Figure 4.21. It is similar to the previous FWM experiment. The 170.8 Gb/s OOK signal and CW pump are amplified by EDFAs and polarization aligned by PCs. They are combined by a 3 dB coupler before being injected into the fiber. To couple signals into and out of the GeAsSe fiber, microlensed fibers with an MFD of 3.1 μm are used. This dimension is close to the core diameter, 3.2 μm, of the two ends of the fiber (described in Section 3.4.4). Total insertion losses between the output of the injected microlensed fiber and the output of the GeAsSe fiber is measured to be 3.5 dB. Total average power measured at the output of the variable attenuator (VA) is 20 dBm (100 mW) in which the power of CW pump is 17.5 dBm (56 mW). At the output of the GeAsSe fiber, a 3 nm flat-top band-pass filter centered at 1545.5 nm is used to select the converted wave. It is amplified by an EDFA and re-filtered by a WS which is programmed to be a Gaussian filter of 2 nm bandwidth at the 3 dB intensity points. The 3 nm flat-top filter with a good extinction eliminates the other waves

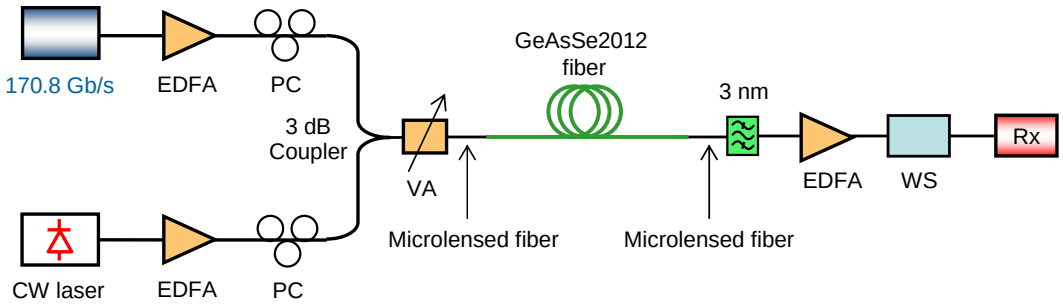

Figure 4.21: Experimental setup of a 170.8 Gb/s OOK signal FWM-based wavelength conversion.

and the programable Gaussian filter is used to reshape the converted wave. The signal is then sent to the receiver for BER analysis.

Figure 4.22 shows an example of the spectra at the input and output of the GeAsSe fiber. In the experiment, the wavelength detuning $\Delta\lambda$ between two signals is 4.65 nm as seen in Figure 4.22(a). The center wavelength of the 170.8 Gb/s OOK signal is 1554.8 nm and the CW pump is 1550.15 nm. The spectrum at the output of the chalcogenide fiber shows strong FWM waves (Figure 4.22(b)). The anti-Stokes idler is chosen to be the converted signal.

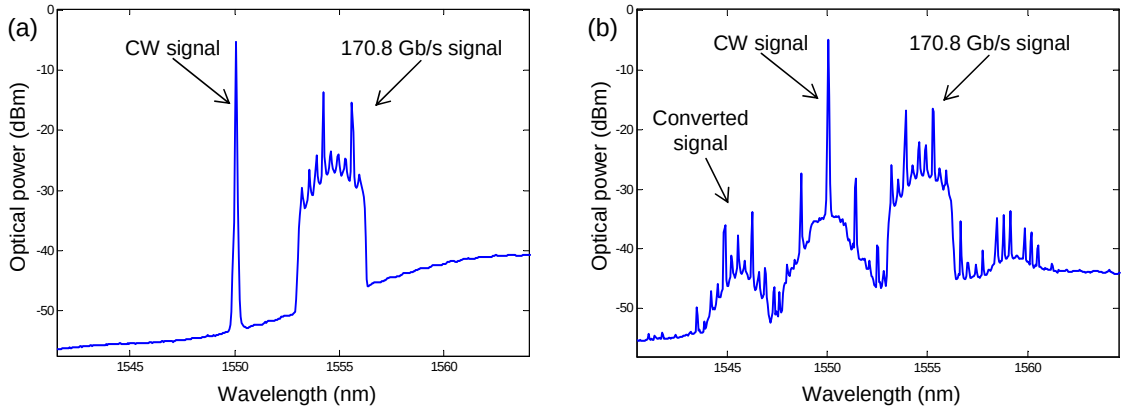

Figure 4.22: (a) spectra of a 170.8 Gb/s OOK signal and a CW at the input and (b) FWM spectra at the output of the GeAsSe2012 fiber.

The WS at the output of the GeAsSe fiber is not only a filter, it also compensates for the chirp of the converted signal which arises due to its propagation through short lengths of connecting fiber. The eye diagram of the 170.8 Gb/s OOK converted signal is illustrated in Figure 4.23. Comparing to the input 170.8 Gb/s OOK signal (Figure 4.20(b)), the eye diagram exhibits more noise on "one" level than the eye diagram before wavelength conversion. It is however cleaner at "zero" level. It can be understood by considering the input power magnitude with the FWM effects and offset filtering of the output filters. The two adjacent pulses in the converted eye diagram slightly overlap in time. This may be caused by the tight output filtering.

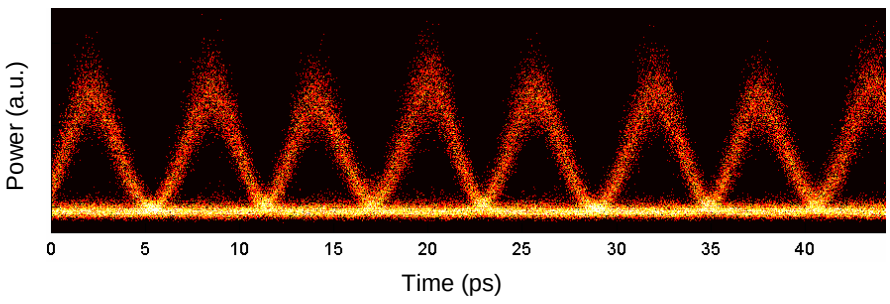

Figure 4.23: Eye diagram of the 170.8 Gb/s OOK converted signal at the wavelength 1545.5 nm.

To assess the wavelength conversion experiment, the BER is measured. The setup to analyse the BER is shown in Figure 4.24. Since our BER tester system is designed for 42.7 Gb/s measurement, the 170.8 Gb/s signal is first time-division demultiplexed to 42.7 Gb/s. This is implemented by using an electroabsorption modulator (EAM). A part of the 170.8 Gb/s signal taken from a 3 dB coupler is used for clock recovery. It is injected into the QD-MLLD to generate a 42.7 GHz optical clock. The 42.7 GHz optical clock is then sent to the clock recovery (CR) to obtain the electrical clock for the EAM. Thus at the output of the EAM, we obtained the 42.7 Gb/s optical signal required for BER testing system. As mentioned in Section 4.2.2, the 42.7 Gb/s signal is electrical time-division demultiplexed 1 : 4 before reaching the BERT.

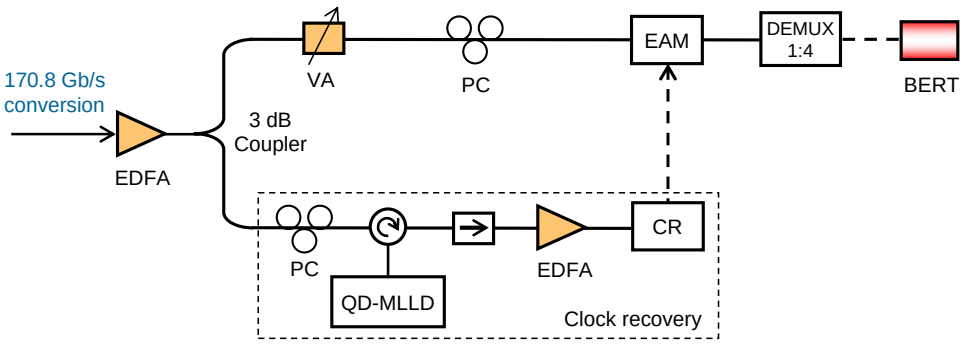

Figure 4.24: Experimental setup to analyse the BER of 170.8 Gb/s signal. Solid lines for optical signal links and dash lines for electrical signal links.

Figure 4.25 describes the BER evolution for the converted and the B2B 170.8 Gb/s OOK signals. It shows about 2 dB of power penalty. This can be attributed to the low power of the converted wave leading to the optical signal-to-noise ratio (OSNR) of the converted signal being lower than the input signal. In the experiment, when the input power increases

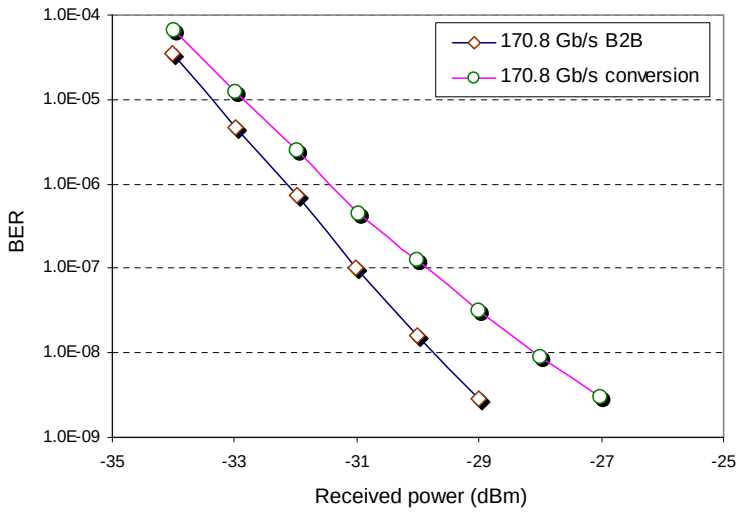

Figure 4.25: BER measurement of the converted 170.8 Gb/s OOK signal and B2B reference.

the power penalty is reduced. Unfortunately, chalcogenide fibers could not tolerate a power higher than about 21 dBm.

Even if there is a power penalty of 2 dB, this is the first time, to the best of our knowledge, that a wavelength conversion at bit rates higher than 160 Gb/s is demonstrated in chalcogenide MOFs. The total input power used in the experiment was 100 mW. One, however, can use longer fibers than 50 cm to reduce the optical power. Longer fibers also helps to increase the FWM efficiency to avoid the power penalty.

4.2.5 Conclusion

Based on FWM in chalcogenide MOFs, we have presented wavelength conversions for four types of modulated signals. A 42.7 GHz clock signal was firstly experimented using the AsSe2011 fiber with the nonlinear coefficient γ of 46000 $W^{-1}km^{-1}$. The high nonlinearity of the fiber allows us to implement a wavelength conversion with a high efficiency of -17.5 dB. The total average power of the signal and the pump was 33.1 mW. The results are reported at *the ECOC conference* in Geneva, Switzerland in 2011 [171] and in *Optics Express* Vol. 19 (26), 2011 [70]. At ECOC2011, the communication was selected to be one of the eight finalists of the ECOC2011 *"Best Student Paper Presentation Award"*.

Using the GeAsSe2011 fiber ($\gamma = 11000$ $W^{-1}km^{-1}$ and $D = -500$ ps/km/nm), 42.7 Gb/s OOK signal and 56 Gb/s DQPSK signal wavelength conversions were demonstrated. In the 42.7 Gb/s wavelength conversion experiment, the total average power used is 56 mW with a CW power of 21.4 mW. The conversion bandwidth was 2.6 nm. We obtained an error-free wavelength conversion with a power penalty of only 0.4 dB (at BER of 10^{-9}). In the case of the 56 Gb/s DQPSK wavelength conversion, the total average power used was 45 mW with a CW power of 24 mW. An error-free wavelength conversion was also achieved with a conversion bandwidth of 3.2 nm. A power penalty of 1 dB was found at a BER of 10^{-9}. To the best of our knowledge, wavelength conversion of a 42.7 Gb/s OOK signal and a 56 Gb/s DQPSK signal in chalcogenide MOFs was demonstrated for the first time. Total input powers used in the experiments were lower than 56 mW. These results were presented at *the OFC conference* in Los Angeles, CA in 2012 [172] and in *Optics Letters* Vol. 37 (22), 2012 [173].

The GeAsSe2012 fiber with higher nonlinearity ($\gamma = 25000$ $W^{-1}km^{-1}$) and lower dispersion ($D = -310$ ps/km/nm) was used to achieve a 170.8 Gb/s OOK signal wavelength conversion experiment. We obtained an error-free wavelength conversion with a total average power of the signal and the pump of 100 mW in which the CW power is 56 mW. The conversion bandwidth is 4.65 nm. Even though, a power penalty of about 2 dB was measured, this was a significant result with a 170.8 Gb/s signal. The 170.8 Gb/s signal wavelength conversion was submitted to *IEEE Photonics Technology Letters* [207]. Table 4.1 summaries the four wavelength conversion experiments using chalcogenide MOFs.

Table 4.1: Wavelength conversion using chalcogenide MOFs

Signal	MOF fiber	Conversion bandwidth (nm)	Total average power (mW)	Publications
42.7 GHz clock	AsSe2011	7.3	33.1	ECOC2011 [171], Opt. Express [70]
42.7 Gb/s OOK	GeAsSe2011	2.6	56	OFC2012 [172], Opt. Lett. [173]
56 Gb/s DQPSK	GeAsSe2011	3.2	45	ECOC2012 [174], Opt.Lett. [173]
170.8 Gb/s OOK	GeAsSe2012	9.3	100	IEEE PTL [207] (submitted)

4.3 All-optical demultiplexing

The principle of fiber-based all-optical signal demultiplexing is similar to FWM-based wavelength conversion as described in the previous section. Instead of utilizing a CW pump, a clock signal is used. Figure 4.26 depicts the principle of demultiplexing of a 160 Gb/s signal to a 40 Gb/s signal with a 40 GHz clock in a nonlinear fiber.

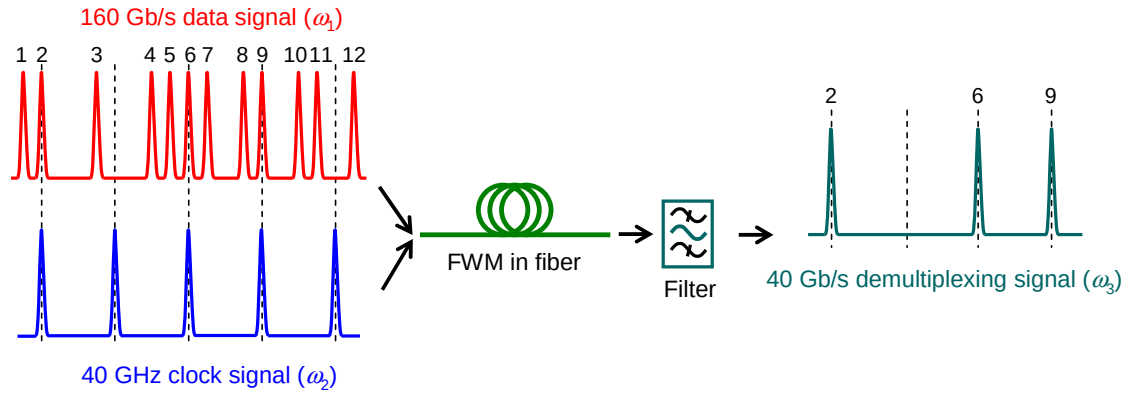

Figure 4.26: Principle of FWM-based demultiplexing from 160 Gb/s to 40 Gb/s in a nonlinear fiber.

The input data signal works at frequency ω_1 and the clock signal at frequency ω_2. FWM effect produces a new frequency ω_3 that is desired as a demultiplexing wave. Only the pulses of the 160 Gb/s data signal that are coincident with the clock pulses are collected. For the example in Figure 4.26, the pulses number 2, 6, and 9 are demultiplexed. By varying the time-delay between the 40 GHz clock signal and the 160 Gb/s data signal, one can select the demultiplexing of one of the four tributary channels of the 160 Gb/s signal.

This section is devoted to the demonstration of FWM-based all-optical demultiplexing in chalcogenide fibers. 85.4 Gb/s and 170.8 Gb/s time-division demultiplexing down to 42.7 Gb/s signal are demonstrated. All experiments are implemented with the GeAsSe2012 fibers which are described in Section 3.4.4.

4.3.1 42.7 Gb/s wavelength conversion

Before implementing directly a time-division demultiplexing experiment of a higher bit rate to a lower bit rate, we did the experiment with two identical bit rates. For this, we chose a signal at 42.7 Gb/s and a clock at 42.7 GHz. This experiment is therefore similar to a wavelength conversion experiment rather than a demultiplexing experiment, but is interesting to valid the principle of time-division demultiplexing.

In this experiment, a pulse clock signal replaces the CW pump. A variable time-delay must then be used to adjust temporally both pulsed signals. Let us notice also that, given the peak power advantage of a pulsed clock signal, the total average power required for the experiments is reduced compared to a case of FWM with a CW signal. In addition, unlike FWM with a CW pump, the group-velocity mismatch (GVM) between two pulsed signals needs to be considered. GVM occurs because two optical pulses propagating at different wavelengths in a fiber have different group velocities. This phenomenon leads to temporal walk-off between the 42.7 Gb/s pulse and the 42.7 GHz pulse. GVM or temporal walk-off depends on the value of the dispersion D, the wavelength detuning between the two pulse signals $\Delta\lambda$, and the pulse durations T_0. Two pulse signals will undergo temporal walk-off when they propagate over a distance which exceeds the walk-off length, L_w, which is defined by Eq. (3-17) in Section 3.4.4. We recall here the formula of the walk-off length:

$$L_w = \frac{T_0}{\Delta\lambda\,|D|} \tag{4-1}$$

The walk-off length is the length of fiber for which two pulses of duration T_0 at different wavelengths separated by $\Delta\lambda$ are delayed by T_0 as seen in Figure 4.27. For example, for two pulses of duration $T_0 = 4.5$ ps, a wavelength detuning $\Delta\lambda = 2.8$ nm, and a dispersion $D = -310$ ps/km/nm, the walk-off length is calculated to be $L_w = 5.2$ m.

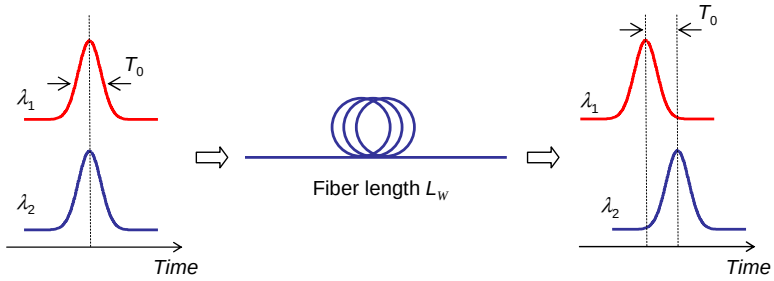

Figure 4.27: Description of the walk-off length for two pulses of duration T_0.

The setup to generate a 42.7 Gb/s signal and a 42.7 GHz clock signal is shown in Figure 4.28. The generation of the 42.7 GHz optical clock signal is similar to the description given in Section 4.2.1. After the 3 dB coupler, one part of the 42.7 GHz optical clock signal is filtered by a tunable 3.5 nm Gaussian filter. It is amplified before being injected into the MZI to be encoded with PRBS pattern of 2^7-1 bit length to obtain a 42.7 Gb/s data signal. It is then re-filtered by a 3 nm filter centered at 1559 nm. The other part of the 42.7 GHz

optical clock signal is passed through a 3 nm filter centered at 1556.2 nm to obtain a clock signal at a different wavelength. An optical delay line ($\Delta\tau$) is inserted after the filter to align temporally the data signal and the clock signal.

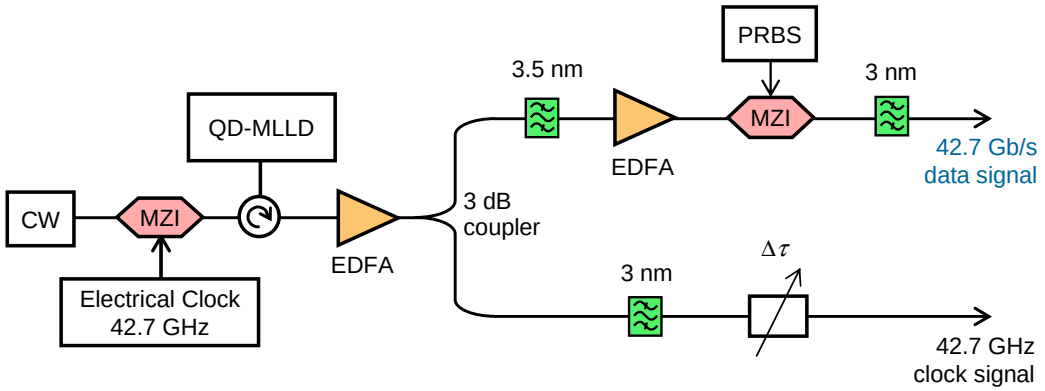

Figure 4.28: Illustration of 42.7 Gb/s and 42.7 GHz signals generation.

Figure 4.29 illustrates the experimental setup for 42.7 Gb/s FWM-based wavelength conversion with a clock signal. The GeAsSe2012 fiber (described in Section 3.4.4) is used. The length of the fiber is 50 cm. This length is much shorter than L_w of 5.2 m for a wavelength detuning of 2.8 nm and a pulse duration of 4.5 ps as calculated above. Two pulse signals are amplified by EDFAs and polarization aligned by PCs. They are then passed through a *Finisar WaveShaper* (WS). The WS serves as filters for both signals. It is programed to be Gaussian filters of 1.5 nm bandwidth at 3 dB intensity point for both signals. They are centered at 1556.2 nm for the clock signal and 1559 nm for the data signal. The pulse width of both signals is 4.5 ps. As calculated in Section 4.2.4, the wavelength conversion range $\Delta\lambda_c$ of this fiber is 5 nm, large enough for both signal spectra. The WS also serves as a coupler to combine the clock signal and the data signal as we can see in Figure 4.29.

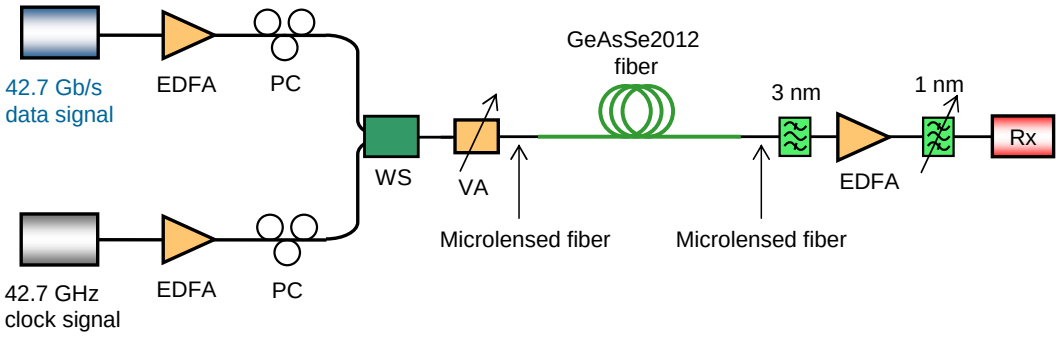

Figure 4.29: Experimental setup for 42.7 Gb/s FWM-based wavelength conversion.

To couple signals in the GeAsSe fiber, microlensed fibers with an MFD of 3.1 μm are used. The total average power launched into the GeAsSe fiber is adjusted by a variable attenuator (VA). In this experiment, no filter is used at the input of the fiber due to a low

ASE noise except for the WS. The spectrum of both signals at the input of the fiber is displayed in Figure 4.30. The wavelength detuning $\Delta\lambda$ is 2.8 nm in this case. At the output of the GeAsSe fiber, the FWM waves appear at both sides as seen in Figure 4.31. Thanks to the fact that both signals are similar, the spectrum at the output of the GeAsSe fiber is symmetric. We can pick out the Stokes wave or anti-Stokes wave for the converted signal.

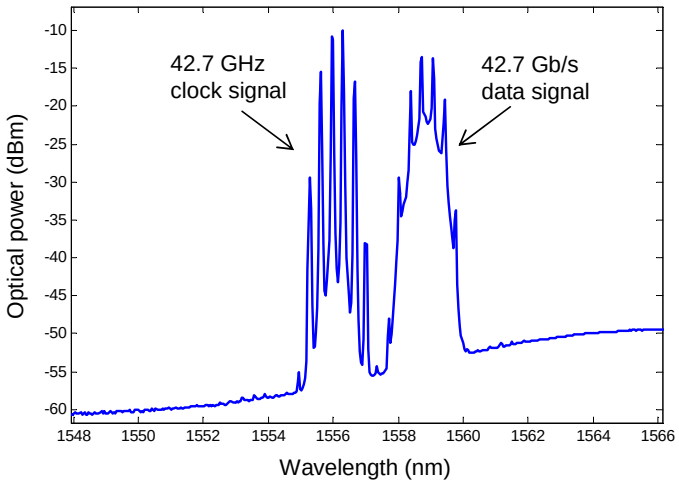

Figure 4.30: Spectrum of 42.7 Gb/s and 42.7 GHz signals at the input of the GeAsSe2012 fiber.

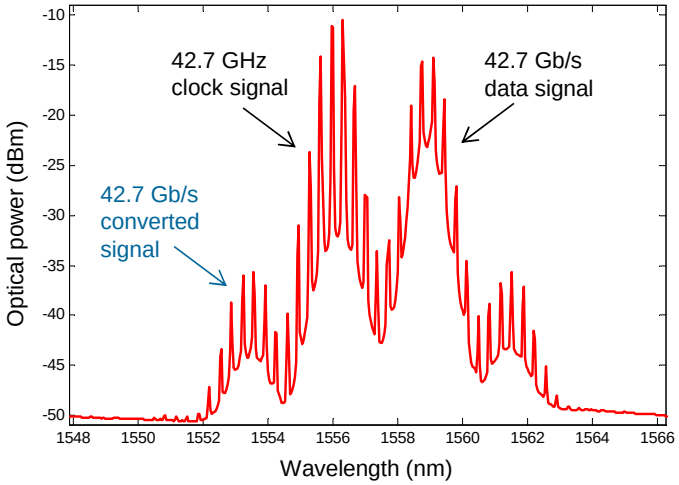

Figure 4.31: Spectrum at the output of the GeAsSe2012 fiber.

In the experiment, the total average power measured at the output of the VA is 16 dBm (40 mW). The clock signal power is set a little higher than the data signal power. The average power of the clock is 13.5 dBm (22 mW). The anti-Stokes wave is thus chosen for the 42.7 Gb/s converted signal. To have a maximum FWM at the output of the fiber, the data signal and the clock must be well synchronized in time. This is done by varying the delay line ($\Delta\tau$). Figure 4.32 gives an example of eye diagrams of both data signal and clock signal in a good alignment.

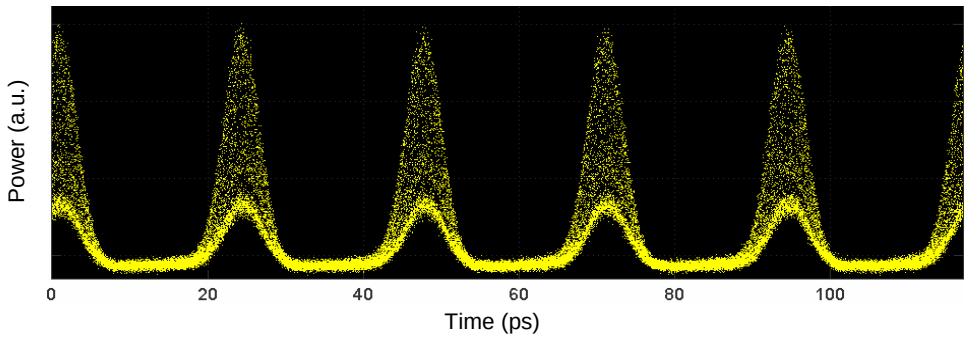

Figure 4.32: Eye diagrams of 42.7 Gb/s data signal and 42.7 GHz clock signal at the input of the GeAsSe2012 fiber.

At the output of the GeAsSe fiber, to filter out the 42.7 Gb/s converted wave, a 3 nm filter is firstly used. The power of the converted signal after the filter is -18.5 dBm. The filtered signal is amplified by an EDFA and then re-filtered by a 1 nm bandwidth Gaussian filter to reshape the waveform. The two filters are centered at 1553.4 nm. The eye diagram of the converted signal is displayed in Figure 4.33. It is widely opened. The pulse duration of the converted signal is 6.5 ps. It is longer than that of the input 42.7 Gb/s signal since the spectrum is more tightly filtered.

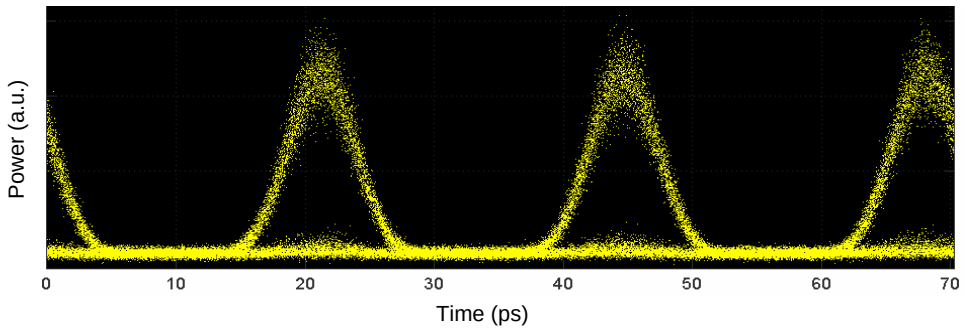

Figure 4.33: Eye diagram of the converted 42.7 Gb/s at the receiver Rx.

The BER measurement of the wavelength conversion experiment is shown in Figure 4.34. There is no significant power penalty for this conversion. The two curves of BER evolution for the B2B case and the conversion case are quasi-coincident. The original 42.7 Gb/s OOK signal at wavelength of 1559 nm is converted by 5.6 nm ($\Delta\lambda = 2.8$ nm) to the wavelength 1553.4 nm. The error-free wavelength conversion of 42.7 Gb/s OOK signal based on FWM with a clock signal is achieved in the GeAsSe fiber. We have also obtained the same result for the red-shifted wavelength conversion by picking out the Stokes wave.

As calculated above, the zero wavelength detuning $\Delta\lambda_0$ of the fiber is 7.2 nm. In other words, the wavelength detuning $\Delta\lambda$ between two signals can be larger than 2.8 nm. The experiment is investigated for a wavelength detuning $\Delta\lambda$ up to 5.2 nm. For this case, the walk-off length L_w of 2.8 m is still longer than the length of fiber (50 cm). With a wavelength detuning $\Delta\lambda$ of 5.2 nm, the signal is converted in wavelength by 10.4 nm. For $\Delta\lambda$ higher

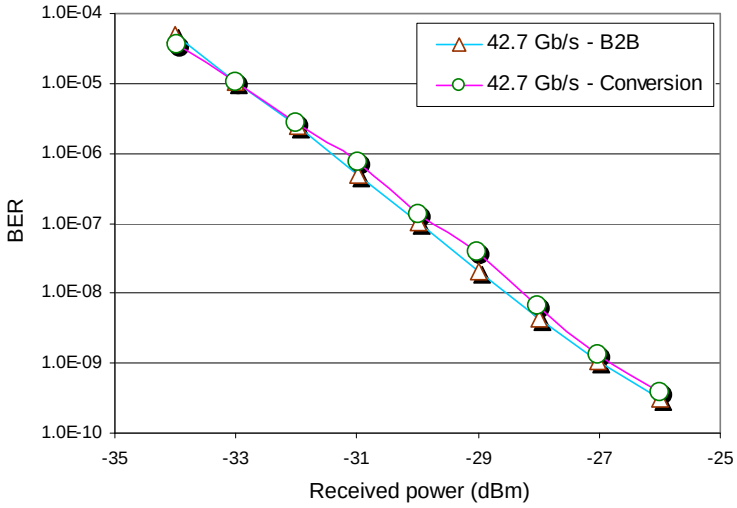

Figure 4.34: Evolution of BER measurement for the 42.7 Gb/s converted signal.

than 2.8 nm, because the Stokes wave is located at the edge of the EDFA gain, only the anti-Stokes wave was considered. The total average power used was 16.5 dBm (45 mW). The same to the case of $\Delta\lambda = 2.8$ nm, no significant power penalty was found. We obtained error-free operation for $\Delta\lambda$ up to 5.2 nm. Figure 4.35 illustrates the spectrum at the output of the GeAsSe2012 fiber for the case of $\Delta\lambda = 5.2$ nm.

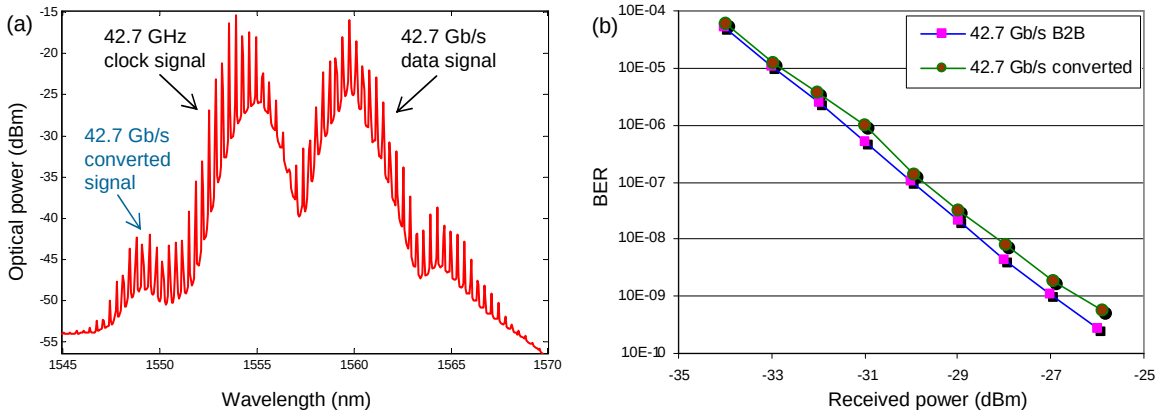

Figure 4.35: (a) spectrum at the output of the GeAsSe2012 fiber for the case of $\Delta\lambda = 5.2$ nm and (b) evolution of BER measurement for the 42.7 Gb/s converted signal for $\Delta\lambda = 5.2$ nm.

4.3.2 85.4 Gb/s OOK demultiplexing

In this section, we continue to exploit FWM effects in the same GeAsSe2012 fiber for time-division demultiplexing. In this section, a 85.4 Gb/s to 42.7 Gb/s time-division demultiplexing is presented. As mentioned previously, two pulses will exhibit temporal walk-off when they propagate along a fiber. The length of the fiber used in the experiment must therefore be much shorter than L_w.

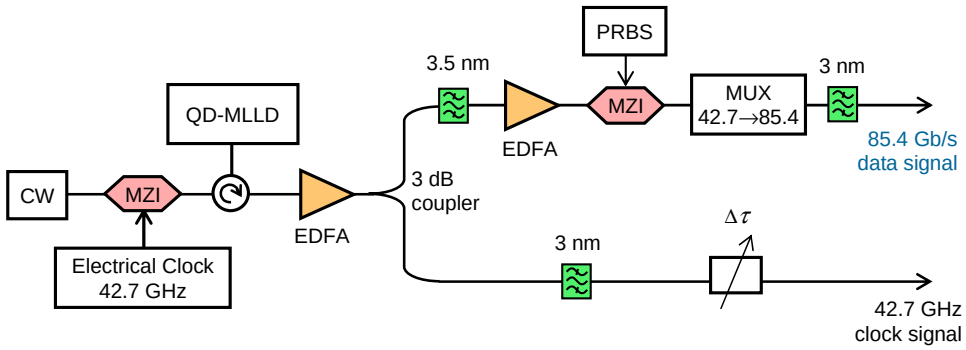

Figure 4.36: Generation of 85.4 Gb/s OOK signal and 42.7 GHz clock signal.

It is useful to recall the values of the nonlinear coefficient $\gamma = 25000$ W^{-1}km^{-1} and the dispersion $D = -310$ ps/km/nm of the fiber. Taking this as an example, for two signals with pulse durations of 5 ps and a wavelength detuning $\Delta\lambda$ of 2.8 nm, the L_w of the fiber is 5.8 m (using Eq. (4-1)). In the demultiplexing experiment of a 85.4 Gb/s signal, we will use the GeAsSe2012 fiber with a length of 50 cm.

The setup to generate 85.4 Gb/s OOK RZ signal and 42.7 GHz clock signal is depicted in Figure 4.36. It is similar to the generation of 42.7 Gb/s and 42.7 GHz signals that is described in the previous section. For the data signal branch, a temporal multiplexer (MUX) is used to time-division multiplex two channels at 42.7 Gb/s to make a 85.4 Gb/s signal. A PRBS pattern with a length of $2^7 - 1$ bits is encoded by a MZI to produce a OOK data signal. The data signal is filtered by a 3 nm bandwidth filter centered at 1559 nm. The clock signal is also filtered by a 3 nm bandwidth filter but centered at a different wavelength of 1556.2 nm. Figure 4.37 presents the eye diagrams of both 85.4 Gb/s and 42.7 GHz signals.

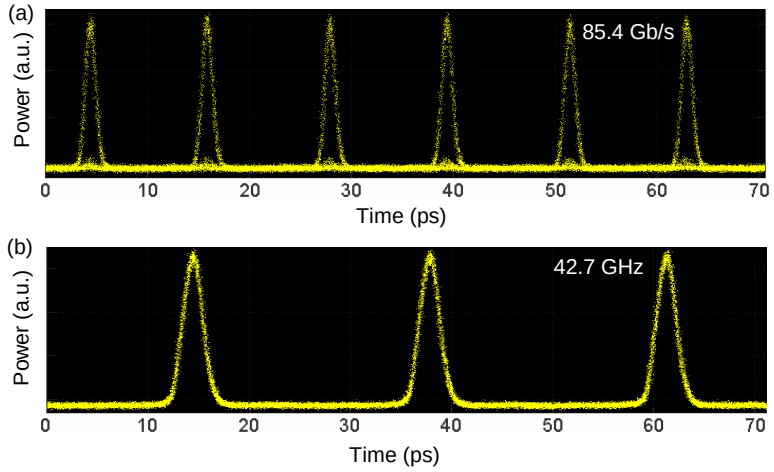

Figure 4.37: Eye diagrams of 85.4 Gb/s signal and 42.7 GHz signal.

The experimental setup for FWM-based time-division demultiplexing of a 85.4 Gb/s signal to a 42.7 Gb/s signal is similar to the 42.7 Gb/s wavelength conversion based on FWM with a 42.7 GHz clock signal. For easy reference, it is re-drawn in Figure 4.38. After

amplification, the two signals are filtered and coupled by a WS. Both signals are programmed to pass Gaussian filters of band-pass 1.5 nm at 3 dB intensity points. The 85.4 Gb/s OOK signal is centered at 1559 nm and the 42.7 GHz clock signal at 1556.2 nm. The filtering effect of the WS makes the pulse duration longer. Both waves thus can be located at closer positions in wavelength. This process helps to reduce the temporal walk-off between the data signal and the clock signal.

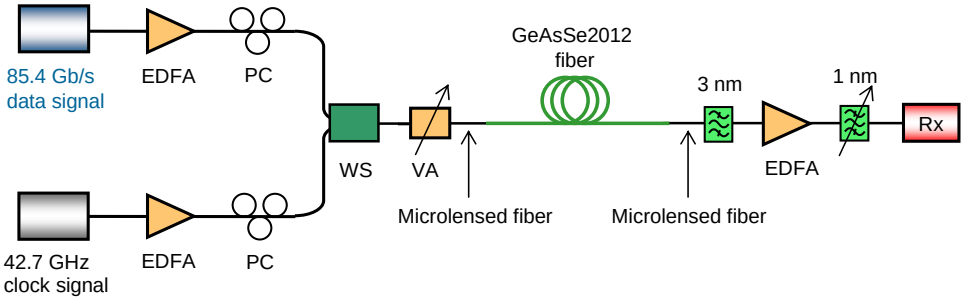

Figure 4.38: Experimental setup of FWM-based 85.4 Gb/s signal demultiplexing

Figure 4.39 shows the eye diagrams of both signals after the WS. They both have a pulse width of 5 ps compared to 2 ps in the original pulses as seen in Figure 4.37. An observation of the spectra of both signals is given in Figure 4.40. For this case, the wavelength detuning $\Delta\lambda$ is 2.8 nm. The spectrum of the 85.4 Gb/s data signal is not quite symmetric due to the amplification band of the EDFA. This does not, however, affect the demultiplexing experiment.

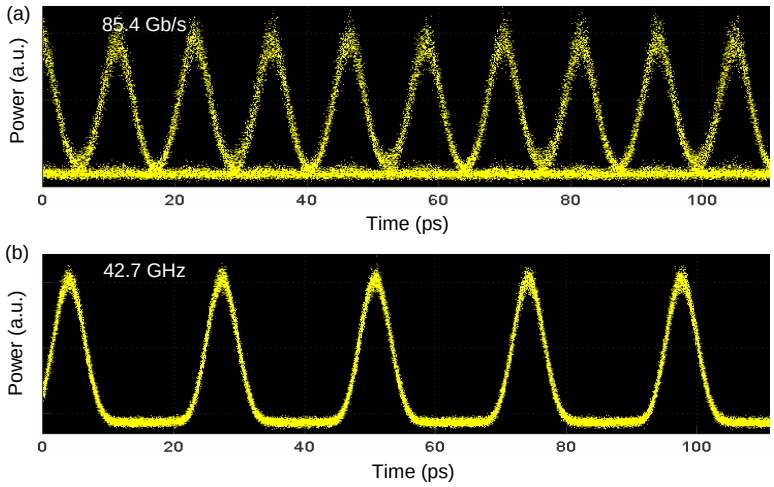

Figure 4.39: Eye diagrams of 85.4 Gb/s data signal 42.7 GHz clock signal after the WS.

Here, for demultiplexing of a 85.4 Gb/s signal, because of a lower duty-cycle we need a little higher power for the experiment compared to the case of 42.7 Gb/s wavelength conversion in the previous section. The total power measured after the VA is 16.5 dBm (45 mW), in which the power of the 42.7 GHz clock signal is 14.7 dBm (29.5 mW). In order

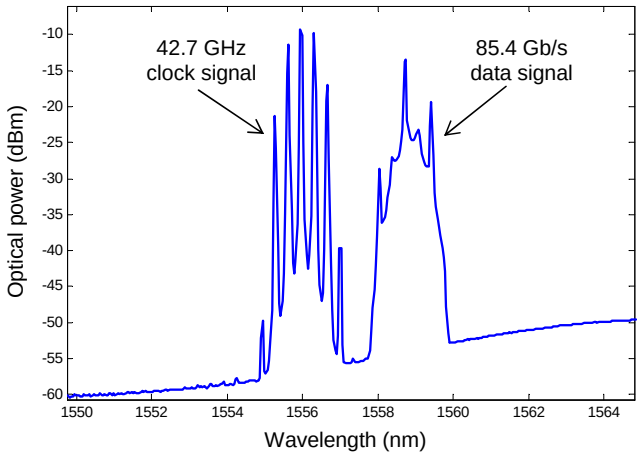

Figure 4.40: Spectra of the 85.4 Gb/s data signal and the 42.7 GHz clock signal at the input of the GeAsSe2012 fiber.

to have maximum FWM efficiency at the output of the GeAsSe fiber, the two pulsed signals must be in good temporal alignment. By controlling the delay line ($\Delta\tau$), we can gradually adjust the clock signal to the optimal setting. Figure 4.41 illustrates the case where two signals are temporally synchronized. The tributary channel 1 is chosen to be time-division demultiplexed from the 85.4 Gb/s OOK signal. By moving forward by one bit-time the clock signal, one can perform time-division demultiplexing for the tributary channel 2.

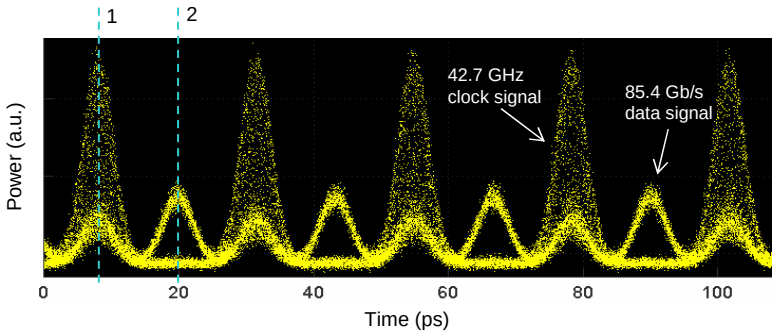

Figure 4.41: Eye diagram of 85.4 Gb/s and 42.7 GHz signals before being injected into the GeAsSe fiber.

An example of the spectrum at the output of the GeAsSe fiber is shown in Figure 4.42. The data signal at 1559 nm and the clock signal at 1556.2 nm interact with each other to generate two new waves around the wavelengths 1553.4 nm and 1561.8 nm. In the experiment, the power of the 42.7 GHz clock signal (14.7 dBm) is higher than the power of the 85.4 Gb/s signal (12 dBm). Therefore, its peak power is much higher than that of the 85.4 Gb/s signal (21.4 dBm compared with 15.7 dBm). The blue-shifted wave (anti-Stokes) intensity is hence larger than the red-shifted one. The blue-shifted wave is thus chosen for demultiplexing.

At the output of the GeAsSe fiber, a 3 nm flattop filter centered at 1553.4 nm is firstly

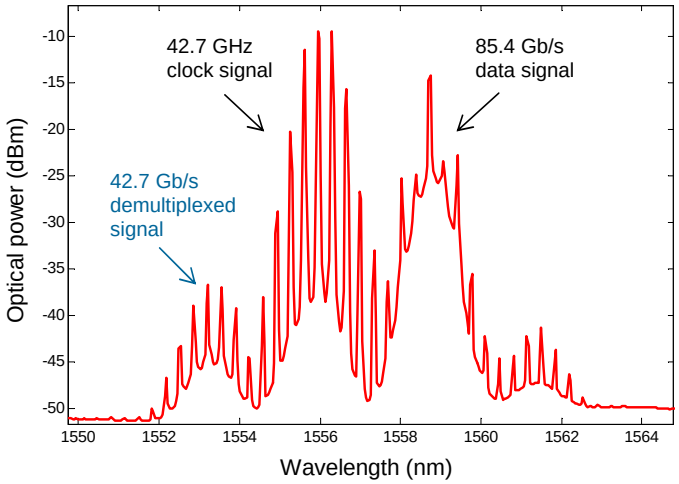

Figure 4.42: Spectrum at the output of the GeAsSe fiber.

used to reject the original 85.4 Gb/s wave and the original 42.7 GHz clock signal which are strong compared to the idler waves. The power of the remaining signal after the filter is measured to be −19 dBm. The signal is then amplified by an EDFA before being re-filtered by a Gaussian filter of 1 nm bandwidth at 3 dB intensity points at 1553.4 nm. It is then straightforwardly sent to a BER tester equipment for BER measurement and to an optical sampling oscilloscope (OSO) for eye diagram observation. Figure 4.43 illustrates the eye diagram of the first tributary signal at 42.7 Gb/s demultiplexed from the 85.4 Gb/s OOK signal. As explained in the previous section, because of the narrow filtered-spectrum, the pulse duration is longer compared to the input 85.4 Gb/s signal. It is measured to be 6.5 ps as seen in Figure 4.43.

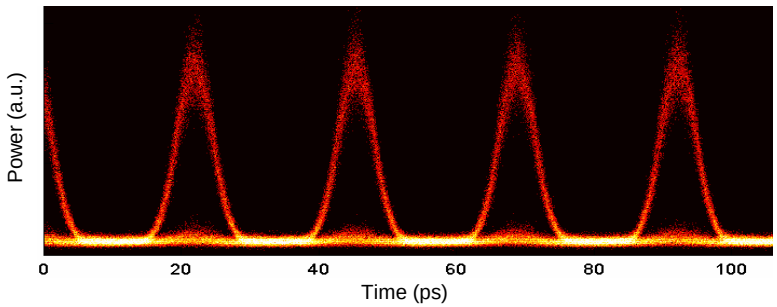

Figure 4.43: Eye diagram of the 42.7 Gb/s signal demultiplexing from a 85.4 Gb/s signal.

To assess the performance of the demultiplexing experiment, the BER on both tributaries is measured. Figure 4.44 depicts the BER evolution for the 42.7 Gb/s B2B case and for the two 42.7 Gb/s demultiplexed tributaries. Similar to the case of the previous 42.7 Gb/s wavelength conversion, they are almost coincident. There is a negligible power penalty for both tributary channels. The measurement thus demonstrates error-free time-division demultiplexing of a 85.4 Gb/s signal to a 42.7 Gb/s OOK RZ signal.

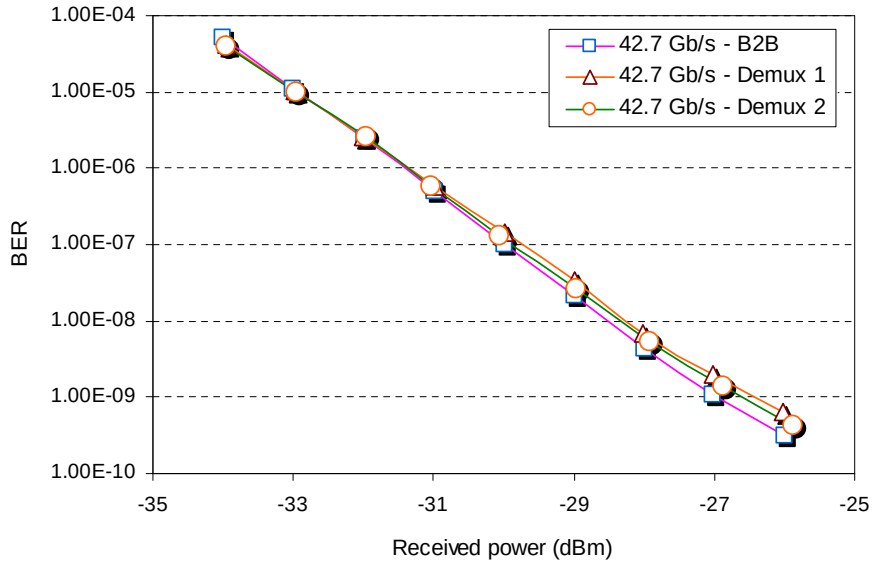

Figure 4.44: BER measurement of the 85.4 Gb/s signal demultiplexing to a 42.7 Gb/s signal.

The 85.4 Gb/s-to-42.7 Gb/s demultiplexing in the chalcogenide MOF was demonstrated with error-free and no power penalty with the total input power of only 45 mW. The power of the demultiplexed signal was −19 dBm. Related work reported in 2012 on 80 Gb/s-to-10 Gb/s demultiplexing using a dispersion-flattened highly nonlinear photonic crystal fiber (HNL-PCF) used an total input power of 26.8 dBm (480 mW) and had a power penalty of 4.6 dB [208]. Another experiment on 80 Gb/s-to-10 Gb/s demultiplexing was reported in 2011 by using a 500 m HNLF, the power is 25 dBm and the power penalty is 2.5 dB [209]. A report on 80 Gb/s-to-40 Gb/s demultiplexing using a SOA [210] has the advantage of low input power (7 dBm). It however has a power penalty of 5 dB.

4.3.3 170.8 Gb/s OOK demultiplexing

This section considers time-division demultiplexing at 170.8 Gb/s in a microstructured chalcogenide fiber. The generation setup of the 170.8 Gb/s OOK signal and the 42.7 GHz clock signal is the same as the setup in Figure 4.36 for 85.4 Gb/s demultiplexing. In the 170.8 Gb/s generation setup, because pulses at the output of the laser are not Fourier transform limited, 20 m of a SMF is used before the 3-dB coupler to compensate for the residual chirp. The temporal width of the pulse is then compressed by the SMF which has an anomalous dispersion ($D > 0$).

The 42.7 GHz clock signal is amplified by an EDFA before being divided into two parts by a 3 dB coupler. One part of the 42.7 GHz clock signal is passed through a 3.5 nm Gaussian filter centered at 1556.2 nm and data encoded with a PRBS by a MZI. The 42.7 Gb/s PRBS-encoded signal has a $2^7 - 1$ bit length. It is then passed through an optical 4:1 time-division multiplexer to produce a 170.8 Gb/s OOK signal. The spectrum of the 170.8 Gb/s data signal is shown in Figure 4.45(a) and its corresponding eye diagram in

Figure 4.46(a). The pulse width of the 170.8 Gb/s signal is 1.2 ps for a bit-time of 5.9 ps.

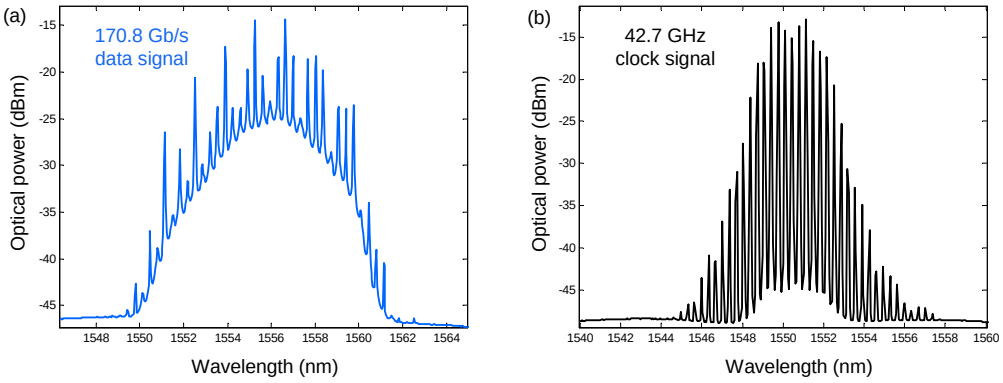

Figure 4.45: Spectra of (a) the 170.8 Gb/s OOK signal and (b) the 42.7 GHz clock signal.

The second part of the 42.7 GHz optical clock signal is filtered by a 3 nm filter centered at 1550.8 nm. Its spectrum and eye diagram can be seen in Figure 4.45(b) and Figure 4.46(b), respectively. The duration of the optical clock pulses is 2 ps. As previously, this clock signal can be temporally detuned by a delay line ($\Delta\tau$) in order to be synchronized with the 170.8 Gb/s data signal.

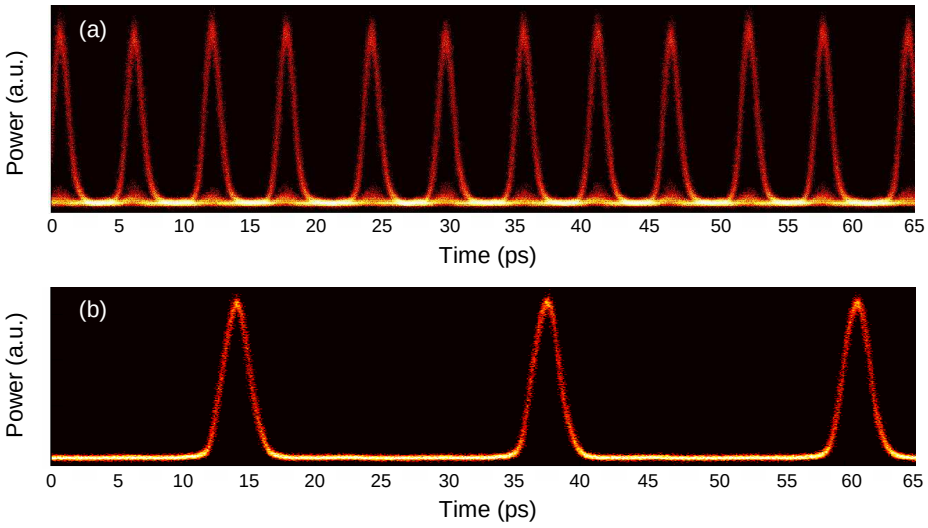

Figure 4.46: Eye diagrams of (a) the 170.8 Gb/s OOK signal and (b) the 42.7 GHz clock signal.

The same experimental setup as for FWM-based 85.4 Gb/s demultiplexing is now used for the demultiplexing of a 170.8 Gb/s signal to 42.7 Gb/s signals (Figure 4.38). Similar to the 85.4 Gb/s demultiplexing, a waveshaper (WS) is used as filters to filter both signals while tailoring the dispersion. It is set to be Gaussian filters for both signals. The 170.8 Gb/s data signal is filtered at a center wavelength of 1556.2 nm. Its has a spectral width at 3 dB intensity point of 2 nm. The spectrum of the 170.8 Gb/s data signal is truncated by the WS programed as a sharp-Gaussian filter (as mentioned in Section 4.2.4) with a total

bandwidth of 3.2 nm centered at 1556.2 nm. The pulse width of the 170.8 Gb/s before injection into the GeAsSe fiber is 2.4 ps. The 42.7 GHz optical clock signal is filtered by the 1.5 nm programed Gaussian filter. Its spectral width is then truncated by a 2.4 nm flattop programed filter. The sharp-Gaussian filter produced by the WS is centered at the wavelength of 1550.8 nm. The pulse duration of the clock signal is 3.4 ps. The WS also serves as a coupler to combine the 170.8 Gb/s data signal and the 42.7 GHz clock signal for FWM experiment as seen in Figure 4.38. Figure 4.47 presents the eye diagram of the 170.8 Gb/s data signal and the 42.7 Gb/s clock signal before the GeAsSe fiber.

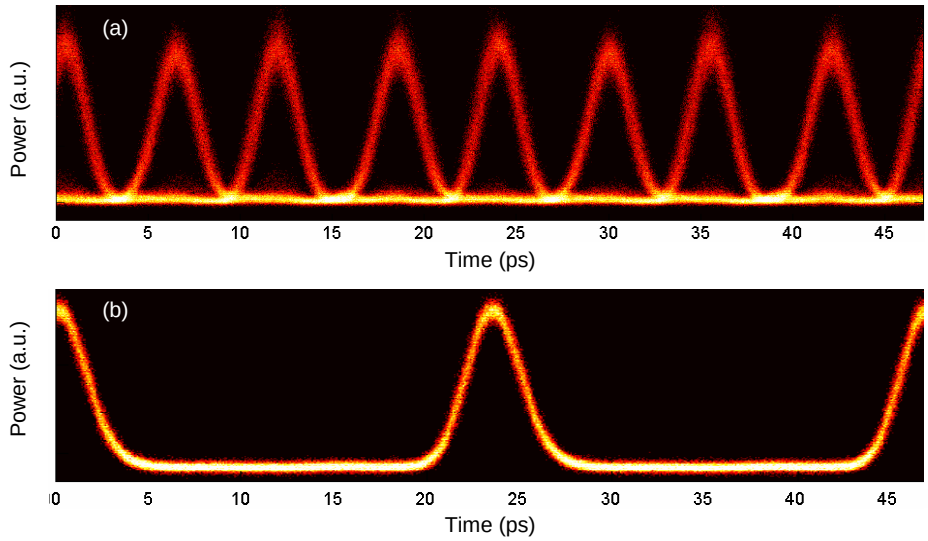

Figure 4.47: Eye diagrams of (a) the 170.8 Gb/s signal and (b) the 42.7 GHz clock signal after the WS.

The 170.8 Gb/s and the 42.7 GHz signals are amplified by an EDFA. They are then passed through a tunable filter which is set to 8 nm bandwidth and centered at the wavelength of 1554 nm. This filter eliminates the ASE noise emitted by the EDFA for the wavelengths beyond 1549.8 nm and 1557.8 nm. Figure 4.48 shows the spectrum of both signals at the input of the GeAsSe2012 fiber.

As discussed in Section 4.3.2, the group-velocity mismatch (GVM) is important during the FWM process of two pulse signals. Due to the pulse duration of the signals ($T_0 = 2.4$ ps), being here shorter than for the 85.4 Gb/s case ($T_0 = 5$ ps), a walk-off length L_w is thus 1.4 m for a wavelength detuning $\Delta\lambda$ of 5.4 nm. With the 50 cm long GeAsSe2012 fiber, we have measured a temporal walk-off of about 900 fs between the two pulse signals after propagating through the fiber. Note that this measurement is not accurate as it is limited by the sampling oscilloscope resolution but the eye diagram of Figure 4.49 clearly shows a temporal mismatch between both signals at the output of the fiber. In a demultiplexing approach, this temporal mismatch will lead to an eye closure and to a reduction of the FWM efficiency. The temporal mismatch also induces fluctuations at "one" level of demultiplexed signals. The GeAsSe2012 fiber with 50 cm length is thus not appropriate for implementing

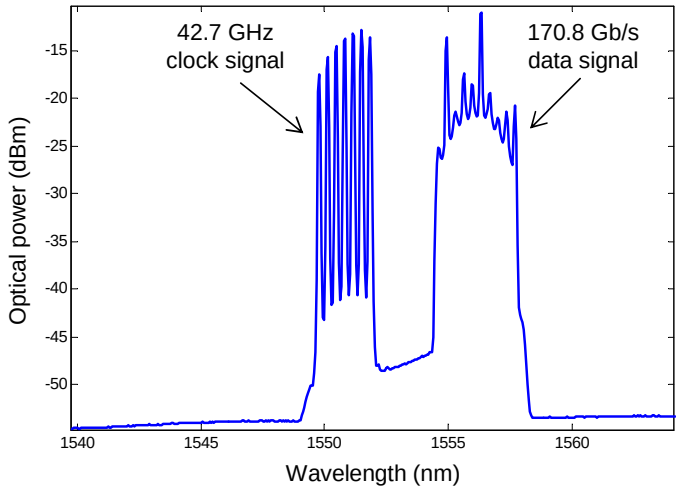

Figure 4.48: Spectra of 170.8 Gb/s OOK signal and 42.7 GHz clock signal at the input of the GeAsSe2012 fiber.

170 Gb/s demultiplexing as it was used in the 85.4 Gb/s signal demultiplexing case.

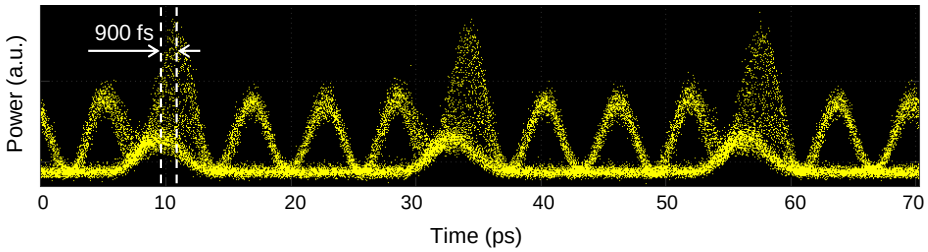

Figure 4.49: Illustration of temporal walk-off of the 170.8 Gb/s signal and the 42.7 GHz clock signal after the 50 cm GeAsSe2012 fiber.

In order to reduce the temporal walk-off, a shorter fiber should be used for the FWM-based experiment at 170.8 Gb/s. As described in Section 3.4.4, in 2012, two GeAsSe2012 fibers with the same characteristics were fabricated. They are just different in length. One is 50 cm length and the other is 30 cm. We use the latter to investigate the 170.8 Gb/s to 42.7 Gb/s demultiplexing. For the 30 cm GeAsSe2012 fiber, the wavelength conversion range $\Delta\lambda_c$ is 6.2 nm as mentioned in Section 3.4.4.

For the 30 cm GeAsSe2012 fiber, the temporal walk-off between the 170.8 Gb/s pulses and the 42.7 GHz pulses is measured to be about 500 fs. Figure 4.50 illustrates an example of spectrum at the output of the 30 cm GeAsSe2012 fiber. The total power of both signals before the GeAsSe fiber is 18 dBm (63 mW) in which the power of the 42.7 GHz clock signal is 15.5 dBm (36 mW). The output spectrum shows the obvious FWM idler waves at both sides. The anti-Stokes wave is more powerful since the peak power of the clock signal is higher than the data signal. Similar to the 85.4 Gb/s demultiplexing, the anti-Stokes wave is chosen to be the signal to be processed.

The FWM efficiency at the output of the GeAsSe fiber depends on how much power

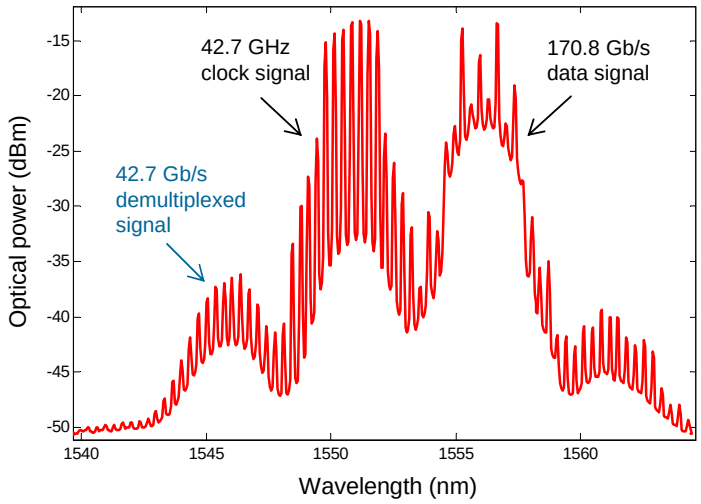

Figure 4.50: Spectral observation at the output of the GeAsSe2012 fiber.

of both signals interact each other. In principle, the maximum power of the idler waves should be obtained when the two pulse signals are perfectly synchronized as illustrated in Figure 4.51. The two pulse signals are, however, at different wavelengths and arrive at the ouput of the fiber with a time delay (about 500 fs), caused by GVM. A trade-off has to be chosen in order to optimize the FWM generation. In practice, the clock signal has to be slightly in advance at the input of the fiber. This helps to have a maximum idler power at the output of the GeAsSe fiber. By advancing the clock by step of one bit-time, each 42.7 Gb/s tributary channel can be time-division demultiplexed. Then, the 4 tributaries are extracted in succession.

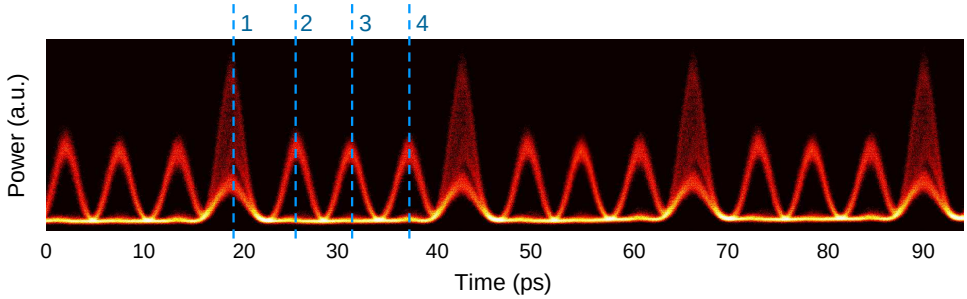

Figure 4.51: Eye diagrams of both the 170.8 Gb/s signal and the 42.7 GHz signal before injection into the GeAsSe2012 fiber.

At the output of the fiber, a 3 nm flat-top filter is firstly used to reject the other waves with high intensity except for the idler wave at 1545.4 nm. The power of the idler wave is measured to be -18.5 dBm. The filtered signal is amplified by an EDFA. It is then passed through a WS. The WS is programed to be a 1 nm Gaussian filter centered at 1545.4 nm. At the output of the WS, we obtain the 42.7 Gb/s demultiplexed wave. This wave is sent to the receiver for eye diagram observation and BER testing. For the 4 tributaries, when adjusting

the time delay by detuning $\Delta\tau$ of 5.9 ps, all the setup of filters are unchanged. Figure 4.52 is an example of eye diagram of the first 42.7 Gb/s tributary time-division demultiplexed channel. It clearly shows an opened eye diagram with a symmetrical pulse-shape. The small noise on "one" level can be attributed to the lower OSNR compared to the original signal and to the temporal walk-off. The pulse duration of the 42.7 Gb/s demultiplexed signal is measured to be 3.9 ps. It is larger than that of the input signal due to the narrow filter used at the output of the fiber.

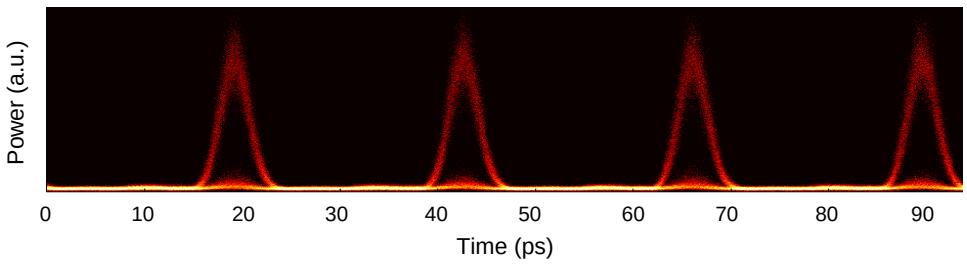

Figure 4.52: Eye diagram of the 42.7 Gb/s demultiplexing signal.

BER measurement is used to assess the performance of the fiber-based all-optical demultiplexer for the 4 tributary demultiplexing signals. The BER evolution as a function of the received power for the best and the worst tributaries are shown in Figure 4.53. The B2B cases at 42.7 Gb/s and 170.8 Gb/s are also represented for reference. We observe a maximum power penalty of 3.5 dB with respect to the 42.7 Gb/s B2B. The power penalty can be attributed to dispersion and nonlinear effects. Indeed, the dispersion introduces a walk-off delay of about 500 fs between the signal and the clock after 30 cm of propagation. This can cause fluctuations on the demultiplexed signals. Spectral broadening of the 42.7 GHz clock, due to self-phase modulation, can also cause optical signal-to-noise degradation of the demultiplexed signal.

Exploiting the high nonlinearity (γ = 25000 $W^{-1}km^{-1}$) of the GeAsSe2012 fiber, to the best of our knowledge, the demultiplexing of the 170.8 Gb/s in a chacogenide MOF was demonstrated with the total power of only 63 mW for the first time. Refering to other publications on demultiplexing, in 2011, a demultiplexing of 160-to-40 Gb/s in a 2.2-m-long lead-silicate fiber was reported. The experiment required a total power of 157 mW and suffered a power penalty of 4 dB [204]. Also in 2011, 160-to-10 Gb/s demultiplexing was reported in an engineered silicon photonic crystal waveguide [211]. A total coupled power in the waveguide was 31 mW and a total insertion loss is 11 dB. The experiment suffered 2.4 dB of power penalty. Using a SOA, 160-to-40 Gb/s demultiplexing with a total power of 21 mW but a power penalty of 9 dB was also reported [212]. By using a $LiNbO_3$ waveguide, a 160-to-10 Gb/s demultiplexing was reported with a total power of 113 mW and a power penalty of 2.5 dB [213].

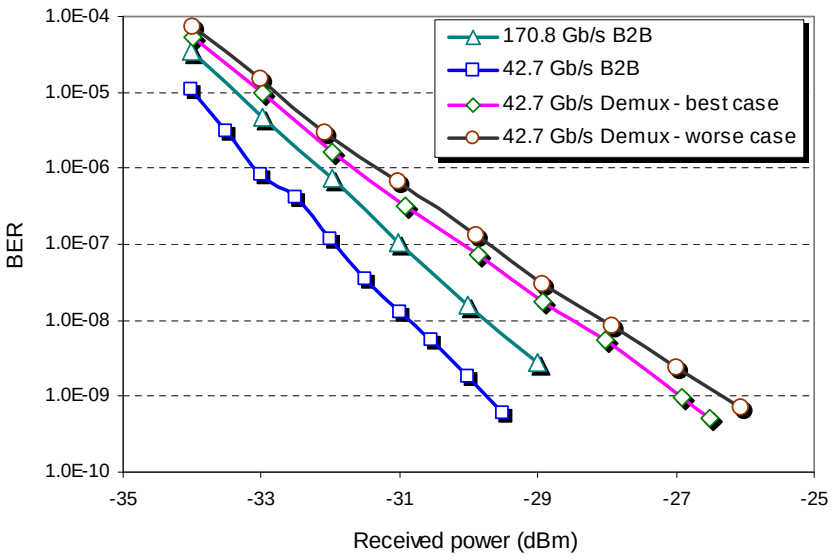

Figure 4.53: BER measurement of the 170.8 Gb/s to 42.7 Gb/s demultiplexing experiment.

4.3.4 Conclusion

In section 4.3, we have reported time-division demultiplexing of a 85.4 Gb/s signal and a 170.8 Gb/s signal to 42.7 Gb/s tributary signals using the GeAsSe2012 MOFs with a total power less than 63 mW. To the best of our knowledge, these are the first all-optical demultiplexing demonstrations in chalcogenide MOFs. Before implementing those two demultiplexing experiments, a 42.7 Gb/s wavelength conversion was tested with a 42.7 GHz pulse clock. This experiment showed the need to choose a suitable fiber length when applying FWM of two pulse signals. The fiber length need to be much less than walk-off length L_w.

For both the 85.4 Gb/s to 42.7 Gb/s demultiplexing and the 170.8 Gb/s to 42.7 Gb/s demultiplexing, GeAsSe2012 fibers were used. Because of a shorter pulse duration, in the experiment of 170.8 Gb/s demultiplexing, we used the shorter fiber of 30 cm length (50 cm fiber length in the case of 85.4 Gb/s demultiplexing). We obtained error-free and no significant power penalty for demultiplexing a 85.4 Gb/s signal down to 42.7 Gb/s with total average power of 45 mW. For the demultiplexing of 170.8 Gb/s signal, we also obtained error-free with a total average power of 63 mW. However, the experiment suffered a power penalty of about 3.5 dB at a BER of 10^{-9} due to temporal walk-off of about 500 fs and probably also nonlinear effects.

The demultiplexing of 170.8 Gb/s down to 42.7 Gb/s was presented in *the ECOC2012 conference* in Amsterdam, Neitherlands [174] and has been accepted for publication in *Electronics Letters* vol. 49, no. 2 [175]. Table 4.2 summaries the FWM-based time-division demultiplexing using the GeAsSe MOFs.

Table 4.2: Time-division demultiplexing using MOF GeAsSe fibers.

Demultiplexing signal	MOF fiber	Total average power (mW)	Power penalty (dB)	Publications
85.4-to-42.7 Gb/s	GeAsSe2012	45	negligible	
170.8-to-42.7 Gb/s	GeAsSe2012	63	3.5	ECOC2012 [174], Electron. Lett. [175]

4.4 Discussion

With the suspended-core AsSe2011 fiber, we have obtained a record nonlinear coefficient γ of 46000 $W^{-1}km^{-1}$ for a microstructured fiber. This fiber, however, was multimode. It has been used for wavelength conversion of clock signals but not for data signals. In 2011, a GeAsSe single-mode fiber was fabricated with a microstructure of 3 rings of air holes. This allowed us to deal with telecommunication data signals.

We succeeded in implementing wavelength conversions of a 42.7 Gb/s OOK signal, a 56 Gb/s DQPSK signal, and a 170.8 Gb/s OOK signal and time-division demultiplexings of a 85.4 Gb/s signal and a 170.8 Gb/s signal with a relatively low total average power. Nevertheless, the wavelength conversion range $\Delta\lambda_c$ is limited to about 6 nm due to the high value of fiber dispersion. In the demultiplexing experiments, high dispersion also causes noise at mark level due to the walk-off effect. This limitation of dispersion should be solved in order to increase the wavelength conversion range $\Delta\lambda_c$.

To decrease the value of dispersion, one can play with the structure of the fiber as well as with material. For a hexagonal 3-rings microstructured fiber (Figure 4.54(a)), an investigation of the dependence of dispersion to the fiber core diameter was simulated as shown in Figure 4.54(b). The simulation was done by L. Provino from PERFOS.

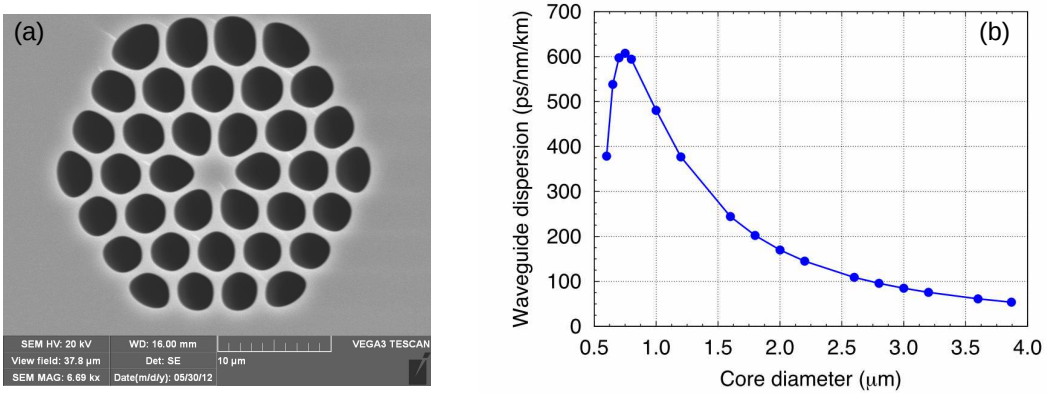

Figure 4.54: (a) Scanning-electron-microscope image of a hexagonal 3 rings of air holes microstructure and (b) its simulated waveguide dispersion D_W with respect to the fiber core diameter.

The simulation shows that the waveguide dispersion D_W increases when the core diameter of the fiber decreases. The maximum value of D_W is about 600 ps/km/nm if the core diameter is as small as 0.7 μm. For a core diameter of 1 μm, the waveguide dispersion D_W is 485 ps/km/nm.

Figure 4.55 illustrates the material dispersion D_M as a function of wavelength for a composition of AsSe and GeAsSe. At the wavelength of 1550 nm, the material dispersion of AsSe is -800 ps/km/nm, and -500 ps/km/nm for GeAsSe glass. As mentioned, by reducing the core diameter, the material dispersion D_M, which is negative, can be compensated by the waveguide dispersion D_W (positive) to have a lower value of fiber dispersion. For example, for a 1 μm core diameter AsSe fiber, the fiber dispersion D will be -315 ps/km/nm. For a 1 μm core diameter GeAsSe fiber, the fiber dispersion D will be -15 ps/km/nm.

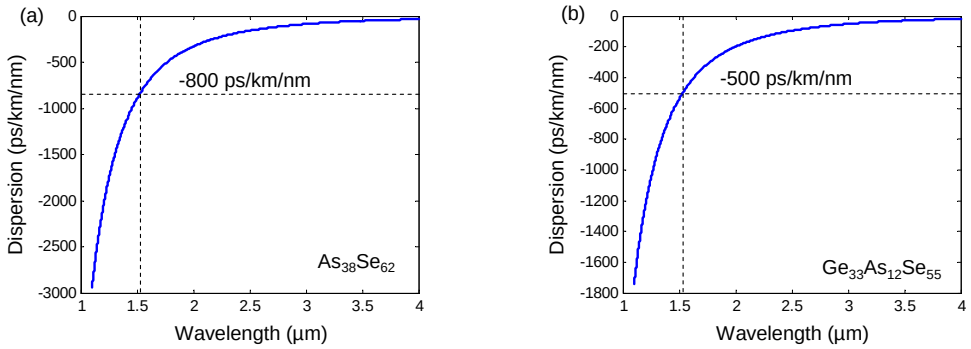

Figure 4.55: Simulated material dispersion D_M with respect to wavelength: (a) composition of $As_{38}Se_{62}$ and (b) composition of $Ge_{33}As_{12}Se_{55}$.

Our future work will now focus on both the fiber structure and the materials with the aim of diminishing the fiber dispersion for further applications. Note that using a smaller core size would enhance more the nonlinear coefficient γ allowing thus signal processing with lower input powers.

4.5 Conclusion

This chapter has presented experimental demonstrations of all-optical signal processing. It has focused on wavelength conversion and time-division demultiplexing based on FWM in chalcogenide microstructured fibers, which are fabricated and characterized in the framework of a collaboration between PERFOS, EVC and Foton.

All-optical wavelength conversion for telecommunication signals in chalcogenide glass fibers has been demonstrated. We have implemented the conversion for both clock signals and data signals. Two modulation formats, intensity modulation (OOK) and phase modulation (DQPSK), have been considered. By using ultra-highly nonlinear fibers made of chalcogenide glasses (AsSe and GeAsSe), error-free wavelength conversions of a 42.7 GHz clock signal, a 42.7 Gb/s OOK RZ-33% data signal, a 170.8 Gb/s OOK data signal and

56 Gb/s DQPSK data signal have been demonstrated. The total average power used in the experiments of the 42.7 Gb/s OOK signal and the 56 Gb/s DQPSK signal were less than 56 mW. For the 170 Gb/s signal, the power was 100 mW because of the shorter fiber used. To the best of our knowledge, wavelength conversion at these bit rates has been demonstrated for the first time in chalcogenide MOFs. The limitation of our experiments is that the wavelength conversion range is just 6 nm due to the high value of the dispersion.

All-optical time-division demultiplexing has also been investigated. We believe that this is the first demonstration of demultiplexing in chalcogenide MOFs. We have considered demultiplexing of a 85.4 Gb/s OOK RZ to two tributaries of 42.7 Gb/s OOK RZ signal and from 170.8 Gb/s OOK RZ signal to four tributaries of 42.7 Gb/s OOK RZ signal. They have both been demonstrated with error-free results with a total average power of less than 65 mW. For the 85.4 Gb/s demultiplexing, we found no significant power penalty for the two tributaries. A 3.5 dB power penalty has been found for the 170.8 Gb/s demultiplexing. This was attributed to the high value of the dispersion of the fibers leading to the GVM of the two signals while propagating along the fiber and the nonlinear effects.

The fibers we have presented have the advantage of ultra-high nonlinearity, they however possess a high value of the dispersion so far. Comparing to other works, the optical power has been reduced [117, 118]. In the future, in order to go to higher bit rates, there is a need to diminish the fiber dispersion. Preliminary simulations show that it is possible by choosing an appropriate microstructure with a smaller core.

Conclusion

All-optical signal processing is a key technology for future optical transmission networks. To implement transparent optical signal processing, an attractive way is to exploit the third-order nonlinearity of optical fibers. Fiber-based signal processing offers a large bandwidth and high speed operation at data rates up to Tb/s owing to the fast response time of fiber nonlinearities. To enable the practical use of optical fibers in all-optical signal processing, an increase of the nonlinearity coefficient of the fiber and progress in tailoring the fiber dispersion are necessary. Optical fibers with high nonlinearity have been studied for several decades and are promising candidates to fulfill the demanding requirements.

The work I have presented dealt with all-optical signal processing by exploiting the third-order nonlinearity of new optical fibers. It has been realized in collaboration with PERFOS and EVC, France and financially supported by the region of Bretagne, France. The appendix at the end of the thesis provides the list of my publications. The results that I have obtained can be classified into two categories: fiber design and fiber characterization on one hand and all-optical signal processing applications on the other hand.

Fiber design and characterization:

In order to tailor fiber dispersion of silica-based optical fibers for 160 Gb/s regeneration, in Chapter 2, the characteristics of DDM fibers were described. We have proposed the use of DDM fibers in order to reduce the influence of chromatic dispersion and higher-order dispersion to perform 160 Gb/s regeneration. Some DDM fibers have been suggested. The parameter variations have also been studied to ensure these DDM fibers are compatible with fiber fabrication technique. The DDM fibers are not highly nonlinear fibers, they however tailor the dispersion of the fiber and can be use for all-optical regeneration.

Highly nonlinear fibers, reported in this thesis are made of chalcogenide glasses. Several fibers with different microstructures and materials have been fabricated. The suspended-core microstructure has the advantage of a smaller core diameter for nonlinear enhancement, but these fibers have been demonstrated to be multimode. The 3-ring microstructure, which is single-mode, is therefore preferable. During the three years of the thesis, several chalcogenide MOFs have been fabricated by PERFOS and EVC. These fibers are chronologically summarized as follows:

- AsSe2010 MOF: Before this thesis started, the highest nonlinearity of chalcogenide MOFs was reported to be 15000 $W^{-1}km^{-1}$ and fiber loss was 15 dB/m. By using a suspended-core structure, we marked an obvious progress. With a core diameter as small as 2 μm, we reached a nonlinear coefficient of 31000 $W^{-1}km^{-1}$. fiber losses of the fiber was measured to be 4.6 dB/m. However, due to the small core diameter, coupling losses were about 10 dB. The FOM_{max} of this fiber was 29.3 W^{-1}.

- AsSe2011 MOF: A year later, the core diameter of a suspended-core fiber was reduced more to be 1.13 μm, leading to a nonlinear coeffcient of 46000 $W^{-1}km^{-1}$. This is so far a record of nonlinearity for MOFs. Moreover, a better purification of chalcogenide glasses allows us to significantly reduce the fiber losses (0.9 dB/m for this fiber). The association of this high value of nonlinear coefficient and low value of loss lead to a FOM_{max} of 222 W^{-1}, which is, to the best of our knowledge, one of the highest FOM_{max} for a nonlinear device. The high nonlinearity of the fiber was demonstrated by a 10 GHz signal wavelength conversion with an efficiency of -5.6 dB and a total average input power of only 17 mW. To reduce the coupling losses due to the small core of the fiber, mode-adaptation sections with a larger core diameter were present at the two ends of the fiber.

- GeAsSe2011 MOF: This fiber was fabricated with a 3-rings of air holes microstructure, which allows single-mode propagation. The composition of the glass is GeAsSe, which is a little less nonlinear than AsSe glass. The nonlinear coefficient of the GeAsSe2011 fiber is 11000 $W^{-1}km^{-1}$ and its attenuation is 2.5 dB/m giving a FOM_{max} of 19.6 W^{-1}. This fiber was also tapered to facilitate light coupling.

- GeAsSe2012 MOF: By qualitatively improving the GeAsSe glass and reducing the core diameter, in the beginning of 2012, two GeAsSe 3-ring MOFs were fabricated. These two fibers have the same characteristics but are different in length, one is 50 cm and the other is 30 cm. The fiber losses are measured to be 0.9 dB/m. The core diameter of the fiber is 1.38 μm leading to a nonlinearity of 25000 $W^{-1}km^{-1}$. The FOM_{max} of the fiber is then increased to 118 W^{-1}. The fiber also includes mode-adaptation sections.

All-optical signal processing:

This thesis has demonstrated three fiber-based all-optical functions such as all-optical regeneration, all-optical wavelength conversion, and all-optical demultiplexing.

- All-optical regeneration: We used a single DDM fiber to numerically demonstrate 160 Gb/s all-optical 2R regeneration. This regenerator is based on SPM (Mamyshev regenerator). The use of DDM fiber offers the advantage of limiting the influence of the third-order dispersion while maintaining average group-velocity dispersion negative

and close to zero. For suitably chosen sets of parameters, a 160 Gb/s regenerator has been numerically demonstrated with a Q-factor improvement of 3.2 dB.

- All-optical wavelength conversion: We have demonstrated all-optical wavelength conversions for telecommunication signals based on FWM effect in chalcogenide fibers. Both clock signals and data signals have been experimented on. Two types of modulation formats, intensity modulation (OOK) and phase modulation (DQPSK), have been considered. The first wavelength conversions was done for clock signals at 10 GHz and 42.7 GHz by using the AsSe2010 fiber and the AsSe2011 fiber, respectively. Both experiments showed high conversion efficiencies. The GeAsSe2011 fiber with a single-mode behaviour was used to implement all-optical wavelength conversion of a 42.7 Gb/s OOK RZ−33% data signal. We have obtained error-free and quasi penalty-free conversion. The GeAsSe2011 fiber was also used for wavelength conversion of a 56 Gb/s DQPSK data signal. We also achieved error-free wavelength conversion with a power penalty of about 1 dB at a BER of 10^{-9}. Wavelength conversion of a 170.8 Gb/s OOK data signal was performed by using the 50 cm GeAsSe2012 fiber. Error-free was obtained for this conversion with a power penalty of about 2 dB. The total average power used in the experiments of 42.7 Gb/s OOK signal and 56 Gb/s DQPSK signal were lower than 56 mW and for the 170.8 Gb/s it was 100 mW.

- All-optical demultiplexing: We have also demonstrated all-optical time-division demultiplexing using the chalcogenide fibers. This was also based on FWM in the GeAsSe2012 fibers. The first experiment was done for a 85.4 Gb/s OOK RZ signal demultiplexed down to 2 tributaries at 42.7 Gb/s using 50 cm of the GeAsSe2012 fiber. We have succeeded in error-free and penalty-free demultiplexing for both 42.7 Gb/s tributary signals. The total input average power was 45 mW. The second all-optical demultiplexing experiment was carried out for a 170.8 Gb/s OOK RZ signal down to 4 tributaries of 42.7 Gb/s signals. In this experiment, because of the temporal walk-off, the shorter 30 cm GeAsSe2012 fiber was used. We demonstrated error-free demultiplexing for the 4 tributary channels with a total input average power of 63 mW. However, a walk-off time of about 500 fs and nonlinear effects caused a power penalty of about 3.5 dB at a BER of 10^{-9} with respect to the 42.7 Gb/s B2B.

Perspectives

Nonlinear fiber optics and MOFs in particular, are now “hot topics” and will continue to be so in the coming years. Chalcogenide MOFs offer a high nonlinearity but also a high dispersion. This limits the use of chalcogenide MOFs for high bit rate signals. Theoretical investigation shows that the waveguide dispersion D_W of chalcogenide MOFs can be increased by decreasing the core diameter of MOFs leading to a reduction of the total fiber dispersion. Therefore, future works will consider the fabrication of chalcogenide MOFs with

lower values of dispersion. Then, all-optical signal processing at higher bit-rates such as 640 Gb/s or 1.28 Tb/s could be possible with also a wider wavelength conversion range.

Silica-based DDM fibers should also be considered for future work. These fibers however are not nonlinear enough leading to high optical power as discussed previously. By decreasing the core size of DDM fibers in the same manner than HNLF, DDM-HNLF might combine the advantage of a high nonlinear coefficient and the management of second- and third-order dispersion simultaneously.

Appendix
List of Publications

Journal articles

[1] **S. D. Le**, M. Gay, L. Bramerie, T. Chartier, M. Thual, J.-C. Simon, L. Brilland, D. Méchin, P. Toupin, and J. Troles, "All-optical time-domain demultiplexing of a 170.8 Gb/s signal in a chalcogenide GeAsSe microstructured fiber," Accepted for publication in *Electronics Letters*, vol. 49, no. 2, 2013.

[2] **S. D. Le**, T. Chartier, M. Gay, L. Bramerie, M. Thual, J.-C. Simon, L. Brilland, D. Méchin, P. Toupin, and J. Troles, "All-optical wavelength conversion of a 170.8 Gb/s signal in a chalcogenide GeAsSe microstrutured fiber," *IEEE Photonics Technology Letters*, 2012. Submitted.

[3] **S. D. Le**, M. Gay, L. Bramerie, M. Costa e Silva, K. Lenglé, T. Chartier, M. Thual, J.-C. Simon, L. Brilland, D. Méchin, P. Toupin, and J. Troles, "Wavelength conversion in a highly nonlinear chalcogenide microstructured fiber," *Optics Letters*, vol. 37, no. 22, 2012.

[4] **S. D. Le**, M. Gay, L. Bramerie, M. Costa e Silva, K. Lenglé, T. Chartier, M. Thual, J.-C. Simon, L. Brilland, D. Méchin, P. Toupin, and J. Troles, "All-optical wavelength conversion of a 42.7 Gb/s signal in a chalcogenide microstructured fiber," *Journal of Science and Technology Special Issue on Electronics*, vol. 3, pp. 1–8, 2012.

[5] T. N. Nguyen, K. Lenglé, M. Thual, P. Rochard, M. Gay, L. Bramerie, S. Malaguti, G. Bellanca, **S. D. Le**, and T. Chartier, "A non-destructive method to measure coupling and propagation losses in optical guided structures," *Journal of the Optical Society of America B*, vol. 29, no. 12, 2012.

[6] D. M. Nguyen, S. Blin, T. N. Nguyen, **S. D. Le**, L. Provino, M. Thual, and T. Chartier, "Modal decomposition technique for multimode fibers," *Applied Optics*, vol. 51, pp. 450–456, 2012.

[7] D. M. Nguyen, **S. D. Le**, T. Chartier, and M. Thual, "Numerical method for simultaneous measurement of group velocity dispersion and nonlinear coefficient in optical fbers," *Optics Communications*, vol. 285, pp. 1461–1465, 2011.

[8] **S. D. Le**, D. M. Nguyen, M. Thual, L. Bramerie, M. C. e Silva, K. Lenglé, M. Gay, T. Chartier, L. Brilland, D. Méchin, P. Toupin, and J. Troles, "Efficient four-wave mixing in an ultra-highly nonlinear suspended-core chalcogenide $As_{38}Se_{62}$ fiber," *Optics Express*, vol. 19, no. 26, pp. B653–B660, 2011.

[9] M. Thual, D. M. Nguyen, **S. D. Le**, K. Lenglé, T. Chartier, J. Troles, Q. Coulombier, D. Méchin, L. Brillant, T. N. Nguyen, S. Blin, C. Bastianelli, and L. Bramerie, "Recent advances on low loss and highly nonlinear AsSe suspended core photonic crystal fiber," *Special Issue on Electronics, Telecommunications and Information Technology*, vol. 1, pp. 1–10, 2010.

[10] D. Nguyen, **S. D. Le**, K. Lenglé, D. Méchin, M. Thual, T. Chartier, Q. Coulombier, J. Troles, L. Bramerie, and L. Brilland, "Demonstration of nonlinear effects in an ultra-highly nonlinear AsSe suspended-core chalcogenide fiber," *IEEE Photonics Technology Letters*, vol. 22, no. 24, pp. 1844–1846, 2010.

International conferences

[1] **S. D. Le**, M. Gay, L. Bramerie, M. Costa e Silva, K. Lenglé, T. Chartier, M. Thual, L. Brilland, D. Méchin, P. Toupin, and J. Troles, "All-optical wavelength conversion of a 56 Gb/s DQPSK signal and all-optical demultiplexing of a 170 Gb/s OOK signal in chalcogenide photonic crystal fibers," in 38^{th} *European Conference and Exhibition on Optical Communication (ECOC)*, 2012.

[2] **S. D. Le**, D. M. Nguyen, M. Thual, L. Bramerie, M. Costa e Silva, K. Lenglé, M. Gay, T. Chartier, J. Simon, L. Brilland, D. Méchin, P. Toupin, and J. Troles, "42.7 Gb/s RZ-33% wavelength conversion in a chalcogenide microstructured fiber," in *Optical Fiber Communication Conference (OFC)*. Optical Society of America, 2012.

[3] **S. D. Le**, K. H. Town, T. Chartier, M. Costa e Silva, L. Bramerie, M. Gay, M. Thual, P. Besnard, J.-C. Simon, L. Brilland, D. Méchin, P. Toupin, and J. Troles, "Nonlinear applications of chalcogenide photonic crystal fibers at 1550 nm," in *ISNOG*, 2012.

[4] **S. D. Le**, D. M. Nguyen, M. Thual, L. Bramerie, M. Costa e Silva, K. Lenglé, M. Gay, T. Chartier, D. Brilland, L. Méchin, P. Toupin, and J. Troles, "Efficient four-wave mixing in a ultra-highly nonlinear suspended-core chalcogenide fiber," in 37^{th} *European Conference and Exhibition on Optical Communication (ECOC)*, 2011. (**In the finalists of the Best Student Paper Presentation Award**)

[5] J. Troles, L. Brilland, P. Toupin, Q. Coulombier, **S. D. Le**, D. Nguyen, M. Thual, T. Chartier, G. Renversez, D. Méchin, and J. Adam, "Chalcogenide suspended-core fibers: Manufacturing and non-linear properties at 1.55 μm," in *IEEE ICTON2011*, 2011.

[6] **S. D. Le**, T. Chartier, M. Gay, M. Costa e Silva, L. Bramerie, J.-C Simon, and T.N. Nguyen, "Dispersion-managed fibers for all-optical regeneration at 160 Gb/s," in *The European Conference on Lasers and Electro-Optics (CLEO/Europe)*. Optical Society of America, 2011.

[7] D. M. Nguyen, **S. D. Le**, L. Brilland, Q. Coulombier, J. Troles, D. Méchin, T. Chartier, and M. Thual, "Demonstration of a low loss and ultra highly nonlinear AsSe suspended-core chalcogenide fiber," in 36^{th} *European Conference and Exhibition on Optical Communication (ECOC)*, 2010.

[8] D. M. Nguyen, G. Gueguen, **S. D. Le**, T. Chartier, and M. Thual, "Simultaneous measurement of group velocity dispersion and nonlinear coefficient in optical fibers based on the self-phase modulation," in *ICPA*, 2010.

[9] D. Méchin, L. Brilland, J. Troles, Q. Coulombier, P. Houizot, A. Monteville, T. Nguyen, D. M. Nguyen, **S. D. Le**, M. Thual, T. Chartier, and J.-L. Adam, "Recent advances in very highly nonlinear chalcogenide photonic crystal fibers and their applications," in *IEEE Photonics Society Summer Topical Meeting Series*, pp. 117–118, 2010.

[10] T. Chartier, T. N. Nguyen, D. M. Nguyen, **S. D. Le**, M. Thual, D. Bosc, K. Messaad, L. Brilland, N. Traynor, A. Monteville, H. Houisot, F. Desevedavy, Q. Coulombier, T. Jouan, J. Troles, C. Fortier, B. Kibler, S. Pitois, G. Gadret, C. Finot, F. Smektala, and J. Fatome, "Recent advances in chalcogenide holey fibers," in *COST 299 FIDES*, 2010.

[11] T. Chartier, D. M. Nguyen, **S. D. Le**, K. Lenglé, L. Bramerie, M. Thual, J. Troles, Q. Coulombier, T. N. Nguyen, L. Brilland, D. Méchin, C. Fortier, J. Fatome, F. Smektala, and G. Renversez, "Chalcogenide photonic crystal fibers for telecommunication applications," in *ICPA*, 2010.

[12] **S. D. Le**. Le and U. Yoshiyori, "Reducing noise for spm based 2r-optical regenerations utilizing filters," in *ITC-CSCC*, Jeju, Korea, 2009.

[13] **S. D. Le** and U. Yoshiyori, "Optimized regime for 2r-optical regenerators based on self-phase modulation," in *IEICE*, Tokyo, 2008.

French national conferences

[1] **S. D. Le**, M. Gay, Laurent Bramerie, M. C. e Silva, K. Lenglé, C. Pareige, T. Chartier, M. Thual, J.-C. Simon, L. Brilland, D. Méchin, P. Toupin, and J. Troles, "Conversion de longueur d'onde et démultiplexage optique dans des fibres optiques microctructurées en verres de chalcogénures," in *JNOG*, 2012.

[2] T. N. Nguyen, K. Lenglé, M. Thual, P. Rochard, M. Gay, L. Bramerie, S. Malaguti, G. Bellanca, **S. D. Le**, and T. Chartier, "Une methode simple et non-destructive de mesure des pertes de couplage et des pertes du guide dans des guides optiques," in *JNOG*, 2012.

[3] **S. D. Le**, D. M. Nguyen, M. Thual, L. Bramerie, M. Costa e Silva, K. Lenglé, M. Gay, T. Chartier, L. Brilland, D. Méchin, P. Toupin, and Troles, "Mélange à quatre ondes dans une fibre optique à coeur suspendu en verre de chalcogénure AsSe très fortement non-linéaire," in *JNOG*, 2011.

[4] D. M. Nguyen, **S. D. Le**, M. Thual, and T. Chartier, "Investigation du mélange à quatre ondes et application a la mesure simultanée de la dispersion et du coefficient Kerr sur des fibres en verres de chalcogénures," in *JNOG*, 2011.

[5] D. M. Nguyen, **S. D. Le**, K. Lenglé, L. Brilland, Q. Coulombier, J. Troles, D. Méchin, T. Chartier, and M. Thual, "fibre optique à coeur suspendu en verre de chalcogénure AsSe très fortement non-linéaire," in *JNOG*, 2010.

[6] D. M. Nguyen, **S. D. Le**, T. Chartier, and M. Thual, "Mesure simultanée de la dispersion et du coefficient non-linéaire Kerr de fibres optiques basé sur l'effet d'automodulation de phase," in *JNOG*, 2010.

References

[1] G. Agrawal, "Nonlinear fiber optics: its history and recent progress [invited]," *JOSA B*, vol. 28, no. 12, pp. A1–A10, 2011.

[2] E. Ippen and R. Stolen, "Stimulated Brillouin scattering in optical fibers," *Appl. Phys. Lett.*, vol. 21, no. 11, pp. 539–541, 1972.

[3] R. Stolen, E. Ippen, and A. Tynes, "Raman oscillation in glass optical waveguide," *Appl. Phys. Lett.*, vol. 20, no. 2, pp. 62–64, 1972.

[4] R. Stolen and C. Lin, "Self-phase-modulation in silica optical fibers," *Phys. Rev. A*, vol. 17, no. 4, p. 1448, 1978.

[5] R. Stolen, "Phase-matched-stimulated four-photon mixing in silica-fiber waveguides," *IEEE J. Quantum Electron.*, vol. 11, no. 3, pp. 100–103, 1975.

[6] M. Onishi, T. Okuno, T. Kashiwada, S. Ishikawa, N. Akaska, and M. Nishimura, "Highly nonlinear dispersion shifted fiber and its application to broadband wavelength converter," in 23^{rd} *European Conference on Optical Communications (ECOC)*, 1997.

[7] G. P. Agrawal, *Fiber-optic communication systems*. Wiley New York, 2002.

[8] S. Sudo, T. Hosaka, H. Itoh, and K. Okamoto, "High-Δn, small-core single-mode fibres for efficient nonlinear optical effects," *Electron. Lett.*, vol. 22, no. 16, pp. 833–835, 1986.

[9] M. Onishi, T. Kashiwada, Y. Ishiguro, Y. Koyano, M. Nishimura, and H. Kanamori, "High-performance dispersion-compensating fibers," *Fiber Integr. Opt.*, vol. 16, no. 3, pp. 277–285, 1997.

[10] S. Watanabe, "Optical signal processing using nonlinear fibers," *J. Opt. Fiber Commun. Res.*, vol. 3, no. 1, pp. 1–24, 2006.

[11] T. Okuno, M. Hirano, T. Nakanishi, and M. Onishi, "Highly-nonlinear optical fibers and their applications," *SEI Technical Rev.*, vol. 62, p. 34, 2006.

[12] J. Fatome, S. Pitois, P. Dinda, G. Millot, E. Le Rouzic, B. Cuenot, E. Pincemin, and S. Gosselin, "Effectiveness of fiber lines with symmetric dispersion swing for 160 Gb/s

terrestrial transmission systems," *IEEE Photon. Technol. Lett.*, vol. 16, no. 10, pp. 2365–2367, 2004.

[13] A. Liang, H. Toda, and A. Hasegawa, "High-speed soliton transmission in dense periodic fibers," *Opt. Lett.*, vol. 24, no. 12, pp. 799–801, 1999.

[14] J. Dudley and J. Taylor, "Ten years of nonlinear optics in photonic crystal fibre," *Nature Photonics*, vol. 3, no. 2, pp. 85–90, 2009.

[15] W. Belardi, J. Lee, K. Furusawa, Z. Yusoff, P. Petropoulos, M. Ibsen, T. Monro, and D. Richardson, "A 10 Gb/s tuneable wavelength converter based on four-wave mixing in highly nonlinear holey fibre," in *28th European Conference on Optical Communication (ECOC)*. IEEE, 2002.

[16] J. Sanghera, C. Florea, L. Shaw, P. Pureza, V. Nguyen, M. Bashkansky, Z. Dutton, and I. Aggarwal, "Non-linear properties of chalcogenide glasses and fibers," *J. Non-Crystalline Solids*, vol. 354, no. 2, pp. 462–467, 2008.

[17] J. Savage and S. Nielsen, "Chalcogenide glasses transmitting in the infrared between 1 and 20micro a state of the art review," *Infrared Phys.*, vol. 5, no. 4, pp. 195–204, 1965.

[18] T. Monro, Y. West, D. Hewak, N. Broderick, and D. Richardson, "Chalcogenide holey fibres," *Electron. Lett.*, vol. 36, no. 24, pp. 1998–2000, 2000.

[19] T. N. Nguyen, "Étude de composants optiques à base de fibres optiques non-linéares," Ph.D. dissertation, Université de Rennes 1, 2008.

[20] D. M. Nguyen, "Investigations et caractérisations de fibres et guides optiques trés fortement non-linéaires," Ph.D. dissertation, Université de Rennes 1, 2011.

[21] T. Nguyen, T. Chartier, Q. Coulombier, P. Houizot, L. Brilland, F. Smektala, J. Troles, C. Fortier, J. Fatome, and M. Thual, "Ultra highly nonlinear asse chalcogenide holey fiber for nonlinear applications," in *35th European Conference on Optical Communication (ECOC)*. IEEE, 2009.

[22] H. Dutton and I. B. M. Corporation, *Understanding optical communications*. Prentice Hall PTR, 1998.

[23] M. Dummer, J. Klamkin, E. Norberg, J. Raring, A. Tauke-Pedretti, and L. Coldren, "Periodic loading and selective undercut etching for high-impedance traveling-wave electroabsorption modulators," in *Optical Fiber Communication Conference (OFC)*. Optical Society of America, 2008.

[24] I. Corporation, "40G QPSK and DQPSK modulation," Inphi Corporation, Tech. Rep., 2009.

[25] I. Joindot, M. Joindot *et al.*, "Les télécommunications par fibres optiques," *DUNOD et CNET-ENST*, 1996.

[26] F. Helbing, G. Steinmeyer, and U. Keller, "Carrier-envelope offset phase-locking with attosecond timing jitter," *IEEE J. Sel. Topics Quantum Electron.*, vol. 9, no. 4, pp. 1030–1040, 2003.

[27] R. Paschotta, B. Rudin, A. Schlatter, G. Spühler, L. Krainer, S. Zeller, N. Haverkamp, H. Telle, and U. Keller, "Relative timing jitter measurements with an indirect phase comparison method," *Appl. Phys. B: Lasers Opt.*, vol. 80, no. 2, pp. 185–192, 2005.

[28] O. Ait Sab and V. Lemaire, "Block turbo code performances for long-haul DWDM optical transmission systems," in *Optical fiber communication conference*. Optical Society of America, 2000.

[29] ITU, "Optical fibres, cables and systems," *Handbook*, 2009.

[30] D. Colladon, "On the reflections of a ray of light inside a parabolic liquid stream," *Comptes Rendus*, vol. 15, pp. 800–802, 1842.

[31] G. Keiser, *Optical fiber communications*. Wiley Online Library, 2000.

[32] D. Gloge, "Weakly guiding fibers," *Appl. Opt.*, vol. 10, no. 10, pp. 2252–2258, 1971.

[33] T. Chartier, *Propagation guidée et microonde*, T. Chartier, Ed. Enssat, 2011.

[34] D. Marcuse, "Gaussian approximation of the fundamental modes of graded-index fibers," *JOSA*, vol. 68, no. 1, pp. 103–109, 1978.

[35] C. Davis, "Fiber optic technology and its role in the information revolution". Available at http://www.ece.umd.edu/~davis/optfib.html.

[36] L. Cohen, C. Lin, and W. French, "Tailoring zero chromatic dispersion into the 1.5–1.6 μm low-loss spectral region of single-mode fibres," *Electron. Lett.*, vol. 15, no. 12, pp. 334–335, 1979.

[37] C. Lin, H. Kogelnik, and L. Cohen, "Optical-pulse equalization of low-dispersion transmission in single-mode fibers in the 1.3–1.7-μm spectral region," *Opt. Lett.*, vol. 5, no. 11, pp. 476–478, 1980.

[38] S. Ramachandran, B. Mikkelsen, L. Cowsar, M. Yan, G. Raybon, L. Boivin, M. Fishteyn, W. Reed, P. Wisk, D. Brownlow *et al.*, "All-fiber grating-based higher order mode dispersion compensator for broad-band compensation and 1000-km transmission at 40 Gb/s," *IEEE Photon. Technol. Lett.*, vol. 13, no. 6, pp. 632–634, 2001.

[39] C. Poole, J. Wiesenfeld, D. Digiovanni, and A. Vengsarkar, "Optical fiber-based dispersion compensation using higher order modes near cutoff," *J. Lightw. Technol.*, vol. 12, no. 10, pp. 1746–1758, 1994.

[40] C. Kurtzke, "Suppression of fiber nonlinearities by appropriate dispersion management," *IEEE Photon. Technol. Lett.*, vol. 5, no. 10, pp. 1250–1253, 1993.

[41] A. Chraplyvy, A. Gnauck, R. Tkach, and R. Derosier, "8×10 Gb/s transmission through 280 km of dispersion-managed fiber," *IEEE Photon. Technol. Lett.*, vol. 5, no. 10, pp. 1233–1235, 1993.

[42] L. Provost, C. Moreau, G. Mélin, X. Rejeaunier, L. Gasca, P. Sillard, and P. Sansonetti, "Dispersion-managed fiber with low chromatic dispersion slope," in *Optical Fiber Communication Conference (OFC)*. Optical Society of America, 2003.

[43] T. Yu, E. Golovchenko, A. Pilipetskii, and C. Menyuk, "Dispersion-managed soliton interactions in optical fibers," *Opt. lett.*, vol. 22, no. 11, pp. 793–795, 1997.

[44] S. Turitsyn, M. Fedoruk, and A. Gornakova, "Reduced-power optical solitons in fiber lines with short-scale dispersion management," *Opt. lett.*, vol. 24, no. 13, pp. 869–871, 1999.

[45] T. Hirooka, T. Nakada, A. Liang, and A. Hasegawa, "160 Gb/s soliton transmission in a densely dispersion-managed fiber in the presence of variable dispersion and polarization-mode dispersion," in *Nonlinear Guided Waves and Their Applications*. Optical Society of America, 1999.

[46] H. Anis, G. Berkey, G. Bordogna, M. Cavallari, B. Charbonnier, A. Evans, I. Hardcastle, M. Jones, G. Pettitt, B. Shaw *et al.*, "Continuous dispersion managed fiber for very high speed soliton systems," in *25th European Conference on Optical Communication (ECOC), Nice, France*, 1999.

[47] G. Agrawal, *Nonlinear fiber optics*. Academic press, 2006.

[48] T. Chartier, *Propagation non-linéaire dans les fibres*, Enssat, Ed. Enssat, 2012.

[49] S. Chernikov, E. Dianov, D. Richardson, and D. Payne, "Soliton pulse compression in dispersion-decreasing fiber," *Opt. lett.*, vol. 18, no. 7, pp. 476–478, 1993.

[50] J. Knight, J. Arriaga, T. Birks, A. Ortigosa-Blanch, W. Wadsworth, and P. Russell, "Anomalous dispersion in photonic crystal fiber," *IEEE Photon. Technol. Lett.*, vol. 12, no. 7, pp. 807–809, 2000.

[51] T. Nguyen, T. Chartier, M. Thual, P. Besnard, L. Provino, A. Monteville, and N. Traynor, "Simultaneous measurement of anomalous group-velocity dispersion and nonlinear coefficient in optical fibers using soliton-effect compression," *Opt. Commun.*, vol. 278, no. 1, pp. 60–65, 2007.

[52] S. Song, C. Allen, K. Demarest, and R. Hui, "Intensity-dependent phase-matching effects on four-wave mixing in optical fibers," *J. Lightw. Technol.*, vol. 17, no. 11, pp. 2285–2290, 1999.

[53] R. Carman, R. Chiao, and P. Kelley, "Observation of degenerate stimulated four-photon interaction and four-wave parametric amplification," *Phys. Rev. Lett.*, vol. 17, no. 26, pp. 1281–1283, 1966.

[54] N. Shibata, R. Braun, and R. Waarts, "Phase-mismatch dependence of efficiency of wave generation through four-wave mixing in a single-mode optical fiber," *IEEE J. Quantum Electron.*, vol. 23, no. 7, pp. 1205–1210, 1987.

[55] J. Sanghera, I. Aggarwal, L. Shaw, C. Florea, P. Pureza, V. Nguyen, and F. Kung, "Nonlinear properties of chalcogenide glass fibers," *J. Optoelectron. Adv. Mater.*, vol. 8, no. 6, pp. 2148–2155, 2006.

[56] R. Smith, "Optical power handling capacity of low loss optical fibers as determined by stimulated Raman and Brillouin scattering," *Appl. Opt.*, vol. 11, no. 11, pp. 2489–2494, 1972.

[57] K. Shiraki, M. Ohashi, and M. Tateda, "Suppression of stimulated Brillouin scattering in a fibre by changing the core radius," *Electron. lett.*, vol. 31, no. 8, pp. 668–669, 1995.

[58] L. Grüner-Nielsen, D. Jakobsen, S. Herstrøm, B. Pálsdóttir, S. Dasgupta, D. Richardson, C. Lundström, S. Olsson, and P. Andrekson, "Brillouin suppressed highly nonlinear fibers," in *European Conference and Exhibition on Optical Communication (ECOC)*. Optical Society of America, 2012.

[59] K. Tow, Y. Léguillon, P. Besnard, L. Brilland, J. Troles, P. Toupin, D. Méchin, D. Trégoat, and S. Molin, "Relative intensity noise and frequency noise of a compact brillouin laser made of $Ass_{38}Se_{62}$ suspended-core chalcogenide fiber," *Opt. Lett.*, vol. 37, no. 7, pp. 1157–1159, 2012.

[60] N. Kotova, V. Kovalev, and R. Harrison, "Dynamics of the stokes pulse in a Brillouin amplifier," *Opt. Lett.*, vol. 37, no. 9, pp. 1547–1549, 2012.

[61] J. Knight, T. Birks, P. Russell, and D. Atkin, "All-silica single-mode optical fiber with photonic crystal cladding," *Opt. lett.*, vol. 21, no. 19, pp. 1547–1549, 1996.

[62] K. Kikuchi, K. Taira, and N. Sugimoto, "Highly-nonlinear bismuth oxide-based glass fibers for all-optical signal processing," in *Optical Fiber Communication Conference (OFC)*. Optical Society of America, 2002.

[63] M. Huang, J. Yu, Y. Huang, E. Ip, and G. Chang, "Wavelength converter for polarization multiplexed 100 G transmission with multilevel modulation using a bismuth oxide-based nonlinear fiber," *IEEE Photon. Technol. Lett.*, vol. 22, no. 24, pp. 1832–1834, 2010.

[64] P. Petropoulos, H. Ebendorff-Heidepriem, V. Finazzi, R. Moore, K. Frampton, D. Richardson, and T. Monro, "Highly nonlinear and anomalously dispersive lead silicate glass holey fibers," *Opt. Exp.*, vol. 11, no. 26, pp. 3568–3573, 2003.

[65] A. Camerlingo, F. Parmigiani, X. Feng, F. Poletti, P. Horak, W. Loh, D. Richardson, and P. Petropoulos, "Multichannel wavelength conversion of 40 Gb/s nonreturn-to-zero DPSK signals in a lead–silicate fiber," *IEEE Photon. Technol. Lett.*, vol. 22, no. 15, pp. 1153–1155, 2010.

[66] M. Liao, X. Yan, G. Qin, C. Chaudhari, T. Suzuki, and Y. Ohishi, "A highly non-linear tellurite microstructure fiber with multi-ring holes for supercontinuum generation," *Opt. Exp.*, vol. 17, no. 18, pp. 15 481–15 490, 2009.

[67] G. Qin, X. Yan, C. Kito, M. Liao, T. Suzuki, A. Mori, and Y. Ohishi, "Highly nonlinear tellurite microstructured fibers for broadband wavelength conversion and flattened supercontinuum generation," *J. Appl. Phys.*, vol. 107, no. 4, pp. 043 108–043 108, 2010.

[68] C. Koos, P. Vorreau, P. Dumon, R. Baets, B. Esembeson, I. Biaggio, T. Michinobu, F. Diederich, W. Freude, and J. Leuthold, "Highly-nonlinear silicon photonic slot waveguide," in *National Fiber Optic Engineers Conference*. Optical Society of America, 2008.

[69] A. Peacock, P. LaMehta, T. Day, J. Sparks, P. Sazio, J. Badding, and N. Healy, "Nonlinear properties of silicon optical fibers," in *Specialty Optical Fibers*. Optical Society of America, 2012.

[70] S. D. Le, D. M. Nguyen, M. Thual, L. Bramerie, M. C. e Silva, K. Lengle, M. Gay, T. Chartier, L. Brilland, D. Mechin, P. Toupin, and J. Troles, "Efficient four-wave mixing in an ultra-highly nonlinear suspended-core chalcogenide $As_{38}Se_{62}$ fiber," *Opt. Exp.*, vol. 19, no. 26, p. B653–B660, 2011.

[71] M. Onishi, T. Okuno, T. Kashiwada, S. Ishikawa, N. Akasaka, and M. Nishimura, "Highly nonlinear dispersion-shifted fibers and their application to broadband wavelength converter," *Opt. Fiber Technol.*, vol. 4, no. 2, pp. 204–214, 1998.

[72] T. Nakanishi, M. Hirano, T. Okuno, and M. Onishi, "Silica-based highly nonlinear fiber with γ= 30 /W/km and its FWM-based conversion efficiency," in *Optical Fiber Communication Conference (OFC)*. Optical Society of America, 2006.

[73] V. Diez-Blanco, J. Siegel, and J. Solis, "Waveguide structures written in SF57 glass with fs-laser pulses above the critical self-focusing threshold," *Applied surface science*, vol. 252, no. 13, pp. 4523–4526, 2006.

[74] K. Kikuchi, K. Taira, and N. Sugimoto, "Highly-nonlinear bismuth oxide-based glass fibers for all-optical signal processing," *Electron. Lett.*, vol. 38, no. 4, 2002.

[75] N. Sugimoto, T. Nagashima, T. Hasegawa, and S. Ohara, "Bismuth-based optical fiber with nonlinear coefficient of 1360 W $^{-1}$km^{-1}," in *Optical Fiber Communication Conference (OFC)*. IEEE, 2004.

[76] R. Slusher, G. Lenz, J. Hodelin, J. Sanghera, L. Shaw, and I. Aggarwal, "Large raman gain and nonlinear phase shifts in high-purity As_2Se_3 chalcogenide fibers," *JOSA B*, vol. 21, no. 6, pp. 1146–1155, 2004.

[77] R. Buczynski, "Photonic crystal fibers," *Acta Phys. Polonica Series. A*, vol. 106, no. 2, pp. 141–168, 2004.

[78] V. Finazzi, T. Monro, and D. Richardson, "Small-core silica holey fibers: nonlinearity and confinement loss trade-offs," *JOSA B*, vol. 20, no. 7, pp. 1427–1436, 2003.

[79] M. Liao, C. Chaudhari, G. Qin, X. Yan, T. Suzuki, and Y. Ohishi, "Tellurite microstructure fibers with small hexagonal core for supercontinuum generation," *Opt. Exp.*, vol. 17, no. 14, pp. 12 174–12 182, 2009.

[80] J. Fatome, C. Fortier, T. Nguyen, T. Chartier, F. Smektala, K. Messaad, B. Kibler, S. Pitois, G. Gadret, C. Finot, J. Troles, F. Desevedavy, P. Houizot, G. Renversez, L. Brilland and N. Traynor, "Linear and nonlinear characterizations of chalcogenide photonic crystal fibers," *J. Lightw. Technol.*, vol. 27, no. 11, pp. 1707–1715, 2009.

[81] L. Fu, M. Rochette, V. Ta'eed, D. Moss, and B. Eggleton, "Investigation of self-phase modulation based optical regeneration in single mode As_2Se_3 chalcogenide glass fiber," *Opt. Exp.*, vol. 13, no. 19, pp. 7637–7644, 2005.

[82] B. Eggleton, B. Luther-Davies, and K. Richardson, "Chalcogenide photonics," *Nature Photonics*, vol. 5, no. 3, pp. 141–148, 2011.

[83] P. Mamyshev, "All-optical data regeneration based on self-phase modulation effect," in *24th European Conference on Optical Communication (ECOC)*. IEEE, 1998.

[84] M. Matsumoto, Y. Shimada, and H. Sakaguchi, "Two-stage SPM-based all-optical 2R regeneration by bidirectional use of a highly nonlinear fiber," *IEEE J. Quantum Electron.*, vol. 45, no. 1, pp. 51–58, 2009.

[85] A. Striegler, M. Meissner, K. Cvecek, K. Sponsel, G. Leuchs, and B. Schmauss, "NOLM-based RZ-DPSK signal regeneration," *IEEE Photon. Technol. Lett.*, vol. 17, no. 3, pp. 639–641, 2005.

[86] K. Cvecek, K. Sponsel, G. Onishchukov, B. Schmauss, and G. Leuchs, "2R-regeneration of an RZ-DPSK signal using a nonlinear amplifying loop mirror," *IEEE Photon. Technol. Lett.*, vol. 19, no. 3, pp. 146–148, 2007.

[87] A. Striegler and B. Schmauss, "All-optical DPSK signal regeneration based on cross-phase modulation," *IEEE Photon. Technol. Lett.*, vol. 16, no. 4, pp. 1083–1085, 2004.

[88] Y. Su, G. Raybon, R. Essiambre, and T. Her, "All-optical 2R regeneration of 40 Gb/s signal impaired by intrachannel four-wave mixing," *IEEE Photon. Technol. Lett.*, vol. 15, no. 2, pp. 350–352, 2003.

[89] E. Ciaramella and S. Trillo, "All-optical signal reshaping via four-wave mixing in optical fibers," *IEEE Photon. Technol. Lett.*, vol. 12, no. 7, pp. 849–851, 2000.

[90] M. Matsumoto, "Efficient all-optical 2R regeneration using self-phase modulation in bidirectional fiber configuration," *Opt. Exp.*, vol. 14, no. 23, pp. 11 018–11 023, 2006.

[91] G. Raybon, Y. Su, J. Leuthold, R. Essiambre, T. Her, C. Joergensen, P. Steinvurzel, K. Feder *et al.*, "40 Gb/s pseudo-linear transmission over one million kilometers," in *Optical Fiber Communication Conference (OFC)*. Optical Society of America, 2002.

[92] T. Her, G. Raybon, and C. Headley, "Optimization of pulse regeneration at 40 Gb/s based on spectral filtering of self-phase modulation in fiber," *IEEE Photon. Technol. Lett.*, vol. 16, no. 1, pp. 200–202, 2004.

[93] F. Parmigiani, S. Asimakis, N. Sugimoto, F. Koizumi, P. Petropoulos, and D. Richardson, "2R regenerator based on a 2-m-long highly nonlinear bismuth oxide fiber," *Opt. Exp.*, vol. 14, no. 12, pp. 5038–5044, 2006.

[94] L. Provost, C. Finot, P. Petropoulos, K. Mukasa, and D. Richardson, "Design scaling rules for 2R-optical self-phase modulation-based regenerators," *Opt. Exp.*, vol. 15, no. 8, pp. 5100–5113, 2007.

[95] L. Provost, C. Finot, P. Petropoulos, and J. Richardson, "A 2R Mamyshev regeneration architecture based on a three-fiber arrangement," *J. Lightw. Technol.*, vol. 28, no. 9, pp. 1373–1379, 2010.

[96] T. Nguyen, T. Chartier, L. Bramerie, M. Gay, Q. Le, S. Lobo, M. Joindot, J. Simon, J. Fatome, and C. Finot, "Self-phase-modulation-based 2R regenerator including pulse compression and offset filtering for 42.6 Gb/s RZ-33% transmission systems," *Opt. Exp.*, vol. 17, no. 20, pp. 17 747–17 757, 2009.

[97] C. Finot, J. Fatome, S. Pitois, G. Millot, and E. Pincemin, "Active Mamyshev regenerator," *Opt. Rew.*, vol. 18, no. 3, pp. 257–263, 2011.

[98] M. Gay, M. Costa e Silva, T. Nguyen, L. Bramerie, T. Chartier, M. Joindot, J. Simon, J. Fatome, C. Finot, and J. Oudar, "Bit-error-rate assessment of 170 Gb/s regeneration using a saturable absorber and a nonlinear-fiber-based power limiter," *IEEE Photon. Technol. Lett.*, vol. 22, no. 3, pp. 158–160, 2010.

[99] T. Nguyen, T. Chartier, and J. Simon, "Simple rules and chart to design an all-optical SPM-based regenerator," in *CLEO/Europe*. IEEE, 2009.

[100] T. Nguyen, M. Gay, L. Bramerie, T. Chartier, J. Simon, and M. Joindot, "Noise reduction in 2R-regeneration technique utilizing self-phase modulation and filtering," *Opt. Exp.*, vol. 14, no. 5, pp. 1737–1747, 2006.

[101] C. Finot, T. Nguyen, J. Fatome, T. Chartier, S. Pitois, L. Bramerie, M. Gay, and J. Simon, "Numerical study of an optical regenerator exploiting self-phase modulation and spectral offset filtering at 40 Gb/s," *Opt. Commun.*, vol. 281, no. 8, pp. 2252–2264, 2008.

[102] G. Berkey, "Dispersion managed fiber," May 14 2002, US Patent 6,389,207.

[103] V. Zakkarov, "Optical solitons: theoretical challenges and industrial perspectives," *Les Houches workshop*, vol. 67, p. 02, 1999.

[104] A. Maruta, Y. Yamamoto, S. Okamoto, A. Suzuki, T. Morita, A. Agata, and A. Hasegawa, "Effectiveness of densely dispersion managed solitons in ultra-high speed transmission," *Electron. Lett.*, vol. 36, no. 23, pp. 1947–1949, 2000.

[105] L. Richardson, W. Forysiak, and N. Doran, "Trans-oceanic 160 Gb/s single-channel transmission using short-period dispersion management," *IEEE Photon. Technol. Lett.*, vol. 13, no. 3, pp. 209–211, 2001.

[106] K. Nakkeeran, Y. Kwan, P. Wai, A. Labruyère, P. Tchofo Dinda, and A. Moubissi, "Analytical design of densely dispersion-managed optical fiber transmission systems with gaussian and raised cosine return-to-zero< i> ansätze</i>," *JOSA B*, vol. 21, no. 11, pp. 1901–1907, 2004.

[107] H. Chung, H. Kim, S. Jin, E. Son, D. Kim, K. Lee, H. Park, and Y. Chung, "320 Gb/s WDM transmission with 50 GHz channel spacing over 564 km of short-period dispersion managed fiber (perfect cable)," *IEEE Photon. Technol. Lett.*, vol. 12, no. 10, pp. 1397–1399, 2000.

[108] T. Yamamoto, E. Yoshida, K. Tamura, K. Yonenaga, and M. Nakazawa, "640 Gb/s optical TDM transmission over 92 km through a dispersion-managed fiber consisting

of single-mode fiber and "reverse dispersion fiber"," *IEEE Photon. Technol. Lett.*, vol. 12, no. 3, pp. 353–355, 2000.

[109] J. Fatome, S. Pitois, P. Tchofo Dinda, and G. Millot, "Experimental demonstration of 160 GHz densely dispersion-managed soliton transmission in a single channel over 896 km of commercial fibers," *Opt. Exp.*, vol. 11, no. 13, pp. 1553–1558, 2003.

[110] A. Evans, "Novel fibers for soliton communications," in *Optical Fiber Communication Conference (OFC)*. IEEE, 1998.

[111] C. corporation, "Single-mode fiber - 28," Corning, Tech. Rep., 2002.

[112] Q. Coulombier, L. Brilland, P. Houizot, T. Chartier, T. Nguyen, F. Smektala, G. Renversez, A. Monteville, D. Méchin, T. Pain, H. Orain, J.-C. Sangleboeuf, and J. Troles, "Casting method for producing low-loss chalcogenide microstructured optical fibers," *Opt. Exp.*, vol. 18, no. 9, pp. 9107–9112, 2010.

[113] J. Sanghera, C. Florea, L. Shaw, V. N. P. Pureza, and, M. Bashkansky, Z. Dutton, and I. Aggarwal, "Non-linear properties of chalcogenide glasses and fibers," *J. Non-Cryst. Solids*, vol. 354, pp. 462–467, 2007.

[114] L. Petit, N. Carlie, K. Richardson, A. Humeau, S. Cherukulappurath, and G. Boudebs, "Nonlinear optical properties of glasses in the system Ge/Ga – Sb – S/Se," *Opt. Lett.*, vol. 31, no. 10, pp. 1495–1497, 2006.

[115] J. Harbold, F. Ilday, F. Wise, J. Sanghera, V. Nguyen, L. Shaw, and I. Aggarwal, "Highly nonlinear As-S-Se glasses for all-optical switching," *Opt. Lett.*, vol. 27, no. 2, pp. 119–121, 2002.

[116] J. Lee, W. Belardi, K. Furusawa, P. Petropoulos, Z. Yusoff, T. Monro, and D. Richardson, "Four-wave mixing based 10 Gb/s tunable wavelength conversion using a holey fiber with a high sbs threshold," *IEEE Photon. Technol. Lett.*, vol. 15, no. 3, pp. 440–442, 2003.

[117] M. Pelusi, F. Luan, S. Madden, D. Choi, D. Bulla, B. Luther-Davies, and B. Eggleton, "Wavelength conversion of high-speed phase and intensity modulated signals using a highly nonlinear chalcogenide glass chip," *IEEE Photon. Technol. Lett.*, vol. 22, no. 1, pp. 3–5, 2010.

[118] L. Fu, M. Pelusi, E. Magi, V. Ta'eed, and B. Eggleton, "Broadband all-optical wavelength conversion of 40 Gb/s signals in nonlinearity enhanced tapered chalcogenide fibre," *Electron. Lett.*, vol. 44, no. 1, pp. 44–46, 2008.

[119] D. Yeom, E. Mägi, M. Lamont, M. Roelens, L. Fu, and B. Eggleton, "Low-threshold supercontinuum generation in highly nonlinear chalcogenide nanowires," *Opt. Lett.*, vol. 33, no. 7, pp. 660–662, 2008.

[120] R. Frerichs, "New optical glasses with good transparency in the infrared," *JOSA*, vol. 43, no. 12, pp. 1153–1157, 1953.

[121] J. Le Person, F. Smektala, T. Chartier, L. Brilland, T. Jouan, J. Troles, and D. Bosc, "Light guidance in new chalcogenide holey fibres from GeGaSbS glass," *Mater. Res. Bull.*, vol. 41, no. 7, pp. 1303–1309, 2006.

[122] F. Désévédavy, G. Renversez, J. Troles, L. Brilland, P. Houizot, Q. Coulombier, F. Smektala, N. Traynor, and J. Adam, "Te-As-Se glass microstructured optical fiber for the middle infrared," *Appl. Opt.*, vol. 48, no. 19, pp. 3860–3865, 2009.

[123] L. Brilland, F. Smektala, G. Renversez, T. Chartier, J. Troles, T. Nguyen, N. Traynor, and A. Monteville, "Fabrication of complex structures of holey fibers in chalcogenide glass," *Opt. Exp.*, vol. 14, no. 3, pp. 1280–1285, 2006.

[124] G. Renversez, B. Kuhlmey, and R. McPhedran, "Dispersion management with microstructured optical fibers: ultraflattened chromatic dispersion with low losses," *Opt. Lett.*, vol. 28, no. 12, pp. 989–991, 2003.

[125] J. Sharping, M. Fiorentino, A. Coker, P. Kumar, and R. Windeler, "Four-wave mixing in microstructure fiber," *Opt. Lett.*, vol. 26, no. 14, pp. 1048–1050, 2001.

[126] [Online]. Available: www.coractive.com

[127] G. Lenz, J. Zimmermann, T. Katsufuji, M. Lines, H. Hwang, S. Spälter, R. Slusher, S. Cheong, J. Sanghera, and I. Aggarwal, "Large kerr effect in bulk se-based chalcogenide glasses," *Opt. Lett.*, vol. 25, no. 4, pp. 254–256, 2000.

[128] E. Magi, D. Yeom, H. Nguyen, L. Fu, and B. Eggleton, "Enhanced kerr nonlinearity in sub-wavelength diameter As_2Se_3 chalcogenide fibre tapers," in *32nd Australian Conference on Optical Fibre Technology*. IEEE, 2007.

[129] T. Vo, H. Hu, M. Galili, E. Palushani, J. Xu, L. Oxenløwe, S. Madden, D. Choi, D. Bulla, M. Pelusi *et al.*, "Photonic chip based transmitter optimization and receiver demultiplexing of a 1.28 Tb/s OTDM signal," *Opt. Exp.*, vol. 18, no. 16, pp. 17 252–17 261, 2010.

[130] R. Ahmad and M. Rochette, "High efficiency and ultra broadband optical parametric four-wave mixing in chalcogenide-PMMA hybrid microwires," *Opt. Exp.*, vol. 20, no. 9, pp. 9572–9580, 2012.

[131] R. Ahmad and M. Rochette, "Chalcogenide optical parametric oscillator," *Opt. Exp.*, vol. 20, no. 9, pp. 10 095–10 099, 2012.

[132] H. Ebendorff-Heidepriem, P. Petropoulos, S. Asimakis, V. Finazzi, R. Moore, K. Frampton, F. Koizumi, D. Richardson, and T. Monro, "Bismuth glass holey fibers with high nonlinearity," *Opt. Exp.*, vol. 12, no. 21, pp. 5082–5087, 2004.

[133] J. Leong, P. Petropoulos, S. Asimakis, H. Ebendorff-Heidepriem, R. Moore, K. Frampton, V. Finazzi, X. Feng, J. Price, T. Monro *et al.*, "A lead silicate holey fiber with γ= 1860 $W^{-1}km^{-1}$ at 1550 nm," in *Optical Fiber Communication Conference (OFC)*. IEEE, 2005.

[134] M. Hirano, T. Nakanishi, T. Okuno, and M. Onishi, "Silica-based highly nonlinear fibers and their application," *IEEE J. Sel. Topics Quantum Electron.*, vol. 15, no. 1, pp. 103–113, 2009.

[135] M. Liao, C. Chaudhari, G. Qin, X. Yan, C. Kito, T. Suzuki, Y. Ohishi, M. Matsumoto, and T. Misumi, "Fabrication and characterization of a chalcogenide-tellurite composite microstructure fiber with high nonlinearity," *Opt. Exp.*, vol. 17, no. 24, pp. 21 608–21 614, 2009.

[136] F. Désévédavy, G. Renversez, L. Brilland, P. Houizot, J. Troles, Q. Coulombier, F. Smektala, N. Traynor, and J. Adam, "Small-core chalcogenide microstructured fibers for the infrared," *Appl. Opt.*, vol. 47, no. 32, pp. 6014–6021, 2008.

[137] L. Brilland, J. TROLES, P. Houizot, F. Desevedavy, Q. Coulombier, G. Renversez, T. Chartier, T. Nguyen, J. Adam, and N. Traynor, "Interfaces impact on the transmission of chalcogenides photonic crystal fibres," *J. Ceramic Society of Japan*, vol. 116, no. 1358, pp. 1024–1027, 2008.

[138] E. Guillevic, X. Zhang, T. Pain, L. Calvez, J. Adam, J. Lucas, M. Guilloux-Viry, S. Ollivier, and G. Gadret, "Optimization of chalcogenide glass in the As-Se-S system for automotive applications," *Opt. Mater.*, vol. 31, no. 11, pp. 1688–1692, 2009.

[139] G. Renversez, F. Bordas, and B. Kuhlmey, "Second mode transition in microstructured optical fibers: determination of the critical geometrical parameter and study of the matrix refractive index and effects of cladding size," *Opt. Lett.*, vol. 30, no. 11, pp. 1264–1266, 2005.

[140] L. Cohen, P. Kaiser, P. Lazay, and H. Presby, "Fiber characterization," *Opt. Fiber Telecommun.*, pp. 344–347, 1979.

[141] R. Driver, G. Leskowitz, L. Curtiss, D. Moynihan, and L. Vacha, "The characterization of infrared transmitting optical fibers," in *MRS Proceedings*, vol. 172, no. 1. Cambridge Univ Press, 1989.

[142] S. Personick, "Photon probe-an optical fiber time-domain reflectometer," *Bell Syst. Tech. J*, vol. 56, no. 3, pp. 355–356, 1977.

[143] K. Aoyama, K. Nakagawa, and T. Itoh, "Optical time domain reflectometry in a single-mode fiber," *IEEE J. Quantum Electron.*, vol. 17, no. 6, pp. 862–868, 1981.

[144] M. Barnoski and S. Jensen, "Fiber waveguides: a novel technique for investigating attenuation characteristics," *Appl. Opt.*, vol. 15, no. 9, pp. 2112–2115, 1976.

[145] Y. Okamura, A. Miki, and S. Yamamoto, "Observation of wave propagation in integrated optical circuits," *Appl. Opt.*, vol. 25, no. 19, pp. 3405–3408, 1986.

[146] M. Tateda, T. Horiguchi, M. Tokuda, and N. Uchida, "Optical loss measurement in graded-index fiber using a dummy fiber," *Appl. Opt.*, vol. 18, no. 19, pp. 3272–3275, 1979.

[147] T. Horiguchi and M. Tateda, "Optical-fiber-attenuation investigation using stimulated Brillouin scattering between a pulse and a continuous wave," *Opt. Lett.*, vol. 14, no. 8, pp. 408–410, 1989.

[148] T. N. Nguyen, K. Lengle, M. Thual, P. Rochard, M. Gay, L. Bramerie, S. Malaguti, G. Bellanca, S. D. Le, and T. Chartier, "A simple and non-destructive method to measure coupling losses and linear losses in single-mode optical fibers or waveguides," *J. Opt. Soc. Am. B*, vol. 29, no. 12, 2012.

[149] M. Artiglia, G. Coppa, P. Di Vita, M. Potenza, and A. Sharma, "Mode field diameter measurements in single-mode optical fibers," *J. Lightw. Technol.*, vol. 7, no. 8, pp. 1139–1152, 1989.

[150] R. Hui and M. O'Sullivan, *Fiber optic measurement techniques.* Academic Press, 2009.

[151] J. Nicholson, A. Yablon, S. Ramachandran, and S. Ghalmi, "Spatially and spectrally resolved imaging of modal content in large-mode-area fibers," *Opt. Exp.*, vol. 16, no. 10, pp. 7233–7243, 2008.

[152] S. Blin, D. Nguyen, T. Nguyen, L. Provino, M. Thual, and T. Chartier, "Simple modal analysis method for multi-mode fibers," in *35th European Conference on Optical Communication (ECOC).* IEEE, 2009.

[153] Y. Namihira, A. Miyata, and N. Tanahashi, "Nonlinear coefficient measurements for dispersion shifted fibres using self-phase modulation method at 1.55 μm," *Electron. Lett.*, vol. 30, no. 14, pp. 1171–1172, 1994.

[154] T. Kato, Y. Suetsugu, M. Takagi, E. Sasaoka, and M. Nishimura, "Measurement of the nonlinear refractive index in optical fiber by the cross-phase-modulation method with depolarized pump light," *Opt. Lett.*, vol. 20, no. 9, pp. 988–990, 1995.

[155] N. Broderick, T. Monro, P. Bennett, and D. Richardson, "Nonlinearity in holey optical fibers: measurement and future opportunities," *Opt. Lett.*, vol. 24, no. 20, pp. 1395–1397, 1999.

[156] L. Prigent and J. Hamaide, "Measurement of fiber nonlinear kerr coefficient by four-wave mixing," *IEEE Photon. Technol. Lett.*, vol. 5, no. 9, pp. 1092–1095, 1993.

[157] C. Vinegoni, M. Wegmuller, and N. Gisin, "Determination of nonlinear coefficient n_2/A_{eff} using self-aligned interferometer and faraday mirror," *Electron. Lett.*, vol. 36, no. 10, pp. 886–888, 2000.

[158] D. Nguyen, S. D. Le, G. Gueguen, D. Méchin, M. Thual, and T. Chartier, "Numerical method for simultaneous measurement of dispersion and nonlinear coefficient in optical fibers," *Opt. Commun.*, 2011.

[159] B. Costa, D. Mazzoni, M. Puleo, and E. Vezzoni, "Phase shift technique for the measurement of chromatic dispersion in optical fibers using led's," *IEEE J. Quantum Electron.*, vol. 18, no. 10, pp. 1509–1515, 1982.

[160] B. Christensen, J. Mark, G. Jacobsen, and E. Bødtker, "Simple dispersion measurement technique with high resolution," *Electron. Lett.*, vol. 29, p. 132, 1993.

[161] H. Shang, "Chromatic dispersion measurement by white-light interferometry on metre-length single-mode optical fibres," *Electron. Lett.*, vol. 17, no. 17, pp. 603–605, 1981.

[162] M. Pelusi, V. Ta'Eed, M. Lamont, S. Madden, D. Choi, B. Luther-Davies, and B. Eggleton, "Ultra-high nonlinear As_2Se_3 planar waveguide for 160 Gb/s optical time-division demultiplexing by four-wave mixing," *IEEE Photon. Technol. Lett.*, vol. 19, no. 19, pp. 1496–1498, 2007.

[163] C. Brès, S. Zlatanovic, A. Wiberg, and S. Radic, "Continuous-wave four-wave mixing in cm-long chalcogenide microstructured fiber," *Opt. Exp.*, vol. 19, no. 26, pp. B621–B627, 2011.

[164] J. Lee, T. Nagashima, T. Hasegawa, S. Ohara, N. Sugimoto, and K. Kikuchi, "Four-wave-mixing-based wavelength conversion of 40 Gb/s nonreturn-to-zero signal using 40-cm bismuth oxide nonlinear optical fiber," *IEEE Photon. Technol. Lett.*, vol. 17, no. 7, pp. 1474–1476, 2005.

[165] F. Parmigiani, R. Slavík, J. Kakande, L. Gruner-Nielsen, D. Jakobsen, S. Herstrom, R. Weerasuriya, S. Sygletos, A. Ellis, P. Petropoulos *et al.*, "All-optical signal processing in highly nonlinear fibres," in *OptoeElectronics and Communications Conference (OECC)*. IEEE, 2010.

[166] M. Thual, P. Rochard, P. Chanclou, and L. Quetel, "Contribution to research on micro-lensed fibers for modes coupling," *Fiber Integr. Opt.*, vol. 27, no. 6, pp. 532–541, 2008.

[167] K. Lengle, A. Akrout, M. Costa e Silva, L. Bramerie, S. Combrié, P. Colman, J. Simon, and A. De Rossi, "10 GHz demonstration of four-wave-mixing in photonic crystal waveguides," in *36th European Conference and Exhibition on Optical Communication (ECOC)*. IEEE, 2010.

[168] D. Nguyen, S. D. Le, L. Brilland, Q. Coulombier, J. Troles, D. Mechin, T. Chartier, and M. Thual, "Demonstration of a low loss and ultra highly nonlinear AsSe suspended-core chalcogenide fiber," in *36th European Conference and Exhibition on Optical Communication (ECOC)*. IEEE, 2010.

[169] D. Nguyen, S. D. Le, K. Lengle, D. Méchin, M. Thual, T. Chartier, Q. Coulombier, J. Troles, L. Bramerie, and L. Brilland, "Demonstration of nonlinear effects in an ultra-highly nonlinear AsSe suspended-core chalcogenide fiber," *IEEE Photon. Technol. Lett.*, vol. 22, no. 24, pp. 1844–1846, 2010.

[170] M. Duhant, W. Renard, G. Canat, T. Nguyen, F. Smektala, J. Troles, Q. Coulombier, P. Toupin, L. Brilland, P. Bourdon *et al.*, "Fourth-order cascaded raman shift in AsSe chalcogenide suspended-core fiber pumped at 2 μm," *Opt. Lett.*, vol. 36, no. 15, pp. 2859–2861, 2011.

[171] S. D. Le, D. Nguyen, M. Thual, L. Bramerie, M. Costa e Silva, K. Lenglé, M. Gay, T. Chartier, D. Brilland, L. Méchin, P. Toupin, and Troles, "Efficient four-wave mixing in a ultra-highly nonlinear suspended-core chalcogenide fiber," in *37th European Conference and Exhibition on Optical Communication (ECOC)*. IEEE, 2011.

[172] S. D. Le, D. Nguyen, M. Thual, L. Bramerie, M. Costa e Silva, K. Lenglé, M. Gay, T. Chartier, J.-C. Simon, L. Brilland, D. Méchin, P. Toupin, and J. Troles, "42.7 Gb/s RZ − 33% wavelength conversion in a chalcogenide microstructured fiber," in *Optical Fiber Communication Conference (OFC)*. Optical Society of America, 2012.

[173] S. D. Le, M. Gay, L. Bramerie, M. Costa e Silva, K. Lenglé, T. Chartier, M. Thual, J.-C. Simon, L. Brilland, D. Méchin, P. Toupin, and J. Troles, "Wavelength conversion in a highly nonlinear chalcogenide microstructured fiber," *Opt. Lett.*, 2012.

[174] S. D. Le, M. Gay, L. Bramerie, M. Costa e Silva, K. Lenglé, C. Pareige, T. Chartier, M. Thual, J. Simon, L. Brilland, D. M´ echin, P. Toupin, and J. Troles, "All-optical wavelength conversion of a 56 Gb/s DQPSK signal and all-optical demultiplexing of a 170 Gb/s OOK signal in chalcogenide photonic crystal fibers," in *38th European Conference and Exhibition on Optical Communication (ECOC)*. Optical Society of America, 2012.

[175] S. D. Le, M. Gay, L. Bramerie, M. Costa e Silva, K. Lenglé, C. Pareige, T. Chartier, M. Thual, J. Simon, L. Brilland, D. Méchin, P. Toupin, and J. Troles, "All-optical demultiplexing of a 170 Gb/s in a chalcogenide GeAsSe microstructured fiber," *Electron. Lett.*, vol. 49, no. 2, 2013.

[176] P. Andersen, T. Tokle, Y. Geng, C. Peucheret, and P. Jeppesen, "Wavelength conversion of a 40-Gb/s RZ − DQPSK signal using four-wave mixing in a dispersion-flattened highly nonlinear photonic crystal fiber," *IEEE Photon. Technol. Lett.*, vol. 17, no. 9, pp. 1908–1910, 2005.

[177] M. Galili, B. Huettl, C. Schmidt-Langhorst, A. Gual i Coca, R. Ludwig, and C. Schubert, "320 Gb/s DQPSK all-optical wavelength conversion using four wave mixing," in *Optical Fiber Communication (OFC)*. IEEE, 2007.

[178] T. Durhuus, B. Mikkelsen, C. Joergensen, S. Lykke Danielsen, and K. Stubkjaer, "All-optical wavelength conversion by semiconductor optical amplifiers," *J. Lightw. Technol.*, vol. 14, no. 6, pp. 942–954, 1996.

[179] Y. Liu, E. Tangdiongga, Z. Li, S. Zhang, H. Waardt, G. Khoe, and H. Dorren, "Error-free all-optical wavelength conversion at 160 Gb/s using a semiconductor optical amplifier and an optical bandpass filter," *J. Lightw. Technol.*, vol. 24, no. 1, p. 230, 2006.

[180] H. Kawaguchi, K. Oe, H. Yasaka, K. Magari, M. Fukuda, and Y. Itaya, "Tunable optical-wavelength conversion using a multielectrode distributed-feedback laser diode with a saturable absorber," *Electron. Lett.*, vol. 23, no. 20, pp. 1088–1090, 1987.

[181] R. Green, M. Haji, L. Hou, G. Mezosi, R. Dylewicz, and A. Kelly, "Fast saturable absorption and 10 GHz wavelength conversion in al-quaternary multiple quantum wells," *Opt. Exp.*, vol. 19, no. 10, pp. 9737–9743, 2011.

[182] K. Yamada, H. Fukuda, T. Tsuchizawa, T. Watanabe, T. Shoji, and S. Itabashi, "All-optical efficient wavelength conversion using silicon photonic wire waveguide," *IEEE Photon. Technol. Lett.*, vol. 18, no. 9, pp. 1046–1048, 2006.

[183] A. Pasquazi, Y. Park, J. Azaña, F. Légaré, R. Morandotti, B. Little, S. Chu, and D. Moss, "Efficient wavelength conversion and net parametric gain via four wave mixing in a high index doped silica waveguide," *Opt. Exp.*, vol. 18, no. 8, pp. 7634–7641, 2010.

[184] K. Inoue and H. Toba, "Wavelength conversion experiment using fiber four-wave mixing," *IEEE Photon. Technol. Lett.*, vol. 4, no. 1, pp. 69–72, 1992.

[185] J. Hansryd and P. Andrekson, "Broad-band continuous-wave-pumped fiber optical parametric amplifier with 49 dB gain and wavelength-conversion efficiency," *IEEE Photon. Technol. Lett.*, vol. 13, no. 3, pp. 194–196, 2001.

[186] V. Ta'Eed, L. Fu, M. Pelusi, M. Rochette, I. Littler, D. Moss, and B. Eggleton, "Error free all optical wavelength conversion in highly nonlinear AsSe chalcogenide glass fiber," *Opt. Exp.*, vol. 14, no. 22, pp. 10 371–10 376, 2006.

[187] N. Verscheure and C. Finot, "Pulse doubling and wavelength conversion through triangular nonlinear pulse reshaping," *Electron. Lett.*, vol. 47, no. 21, pp. 1194–1196, 2011.

[188] A. Camerlingo, F. Parmigiani, X. Feng, F. Poletti, P. Horak, W. Loh, D. Richardson, and P. Petropoulos, "Wavelength conversion in a short length of a solid lead–silicate fiber," *IEEE Photon. Technol. Lett.*, vol. 22, no. 9, pp. 628–630, 2010.

[189] H. Hu, H. Ji, M. Galili, M. Pu, C. Peucheret, H. Christian, H. Mulvad, K. Yvind, J. Hvam, P. Jeppesen, and L. Oxenlowe, "Ultra-high-speed wavelength conversion in a silicon photonic chip," *Opt. Exp.*, vol. 19, no. 21, pp. 19 886–19 894, 2011.

[190] K. Wang and A. Foster, "Ultralow power continuous-wave frequency conversion in hydrogenated amorphous silicon waveguides," *Opt. Lett.*, vol. 37(8), pp. 1331–1333, 2012.

[191] N. Ophir, R. Lau, M. Menard, X. Zhu, K. Padmaraju, Y. Okawachi, R. Salem, M. Lipson, A. Gaeta, and K. Bergman, "Wavelength conversion and unicast of 10-gb/s data spanning up to 700 nm using a silicon nanowaveguide," *Opt. Exp.*, vol. 20, no. 6, pp. 6488–6495, 2012.

[192] S. Kawanishi, H. Takara, T. Morioka, O. Kamatani, and M. Saruwatari, "200 Gb/s, 100 km time-division-multiplexed optical transmission using supercontinuum pulses with prescaled PLL timing extraction and all-optical demultiplexing," *Electron. Lett.*, vol. 31, no. 10, pp. 816–817, 1995.

[193] N. Patel, K. Rauschenbach, and K. Hall, "40 Gb/s demultiplexing using an ultrafast nonlinear interferometer (UNI)," *IEEE Photon. Technol. Lett.*, vol. 8, no. 12, pp. 1695–1697, 1996.

[194] T. Ohara, H. Takara, I. Shake, K. Mori, K. Sato, S. Kawanishi, S. Mino, T. Yamada, M. Ishii, I. Ogawa *et al.*, "160 Gb/s OTDM transmission using integrated all-optical MUX/DEMUX with all-channel modulation and demultiplexing," *IEEE Photon. Technol. Lett.*, vol. 16, no. 2, pp. 650–652, 2004.

[195] E. Tangdiongga, Y. Liu, H. De Waardt, G. Khoe, A. Koonen, H. Dorren, X. Shu, and I. Bennion, "All-optical demultiplexing of 640 to 40 Gb/s using filtered chirp of a semiconductor optical amplifier," *Opt. Lett.*, vol. 32, no. 7, pp. 835–837, 2007.

[196] N. Bergano, C. Davidson, C. Chen, B. Pedersen, M. Mills, N. Ramanujam, H. Kidorf, A. Puc, M. Levonas, and H. Abdelkader, "640 Gb/s transmission of sixty-four 10 Gb/s

WDM channels over 7200 km with 0.33 (bits/s)/Hz spectral efficiency," in *Optical Fiber Communication Conference (OFC)*. IEEE, 1999.

[197] B. Olsson and D. Blumenthal, "All-optical demultiplexing using fiber cross-phase modulation (XPM) and optical filtering," *IEEE Photon. Technol. Lett.*, vol. 13, no. 8, pp. 875–877, 2001.

[198] J. Lee, T. Tanemura, K. Kikuchi, T. Nagashima, T. Hasegawa, S. Ohara, and N. Sugimoto, "Use of 1-m Bi_2O_3 nonlinear fiber for 160 Gb/s optical time-division demultiplexing based on polarization rotation and a wavelength shift induced by cross-phase modulation," *Opt. Lett.*, vol. 30, no. 11, pp. 1267–1269, 2005.

[199] T. Yamamoto, E. Yoshida, and M. Nakazawa, "Ultrafast nonlinear optical loop mirror for demultiplexing640 Gb/s TDM signals," *Electron. Lett.*, vol. 34, no. 10, pp. 1013–1014, 1998.

[200] P. Andrekson, N. Olsson, J. Simpson, D. Digiovanni, P. Morton, T. Tanbun-Ek, R. Logan, and K. Wecht, "64 Gb/s all-optical demultiplexing with the nonlinear optical-loop mirror," *IEEE Photon. Technol. Lett.*, vol. 4, no. 6, pp. 644–647, 1992.

[201] Q. Xu, B. Schmidt, S. Pradhan, and M. Lipson, "Micrometre-scale silicon electro-optic modulator," *Nature*, vol. 435, no. 7040, pp. 325–327, 2005.

[202] J. Li, B. Olsson, M. Karlsson, and P. Andrekson, "OTDM demultiplexer based on XPM-induced wavelength shifting in highly nonlinear fiber," in *Optical Fiber Communication Conference (OFC)*. Optical Society of America, 2003.

[203] M. Scaffardi, F. Fresi, G. Meloni, A. Bogoni, L. Poti, N. Calabretta, and M. Guglielmucci, "Ultra-fast 160:10 Gb/s time demultiplexing by four wave mixing in 1m-long B_2O_3-based fiber," *Opt. Commun.*, vol. 268, no. 1, pp. 38–41, 2006.

[204] A. Camerlingo, F. Parmigiani, X. Feng, F. Poletti, W. Loh, D. Richardson, and P. Petropoulos, "160-to-40 Gb/s time demultiplexing in a low dispersion lead-silicate w-index profile fiber," in *Optical Fiber Communication Conference (OFC)*. Optical Society of America, 2011.

[205] M. Costa e Silva, A. Lagrost, L. Bramerie, M. Gay, P. Besnard, M. Joindot, J. Simon, A. Shen, and D. Duan, "Up to 427 GHz all optical frequency down-conversion clock recovery based on quantum-dash fabry–perot mode-locked laser," *J. Lightw. Technol.*, vol. 29, no. 4, pp. 609–615, 2011.

[206] Q. Le, L. Bramerie, M. Gay, M. Joindot, J. Simon, A. O'Hare, H. Nguyen, and J. Oudar, "All-optical phase-preserving amplitude regeneration of 28 Gbaud RZ-DQPSK signals with a microcavity saturable absorber in a recirculating loop experiment," in *Optical Fiber Communication Conference and Exposition (OFC)*. IEEE, 2011.

[207] S. D. Le, M. Gay, L. Bramerie, M. Costa e Silva, K. Lenglé, C. Pareige, T. Chartier, M. Thual, J. Simon, L. Brilland, D. Méchin, P. Toupin, and J. Troles, "Wavelength conversion of a 170 Gb/s signal in a chalcogenide GeAsSe microstructured fiber," *IEEE Photon. Technol. Lett.*, 2012.

[208] Z. Hui and J. Zhang, "Wavelength conversion, time demultiplexing and multicasting based on cross-phase modulation and four-wave mixing in dispersion-flattened highly nonlinear photonic crystal fiber," *J. Opt.*, vol. 14, no. 5, p. 055402, 2012.

[209] X. Wu, A. Bogoni, M. Scaffardi, G. Berrettini, P. Ghelfi, L. Potì, G. Meloni, and A. Willner, "Multiplexing two 40 Gb/s WDM signals into an 80 Gb/s signal using XPM in 0.8 metre Bi-HNLF," *Electron. Lett.*, vol. 45, no. 5, pp. 281–282, 2009.

[210] J. Xu, Y. Ding, C. Peucheret, J. Seoane, H. Mulvad, M. Galili, W. Xue, J. Mørk, and P. Jeppesen, "Demultiplexing of OTDM-DPSK signals based on a single semiconductor optical amplifier and optical filtering," *Opt. Lett.*, vol. 36, no. 9, pp. 1560–1562, 2011.

[211] B. Corcoran, M. Pelusi, C. Monat, J. Li, L. O'Faolain, T. Krauss, and B. Eggleton, "Ultracompact 160 Gbaud all-optical demultiplexing exploiting slow light in an engineered silicon photonic crystal waveguide," *Opt. Lett.*, vol. 36, no. 9, pp. 1728–1730, 2011.

[212] S. Jansen, M. Heid, S. Spalter, E. Meissner, C. Weiske, A. Schopflin, D. Khoe, and H. De Waardt, "Demultiplexing 160 Gb/s OTDM signal to 40 Gb/s by FWM in SOA," *Electron. Lett.*, vol. 38, no. 17, pp. 978–980, 2002.

[213] Y. Fukuchi, T. Sakamoto, K. Taira, and K. Kikuchi, "All-optical time-division demultiplexing of 160 Gb/s signal using cascaded second-order nonlinear effect in quasi-phase matched $LiNbO_3$ waveguide device," *Electron. Lett.*, vol. 39, no. 10, pp. 789–790, 2003.

Index

VU :

Le Directeur de thèse

VU :

Le Responsable de l'École Doctorale

Pr. J-F. CARPENTIER
Directeur Ecole Doctorale SDLM

N° UR1 2012/ENSSAT/12 n°202

VU pour autorisation de soutenance
Rennes, le 21 novembre 2012
Le Président de l'Université de Rennes 1

Guy Cathelineau

P/le Président et par délégation
le Vice-Président

VU après soutenance pour autorisation de publication :
Le Président de Jury,

Abstract:

The growth of optical transmission network capacity leads to a requirement for all-optical signal processing. In this thesis, based on nonlinear effects in optical fibers, three fundamental functions were all-optically demonstrated at high bit-rates. Regeneration of a 160 Gb/s signal was theoretically demonstrated in dense-dispersion-managed silica fibers for the first time. Wavelength conversion and time-division demultiplexing of optical signals at bit-rates up to 170.8 Gb/s were successfully experimented, also for the first time, by using chalcogenide microstructured fibers. These results show the high potentiality of chalcogenide fibers for all-optical signal processing in the future high-speed transmission systems.

Key words: all-optical signal processing, regeneration, wavelength conversion, time-division demultiplexing, chalcogenide glass, microstructured fibers.

Résumé :

L’augmentation de la capacité du réseau de transport optique se traduit par le besoin de fonctions de traitement tout-optique du signal. Dans cette thèse, trois fonctions fondamentales de traitement du signal, basées sur les effets non-linéaires dans les fibres optiques, sont démontrées à de très hauts débits. La régénération d'un signal à 160 Gbit/s a été démontrée théoriquement dans des fibres en silice à gestion dense de la dispersion pour la première fois. La conversion de longueur d'onde et de démultiplexage temporel de signaux optiques à des débits allant jusqu'à 170,8 Gbit/s ont également été démontrés expérimentalement pour la première fois à l'aide de fibres microstructurées en verres de chalcogénures. Ces résultats montrent la forte potentialité des fibres en verres de chalcogénures pour le traitement du signal tout-optique dans les futurs systèmes de transmission optique à très haut débit.

Mots clès : traitement tout-optique du signal, régénération, conversion de longueur d’onde, démultiplexage temporel, verre de chalcogénure, fibre microstructurée